Development of a contactless capacitive immunosensor

THÈSE N^{O} 4763 (2011)

PRÉSENTÉE LE 25 FÉVRIER 2011

À LA FACULTÉ SCIENCES DE BASE
LABORATOIRE D'ÉLECTROCHIMIE PHYSIQUE ET ANALYTIQUE
PROGRAMME DOCTORAL EN CHIMIE ET GÉNIE CHIMIQUE

ÉCOLE POLYTECHNIQUE FÉDÉRALE DE LAUSANNE

POUR L'OBTENTION DU GRADE DE DOCTEUR ÈS SCIENCES

PAR

Brice Emmanuel PERRUCHE

acceptée sur proposition du jury:

Prof. P. Vogel, président du jury
Prof. H. Girault, directeur de thèse
Prof. R. Ferrigno, rapporteur
Dr L. Murtomäki, rapporteur
Dr S. Terrettaz, rapporteur

ÉCOLE POLYTECHNIQUE
FÉDÉRALE DE LAUSANNE

Suisse
2011

Everything we call real is made of things that cannot be regarded as real.

Niels Bohr

Remerciements

Je tiens à exprimer au Professeur Hubert Girault toute ma gratitude pour m'avoir accueilli dans son laboratoire afin d'effectuer ce travail de thèse. Durant ces années, j'ai pu apprécier toute l'étendue de ses connaissances scientifiques, et ses conseils avisés m'ont été très profitables. Ses nombreux encouragements et commentaires constructifs durant ce travail ont été pour moi une importante source de motivation.

Je voudrais remercier chaleureusement mes collègues, le Dr Niels Lion pour son aide en début de thèse, ainsi que le Dr Jean-Marc Busnel pour son éternelle bonne humeur et sa grande disponibilité, ses nombreux et précieux conseils et suggestions en matière de biologie. Merci au Dr Jacques Josserand pour nos longues conversations sur les simulations, les équations et les modèles. Mais également sur bien d'autres sujets non-scientifiques ainsi que son approche de la vie, qui m'ont permis de prendre un peu de recul durant cette thèse. Merci également pour le temps passé à la relecture du chapitre de simulations de ma thèse. Merci à Valérie Devaud pour son aide technique mais surtout son soutien moral quand rien ne fonctionnait ainsi que pour toutes les discussions que nous avons pu avoir. Merci également à Loïc et Mélanie pour leur amitié durant la majeure partie de ce travail.

Mes remerciements vont également à Maria Szuman et Anne-Lene Odegaard pour pour toutes les démarches effectuées durant ce travail. Je ne saurais oublier le personnel de l'atelier mécanique, en particulier André Fattet, Roger Mottier et Cédric Mora, pour leur bonne humeur et leur talent, sans lequel ce travail n'aurait pas été possible.

Merci également aux personnes de l'atelier électronique, et en particulier Gabriel Roch, pour leurs conseils.

Le projet Allergy Card fut l'occasion de rencontres intéressantes. Je tiens à remercier les membres des différents laboratoires participant au projet, dont le Dr Stéphanie Descroix et le Prof Gabriel Peltre, pour les bons moments passés en leur compagnie. Merci également au Dr Jacques Morandini d'Astek pour les échanges intéressants que nous avons eu autour de Flux-Expert.

Je tiens à remercier les membres de mon jury de thèse, les Prof Rosaria Ferrigno, Dr Samuel Terretaz et Dr Lasse Murtomäki, pour leur lecture attentive de mon manuscrit, ainsi que pour leurs conseils et commentaires constructifs. Merci au Prof Pierre Vogel d'avoir accepté d'être le président de mon jury.

Merci aux autres membres du laboratoire, anciens ou présents, avec lesquels j'ai eu beaucoup de plaisir à partager des moments et soirées : Fernando, Manuel, Astrid, Mohamad, Imren, Liang, Reza, Dmitri, Gaëlle, Nicolas, Lydie, Hong Xu, Christophe, Bin. Je remercie également mes amis lyonnais Michael, Christophe, Jérome, Paolo, Loïc, mais également mes amis lausannois, Sandie et Cédric, pour leurs encouragements.

Je tiens à terminer ces remerciements par ma famille, qui a toujours été là dans les bons et mauvais moments. Merci à mes parents, Annette et Georges, pour leur soutien et leur compréhension durant ces dernières années, ainsi que mon frère Julien pour sa présence. Merci également à Bernadette et Daniel pour leurs encouragements. Je tiens aussi à remercier Raphaël ainsi que mes beaux-parents, Vivianne et Philippe, pour leur soutien.

Enfin, merci de tout coeur à Anne-Laure de m'avoir supporté, ainsi que du temps passé à la relecture de certains chapitres de ma thèse. Merci pour sa patience, pour avoir cru en moi et m'avoir encouragé durant ces années de thèse, et d'avoir été là même dans les moments les plus pénibles.

Abstract

In the present work, a label-free, contactless and capacitive immunosensor is developed using impedance spectroscopy, in the aim to perform low-cost immunoassays. Chapter 1 puts this work in perspective with some existing techniques, while a presentation of impedance theory used in this work is carried out in chapter 2.

In Chapter 3, numerical simulations using a commercial finite element method software is carried out. The response of coplanar and face-to-face designs using an insulating layer is studied with respect to a frequency ranging from 100 Hz to 10 MHz . Two levels of capacitance were observed across the frequency range : the low frequency capacitance created by the insulating layer and the high frequency capacitance created by the solution. These capacitances depends on parameters like the solution conductivity, the distance between the electrodes, the electrodes width or the insulating layer thickness. A dimensionless parameter is defined to evaluate the quality of the geometry at high frequencies.

Microchips using a coplanar design are developed in Chapter 4. They are composed of two silver electrodes drilled in a PET sheet by laser photoablation. The design of both holder and of the microchips is optimized to increase as much as possible the signal-to-noise ratio. Bovine Serum Albumin is detected by a variation of the channel conductivity.

Chapter 5 introduces the design of a sensor using electrodes made of a mass market aluminium foil. The study of the frequency response of the electrodes led to the creation of a discrete analytical model. The electrodes are then mounted into a holder using a face-to-face or coplanar design. The system is characterized through the variation of several geometrical parameters (height of fluid in the reservoir, electrode surface area, solution conductivity, ...). The coplanar design is also optimized to be able to work in a holder equipped with a fluidic channel.

Finally, the ability of the aluminium electrodes based sensor to monitor an adsorption is studied in Chapter 6. The resonance is used to detect the adsorption of proteins like BSA on the electrodes using coplanar and face-to-face designs. The adsorption is found to follow a Langmuir isotherm and an adsorption equilibrium constant is extracted. The second adsorbate layer is detected using a coplanar design, enabling the achievement of a immunoassay..

Keywords: Immunosensor, biosensor, label-free, contactless, capacitive, impedance.

Résumé

Dans ce travail de thèse est développé un capteur permettant, en utilisant la spectroscopie d'impédance, de réaliser des tests immunologiques de manière capacitive, sans contact avec la solution et sans besoin d'utiliser d'espèces marquées, dans le but d'effectuer des test immunologiques peu coûteux. Le Chapitre 1 met ce travail en perspective avec certaines techniques actuelles. Une présentation des principes d'impédance utilisés dans ce travail est effectuée dans le Chapitre 2.

Des simulations numériques sont effectuées avec un logiciel commercial éléments finis. La réponse de géométries coplanaires et face-à-face utilisant un isolant est étudiée pour une gamme de fréquences comprises entre 100 Hz and 10 MHz. Deux niveaux de capacitance sont observés sur la gamme de fréquence : la capacitance à basse fréquence créée par l'isolant, et la capacitance à haute fréquence créée par la solution. Ces capacitances sont dépendantes de paramètres comme la conductivité de la solution, la distance entre les électrodes, la largeur des électrodes ou l'épaisseur de l'isolant. Un nombre adimensionnel est défini pour évaluer la qualité du signal à haute fréquence.

Des capteurs miniaturisés utilisant un microcanal et une géométrie coplanaire sont développés dans le Chapitre 4. Ils sont composés de deux électrodes d'argent creusées dans une feuille de PET par photoablation laser. Les géométries du conteneur et du capteur miniaturisé sont optimisées pour augmenter autant que possilbe le rapport signal-sur-bruit. De l'Albumine Sérique Bovine (ASB) est détectée grâce à une varia-

tion de la conductivité du canal.

Le chapitre 5 introduit la géométrie d'un capteur utilisant des électrodes réalisées à partir d'une feuille d'aluminium de grande consommation. L'étude de la réponse en fréquence des électrodes a permis la création d'un modèle analytique discret. Les électrodes sont alors montées dans un conteneur en utilisant une géométrie de type face-à-face ou coplanaire. Le systèmes est caractérisé à travers la variation de plusieurs paramètres géométriques (hauteur de fluide dans le réservoir, surface d'électrode, conductivité de la solution, ...) La géométrie coplanaire est également optimisée de façon à pouvoir être utilisée dans un conteneur équipé d'un canal fluidique.

Finalement, la capacité du capteur basé sur les électrode d'aluminium à monitorer une adsorption est étudiée dans le Chapitre 6. La résonance est utilisée pour détecter l'adsorption de protéines comme de l'ASB sur les électrodes utilisant une géométrie ou face-à-face. L'adsorption suit une isotherme de Langmuir et une constant d'équilibre d'adsorption est extraite. La seconde couche adsorbée est détectée en utilisant une géométrie coplanaire, permettant la réalisation d'un test immunologique.

Mots-clé: capteur immunologique, biocapteur, sans-marqueur, sans-contact, capacitif, impédance.

Contents

Chapter 1

Introduction

This thesis work was part of the Allergy Card European project, involving four laboratories : The Pierre and Marie Curie Institute (France), Ecole Centrale de Paris (France), Politechnico Milano (Italia), and our laboratory. This project aimed at developping a novel kind of immunologic device within a credit card size (Figure 1.1), while keeping the device cost at the lowest possible level as it would have been used only once. As the involved technologies were cutting edge, this project was very ambitious. The Ecole Centrale de Paris was responsible for the separation unit (CABCE)[1–5], from the blood patient injection to the entry of the detector, this latter element being under the responsability of our laboratory. Fluidics management of the device was assured by the Pierre and Marie Curie institute[6], while Politechnico Milano was in charge of providing a suitable separation gel for the CABCE[7–11].

The initial goal of this thesis was to optimize the electrodes design of an existing detector, previously developed by Gamby et al in our laboratory[12, 13]. It quickly turned out that everything had to be redesigned for the Allergy Card project, and the goal of this work became a whole immunosensor development.

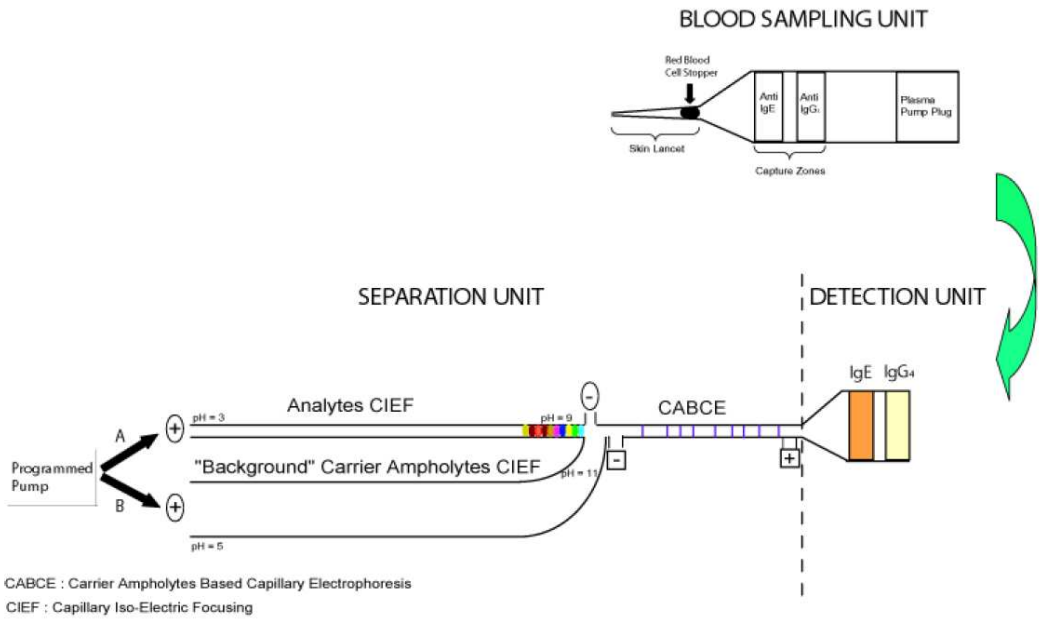

Figure 1.1: Scheme of the Allergy card device

Being part of Allergy Card, the detector development was aimed at allergens detection. Allergens are antigens recognised by IgE antibodies from allergic patients. Allergy is a rapidly growing disease which has seen a doubling of the cases in the last 15 years. Some new allergy cases are particularly difficult to diagnose since they are directed to food allergens. In this context, the importance of biosensors is increasing.

1.1 A large family of biosensors

Detection of protein, IgG and other biological species have been studied for a long time. Almost any physical or chemical effect has been used to detect biological species: calorimetry, resistance, capacitance, evanescent waves, pH variation, fluorescence. Considering the vast amount of methods involving these effects, this leads to a huge quantity of techniques developped to detect species. However a difference can be made between detectors that can detect only one or more species, and detectors that can detect at least a reaction between two species. The first family includes DNA sensors,

conductive and capacitive channel conductivity detection, and many others. The other family will be developed in the coming sections. However, so many sensors exist, so that this introduction cannot be exhaustive. Thus, some sensors like calorimetry[14, 15], capillary electrophoresis[16, 17] or quartz cristal microbalance[18, 19] will not be developed.

Two large classes of immunosensors can be defined : Labeled and label-free. Labeled biosensors are derived from the immunoassay technology. This type of sensor, like the fluorescence, is expensive, and makes real-time measurements impossible. Biosensors for direct, label-free measurements of various analytes are attractive, as they also provide real-time monitoring. Optical biosensors has been the most studied, but electrochemical biosensors might offer at least the same detection range and provide a less complicated instrumentation.

1.2 Labeled immunosensors

1.2.1 Fluorescence techniques

Fluorescence requires the tagging of a recognition species to be detected by a fluorophore. Fluorescence analyses have traditionally been done in microliter plates, usually using 96 to 384 wells. The most common of these analyses is the ELISA test, whose sandwich variant[20] is often used (Figure 1.2):

- Capture antibodies are adsorbed on the wall.
- After washing, patient serum is injected in the well. If present, antigens bind specifically to the adsorbed antibody.
- An enzymed linked antibody is added after washing, and binds the antigen, if present.

- After a third wash, the substrate is finally added, reacts with the enzyme. Photons are produced from the reaction.

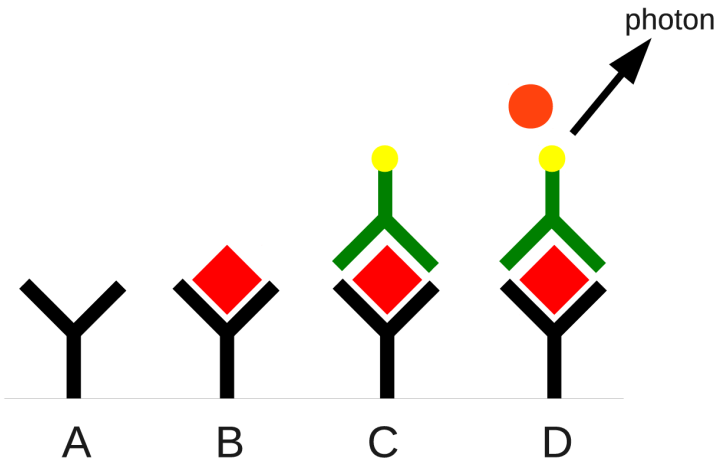

Figure 1.2: Scheme of a Sandwich ELISA. Antibody is adsorbed on the wall (A). Patient antigen binds on it (B). A tagged antibody binds to the antigen, if present (C). The enzyme reacts with the substrate to produce photons (D).

In order to detect the adsorption and/or immuno-capture of the tagged analyte on a surface in real time, while excess of tagged analyte are present in solution, confocal microscopy can be used [21, 22]. This technique illuminates the whole solution, but

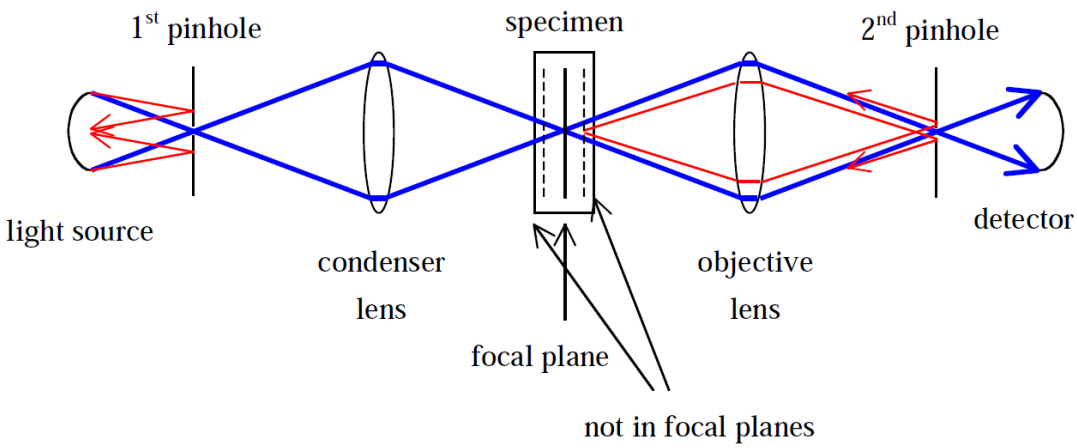

Figure 1.3: Scheme of confocal microscopy. The light is focused on one plane[23].

collects light from a thin section above the sensing surface only. Evanescent waves

techniques can also be used. This technique illuminates only a thin section of liquid above the sensing surface [24].

Fluorescence has been miniturized using confocal microscopy and microchannels. Figure 1.4 shows the sensogram obtained by confocal microscopy of the adsorption of IgG on a plastic substrate in a microchannel, as demonstrated by Andrea Lionello [23].

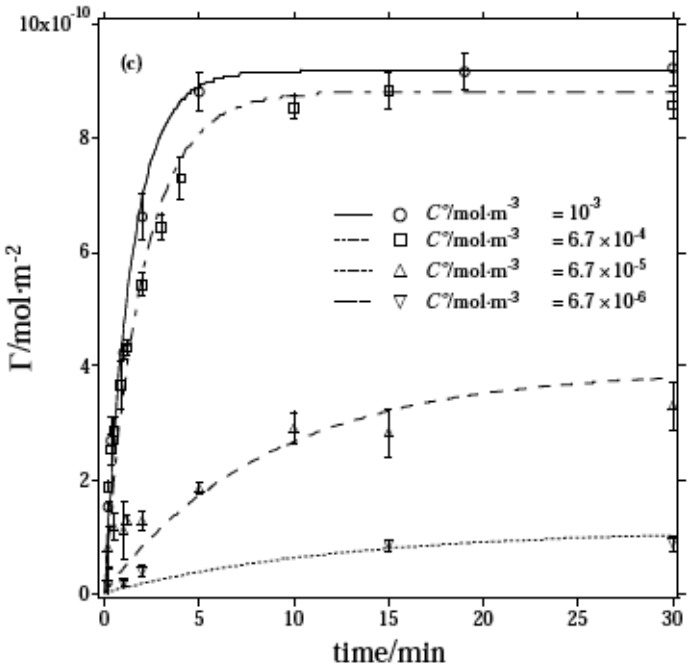

Figure 1.4: IgG adsorption on a polyethylene terephthalate substrate monitored on a home-made confocal microscope[23].

Fluorescence techniques usually exhibit sensitivities in the low nanomolar range. Latest developments of fluorescence include quantum dots as fluorescent tag to enhance sensitivity[25]. Quantum dots are semiconductor nanocrystals[26]. The three dimensions of the cristal are limited to less than one exciton (quasi-particle) radius. This creates a potential well where electrons and holes are confined in a distance equal to the luminescent wavelength. The main advantage of quantum dots over traditional

fluorophore is a narrow emission bandwidth, and a high brightness and stable photoluminescence.

The major drawback of fluorescence is that it requires the tagging of the recognition species, and that fluorescence instrumentation is relatively expensive and delicate to operate (at least in the confocal or evanescent-wave modes).

1.2.2 Electrochemical detection

Labeled electrochemical detection can be based, like the fluorescence, on a sandwich ELISA. The main difference in the technique is that the enzyme reaction with the substrate does not produce photons but electrons. These electrons are collected by electrodes, usually made from gold, and the signal is monitored by amperometry.

The detection has traditionaly been performed in reservoirs[27–29]. However the trend is to go to microchannels, which reduces the diffusional effects and thus the adsorption and reaction times[30–34]. When using a microchannel, the species are typically adsorbed on the channel walls. A good way to increase the signal response would be to increase the specific surface of the sensor. This can be done by adsorbing nanoparticles on the channel walls [35]. Another solution would be to dispose nanoscale magnetic beads in the channel [36, 37] to trap more species when flowing through the channel.

Commercial applications of ELISA electrochemical detection are numerous. Diagnoswiss has been selling since 2005 ELISA in microchannel, using gold microelectrodes[38]. ELISA electrochemical detection limit is low, and the use of a microchannel decreased the time needed to make an analysis. However, some drawbacks are still present, like the lack of real time monitoring of the binding reaction.

1.3 Label-free biosensors

1.3.1 IS-FET

The transistor was invented in 1947 by Bardeen and Brattain [39] . 60 years later, billions of them can be found in the latest microprocessors : This circuit element is the heart of our modern world. However, the transistor has been used for 40 years as biosensors in the form of IS-FETs (Ion-Sensitive Field Effect Transistor) [40].

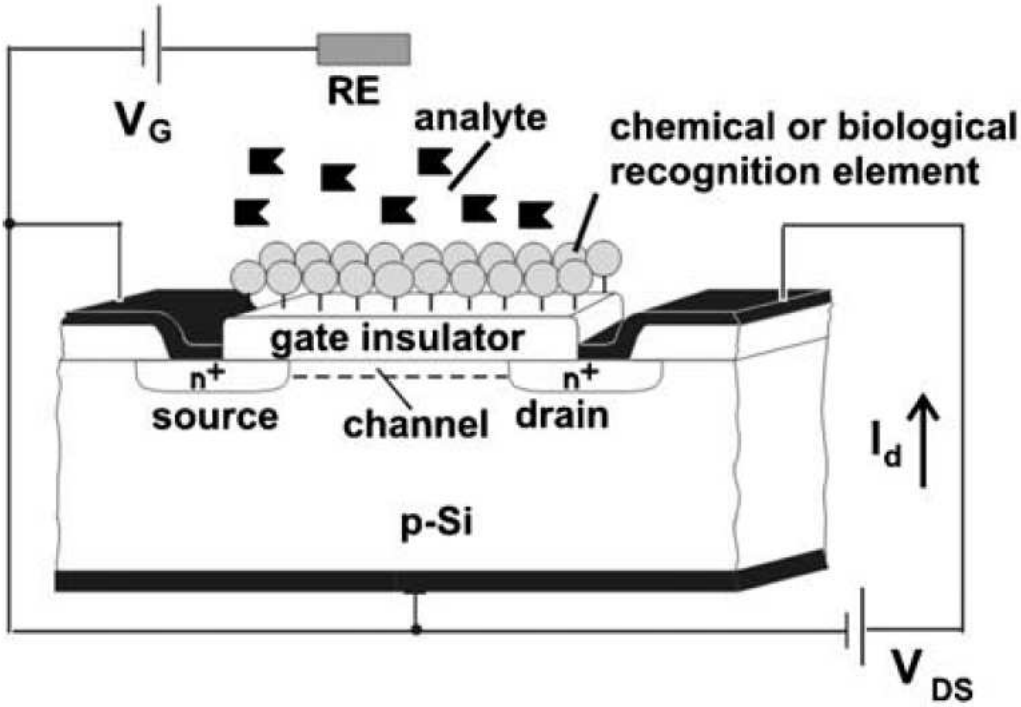

Figure 1.5: Scheme of a P-channel IS-FET[41].

A transistor is made of three parts : A source, a gate and a drain (Figure 1.5). Two large transistor families exist: Bipolar transistor and Field Effect Transistor (FET). Bipolar transistors are driven by the current flowing through the base, while Field Effect transistors are driven by the potential difference between the gate and the source. FET families are composed of Junction FET (JFET) and Insulated Gate FET (IGFET). Most IGFET are actually Metal-Oxyde Semiconductor FET (MOSFET). IS-FET take place into

the IGFET family: As can be observed on Figure 1.5, the species are recognized on the gate insulator part of the transistor [41], the gate electrode being replaced by the solution. Changes in the chemical composition of the analyte induces changes in the electrical surface charge of the FET, and as a consequence modulate the current in the IS-FET channel. The Reference Electrode (RE) is placed in the solution, and is used as a reference of the gate surface charge variations.

Charges variations on the gate surface can be induced by a pH variation, ion concentration variation due to enzymatic variations, or adsorption of charged molecules. IS-FET based devices have then been used to detect DNA [42–44], polyelectrolytes, or proteins [45–50].

The gate insulating material is crucial as it governs the adsorption properties of the IS-FET. Most IS-FETs use SiO_2 as gate insulating material. However, Al_2O_3 has been used as gate insulator for some IS-FET[51, 52], which have been commercialized. Recently, some ways have been explored to enhance transistor sensitivity and reduce device size. Silicon nanowires[53] were used to detect cancer antigens[54]. The signal was measured using a conductivity variation of the nanowire. Carbon nanotubes, and especially Single-Wall nanotubes (SWNT) have also been investigated. SWNT-FET[55, 56] have been used to detect Escherichia coli[57] or Hepathisis C virus[58].

1.3.2 Surface Plasmon Resonance

Surface plasmons are surface electromagnetic waves that propagate parallel to a metal/dielectric interface [59, 60]. The electric field amplitude of the evanescent wave extends to a few nanometers in the dielectric material, and decreases exponentially. The main components of the SPR technique are a laser whose light is polarized, a prism and a piece of glass sputtered with a metal layer (in general gold). The piece of glass

(sensor) is sticked on a face of the prism with some special oil whose refrative index is close to the prism's (Figure 1.6).

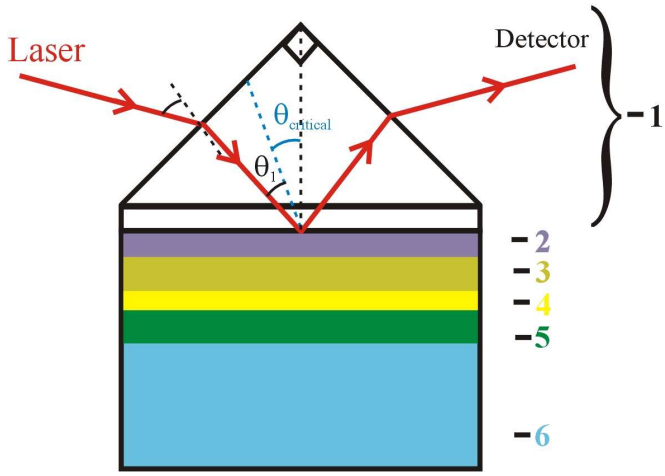

Figure 1.6: Principle of the SPR technique measurement

The thin metal layer sputtered on the glass acts as a resonator[59]. The resonance is driven by the laser beam, and depends on the angle between the laser beam and the surface (Figure 1.7).

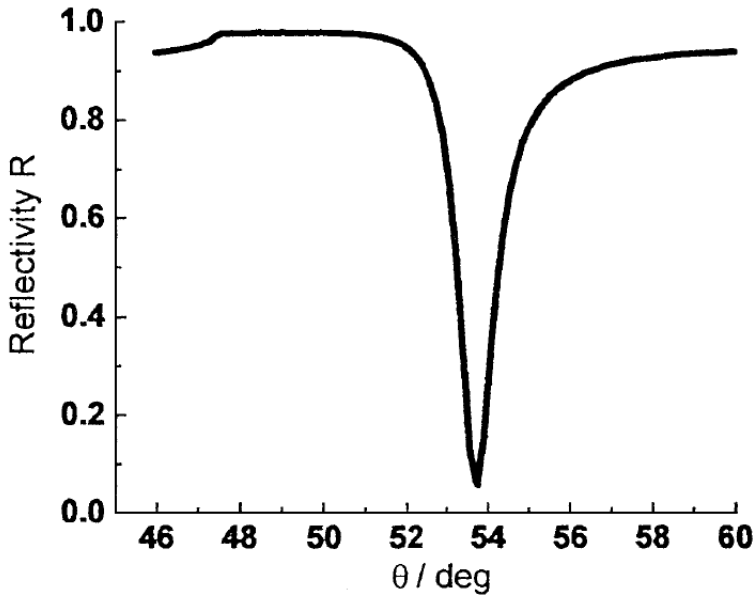

Figure 1.7: Reflectivity with respect to the laser beam angle[59].

When adsorbing, the species (DNA, molecule) change the local index of refraction

of the metal surface. This shifts the resonance to a lower or higher angle, depending on the index of refraction variation. Many layers can be adsorbed, which makes the SPR technique useful to study the interactions between several molecules, or run immunoasays[61–65] and extract kinetics constants of the reaction.

Many commercial applications using SPR technique appeared among the years. The most popular are BIAcore's products, which can be found in fields like antibody characterization, proteomics, immunogenicity. BIAcore has been extensively used to find kinetic constants of different mechanisms.

The SPR technique is label-free and allows real time monitoring of adsorption and desorption. However, the need of a laser and prism makes the technique not carryable in its standard configuration. Reducing sample volume has been a key challenge in SPR. This has been done by using microchannels and creating portable SPR[61, 66–68].

1.3.3 Surface enhanced Raman scattering

Raman spectroscopy

Raman spectroscopy was discovered in 1928 by Chandrasekhara Venkata Raman et al[69]. This technique is non-destructive and consists in studying vibrational transitions from inelastic diffusion of light. A monochromatic wave (typically a laser beam) is sent on a sample and propagates through it. The diffusion is elastic when the photon diffuses with no energy variation (Raleygh diffusion).

The diffusion is inelastic when the photon diffuses with a positive (Stokes variation) or negative (Anti-Stokes) energy variation. As can be observed on Figure 1.8a, Stokes diffusion is the result of a diffused photon whose energy is lower than the incident photon. The energy loss is due to the creation of a phonon in the sample. The Anti-Stokes diffusion results in the destruction of a phonon: The diffused photon energy is higher than the incident photon one.

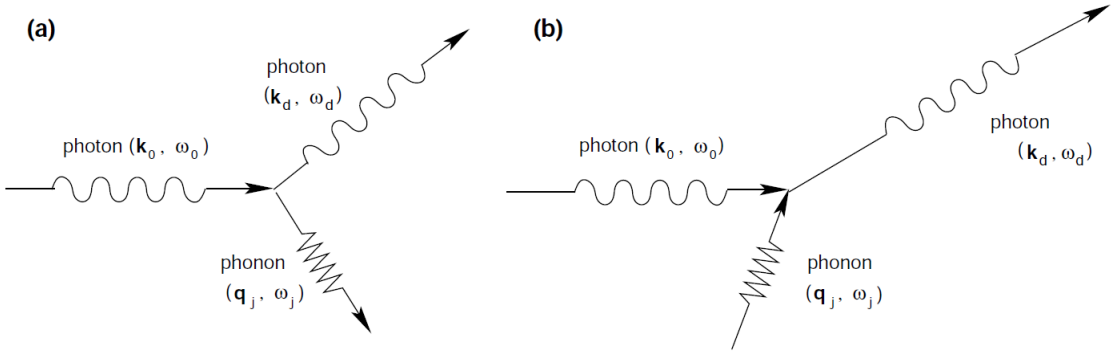

Figure 1.8: Stokes (a) and Anti-Stokes (b) diffusion created from an incident photon[70].

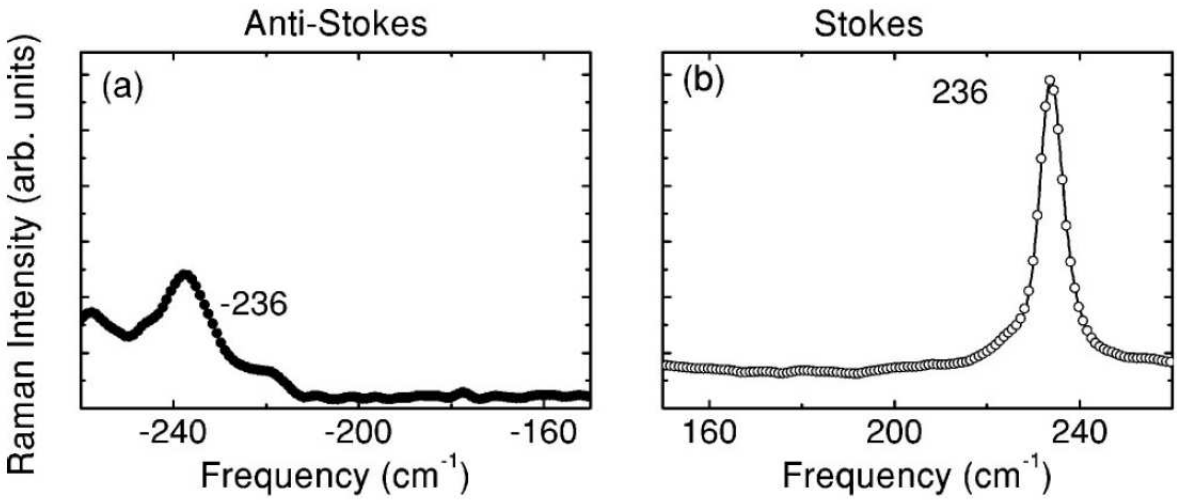

Figure 1.9: Anti-Stokes and Stokes diffusion peaks. The Anti-Stokes peaks are negative values, while positive values represent the Stokes diffusion[71].

Figure 1.9 presents Anti-Stokes and Stokes peaks for Raman spectroscopy of Multi-Wall Carbon nanotubes[71]. Peaks due to Anti-Stokes diffusion are negative, as the diffuse photon energy is higher than the incident photon one. This is the reverse the for Stokes diffusion.

SERS

SERS (Surface Enhanced Raman Scattering) was discovered in 1974 by Fleischmann et al when studying the adsorption of pyridine on a silver electrode, using Raman

spectroscopy[72]. This technique is somewhat close to the SPR, as it consists in illuminating a metal with a laser beam, most of the time silver (but also gold). The laser beam produces surface plasmons on the metal. From the explaination given by Jeanmaire and Van Duyne in 1977[73], the plasmons create an electric field that amplifies the electric field of the species adsorbed on the metal, by a factor up to 10^{11}. This leads to a huge signal from the adsorbed molecules. The technique has been used to perform immunoassays[74, 75].

Nowadays, SERS is used by adsorbing species on silver or gold nanoparticles[76]. As nanoparticles enhance the surface to volume ratio, higher sensitivities can be reached than on planar metal substrates. Detection limit has been reported to be in the femtomolar range[77], and even of a single molecule[78]. SERS has been commercialized as Klarite, a planar gold electrode product.

1.3.4 Capacitive biosensors

The capacitive biosensor field is rather new, as the first article of a biosensor based on a capacitive transducer for liquids was published in 1986. From then, "Capacitive biosensors" emerged and cover today a wide range of biosensors types. Two main kinds of capacitive biosensors phenomena can be distinguished: Interelectrode capacitance, and surface capacitance.

Interelectrode capacitance

Interelectrode capacitance aimed at measuring the capacitance variation between two electrodes separated by an aqeous solution. The capacitance variation results in the modification of the solution relative permittivity when species are present between the electrodes. The relative permittivity of species like antibodies or proteins is lower than those of a saline solution. The resulting capacitance will then be lower than initially when such species are present between the electrodes.

Chen et al used a coplanar electrode design to detect droplets position in microfluidic devices [79]. The capacitance of the device is directly influenced by the channel height. The position of the droplets is monitored by measuring the variation of capacitance between the two electrodes, through a relative permittivity variation of the element introduced in the channel (air or water).

Biosensors using interdigitated electrodes (Figure 1.10) can work in creating multiple volume capacitors, using solution between each finger as a dielectric [80].

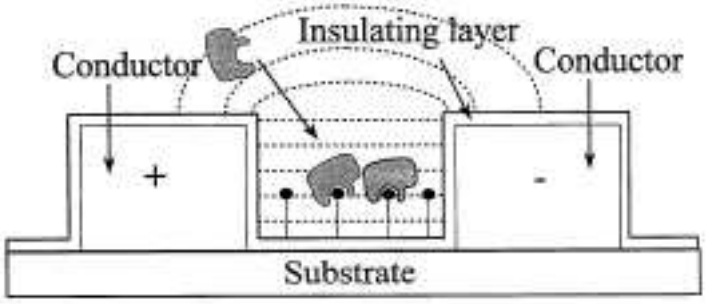

Figure 1.10: Scheme of the recognition of species using interdigitated electrodes covered by an insulating layer[80]

Although this kind of electrodes allows a high global capacitance, the distance between two fingers need to be as small as possible and is then difficult to reproduce.

Surface capacitance

Surface capacitance biosensors are based on the electrical double-layer theory. Original surface capacitive sensors were designed using a metallic (gold, silver) or carbon electrode. The electrode is then put in contact with the solution, and an electrical double-layer is created at the electrode-solution interface.

Electrical double-layer is composed of a Gouy-Chapman diffuse layer, and then of a Helmholtz layer[81]. The diffuse layer thickness depends on the solution conductivity,

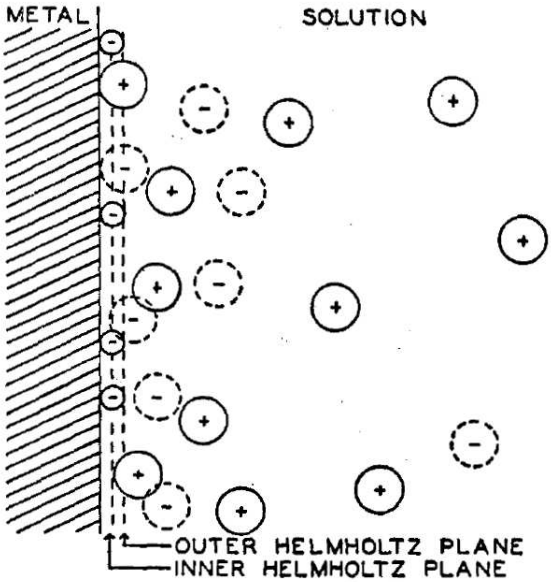

Figure 1.11: Scheme of the Electrical Double-Layer (EDL). The EDL is composed of the Helmholtz layer and Gouy-Chapman diffuse layer. The Helmholtz plane itself is composed of two layers : The Stern and outer Helmholtz layers[81].

and can be calculated using the Debye length. It extends into the bulk solution. The Helmoltz layer is actually conposed of two layers.

- The inner Helmholtz layer, or Stern layer, is found at the immediate vicinity of the electrode. The ions are strongly adsorbed
- The outer Helmholtz layer is situated between the Stern layer and the diffuse layer. Solvated ions are found in this layer.

The adsorption of species is usually measured using impedance technique. Contact sensors are affected by electrode passivation, but also by faradic currents which can degrade the sample in solution. To solve these problems, contactless devices have been created. Their principle is to add an insulating layer between the electrode and the solution. The electrical double-layer takes place at the insulator-solution interface.

Insulating layers can be made of organic species. Wu et al made immunoassays based on electropolarized films [29]. A gold electrode was polished and electrochemi-

cally treated in 0.5M H_2SO_4. Then, a tyramine material was electropolimerized on the electrode, creating a 50nm thickness insulating layer. This layer resisted to acid solutions, used to regenerate the sensor.
An other way is the use of Self-Assembled Monolayers (SAM)[82, 83]. These layers are formed spontaneously by adsorption of film components from a solution, directly onto the surface of the electrode. Thiols-anchored groups are part of the most studied self-assembled monolayers on gold and other metals.

Insulating layer can also be made from oxides. Contactless microelectrodes were then fabricated using SiO_2 or Al_2O_3. Interdigitated electrodes sputtered with Al_2O_3 were used to monitor the adsorption of DNA[84, 85].

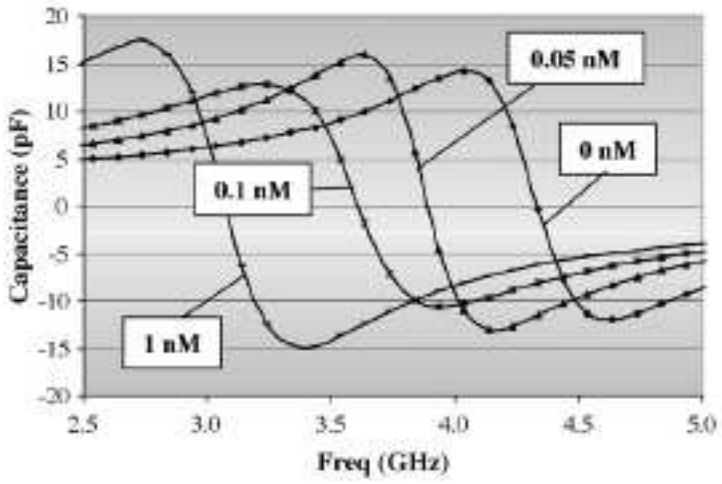

Figure 1.12: Resonance frequency shift due to the shift of capacitance when adsorbing DNA[84].

The tendency is to measure the adsorption directly in the surface capacitive frequency range of the sensor. However, a second way to work with such electrodes is to use a capacitance shift based on a resonance situated at high frequencies[84, 85] (Figure 1.12).

1.4 Goals of the work

The goal of this work is to design a low-cost, capacitive immunosensor, whose electrodes would be separated from the solution by an insulating layer. This immunosensor should monitor in real-time the adsorption of species (proteins, antibodies, DNA) on the electrodes. As a final goal, it might be able to monitor the reaction between species present in the aqueous solution and adsorbed species.

Chapter 2 introduces the theoretical elements of impedance that will be used in this work. It also introduces some theoretical circuits and presents the various kind of plots that will be used in the following chapters. In Chapter 3, numerical simulations of face-to-face and coplanar geometries will be carried out. The response with respect to the frequency will be studied for various geometrical parameters variation.

Microchips using a coplanar design will be developed in Chapter 4. This microchip is made of PET and uses two silver electrodes separated from a microchannel by a PET insulating layer. As the useful signal strength of this chip is rather low, an important optimization work will be done on the chip and on the holder used to connect the chip to the fluidic system.

Chapter 5 introduces the design of a sensor using electrodes made from a mass market aluminium foil. This electrode is composed of a metallic aluminium material covered by a nanometric thick alumina layer. Face-to-face and coplanar designs were developed. Each version was characterized using a holder equipped with a reservoir and testing the influence of geometrical parameters. Some analytical models will be created.

The design developed in the Chapter 5 is used in the chapter 6 to study the ability of the sensor to monitor an adsorption. A working frequency that enables the monitoring of the adsorption will be investigated. The adsorption of the first layer onto the electrodes will be studied using both coplanar and face-to-face designs, with various methods. Then, the reaction of a species in solution with adsorbed species on the electrode will be made, and an immunoassay will be achieved.

Bibliography

[1] J. M Busnel et al. "Carrier ampholytes-based capillary electrophoresis as an alternative to capillary zone electrophoresis in classical background electrolytes". In: *Journal of Chromatography A* 1087.1-2 (2005), pp. 183–188. ISSN: 0021-9673.

[2] J. M Busnel, M. C Hennion, and G. Peltre. "Carrier ampholytes as potential buffers in electrophoresis: physico-chemical study". In: *Journal of Chromatography B* 818.1 (2005), pp. 99–107. ISSN: 1570-0232.

[3] J. M Busnel et al. "Protein tryptic digests analyzed by carrier ampholyte-based capillary electrophoresis coupled to ESI-MS". In: *Electrophoresis* 27.8 (2006), pp. 1481–1488. ISSN: 1522-2683.

[4] Jean-Marc Busnel et al. "Transient isotachophoresis in carrier ampholyte-based capillary electrophoresis for protein analysis". In: *ELECTROPHORESIS* 27.18 (2006), pp. 3591–3598. ISSN: 0173-0835. DOI: 10.1002/elps.200600230.

[5] Jean-Marc Busnel et al. "Loading capacity of carrier ampholytes – based buffers in capillary electrophoresis". In: *ELECTROPHORESIS* 27.3 (2006), pp. 563–571. ISSN: 0173-0835. DOI: 10.1002/elps.200500646.

[6] J. Zhang et al. "Poly (N, N-dimethylacrylamide)-grafted polyacrylamide: A self-coating copolymer for sieving separation of native proteins by CE". In: *Electrophoresis* 27.15 (2006), pp. 3086–3092. ISSN: 1522-2683.

[7] P. Antonioli et al. "Quasi-isoelectric buffers for protein analysis in a fast alternative to conventional capillary zone electrophoresis". In: *Journal of Chromatography B* 833.1 (2006), pp. 19–25. ISSN: 1570-0232.

[8] Frederic Fortis et al. "A New Approach for the Detection and Identification of Protein Impurities Using Combinatorial Solid Phase Ligand Libraries". In: *Journal of Proteome Research* 5.10 (2006), pp. 2577–2585. ISSN: 1535-3893. DOI: 10.1021/pr060090s.

[9] M. E Mendieta et al. "Effect of barium tetraborate on the separation of tryptic digests of proteins by zone electrophoresis in uncoated capillaries". In: *Electrophoresis* 27.20 (2006), pp. 4016–4024. ISSN: 1522-2683.

[10] R. Sebastiano et al. "Organic and inorganic di-cations for capillary silica coating and EOF modulation in CE: Example of application in PEG analysis". In: *Electrophoresis* 27.8 (2006), pp. 1495–1501. ISSN: 1522-2683.

[11] R. Sebastiano et al. "Mass distribution and focusing properties of carrier ampholytes for isoelectric focusing: I. Novel and unexpected results". In: *Electrophoresis* 27.20 (2006), pp. 3919–3934. ISSN: 1522-2683.

[12] J. Gamby, J.-P. Abid, and H.H. Girault. "Supercapacitive admittance tomoscopy". In: *Journal of the American Chemical Society* 127.38 (2005), pp. 13300–13304.

[13] J. Gamby et al. "Nanowires network for biomolecular detection using contactless impedance tomoscopy technique". In: *Analytical Chemistry* 78.15 (2006), pp. 5289–5295.

[14] M. Dani, F. Manca, and G. Rialdi. "Calorimetric study of the binding reaction of concanavalin A with immunoglobulins". In: *Molecular Immunology* 19.7 (1982), pp. 907–911. ISSN: 0161-5890.

[15] T. H. Scheper et al. "Two FIA-based biosensor systems studied for bioprocess monitoring". In: *Journal of biotechnology* 31.3 (1993), pp. 345–356. ISSN: 0168-1656.

[16] N. Chiem and D.J. Harrison. "Microchip-based capillary electrophoresis for immunoassays: Analysis of monoclonal antibodies and theophylline". In: *Analytical Chemistry* 69.3 (1997), pp. 373–378.

[17] H.-X. Chen et al. "Capillary electrophoresis immunoassay using magnetic beads". In: *Electrophoresis* 29.16 SPEC. ISS. (2008), pp. 3414–3421.

[18] K.A. Marx. "Quartz crystal microbalance: A useful tool for studying thin polymer films and complex biomolecular systems at the solution - Surface interface". In: *Biomacromolecules* 4.5 (2003), pp. 1099–1120.

[19] X.-L. Su and Y. Li. "A QCM immunosensor for Salmonella detection with simultaneous measurements of resonant frequency and motional resistance". In: *Biosensors and Bioelectronics* 21.6 (2005), pp. 840–848.

[20] U.B. Nielsen and B.H. Geierstanger. "Multiplexed sandwich assays in microarray format". In: *Journal of Immunological Methods* 290.1-2 (2004), pp. 107–120.

[21] L. Mezzasoma et al. "Antigen microarrays for serodiagnosis of infectious diseases". In: *Clinical Chemistry* 48.1 (2002), pp. 121–130.

[22] D.F. Ma et al. "Differential tissue expression of enhanced green fluorescent protein in 'green mice'." In: *Histology and histopathology* 25.6 (2010), pp. 749–754.

[23] Andrea Lionello. *Controlled Protein Adsorption for Microimmunoassays*. Lausanne, 2006.

[24] C.R. Taitt, G.P. Anderson, and F.S. Ligler. "Evanescent wave fluorescence biosensors". In: *Biosensors and Bioelectronics* 20.12 (2005), pp. 2470–2487.

[25] B.N.G. Giepmans et al. "The fluorescent toolbox for assessing protein location and function". In: *Science* 312.5771 (2006), pp. 217–224.

[26] A.P. Alivisatos. "Semiconductor clusters, nanocrystals, and quantum dots". In: *Science* 271.5251 (1996), pp. 933–937.

[27] H. Maupas et al. "Direct immunosensing using differential electrochemical measurements of impedimetric variations". In: *Journal of Electroanalytical Chemistry* 421.1-2 (1997), pp. 165–171.

[28] Y.-H. Yun et al. "A label-free electronic biosensor for detection of bone turnover markers". In: *Sensors* 9.10 (2009), pp. 7957–7969.

[29] Z.-S. Wu et al. "A sensitive immunoassay based on electropolymerized films by capacitance measurements for direct detection of immunospecies". In: *Analytical Biochemistry* 337.2 (2005), pp. 308–315.

[30] O. Laczka et al. "Detection of Escherichia coli and Salmonella typhimurium using interdigitated microelectrode capacitive immunosensors: The importance of transducer geometry". In: *Analytical Chemistry* 80.19 (2008), pp. 7239–7247.

[31] C.-C. Lin et al. "Microfluidic Immunoassays". In: *JALA - Journal of the Association for Laboratory Automation* 15.3 (2010), pp. 253–274.

[32] A.E. Herr et al. "Microfluidic immunoassays as rapid saliva-based clinical diagnostics". In: *Proceedings of the National Academy of Sciences of the United States of America* 104.13 (2007), pp. 5268–5273.

[33] B.C. Heinze et al. "Microfluidic immunosensor for rapid and sensitive detection of bovine viral diarrhea virus". In: *Sensors and Actuators, B: Chemical* 138.2 (2009), pp. 491–496.

[34] G. Suarez et al. "Lab-on-a-chip for multiplexed biosensing of residual antibiotics in milk". In: *Lab on a Chip - Miniaturisation for Chemistry and Biology* 9.11 (2009), pp. 1625–1630.

[35] G.K. Ahirwal and C.K. Mitra. "Gold nanoparticles based sandwich electrochemical immunosensor". In: *Biosensors and Bioelectronics* 25.9 (2010), pp. 2016–2020.

[36] S. Centi et al. "Development of an electrochemical immunoassay based on the use of an eight-electrodes screen-printed array coupled with magnetic beads for the detection of antimicrobial sulfonamides in honey". In: *Electroanalysis* 22.16 (2010), pp. 1881–1888.

[37] M. Eguilaz et al. "An electrochemical immunosensor for testosterone using functionalized magnetic beads and screen-printed carbon electrodes". In: *Biosensors and Bioelectronics* 26.2 (2010), pp. 517–522.

[38] J.S. Rossier and H.H. Girault. "Enzyme linked immunosorbent assay on a microchip with electrochemical detection". In: *Lab on a Chip - Minituarization for Chemistry and Biology* 1.2 (2001), pp. 153–157.

[39] J. Bardeen and W.H. Brattain. "The transistor, a semi-conductor triode [14]". In: *Physical Review* 74.2 (1948), pp. 230–231.

[40] Bergveld. "Development of an ion-sensitive solid-state device for neurophysiological measurements". In: *IEEE Transactions on Biomedical Engineering* BME-17.1 (1970), pp. 70–71.

[41] M.J. Schoning and A. Poghossian. "Bio FEDs (Field-Effect Devices): State-of-the-art and new directions". In: *Electroanalysis* 18.19-20 (2006), pp. 1893–1900.

[42] T. Ohtake et al. "Immobilization of probe DNA on Ta2O2 thin film and detection of hybridized helix DNA using IS-FET". In: *Japanese Journal of Applied Physics, Part 2: Letters* 43.9 AB (2004).

[43] M. Harnois et al. "Low concentrated DNA detection by SGFET". In: *TRANSDUCERS and EUROSENSORS '07 - 4th International Conference on Solid-State Sensors, Actuators and Microsystems*. 2007, pp. 1983–1986.

[44] T. Uno, H. Tabata, and T. Kawal. "Peptide-nucleic acid-modified ion-sensitive field-effect transistor-based biosensor for direct detection of DNA hybridization". In: *Analytical Chemistry* 79.1 (2007), pp. 52–59.

[45] P. Estrela et al. "Label-free sub-picomolar protein detection with field-effect transistors". In: *Analytical Chemistry* 82.9 (2010), pp. 3531–3536.

[46] L. Wang et al. "Fabrication of BioFET linear array for detection of protein interactions". In: *Microelectronic Engineering* 87.5-8 (2010), pp. 753–755.

[47] P. Hu et al. "Carbon nanostructure-based field-effect transistors for label-free chemical/biological sensors". In: *Sensors* 10.5 (2010), pp. 5133–5159.

[48] Y. Ohno et al. "Electrolyte-gated graphene field-effect transistors for detecting ph and protein adsorption". In: *Nano Letters* 9.9 (2009), pp. 3318–3322.

[49] E. Stern et al. "Label-free immunodetection with CMOS-compatible semiconducting nanowires". In: *Nature* 445.7127 (2007), pp. 519–522.

[50] K. Maehashi et al. "Label-free protein biosensor based on aptamer-modified carbon nanotube field-effect transistors". In: *Analytical Chemistry* 79.2 (2007), pp. 782–787.

[51] B.H. Van der Schoot et al. "The isfet in analytical chemistry". In: *Sensors and Actuators* 4.C (1983), pp. 267–272.

[52] L. Fu et al. "Carbon nanotubes coated with alumina as gate dielectrics of field-effect transistors". In: *Advanced Materials* 18.2 (2006), pp. 181–185.

[53] Y. Cui et al. "Nanowire nanosensors for highly sensitive and selective detection of biological and chemical species". In: *Science* 293.5533 (2001), pp. 1289–1292.

[54] G. Zheng et al. "Multiplexed electrical detection of cancer markers with nanowire sensor arrays". In: *Nature Biotechnology* 23.10 (2005), pp. 1294–1301.

[55] R. Martel et al. "Carbon nanotube field-effect transistors and logic circuits". In: *Proceedings - Design Automation Conference*. 2002, pp. 94–98.

[56] T. Shimada et al. "Double-wall carbon nanotube field-effect transistors: Ambipolar transport characteristics". In: *Applied Physics Letters* 84.13 (2004), pp. 2412–2414.

[57] H.-M. So et al. "Detection and titer estimation of Escherichia coli using aptamer-functionalized single-walled carbon-nanotube field-effect transistors". In: *Small* 4.2 (2008), pp. 197–201.

[58] T. Dastagir et al. "Electrical detection of hepatitis C virus RNA on single wall carbon nanotube-field effect transistors". In: *Analyst* 132.8 (2007), pp. 738–740.

[59] W. Knoll. *Interfaces and thin films as seen by bound electromagnetic waves*. Vol. 49. 1998.

[60] W.L. Barnes, A. Dereux, and T.W. Ebbesen. "Surface plasmon subwavelength optics". In: *Nature* 424.6950 (2003), pp. 824–830.

[61] R. Kurita et al. "On-chip enzyme immunoassay of a cardiac marker using a microfluidic device combined with a portable surface plasmon resonance system". In: *Analytical Chemistry* 78.15 (2006), pp. 5525–5531.

[62] S. Kumbhat et al. "Surface plasmon resonance based immunosensor for serological diagnosis of dengue virus infection". In: *Journal of Pharmaceutical and Biomedical Analysis* 52.2 (2010), pp. 255–259.

[63] S. Scarano et al. "Surface plasmon resonance imaging for affinity-based biosensors". In: *Biosensors and Bioelectronics* 25.5 (2010), pp. 957–966.

[64] J.S. Mitchell and Y. Wu. "Surface plasmon resonance signal enhancement for immunoassay of small molecules." In: *Methods in molecular biology (Clifton, N.J.)* 627 (2010), pp. 113–129.

[65] S.D. Mazumdar et al. "Surface plasmon resonance (SPR) as a rapid tool for serotyping of Salmonella". In: *Biosensors and Bioelectronics* 25.5 (2010), pp. 967–971.

[66] H.J. Lee, T.T. Goodrich, and R.M. Corn. "SPR imaging measurements of 1-D and 2-D DNA microarrays created from microfluidic channels on gold thin films". In: *Analytical Chemistry* 73.22 (2001), pp. 5525–5531.

[67] H. Kawazumi et al. "Compact surface plasmon resonance (SPR) immunosensor using multichannel for simultaneous detection of small molecule compounds". In: *Sensors and Actuators, B: Chemical* 108.1-2 SPEC. ISS. (2005), pp. 791–796.

[68] S.J. Kim et al. "Novel miniature SPR immunosensor equipped with all-in-one multi-microchannel sensor chip for detecting low-molecular-weight analytes". In: *Biosensors and Bioelectronics* 23.5 (2007), pp. 701–707.

[69] C.V. Raman and K.S. Krishnan. "A new type of secondary radiation [11]". In: *Nature* 121.3048 (1928), pp. 501–502.

[70] H Portales. *Etude par diffusion Raman de nanoparticules metalliques en matrice dielectrique amorphe*. Universite Claude Bernard Lyon1, Dec. 2001.

[71] A. Souza Filho et al. "Stokes and anti-Stokes Raman spectra of small-diameter isolated carbon nanotubes". In: *Physical Review B* 69.11 (2004). ISSN: 1098-0121. DOI: 10.1103/PhysRevB.69.115428.

[72] M. Fleischmann, P.J. Hendra, and A.J. McQuillan. "Raman spectra of pyridine adsorbed at a silver electrode". In: *Chemical Physics Letters* 26.2 (1974), pp. 163–166.

[73] D.L. Jeanmaire and R.P. Van Duyne. "Surface Raman spectroelectrochemistry Part I. Heterocyclic, aromatic, and aliphatic amines adsorbed on the anodized silver electrode". In: *Journal of Electroanalytical Chemistry* 84.1 (1977), pp. 1–20.

[74] H. Li, J. Sun, and B.M. Cullum. "Label-free detection of proteins using SERS-based immuno-nanosensors". In: *Nanobiotechnology* 2.1-2 (2006), pp. 17–28.

[75] Hansang Cho et al. "Label-free and highly sensitive biomolecular detection using SERS and electrokinetic preconcentration". In: *Lab on a Chip* 9.23 (2009), p. 3360. ISSN: 1473-0197. DOI: 10.1039/b912076a.

[76] C.E. Talley et al. "Surface-enhanced Raman scattering from individual Au nanoparticles and nanoparticle dimer substrates". In: *Nano Letters* 5.8 (2005), pp. 1569–1574.

[77] D.S. Grubisha et al. "Femtomolar Detection of Prostate-Specific Antigen: An Immunoassay Based on Surface-Enhanced Raman Scattering and Immunogold Labels". In: *Analytical Chemistry* 75.21 (2003), pp. 5936–5943.

[78] K. Kneipp et al. "Single molecule detection using surface-enhanced Raman scattering (SERS)". In: *Physical Review Letters* 78.9 (1997), pp. 1667–1670. ISSN: 1079-7114.

[79] J.Z. Chen et al. "Capacitive sensing of droplets for microfluidic devices based on thermocapillary actuation". In: *Lab on a Chip - Miniaturisation for Chemistry and Biology* 4.5 (2004), pp. 473–480.

[80] C. Berggren, B. Bjarnason, and G. Johansson. "Capacitive biosensors". In: *Electroanalysis* 13.3 (2001), pp. 173–180.

[81] D.G. Grahame. "The electrical double layer and the theory of electrocapillarity". In: *Chemical Reviews* 41.3 (1947), pp. 441–501.

[82] J.C. Love et al. "Self-assembled monolayers of thiolates on metals as a form of nanotechnology". In: *Chemical Reviews* 105.4 (2005), pp. 1103–1169.

[83] W. Limbut et al. "A comparative study of capacitive immunosensors based on self-assembled monolayers formed from thiourea, thioctic acid, and 3-mercaptopropionic acid". In: *Biosensors and Bioelectronics* 22.2 (2006), pp. 233–240.

[84] L. Moreno-Hagelsieb et al. "Electrical detection of DNA hybridization: Three extraction techniques based on interdigitated Al/Al2O3 capacitors". In: *Biosensors and Bioelectronics* 22.9-10 (2007), pp. 2199–2207.

[85] L. Moreno-Hagelsieb et al. "CMOS Compatible Anodic Al2O3 Based Sensors for Bacteria Detection". In: *Procedia Chemistry* 1.1 (2009), pp. 1283–1286.

Chapter 2

Electrochemical impedance spectroscopy

2.1 Circuit elements

2.1.1 General definitions of some passive elements

Resistor

The relationship between the current and the potential difference at the terminals of a resistor is given by Ohm's law [1]:

$$V(t) = RI(t) \tag{2.1}$$

where V represents the potential difference at the terminals of the resistor [V], I the current [A] and R the value (resistance) of the resistor [Ω]. For a linear resistor, R can be defined as:

$$R = \frac{\rho L}{S} \tag{2.2}$$

with L [m] and S [m^2] respectively the resistor length and the resistor cross section,

ρ [Ω.m] the material resistivity.

Figure 2.1: Electrical scheme of a resistor of resistance R

Inductor

The relationship between current and potential difference for the inductor is defined by :

$$V(t) = L\frac{dI(t)}{dt} \tag{2.3}$$

Under steady state conditions, *dI(t)/dt* = 0 and consequently *V(t)* = 0, making an inductor equivalent to a wire.

Figure 2.2: Electrical scheme of an inductor of inductance *L*

Capacitor

The capacitor is defined by :

$$C = \frac{dq(t)}{dV(t)} \tag{2.4}$$

where *q(t)* is the electric charge [C] and *C* the capacity of a capacitor [F] calculated in the case of a parallel plates capacitor by:

$$C = \frac{\varepsilon_0 \varepsilon_r S}{d} \tag{2.5}$$

with ε_0 being the permittivity of vacuum (8.85x10^{-12} F.m^{-1}), ε_r [F.m^{-1}] the relative permittivity of the insulator between the plates of the capacitor, *S* the surface area of the capacitor and *d* [m] the distance between the plates of the capacitor.

The current flowing through the capacitor is expressed as:

$$I(t) = \frac{dq(t)}{dt} \tag{2.6}$$

From equations 2.4 and 2.6, the relationship between the current *I(t)* and the potential difference at the terminals of a capacitor can be written:

$$I(t) = C\frac{dV(t)}{dt} \tag{2.7}$$

Under steady state condition, *dV(t)/d(t)*=0 and consequently *I(t)*=0. The capacitor behaves in this case like an open circuit.

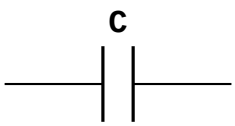

Figure 2.3: Electrical scheme of a capacitor of capacitance C

2.1.2 Response to a sinusoidal signal

A linear system is characterised by an input function *x(t)* and an output function *y(t)*. A *transfer function* $H(s)$ can be defined as the Laplace transforms ratio between the output and the input functions[2], respectively $\overline{y}(s)$ and $\overline{x}(s)$, as:

$$H(s) = \frac{\Delta\overline{y}(s)}{\Delta\overline{x}(s)} \tag{2.8}$$

Applying a pure sinusoidal excitation,

$$\Delta x(t) = \Delta x sin(\omega t) \tag{2.9}$$

the Laplace transform is:

$$\Delta\overline{x}(s) = \Delta x \frac{\omega}{s^2 + \omega^2} \tag{2.10}$$

with ω being the angular frequency, defined by ω = 2 πf, f being the applied frequency [Hz],

The output function is:

$$\Delta\overline{y}(s) = H(s)\Delta\overline{x}(s) \tag{2.11}$$

Taking s=$\jmath\omega$ in the Laplace transform, Equation 2.11 is transfered to the *frequency domain*, which depends on the angular frequency ω, $\jmath$ being the pure imaginary number defined as $\jmath^2$ = -1.

$$\Delta\overline{y}(\omega) = H(\omega)\Delta\overline{x}(\omega) \tag{2.12}$$

In the inverse transform of Equation 2.12, the frequency domain corresponds to the sinusoidal part of the output function.

$$\Delta y(t) = \Delta x|H(\omega)||sin|(\omega t + \varphi) \tag{2.13}$$

with $|H(\omega)|$ being the modulus of the transfer function, defined in the frequential domain by:

$$|H(\omega)| = \sqrt{[\Re H(\omega)]^2 + [\Im H(\omega)]^2} \tag{2.14}$$

and φ the argument defined by

$$\varphi = |Arg|\,(H(\omega) = |arctan|\left(\frac{\Im H(\omega)}{\Re H(\omega)}\right) \tag{2.15}$$

For an electrical circuit, the transfer function from the potential (input) to the current (output) is called the *admittance* of the system and is noted **Y** [S]. In the frequency domain, it is defined by a relation between the complex current $\overline{I}(\omega)$ and the complex

potential $\overline{E}(\omega)$ such as:

$$\Delta\overline{I}(\omega) = Y(\omega)\Delta\overline{E}(\omega) \tag{2.16}$$

On the other side, the transfer function from the current (input) to the potential (output) is called the *impedance* of the system and is noted Z *[Ω]*.

$$\Delta\overline{E}(\omega) = Z(\omega)\Delta\overline{I}(\omega) \tag{2.17}$$

2.1.3 Impedance of circuit elements

Resistor

Taking the Laplace transform of Equation 2.1, we obtain:

$$\Delta\overline{V}(s) = R\Delta\overline{I}(s) \tag{2.18}$$

The impedance of the resistor Z_R in the frequency domain is then obtained by taking $s = \jmath\omega$

$$Z_R = \frac{\Delta\overline{V}(\omega)}{\Delta\overline{I}(\omega)} = R \tag{2.19}$$

A resistor does not introduce dephasing.

Inductor

Taking the Laplace transform of Equation 2.3 gives

$$\Delta\overline{V}(s) = Ls\Delta\overline{I}(s) \tag{2.20}$$

The impedance of the inductor Z_L in the frequency domain is then

$$Z_L = \frac{\Delta\overline{V}(\omega)}{\Delta\overline{I}(\omega)} = \jmath\omega L \tag{2.21}$$

Capacitor

Taking the Laplace transform of Equation 2.7 gives

$$\Delta\overline{I}(s) = Cs\Delta\overline{E}(s) \tag{2.22}$$

The admittance of the capacitor Y_C in the frequency domain is then

$$Y_C = \frac{\Delta\overline{I}(\omega)}{\Delta\overline{V}(\omega)} = \jmath\omega C \tag{2.23}$$

As an admittance is the reverse of an impedance, the impedance Z_C of a capacitor is defined as:

$$Z_C = \frac{1}{\jmath\omega C} \tag{2.24}$$

In the rest of this thesis work, the capacitance presented on every plot will be called "capacitance" by abuse of language, and will be calculated by dividing the Imaginary part of the admittance by ω, such as:

$$\text{Plotted capacitance} = \frac{Y_C}{\omega} \tag{2.25}$$

The Constant Phase Element

The capacitor studied in 2.1.3 was considered perfect. This assumption might not be valid for electrolytic capacitors, where the electrode geometry is generally imperfect (most of the time affected by surface roughness). In that case some frequency dispersion can be observed, which is generally modelized through a Constant Phase Element (CPE). The hypothesis of the Constant Phase Element (CPE) was first formulated in 1931 by Fricke[3] and was attributed to a dispersion of capacitance. This dispersion of capacitance leads to a dispersion in the time constants of the circuit. A global CPE

behaviour is then the result of a distribution of local impedances[4]. The origin of the CPE is still not perfectly understood, and has been attributed to surface roughness of the electrodes[5–7], electrode porosity[8–10]. These two assumptions were related to fractal theories concerning the electrode surface[11–14]. The origin of the CPE was also attributed to a non-uniform potential distribution[15, 16], or just the electrical double-layer[17]. The CPE can be defined as[18]:

$$Z_{CPE} = \frac{1}{C(j\omega)^{\alpha}} \tag{2.26}$$

with α ranging from 0 to 1. From Equation 2.26, the value of the real part is:

$$\Re(Y_{CPE}) = C\omega^{\alpha} cos\left(\frac{\alpha\pi}{2}\right) \tag{2.27}$$

while the value of the imaginary parts is

$$\Im(Y_{CPE}) = C\omega^{\alpha} sin\left(\frac{\alpha\pi}{2}\right) \tag{2.28}$$

Figure 2.4 presents the evolution through the frequency of a CPE with a value of 1 μF capacitance and a 0.9 α factor. It can be observed that the value of the phase is higher than $\frac{-\pi}{2}$. This is due to the sine and cosine values of the imaginary and real parts of the admittance. The imaginary part of the admittance looks, at first sight, the same as for a perfect capacitor. However it can be seen that the capacitance calculated from this imaginary part is far from being constant against the frequency. The value of the real part of the impedance also evolves with the frequency. This was not the case for the perfect capacitor, as it has no component on the real part of the admittance. It has to be noted that a value of 1 for α would make the capacitor perfect. In that case the spectra would be the same as those of a perfect capacitor.

Figure 2.5 presents the Nyquist plots of impedance and admittance of a CPE whose

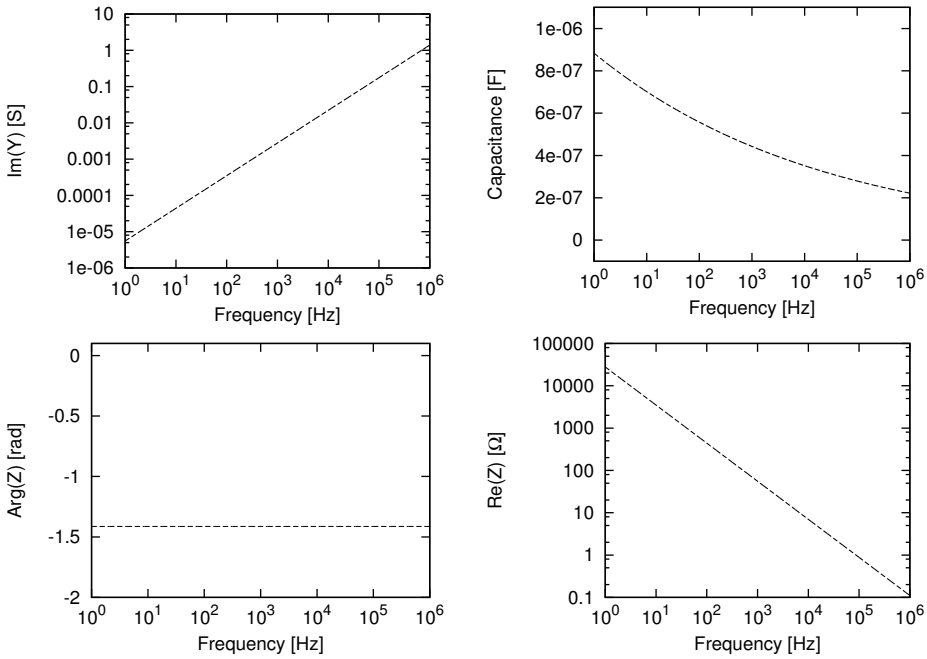

Figure 2.4: Spectra of various parameters representing the behaviour of a Contant Phase Element, plotted from Equation 2.26

capacitance is 1 μF and α coefficient 0.9. Contrary to the perfect capacitor whose impedance and admittance is purely imaginary, the line on the impedance and admittance plots are not purely vertical. As the α value is lower than 1, a part of the signal goes to the real part of the impedance and admittance.

2.2 The RC circuit

The RC circuit is composed of one resistor and one capacitor. These elements can be assembled in series or in parallel.

2.2.1 RC circuit in series : Signal at the terminals of the capacitor

Taking into consideration the serial circuit, the additivity of the potentials gives $E = U_R + U_C$ (Figure 2.6).

Combining Equation 2.7 and Equation 2.1, the relation becomes

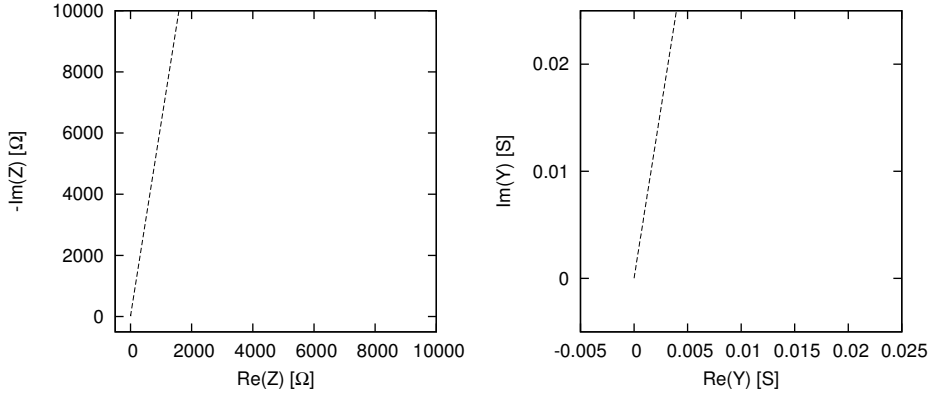

Figure 2.5: Nyquist plots of a 1 μF capacitance CPE.

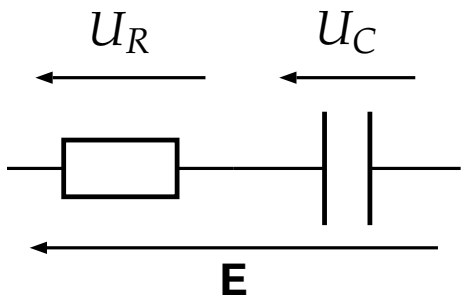

Figure 2.6: Electrical scheme of a RC circuit in series

$$E = RC\frac{dU_C(t)}{dt} + U_C(t) \tag{2.29}$$

Solving equation 2.29 leads to

$$U_C(t) = E(1 - e^{\frac{-t}{RC}}) \tag{2.30}$$

U_C(t) is plotted on Figure 2.7 for a resistor whose resistance is 50 Ω and a capacitor whose capacitance is 1 μF.

It can be seen on this figure that the capacitor is close to full charge after 0.3 ms. The time constant τ is defined as

$$\tau = RC \tag{2.31}$$

The capacitor reaches 62% of its capacity after a charging time equal to the value of

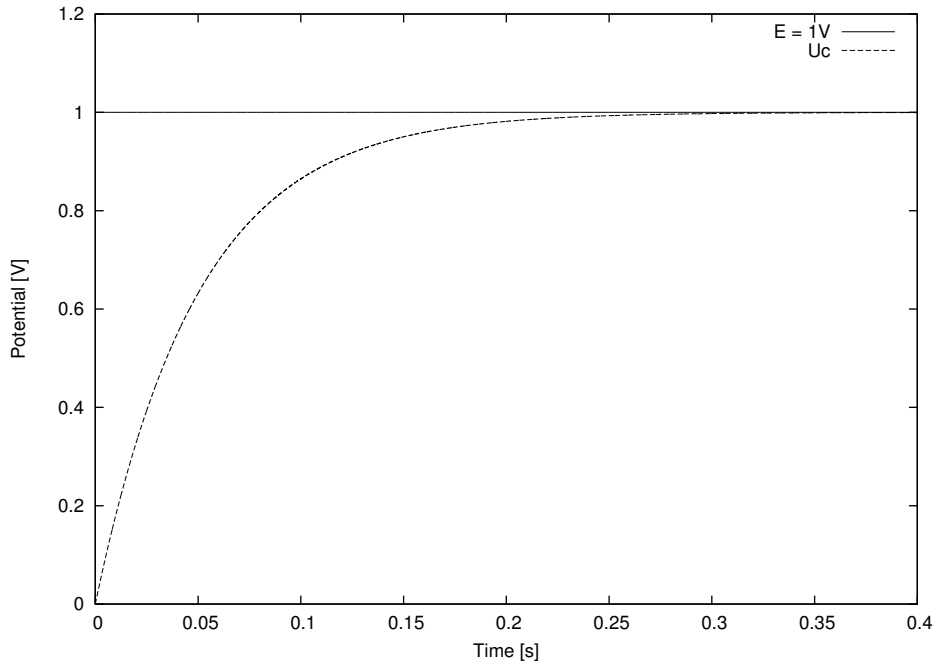

Figure 2.7: Response at the terminals of a capacitor when applying a constant potential.

τ.

When an alternating potential $E(t) = Ecos(\omega t)$ is applied to the circuit, the signal at the terminals of the capacitor becomes:

$$U_C(t) = \frac{E\omega R^2 C^2 e^{(\frac{-t}{RC})}}{RC(1+(RC\omega)^2)} - \frac{ERC(cos(\omega t)\omega RC - sin(\omega t))}{RC(1+(RC\omega)^2)} \tag{2.32}$$

The potential at the terminals of the capacitor is plotted on Figure 2.8 for a 40 Hz frequency. As the capacitor has enough time to charge and discharge completely, the input signal and the signal at the terminals of the capacitor are the same.

Things are different when the frequency of the input signal is fixed to 3.2 kHz, as can be seen on Figure 2.9. The capacitor does not have enough time to charge and discharge completely, and at this frequency the amplitude equals about 70% of the input signal.

When meeting an equation such as Equation 2.32, it is simpler to work with impedance to study the response of the circuit. The impedance $\overline{Z}$ of the whole RC circuit in serial

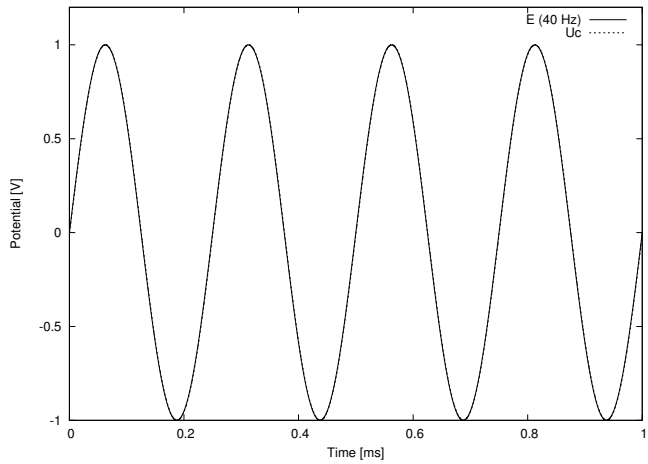

Figure 2.8: Response of the RC circuit at the terminals of the capacitor when applying a 40 Hz frequency AC signal.

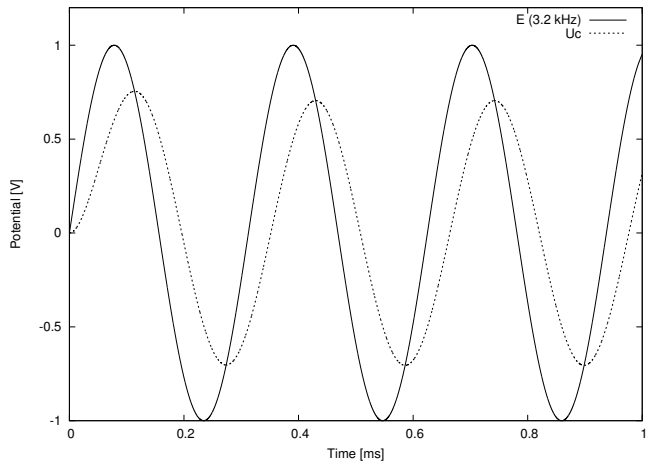

Figure 2.9: Response of the RC circuit at the terminals of the capacitor when applying a 4 kHz frequency AC signal.

is equal to $\overline{Z}_R + \overline{Z}_C$, that is to say that :

$$Z(\omega) = R + \frac{1}{j\omega C} \tag{2.33}$$

Using the theorem of the potential divider, like when a continuous potential is applied, the gain G at the terminals of the capacitor is:

$$G = \frac{Z_C(\omega)}{Z_R(\omega) + Z_C(\omega)} = \frac{1}{1 + j\omega RC} \tag{2.34}$$

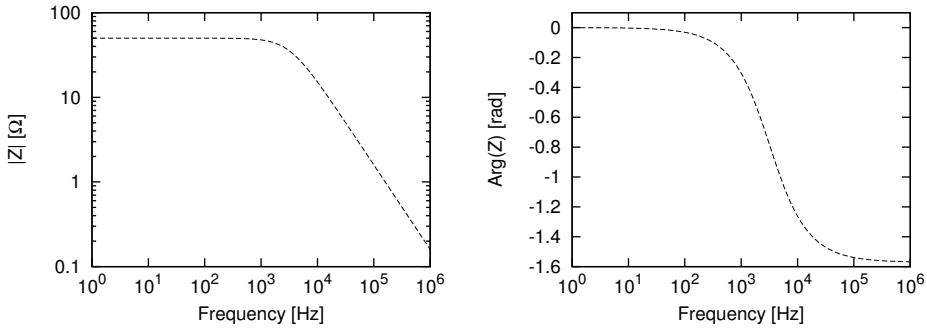

Figure 2.10: Frequency response at the terminals of a capacitor when applying an alternative signal

Plotting the absolute value of equation 2.34 with a resistor of 50 Ω and a capacitor of 1 μF leads to the plot on Figure 2.10. It can be seen that the value of the gain is 1 from 1 Hz to about 1 kHz, and that the value of the phase equals 0 for the same frequency range. This means that the electrical signal measured at the terminals of the capacitor is the same as the input signal, as can be observed with the temporal response on Figure 2.8. Moreover, the value of 0 for the phase means that the signal is governed by resistive effects.

The gain of the electrical signal at the terminals of the capacitor decreases after 1 kHz. This effect can also be observed in the temporal response on Figure 2.9 as the amplitude of U_C is lower than the amplitude of the input signal. In the same time, the value of -$\pi/2$ for the phase on Figure 2.10 between 100 kHz and 1 MHz means that the circuit is governed by capacitive effects in this frequency range.

The transition from the resistive state to this capacitive state occurs at the same frequency as the transition from the gain of 1 and the attenuation of the signal. This frequency is called the *cut-off frequency* f_c. The value of the phase at this frequency is $-\pi/4$, and the value of the frequency depends on the value of the resistance and the capacitance as:

$$f_c = \frac{1}{2\pi RC} \tag{2.35}$$

In the case of a circuit with a 50 Ω resistance and a 1 μF capacitance, the value of the cut-off frequency is 3183 Hz. The gain at the terminals of the capacitor at the cut-off frequency of the sensor is attenuated by -3 dB, also meaning that the amplitude of the output signal is 70% of the input signal. This is confirmed by the output signal on Figure 2.9.
As the output signal reproduces the input signal only for the frequencies below 3.2 kHz, the conclusion of this study is that taking the output signal at the terminals of a capacitor involved in a RC circuit in series leads to the creation of a *low-pass filter*.

2.2.2 RC circuit in series : Whole circuit

Each sensor design studied in the present work relies on only two electrodes. This means that the output signal is extracted from the same circuit as the input signal and the whole sensor has to be considered like a global circuit element. In this scope, considering the impedance data of a global RC circuit is a good start for the study of the data measured with the sensor.

Four plots presenting various parameters of the RC circuit defined by Equation 2.33 can be seen on Figure 2.11. The first plot represents the imaginary part of the admittance Y of Equation 2.33, that is to say :

$$\Im Y(\omega) = \frac{C\omega}{1 + R^2C^2\omega^2} \tag{2.36}$$

As illustrated by the phase plot, the circuit is capacitive at low frequencies until the cut-off frequency of 3.2 kHz. The capacitance plot also shows that the capacitance of 1 μF is reached at low frequencies. The behaviour of the circuit after the cut-off frequency is resistive, illustrated by the phase and capacitance values, being equal to 0 in the latter case. The value of the real part of impedance is 50 Ω, which is correct as the value of real part of Equation 2.33 is R.

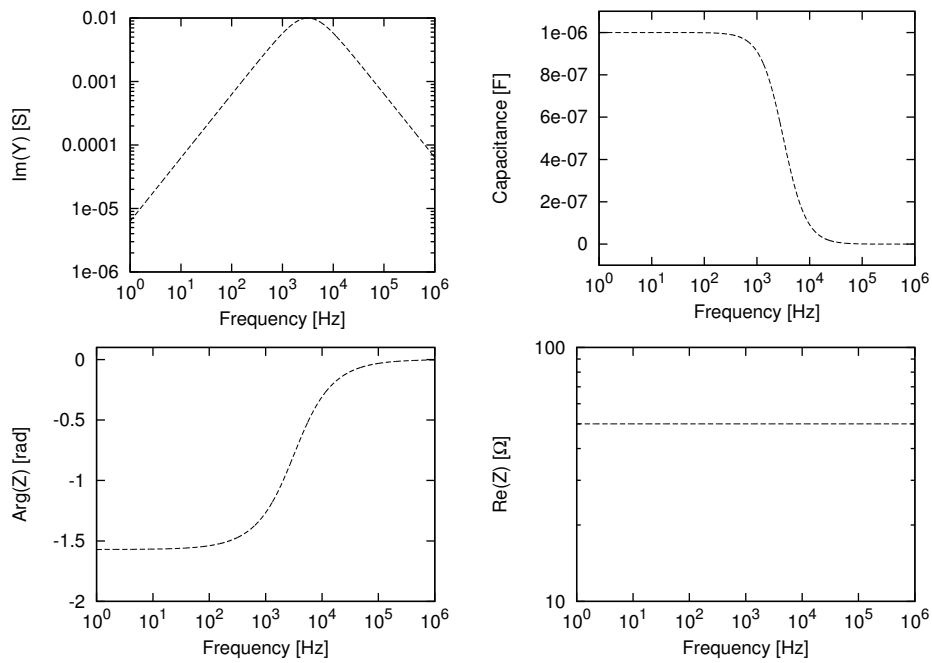

Figure 2.11: Response of the whole RC circuit with a perfect 50 Ω resistance and 1 μF capacitor in series. Are plotted the imaginary part of the admittance, the capacitance, the phase, and the real part of the impedance.

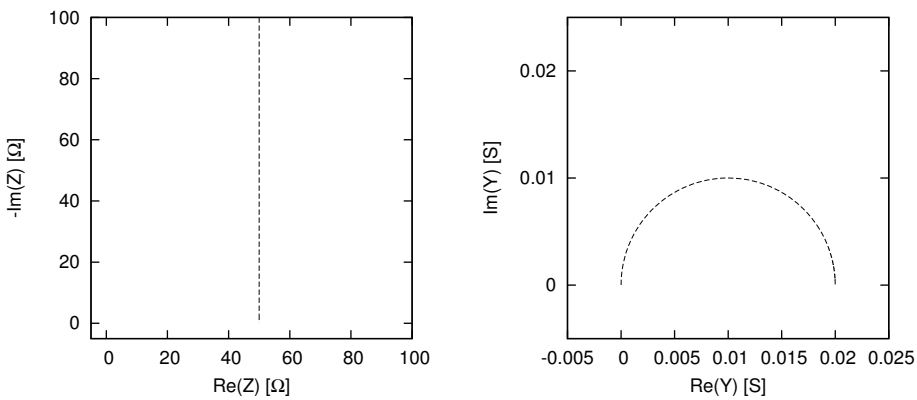

Figure 2.12: Nyquist plots of the impedance and admittance of the global RC circuit in series using a perfect 50 Ω resistance and 1 μF capacitor

Figure 2.12 presents the Nyquist plots of the global RC circuit in series. The Nyquist plot in impedance presents only one vertical line as if the circuit was purely capacitive. However the x-coordinate of this line is situated at 50 Ω. As the real part of Equation 2.33 is R=50 Ω and the imaginary part is $\frac{1}{j\omega C}$, this result is logical. The Nyquist plot in admittance represents half a circle. This is proper to a serial RC circuit.

2.2.3 RC circuit in parallel : Global circuit

The impedance Z_{eq} of two elements in parallel can be calculated by :

$$Z_{eq} = \left(\frac{1}{Z_1} + \frac{1}{Z_2}\right)^{-1} = \frac{Z_1 Z_2}{Z_1 + Z_2} \tag{2.37}$$

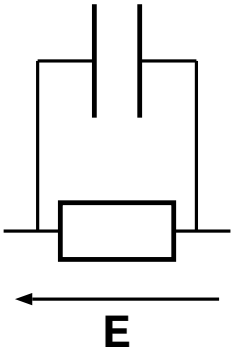

Figure 2.13: Electric scheme of a RC circuit in parallel

Applying Equation 2.37 to a resistor of resistance R and a capacitor of capacitance C gives the impedance Z_{RC}:

$$Z_{RC}(\omega) = \left(\frac{1}{Z_R(\omega)} + \frac{1}{Z_C(\omega)}\right)^{-1} = \frac{R}{1 + jRC\omega} \tag{2.38}$$

Equation 2.38 is used to plot the spectra on Figure 2.14 using a resistor of 50Ω resistance and a capacitor of 1μF. The spectrum of the imaginary part of the admittance increases with a slope of 1 decade. This means that the imaginary part of the admittance is governed by the capacitance on all the frequency range. This is quite logical as the imaginary part of the admittance is equal to $jC\omega$. It is then not surprising for the value of the capacitance spectrum to be equal to 1 μF on all the frequency range. However, the global behaviour of the circuit is resistive until the cut-off frequency of 3.2 kHz, as can be observed on the phase spectrum. After the cut-off frequency, the behaviour of the circuit is capacitive. This general behaviour is illustrated by the spectrum of the real part of the impedance. The value of the latter the one of the resistor

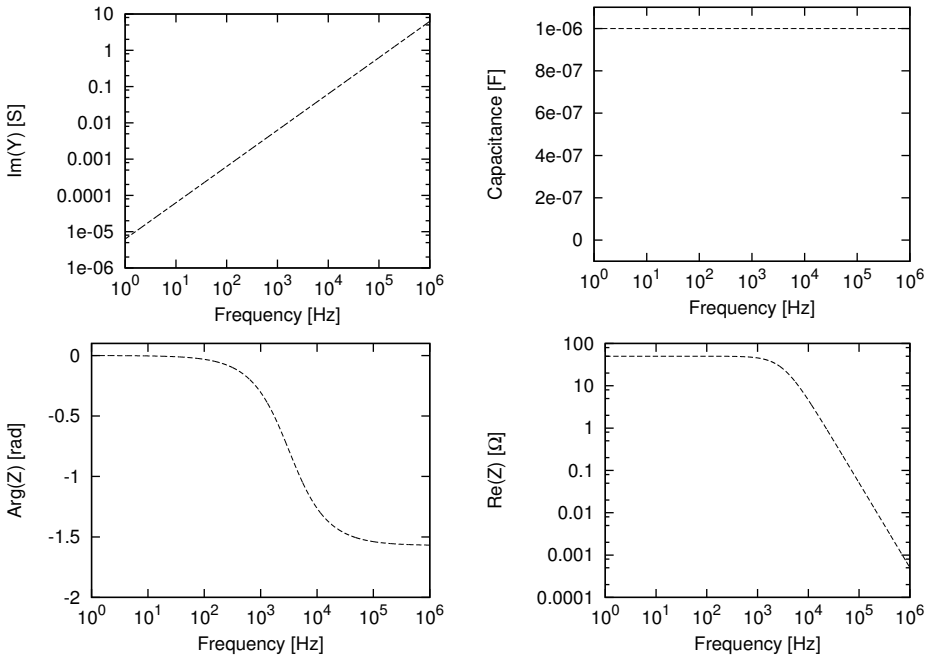

Figure 2.14: Bode plot of various responses of the RC parallel circuit from 1 Hz to 1 MHz, using a perfect 50 Ω resistance and 1 μF capacitor.

from 1 Hz to 3.2 kHz. After this frequency, the value decreases with a slope of 1, as it is influenced by a capacitive behaviour.

Compared to the behaviour of the RC circuit in serial plotted on Figure 2.12, those of the RC circuit in parallel, plotted on Figure 2.15, is reversed. So, the semi-circle appears on the Nyquist plot in impedance, and the vertical line appears on the Nyquist plot in admittance. As the formula of the admittance of the circuit is $\frac{1}{R} + jC\omega$, the x-coordinate of this vertical line is 0.02 S.

2.3 RLC circuit in series : Tantalum capacitor

All the circuits studied until now were constituted of pure and perfect theoretical elements. However real circuits are affected by some effects like capacitance and inductance. It was thus chosen to study a classical resistor with a resistance value of 50 Ω (Radiospares, Beauvais) while the capacitor (Radiospares, Beauvais) was made of two

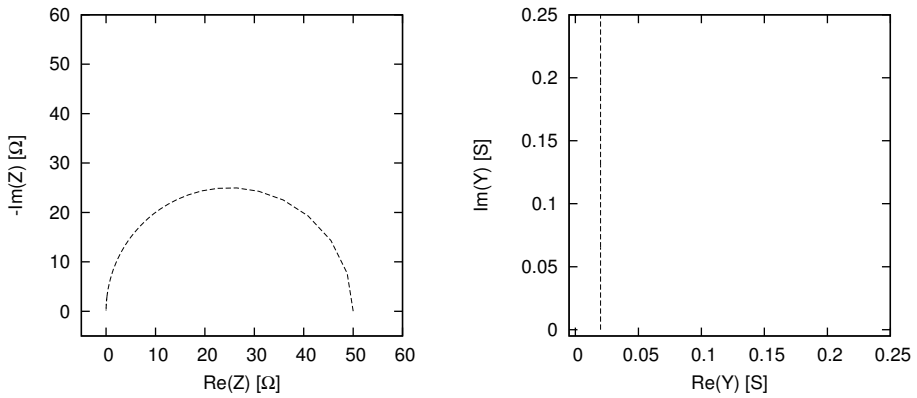

Figure 2.15: Nyquist plots of the impedance and admittance of the global RC circuit in parallel, using a perfect 50 Ω resistance and 1 μF capacitor.

metallic electrodes separated by a tantalum dielectric material (tantalum capacitor), with a 1μF capacitance value. Using a solid capacitor ensures a better signal quality, by avoiding the electrochemical effects of the electrolytic capacitors[19]. A DC potential of 0 V and an AC potential of 1 V were applied to the circuit, with frequencies ranging from 1 Hz to 1 MHz.

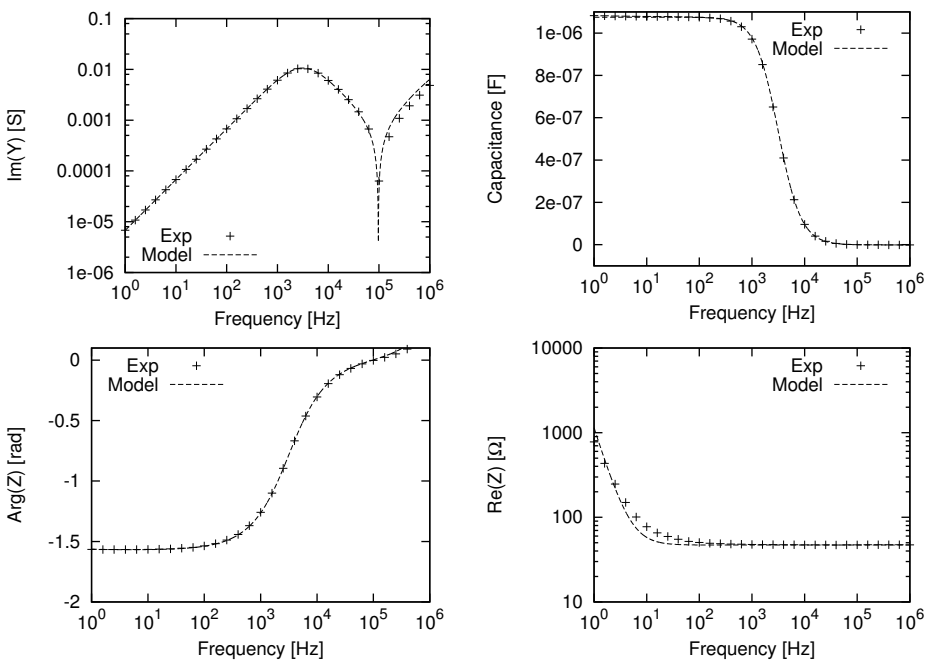

Figure 2.16: Bode plots of an RLC circuit using a 50 Ω resistor and a 1 μF tantalum capacitor. The data are fitted using the model described on Figure 2.17.

Figure 2.16 presents the results of this experiment. It can be observed that the plots are similar to the plots of the RC circuit in serial on Figure 2.11 from 1 Hz to 1 MHz, and are even the same for the capacitance plot. The major differences compared to Figure 2.11 are that:

- The phase increases at values superior to 0 after 100 kHz.
- A resonance appears on the imaginary part of the admittance plot around 100 kHz.
- The resistance of the circuit is far higher than 50 Ω at low frequencies on the real part of the impedance plot.

To understand these differences, the model on Figure 2.17 is proposed. Like the model presented on Figure 2.6 it has a resistor of resistance R and a capacitor of capacitance C.

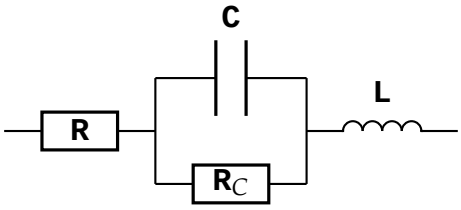

Figure 2.17: Model of a RLC circuit in serial

An inductor of inductance L is added in serial with the resistor and the capacitor. This inductor is supposed to be created by the wires connecting the circuit to the measurement instrument, but also by the wires composing the circuit itself.
Until now the capacitors were considered as perfect. Actually, the medium between the two plates composing the capacitor, being vacuum, air or even water, has a finite resistance value. So, a capacitor has an internal resistance, which is represented by the resistor R_C in parallel with the capacitor C on Figure 2.17 The impedance Z_{model} of this model is described by Equation 2.39 :

$$Z_{model}(\omega) = \frac{R_C}{1 + jR_C C\omega} + R + jL\omega \tag{2.39}$$

The data presented on Figure 2.16 were recorded with a 50Ω resistor in series with a 1 μF tantalum capacitor, using a Solartron 1296 dielectric interface coupled to a Solartron 1255B Frequency Response Analyser. The data were fitted by the model developped in Equation 2.39 . A value of 47 Ω was found for R, 1.075 μF for C, 2.5 μH for L and 20 MΩ for R_C. This is a value 6% lower than expected value for R, and 7.5% higher for C, which nevertheless respects the manufacturer tolerance. As no inductor is physically present in the circuit, the value of 2.5 μH found for L can be attributed to the self-inductance of the wires connecting the Solartron interface to the electrical elements.

Taking the real part of Equation 2.39, we extract:

$$\Re Z_{model}(\omega) = \frac{R + R_C + RR_C^2 C^2\omega^2}{1 + R_C^2 C^2\omega^2} \tag{2.40}$$

At low frequencies, the high value of the real part of the impedance is due to the resistance R_C in parallel with the capacitor, as Equation 2.40 is dominated by the R_C term. At high frequencies, the real part of the impedance tends towards R, as can be observed on Figure 2.16

The huge peak observed around 100 kHz on the imaginary part of the admittance on Figure 2.16 is due to a resonance phenomenon. The resonance peak frequency is linked to the capacitance and the inductance such as:

$$LC\omega^2 = 1 \tag{2.41}$$

With the inductance value fitted to 2.5 μH and the capacitance value fitted to 1.075 μF, the peak frequency calculated with Equation 2.41 is 97 kHz.

R	47 Ω
C	1.075 μF
R_C	20 MΩ
L	2.5 μH

Table 2.1: Summary of the parameters found by fitting Figure 2.16 with the model defined by Equation 2.39

Finally, the phase value higher than 0 after 100 kHz is due to the resonance, and more specifically to the inductor. As the phase of an inductor is equal to $\frac{\pi}{2}$, the resonance is a transition from the resistive state of the circuit to an inductive state at frequencies higher than 1 MHz.

The summary of the values fitted by the model can be found on Table 2.1.

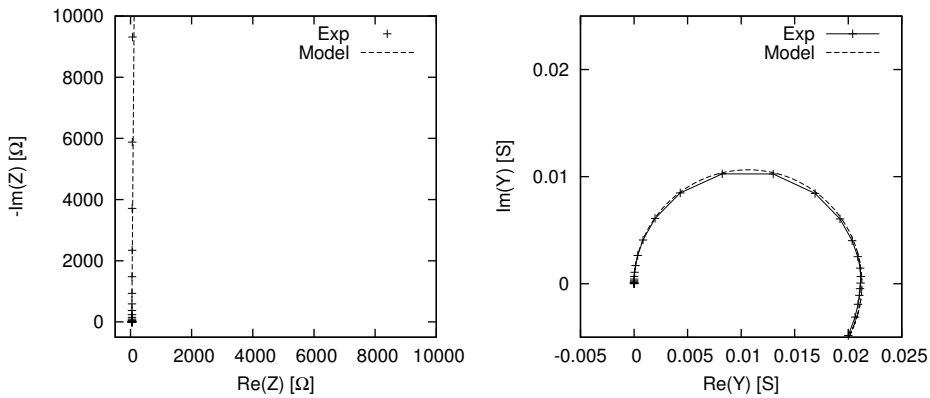

Figure 2.18: Nyquist plots in impedance and admittance of the global RLC circuit using a 50 Ω resistor and a 1 μF tantalum capacitor.

On Figure 2.18 are presented the Nyquist plots in impedance and admittance of the circuit. Like for a perfect capacitor, a vertical line can be observed on the Nyquist plot in impedance. The x-coordinate of this line is 47 Ω, as the beginning of the plot represent the points recorded at high frequencies. The Nyquist plot in admittance represents a semi-circle similar to the one studied with the RC circuit in serial in Figure 2.12. However it can be observed that part of the values around an x-coordinate of 0.02 S are negative. As already seen with the inductor on Equation 2.21, the value of the imaginary part of the admittance of an inductor is negative. The negative values on

the Nyquist plot in admittance on Figure 2.18 are due to the circuit becoming inductive around 1 MHz.

2.4 RLC circuit in series : Electrolytic capacitor

The study of an RLC circuit made of real elements brings changes from the study developed in 2.2.2. An electrolytic capacitor is even less perfect than a tantalum capacitor. Compared to the solid tantalum capacitor whose dielectric material is made of tantalum material, the dielectric material of an electrolytic capacitor is made of an electrically conductive solution called an electrolyte.
The capacitor proposed in the model detailed on Figure 2.17 can be replaced by a CPE.

Replacing the perfect capacitor used in the model defined by Equation 2.39 by a CPE gives the following model:

$$Z_{model}(\omega) = \frac{R_C}{1 + (jC)^{\alpha} R_C \omega} + R + jL\omega \tag{2.42}$$

with α being the power coefficient of the CPE.

Figure 2.19 was recorded with a 2.2 μF electrolytic capacitor (Radiospares, Beauvais) instead of the tantalum capacitor. The four spectra are close to Figure 2.16 where the circuit was composed of a tantalum capacitor. The main variation concerns the capacitance and phase values.

Using the model defined by Equation 2.42, the value of the capacitance was fitted at 2.4 μF while the value of the α parameter was fitted at 0.995. As the value of α is lower than 1, the value of the phase is higher than $\frac{-\pi}{2}$ and was found to be equal to -1.554. It can be observed on Figure 2.19 that, between 1 Hz and 100 Hz, the value of the capacitance decreases when the frequency increases, while it was constant on Figure 2.16. Actually this variation is due to the CPE, which decreases the value of the

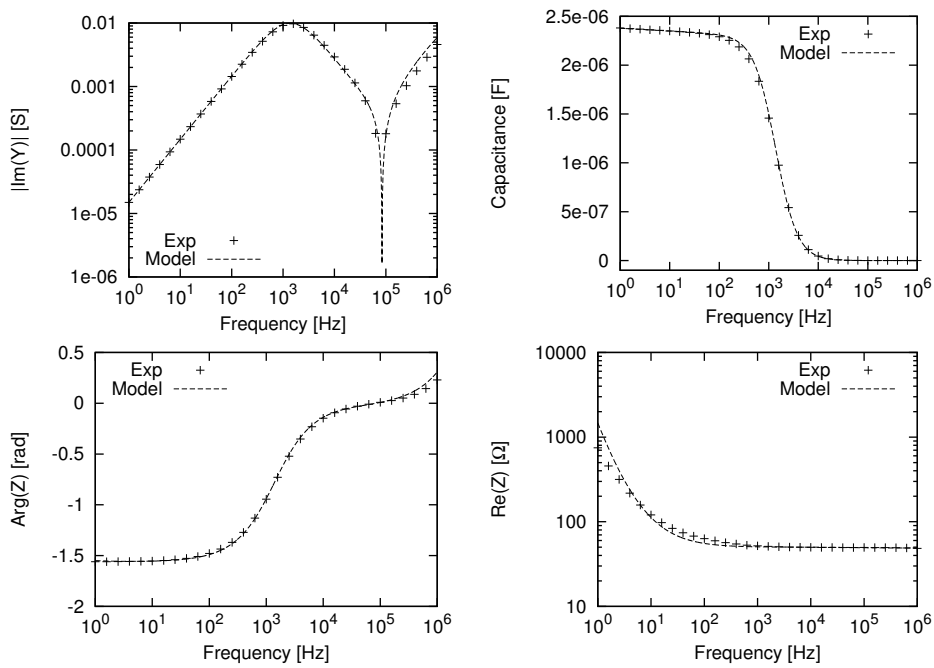

Figure 2.19: Bode plots of the global RLC circuit using a 50 Ω resistor and a 2.2 μF electrolytic capacitor

R	47 Ω
C	2.4 μF
α	0.995
R_C	5 MΩ
L	2.5 μH

Table 2.2: Summary of the parameters found fitting Figure 2.19 using the model defined by Equation 2.39

imaginary part of the admittance when the frequency increases and when the value of α is lower than 1. The summary of the values fitted by the model can be found in Table 2.2.

On figure 2.20 are presented the Nyquist plot in impedance and admittance. These plots are similar to the Nyquist plots of the RLC circuit with the tantalum capacitor on Figure 2.18. The main difference between the two plots is that the Nyquist plot in impedance for the electrolytic capacitor does not describe a completely vertical line. This is due to the constant phase element which affect a part of the impedance signal

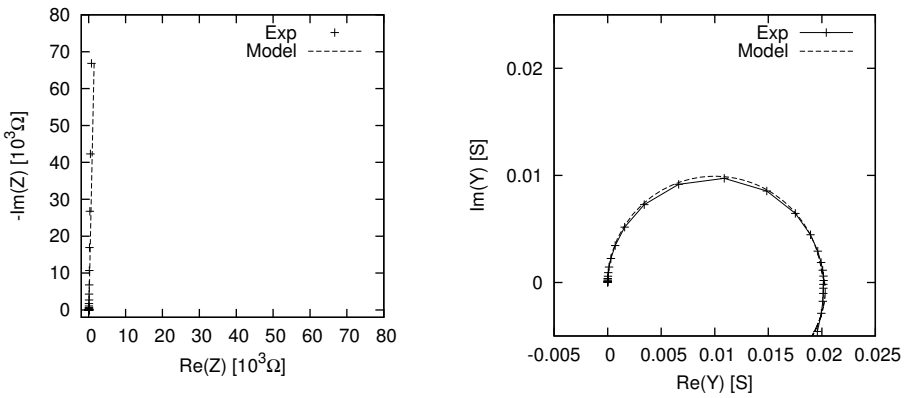

Figure 2.20: Nyquist plots of the impedance and admittance of the global RLC circuit using a 50 Ω resistor and a 2.2 μF electrolytic capacitor

to the real part of the impedance (Equation 2.27)

2.5 Conclusion

Impedance spectroscopy is the key technique to exploit the sensor. In order to understand the models presented in this work, the most used elements (resistor, capacitor, inductor, CPE) were presented. Although its nature did not reach a formal agreement in the scientific community, the Constant Phase Element (CPE) was presented as a distribution of time constants. This distribution might be due to the surface roughness of an electrode, or by capacitance dispersion. RC and RLC models were introduced, both theoretically and experimentally with real circuits. It could be observed that real circuits were affected by inductive effects, which could produce a resonance. Some differences between solid and electrolytic capacitors could also be noted, the latter being far less perfect than the former, and presenting a CPE effect.

Bibliography

[1] Mark E. Orazem and Bernard Tribollet. *Electrochemical Impedance Spectroscopy*. Wiley-Interscience, Sept. 2008. ISBN: 0470041404.

[2] Girault. *Electrochimie physique et analytique*. PPUR, 2007.

[3] H. Fricke. "The electric conductivity and capacity of disperse systems". In: *Journal of Applied Physics* 1.2 (1931), pp. 106–115.

[4] J.-B. Jorcin et al. "CPE analysis by local electrochemical impedance spectroscopy". In: *Electrochimica Acta* 51.8-9 (2006), pp. 1473–1479.

[5] B. Sapoval. "Linear and non-linear behavior of fractal and irregular electrodes". In: *Solid State Ionics* 75.C (1995), pp. 269–273.

[6] M. Ujvari, G. Lang, and G. Inzelt. "The problem of the low-frequency dispersion in the case of polymer film electrodes - An experimental impedance study on Au|poly (o-phenylenediamine) electrodes". In: *Electrochemistry Communications* 2.7 (2000), pp. 497–502.

[7] J. Bisquert et al. "Impedance of constant phase element (CPE)-blocked diffusion in film electrodes". In: *Journal of Electroanalytical Chemistry* 452.2 (1998), pp. 229–234.

[8] H.-K. Song et al. "Effect of pore size distribution on the frequency dispersion of porous electrodes". In: *Electrochimica Acta* 45.14 (2000), pp. 2241–2257.

[9] J. Bisquert. "Influence of the boundaries in the impedance of porous film electrodes". In: *Physical Chemistry Chemical Physics* 2.18 (2000), pp. 4185–4192.

[10] C. Hitz and A. Lasia. "Experimental study and modeling of impedance of the her on porous Ni electrodes". In: *Journal of Electroanalytical Chemistry* 500.1-2 (2001), pp. 213–222.

[11] L. Nyikos and T. Pajkossy. "Fractal dimension and fractional power frequency-dependent impedance of blocking electrodes". In: *Electrochimica Acta* 30.11 (1985), pp. 1533–1540.

[12] U. Rammelt and G. Reinhard. "On the applicability of a constant phase element (CPE) to the estimation of roughness of solid metal electrodes". In: *Electrochimica Acta* 35.6 (1990), pp. 1045–1049.

[13] W.H. Mulder et al. "Tafel current at fractal electrodes. Connection with admittance spectra". In: *Journal of Electroanalytical Chemistry* 285.1-2 (1990), pp. 103–115.

[14] D. Risovic et al. "Inferring fractal dimension of rough/porous surfaces-A comparison of SEM image analysis and electrochemical impedance spectroscopy methods". In: *Applied Surface Science* 255.5 PART 2 (2008), pp. 3063–3070.

[15] Peter Appel and John Newman. "Radially Dependent Corrective Warburg Problem for a Rotating Disk". In: *Journal of The Electrochemical Society* 124.12 (Dec. 1977), pp. 1864–1868. DOI: 10.1149/1.2133177.

[16] John Newman. "Current Distribution on a Rotating Disk below the Limiting Current". In: *Journal of The Electrochemical Society* 113.12 (Dec. 1966), pp. 1235–1241. DOI: 10.1149/1.2423795.

[17] G.J. Brug et al. "The analysis of electrode impedances complicated by the presence of a constant phase element". In: *Journal of Electroanalytical Chemistry* 176.1-2 (1984), pp. 275–295.

[18] P. Zoltowski. "On the electrical capacitance of interfaces exhibiting constant phase element behaviour". In: *Journal of Electroanalytical Chemistry* 443.1 (1998), pp. 149–154.

[19] I. Sadli et al. "Contributions of fractional differentiation to the modelling of electric double layer capacitance". In: *Energy Conversion and Management* 51.12 (2010), pp. 2993–2999.

Chapter 3

Numerical simulations

3.1 Introduction

Many techniques have been developed to perform numerical simulations. The most used are certainly the finite differences, the finite elements, and the finite volumes. Finite differences is the simplest technique but has some geometry restrictions. Finite volumes method (FVM) on the other hand is very flexible on the geometry and so was well adopted for fluid mechanics[1–4], but requires heavy calculations. Finite elements method (FEM) requires, following the case, more or less computing power than the finite volumes method[5], is less accurate[6] than FVM but more flexible on geometry[7]. FEM is well suited for electromagnetic studies[8–12].

A physical problem, continous and with infinite degrees of freedom is posed on a domain D. The flux conservation can be first expressed in the local form (Equation 3.1), presented here in steady-state conditions[13]. It is completed by the boundary conditions (BC), expressed at the borders of the domain.

$$Div.(Flux) = 0 \tag{3.1}$$

The equations are then integrated on the domain D using Galerkin's formulation (Equation 3.2).

$$\int_D \nabla\alpha.Flux.ds = \int_F \alpha.f(BC).dl \tag{3.2}$$

The equation is multiplied by a projection function and integrated by parts on the domain D. The boundary conditions are expressed by fixing some boundary flux (unknown gradient : Neumann conditions), or by fixing the value of the unknown at the boundaries (Dirichlet conditions).

The domain is then meshed in finite elements, and the previous functions are interpolated by linear combination of polynomes of order 1 or 2. Once the problem has been discretized on a finite number of nodes, it is transformed into a matricial system (Equation 3.3).

$$[A_{ij}].[X_j] = [B_j] \tag{3.3}$$

The system is solved by reversing the global matrix. The solution (vector X_j) is then given at each node of the geometry and interpolated at each point.

Finite elements were used to simulate the frequency response of face-to-face and coplanar geometries of sensors using two contactless electrodes, in order to find the optimal working parameters to apply to physical chips.

3.2 Material and methods

Numerical simulations were carried out with the software Flux-Expert® in version 4.2, running on a 64-bit Ubuntu Linux 8.04 system. The computer was a Mac Pro

(Apple, USA) configured with two Intel Xeon Woodcrest clocked at 2.66 GHz and 8 GB of RAM.

3.2.1 Equation

The goal of the model is to simulate a system composed of two electrodes, an insulator and an electrolyte for a frequency range from 100 Hz to 10 MHz. It takes into account the ohmic current in solution (water resistance), and the displacement current arising at high frequencies (water capacitance). The capacitance values involved in this study were far lower compared to those of the electrical double-layer. The goal of these simulations being to study the geometry and the influence of the capacitance created by an insulating layer, the electrical double-layer was not taken into account. The problem was solved using Maxwell's equations [14]:

$$\nabla \cdot \mathbf{E} = \frac{\rho}{\varepsilon_0} \tag{3.4}$$

$$\nabla \times E = -\frac{\partial \mathbf{B}}{\partial t} \tag{3.5}$$

$$\nabla \cdot \mathbf{B} = 0 \tag{3.6}$$

$$c^2 \nabla \times \mathbf{B} = \frac{j}{\varepsilon_0} + \frac{\partial \mathbf{E}}{\partial t} \tag{3.7}$$

with **E** and **B** being respectively the electric field and the magnetic field, j the ohmic current density, $\varepsilon_0 \frac{\partial \mathbf{E}}{\partial t}$ the displacement current density, ρ the density of charge, c the velocity of the light and ε_0 the permittivity of vacuum. As the electrical double-layer is not taken into account, and the charges at the wall are ignored, $\nabla \cdot \mathbf{E} = 0$ and Equation 3.4 does not need to be used. Due to the low value of the current flowing in the system, the induced magnetic field is considered too weak to have an influence and induce an electric field. Equations 3.5 and 3.6 are then neglected. Taking the divergence of

Equation 3.7, we obtain:

$$\nabla \cdot \left(j + \varepsilon_0 \frac{\partial \mathbf{E}}{\partial t} \right) = 0 \tag{3.8}$$

The problem is solved for a harmonic signal ranging from 100 Hz to 10 MHz. In consequence, the partial derivative of **E** with respect to time can be expressed in the complex plane. Secondly, $j = \sigma \mathbf{E}$, where σ is treated as a complex conductivity. Equation 3.8 becomes:

$$\nabla \cdot \left[\left(\sigma + \imath \omega \varepsilon_0 \right) \mathbf{E} \right] = 0 \tag{3.9}$$

At low frequencies, the complex term (displacement current) of the Equation 3.9 can be ignored, and it comes:

$$\nabla \cdot \left(\sigma \mathbf{E} \right) = 0 \tag{3.10}$$

which gives the classical Laplace equation ($\nabla^2 \Phi = 0$) when σ is uniform.

At high frequencies, the displacement current cannot be ignored, and Equation 3.9 can be used to describe both ohmic and dielectric phenomena. Equation 3.9 was integrated using Galerkin's formulation.

3.2.2 Calculation of the capacitance

When working with a harmonic signal, Ohm's law, in the case of capacitance, can be written as:

$$\overline{I} = \jmath C \omega \overline{U} \tag{3.11}$$

with $\overline{U}$ being the potential applied to the terminals of the capacitor and $\overline{I}$ the current. Taking the imaginary part of Equation 3.11, we obtain:

$$C = \frac{I}{\omega U} \tag{3.12}$$

I was obtained by integrating the current density on the desired line, and multiplied by the depth of the considered geometry. In the case of the first mesh described on Figure 3.1, the line was taken on the whole electrode length at $h/2$ y-coordinate. For the second mesh presented in Figure 3.1, the line was taken from 0 to $2e+w$ but always on a $h/2$ y-coordinate. However, for a coplanar design (Figure 3.9), the line was taken on the symmetry line, from 0 to $i+h$ on the y-coordinate. A depth D of 200 μm was chosen, representative of the width of the channel studied in Chapter 4.

3.3 Face-to-face design in 2 dimensions

3.3.1 Mesh

A face-to-face design mesh was created to study the properties of systems going from the size of a microchip to the dimension of a sensor in a 6 mm diameter reservoir.

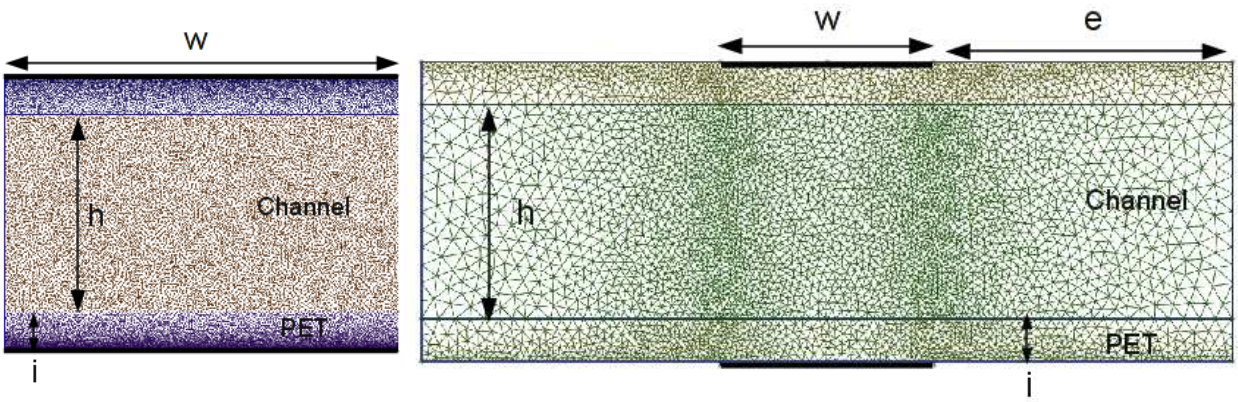

Figure 3.1: Meshes of the face-to-face design, without and with edge effects

Three surfaces were created, the top and the bottom ones being the insulating layers while the channel was represented by the middle surface. In the general configuration, the thickness i of the insulating layers is 1 μm while the height h of the channel is set to 50 μm . The electrodes are simulated by equipotential lines situated at the top and the bottom of the mesh, at the center of the design. Their width w is set to 50 μm . Spaces were left at both sides of the electrodes to model the edge effects. The width of these

	Face-to-face	Face-to-face + Edges
w	50 μm	50 μm
h/w	1	1
i/w	2x10^{-2}	2x10^{-2}
e/w		4
anode	1.5 V	1.5 V
cathode	-1.5 V	-1.5 V
σ_{sol}	10^{-3} S.m^{-1}	10^{-3} S.m^{-1}
σ_{PET}	0 S.m^{-1}	0 S.m^{-1}
ε_R sol	78 F.m^{-1}	78 F.m^{-1}
ε_R PET	3 F.m^{-1}	3 F.m^{-1}

Table 3.1: Summary of the general parameters of the face-to-face design study

spaces were set to 200μm . The dimensions can be normalized by the electrodes width, that is to say the w parameter. We can then define dimensionless parameters such as *h/w*, *e/w* and *i/w*. The electrodes are considered rectangular.

The electrical conductivity and the relative permittivity values of the insulating layers were chosen as to model PET insulating layers. Thus, their conductivity was set to 0 S.m^{-1} while their relative permittivity was set to 3 F.m^{-1}. The channel was supposed to be filled with a solution. Its conductivity was therefore set to 10^{-3} S.m^{-1} and its relative permittivity to 78 F.m^{-1}.

Boundary conditions

The potential difference between the electrodes was set to 3 V. The boundary conditions around the mesh, excepted at the electrodes, were fixed so that the flux normal to the surface equals 0 (Neumann conditions).

3.3.2 Cut-off frequency

Figure 3.2 shows the capacitance and phase angle spectra from 100 Hz to 10 MHz obtained with the parameters described in 3.3.1, using a face-to-face design without

edge effects (First mesh of Figure 3.1).

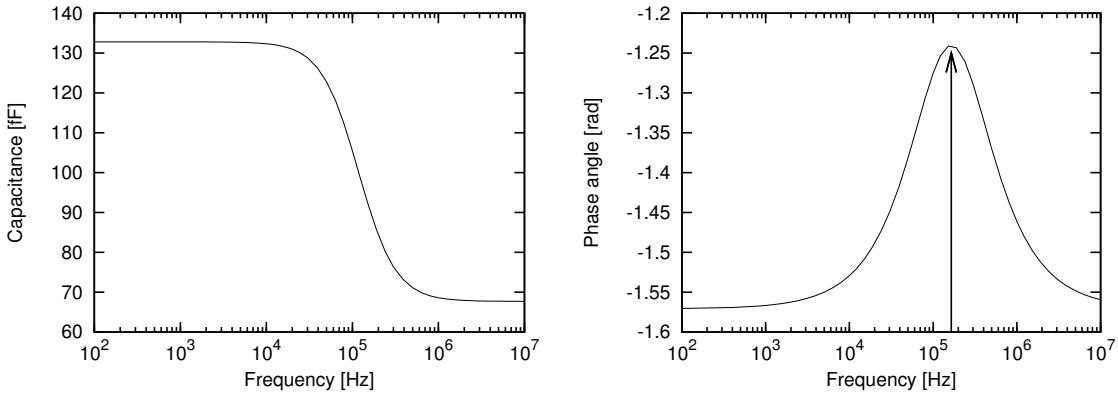

Figure 3.2: Capacitance and phase angle against the frequency for a face-to-face design without edge effects.

Two capacitance values can be observed at low and high frequencies. The low frequency capacitance is created by the insulating PET layer and would theoretically be equal to 266 fF. As the two capacitors created by the each PET layer are in series, the resulting capacitance value is 133 fF. The high frequency capacitance is the resultant of the two PET capacitances in series with the capacitance due to the solution. Without taking into account the edge effects, the theoretical value of the solution capacitance is 138 fF. The resulting theoretical high frequency capacitance is then of 68 fF.

In the case of a first order RC filter, the cut-off frequency f_c is given by Equation 2.35. In the case of the channel, the resistor and the capacitor share the same distance between the electrodes and the surface area. The cut-off frequency can therefore be expressed as:

$$f = \frac{\sigma}{2\pi\varepsilon_0\varepsilon} \tag{3.13}$$

The cut-off frequency corresponds to the equilibrium frequency between the ohmic and dielectric effects. With a 10^{-3} S.m^{-1} solution conductivity, the cut-off frequency calculated with Equation 3.13 should be equal to 230 kHz. However, it can be observed

on Figure 3.2 that the cut-off frequency was found to be equal to about 170 kHz. This difference might be due to the capacitances created by the PET layers. The mesh can be modeled with the elements described on Figure 3.3.

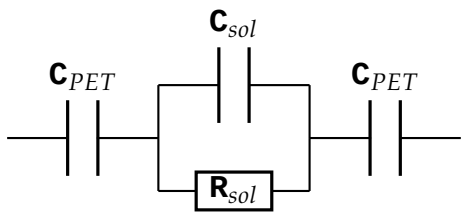

Figure 3.3: Equivalent circuit of the simulated face-to-face geometry

The total impedance Z_{FTF} of this circuit is:

$$Z_{FTF}(\omega) = \frac{2}{\jmath\omega C_{PET}} + \frac{R_{sol}}{1 + \jmath\omega R_{sol} C_{sol}} \tag{3.14}$$

The argument of the impedance is then equal to:

$$Arg(Z_{FTF}(\omega)) = -\frac{R_{sol}C_{sol}}{C_{PET}}(2C_{sol} + C_{PET})\omega - \frac{2}{RC_{sol}\omega} \tag{3.15}$$

The cut-off frequency corresponds to the maximum of the phase angle. Then, the cut-off frequency can be found by studying the variations of the phase angle. Arg(Z_{FTF}) is defined and derivable across the whole frequency range, so it comes:

$$\frac{dArg(Z_{FTF}(\omega))}{d\omega} = \frac{-\frac{R_{sol}^2 C_{sol}^2}{C_{PET}^2}(2C_{sol} + C_{PET})^2 + \frac{2}{R_{sol}C_{sol}}}{\frac{R_{sol}^2 C_{sol}^2}{C_{PET}^2}(2C_{sol} + C_{PET})^2\omega^2 + \left(1 + \frac{4R_{sol}C_{sol}}{R_{sol}C_{PET}^2}\right)\omega + \frac{4}{R_{sol}^2 C_{PET}^2}} \tag{3.16}$$

As the denominator is strictly positive, the value of the cut-off frequency can be found by zeroing the numerator of Equation 3.16. It comes that f_c equals to:

$$f_c = \frac{1}{2\pi R_{sol}}\sqrt{\frac{2}{C_{sol}(2C_{sol} + C_{PET})}} \tag{3.17}$$

R_{sol}	$5\times10^6\ \Omega$
C_{PET}	266 fF
C_{sol}	138 fF

Table 3.2: Summary of the parameters due to the geometry presented on the first mesh in Figure 3.1

For the considered face-to-face design (values summarized in Table 3.2), the cut-off frequency would then be 164 kHz, which corresponds to the observed value on Figure 3.2.

3.3.3 Edge effects

The edge effects were simulated by adding the edge space at the left and the right of the electrode. The added capacitance due to the edge effects can usually be calculated using conformal mapping formulations[15]. It can also be calculated from Newman law[16]. However in his course of Physics, Feynman gave a good approximation of the capacitance added by the edge effects[14]: in the case of a parallel plate capacitor, the width of the plate might be added by 3/8 of the distance between the plates. This would increase the capacitance value created by the insulator by 0.75 %, to 267 fF. The value of the capacitance created by the solution would increase to 190 fF. The value of the resulting global capacitance at high frequency would then be 78 fF.

From the numerical simulations (Figure 3.4) the capacitance at low frequencies increases from 133 fF to 135 fF, while the capacitance at high frequencies increases from 67 fF to 78 fF. The capacitance values at high frequencies is in agreement with the capacitance calculated using Feynman's approximation. At low frequencies, the values of the capacitance ranged from 133.5 to 135 fF (an error of 1.1%) depending on the mesh quality.

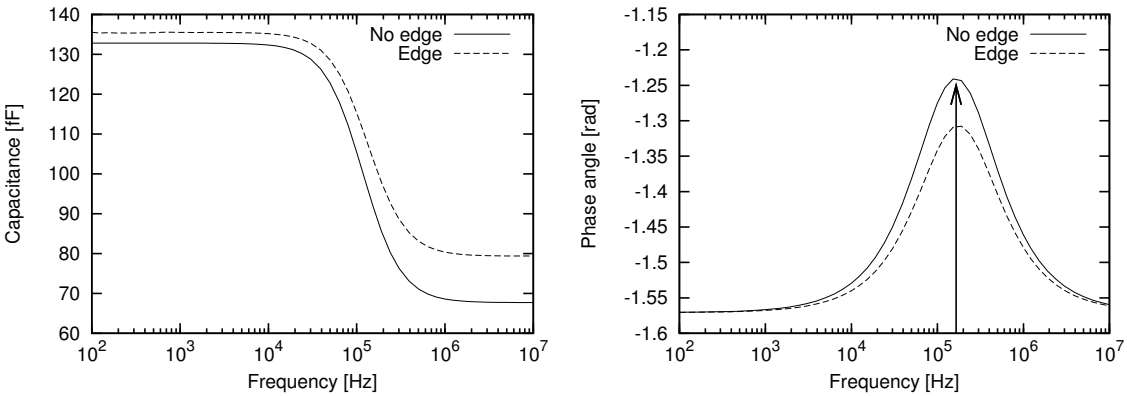

Figure 3.4: Capacitance and Phase angle of a face-to-face design with and without edge effects

It can also be noted on the phase angle plot that the value of the phase at the cut-off frequency is lower with the edge effects. As the equivalent electrode width is higher, the value of the resistance created by the solution is lower with the edge effects. In a perfect RC filter, the variation of the resistance value depending on the width of the electrode would be canceled by the varying value of the capacitor. However, from Equation 3.17, the capacitance variation is amplified by the value of the capacitance created by the insulator. As a result, the variation of the capacitance is more important than the variation of the resistance, and so decreases the cut-off frequency.

3.3.4 Influence of the solution conductivity

The influence of the solution conductivity on the model was studied for values ranging from 10^{-1} to 10^{-4} S.m^{-1}. The cut-off frequency should vary linearly with the solution conductivity value (Equation 3.17). This can be checked on the phase angle plot (Figure 3.5), where the cut-off frequency value is increased by a factor 10 when the solution conductivity increases by the same quantity.

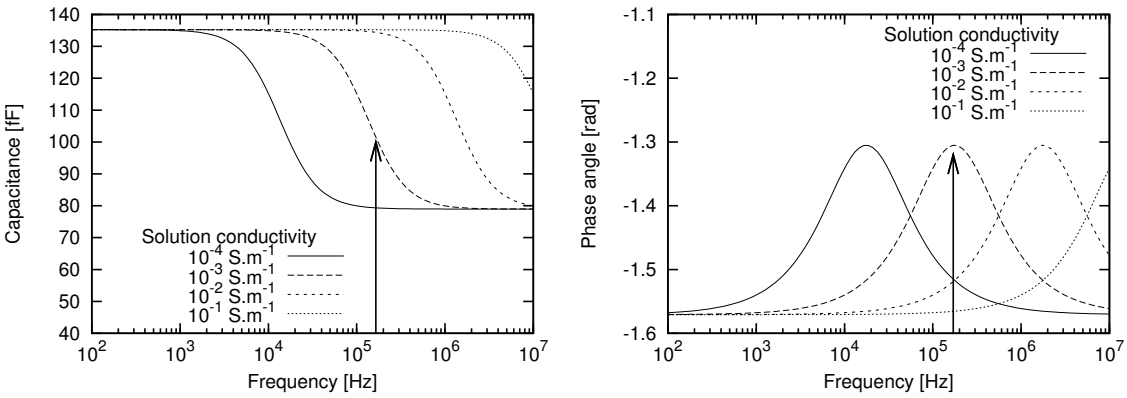

Figure 3.5: Capacitance against the frequency for different channel conductivity values using a face-to-face design.

3.3.5 Influence of the channel height

In a face-to-face geometry, the channel height influences directly its resistance, but also the capacitance created by the solution (volume capacitance). When computing the capacitance value from 100 Hz to 10 MHz for different distances between the electrodes (Figure 3.6), it can be seen that the capacitance value does not change at low frequencies, but evolves considerably after 100 kHz.

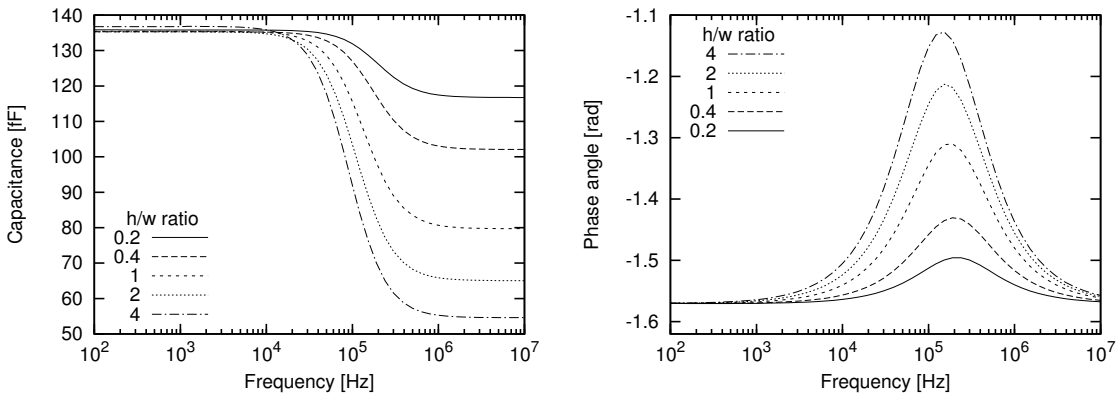

Figure 3.6: Capacitance against the frequency for different height values of the reservoir using a face-to-face design.

At low frequencies, the surface capacitors are not affected by a variation of the distance between the electrodes, as their geometry remains unchanged. At high frequen-

cies, the volume capacitance value decreases as the distance between the electrodes increases. The resulting capacitance is then lower. It can be observed on the Phase angle plot that the transition is higher between the two capacitive states when the h/w ratio increases.

It can also be observed on the phase angle spectrum that the cut-off frequency value decreases when the distance between the electrodes increases. Considering the resistive and capacitive terms of the channel of the Equation 3.17 with respect to their geometrical parameters, we obtain:

$$f_c = \frac{wd}{2\pi}\sqrt{\frac{2}{\varepsilon_0\varepsilon_R wd(2\varepsilon_0\varepsilon_R wd + hC_{PET})}} \tag{3.18}$$

As a result, the cut-off frequency is dependant on the channel height. Increasing the channel height leads to decreasing the cut-off frequency value, as can be observed on Figure 3.6.

Edge effects

The channel height has a strong influence on the capacitance created by the solution (Figure 3.7).

The difference of volume capacitance with added edge effects is almost negligible for a 2 μm height value (3.3 %). However the capacitance value with the edge effects is increased by 150 % with respect to the capacitance without edge effects when the distance between the electrodes reaches 200 μm .

3.3.6 Influence of the insulator thickness

The insulator separating the metallic material of an electrode from the solution makes the capacitance created by the PET layer dependent on the insulator thickness.

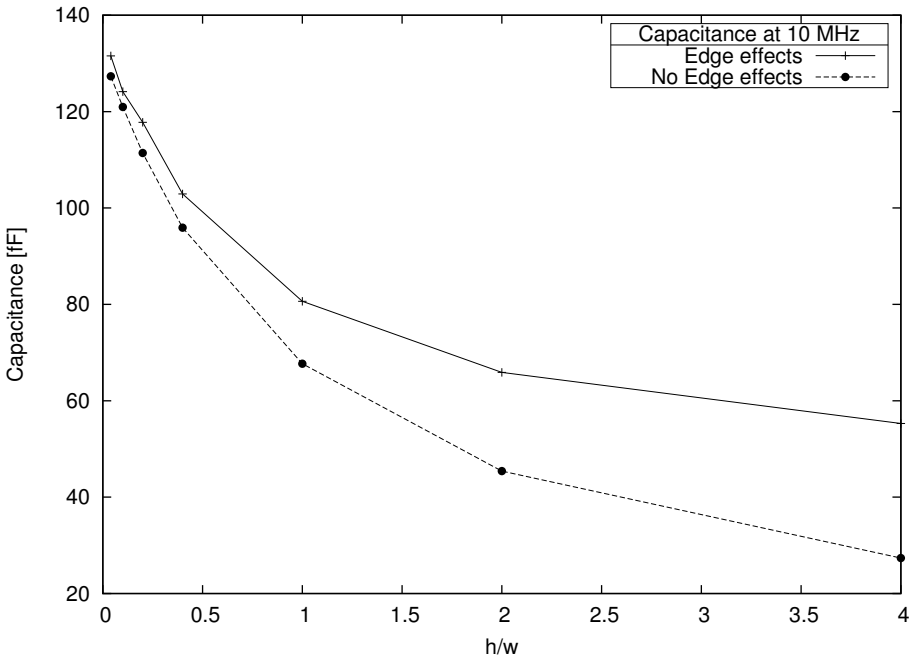

Figure 3.7: Influence of the edge effects in a face-to-face design. Capacitance against the channel height.

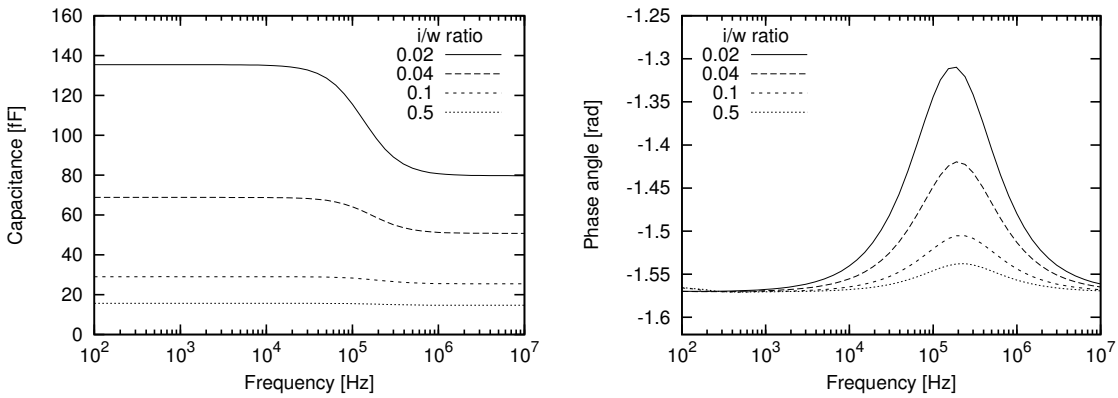

Figure 3.8: Capacitance against the frequency for various insulator thickness values using a face-to-face design

Changing the insulator thickness from 1 μm to 10 μm changes the value of the capacitance created by the PET layer, which increases when the insulator thickness decreases (Figure 3.8). As the high frequency capacitance is composed of two capacitances created by the PET layer in series with the capacitance created by the solution, the value of the high frequency capacitance also decreases when the insulator thickness

increases.

It can be observed that the value of the cut-off frequency decreases when the insulator thickness decreases. Following Equation 3.18, the value of the cut-off frequency depends on the value of the capacitance created by the insulator. Thus, a lower insulator thickness increases the capacitance C_{PET}, and then the value of the cut-off frequency decreases.

3.4 Coplanar design in 2 dimensions

The coplanar design in 2 dimensions adds a new parameter compared to the face-to-face design : The distance between the electrodes.

3.4.1 Mesh

The mesh (Figure 3.9) represents half of the reservoir.

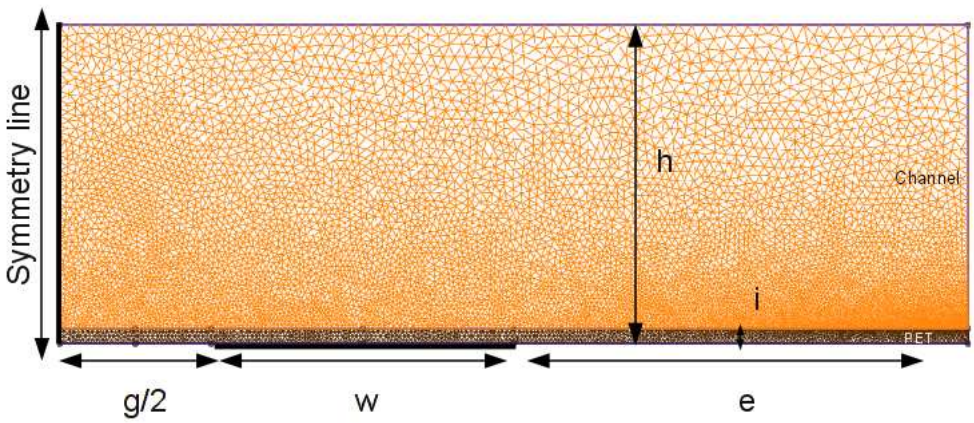

Figure 3.9: Mesh of the geometry used to make the simulations in contactless mode. Half of the reservoir and only one electrode are modelized.

Using a vertical symmetry axis (left vertical edge), only one electrode was modeled. The electrode and the symmetry line (mirror) were considered as physical lines while the reservoir was considered as a physical surface. The insulator is represented by a

physical surface between the electrodes and the channel. The distance between the beginning of the two electrodes was defined by the gap parameter g, the electrode width by the w parameter and the height of the fluid in the reservoir by the h parameter. The distance between the end of the electrode and the end of the channel was defined by the edge parameter e while the insulator thickness was defined by the insulator parameter i.

Boundary conditions

The meshed electrode potential was fixed to 1.5 V. Using the symmetry axis, the potential of the other electrode was automatically fixed to -1.5 V, leading to a potential difference of 3 V. Like with the face-to-face design, the boundary conditions at the wall, excluding the electrodes, fixed a normal flux density equals to zero.

3.4.2 Normalization

Some normalized distances can be defined from the previous parameters. w/g defines the relative electrode width while h/g defines the relative channel height, i/g the relative insulator thickness, and e/g the relative edge distance. The behaviour of the sensor was simulated for two configurations. The parameters of the first geometry was g=10 μm , h=50 μm , e=15 μm , i=1 μm and w=50 μm while those of the second was g=100 μm , h=500 μm , e=150 μm , i=10 μm and w=500 μm .

For each applied frequency, the capacitance and phase values are identical for the two geometries (Figure 3.10). At low frequencies, the capacitance remains unchanged as both the insulator thickness and the electrode width are increased 10 times. The channel resistance and channel capacitance values remain also unchanged as each modified parameter (height, surface area) is compensated by an other.

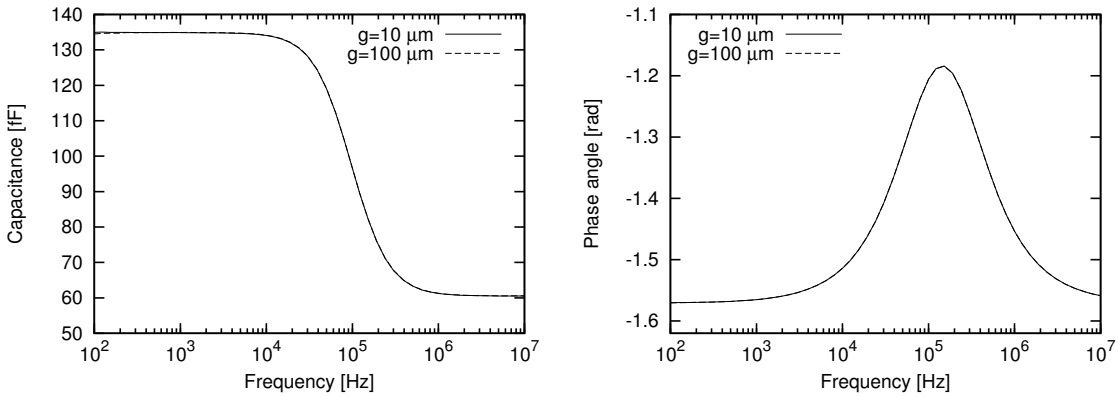

Figure 3.10: Capacitance versus frequency for a variation of the gap value between the two electrodes from 10 μm to 100 μm , while keeping all the ratios constant.

	Coplanar	Coplanar + Edges
g	10 μm	10 μm
w/g	5	5
h/g	5	5
e/g	0	1.5
i/g	0.1	0.1
anode	1.5 V	1.5 V
cathode	-1.5 V	-1.5 V
σ_{sol}	10^{-3} S.m^{-1}	10^{-3} S.m^{-1}
σ_{PET}	0 S.m^{-1}	0 S.m^{-1}
ε_R sol	78 F.m^{-1}	78 F.m^{-1}
ε_R PET	3 F.m^{-1}	3 F.m^{-1}

Table 3.3: Summary of the general parameters and boundary conditions of the coplanar design study

3.4.3 Influence of the electrodes width

The w/g parameter was set in a range from 0.5 to 10 (Figure 3.11). Changing the electrode width has the same effect on the capacitance created by the PET layer than changing the insulating material thickness : The capacitance decreases linearly when the value of the w/g parameter decreases. It can be noted that the cut-off frequency is shifted to lower frequencies and that the high frequency capacitance evolution is limited for a w/g value higher than 5.

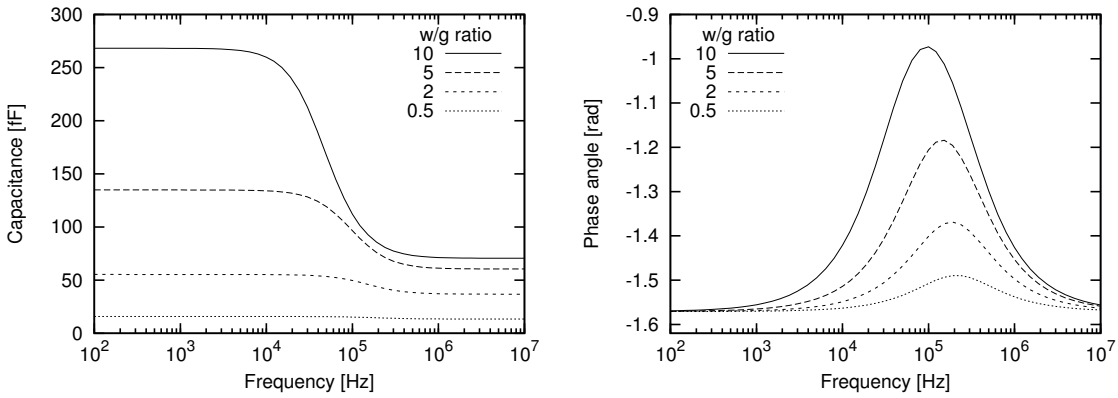

Figure 3.11: Capacitance against the frequency for a variation of w/g

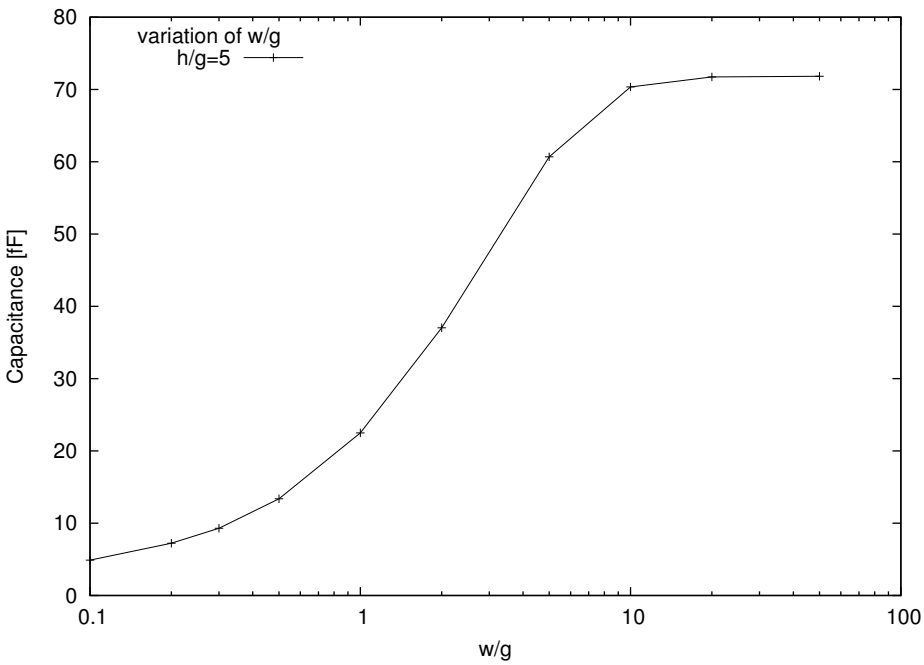

Figure 3.12: Capacitance against the variation of w/g

The evolution of this capacitance is detailed on the high frequency capacitance plotted at 10 MHz (Figure 3.12). The slope decreases after a w/g value of 5 and is almost flat after a w/g value of 10. In this geometry, the h/g value is equal to 5.

As the potential distribution between two coplanar electrodes is roughly elliptic[17, 18], the region of the solution at the outer part of the electrode might be equipotential and no displacement current might take place in this region when the electrode width

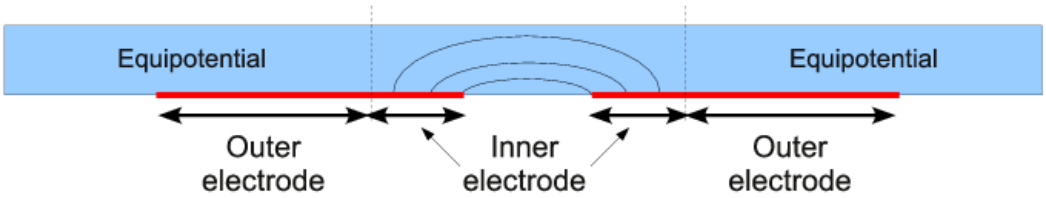

Figure 3.13: Picture of the geometry with an electrode width higher than the channel height.

is larger than the channel height. The fact that the capacitance keeps increasing from w/g equals 5 to 10 might be due to the gap value. With a 1 μm gap value, a 5 μm electrode width and a 5 μm channel height, only 4.5 μm of the electrode width is used to produce the potential gradient at high frequencies. In this case, a 10 μm channel height would let the potential gradient in the solution be developed from the gap to the end of the space devoted to the outer edge effects .

3.4.4 Influence of the insulator thickness

The effect of the insulator thickness was studied for i/g ranging from 0.1 to 1 (Figure 3.14).

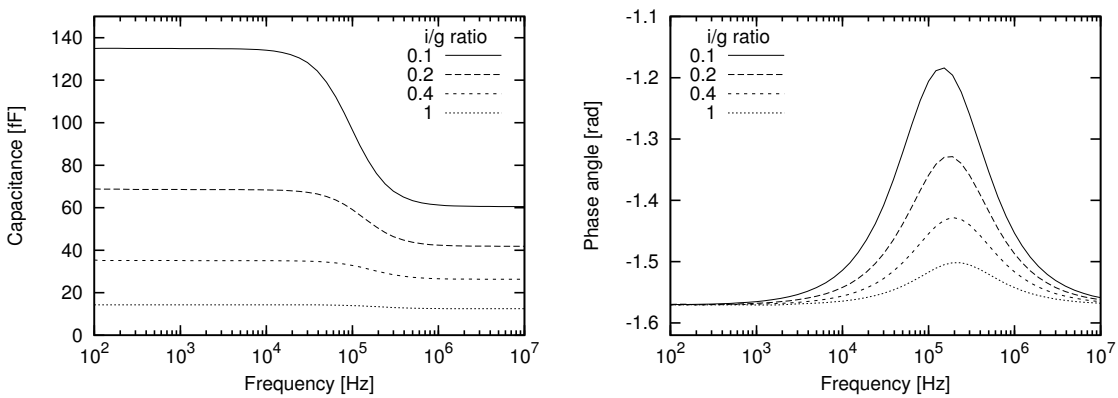

Figure 3.14: Capacitance against the frequency for a variation of i/g

The behaviour is close to the face-to-face geometry, as doubling the insulator thick-

ness decreases by a factor 2 the capacitance created by the PET layer. The effect at high frequencies is also close to the behaviour observed with the face-to-face geometry. However, it can be observed on the phase angle plot that the cut-off frequencies shifts to lower frequencies when the insulator thickness decreases.

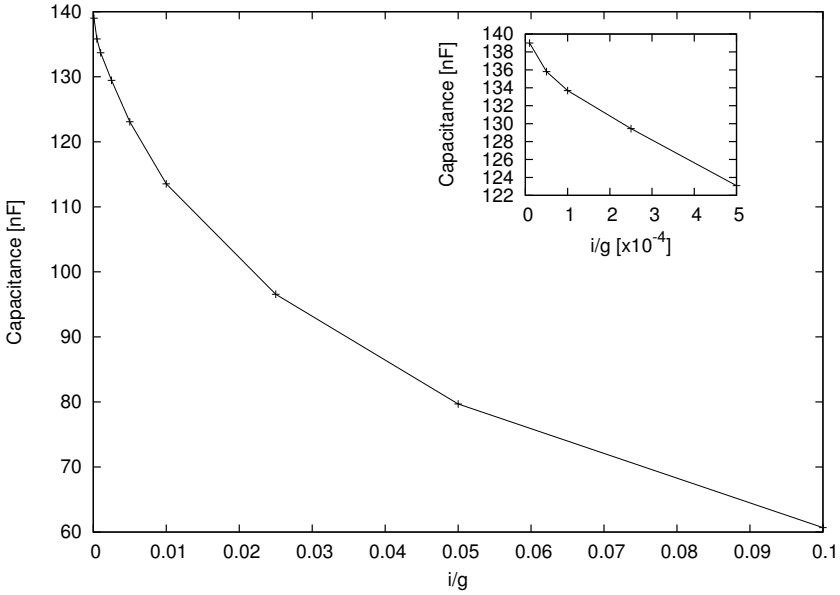

Figure 3.15: Capacitance against the variation of i/g

The insulator thickness effect was also studied at 1 MHz for i/g ranging from 10^{-5} to 0.1 (Figure 3.15). It can be noted that the impact of the insulating layer at 1 MHz for a i/g value lower than 10^{-2} is negligible. As the PET layer capacitance is orders of magnitude higher than the solution capacitance, the latter limits the global capacitance.

3.4.5 Influence of the channel height

The h/g parameter was set in a range from 0.5 to 10 (Figure 3.16). As the PET layer capacitance is not affected by a fluid height variation, the capacitance does not evoluate at low frequencies. However, the solution capacitance value is directly affected by a channel height variation, and so is the value of the high frequency capacitance. This capacitance decreases dramatically when h/g decreases, and in the other way is limited

for h/g values higher than 5.

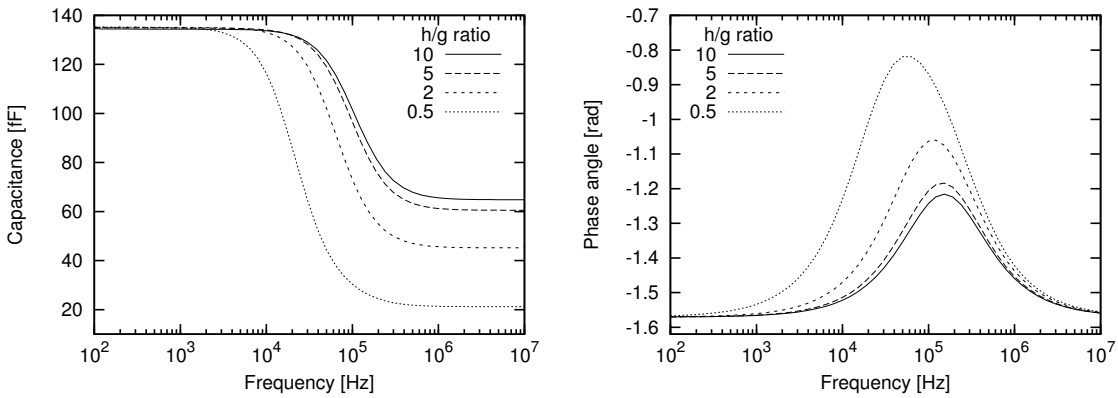

Figure 3.16: Capacitance against the frequency for a h/g variation.

This tendancy is confirmed on Figure 3.17 where it can be observed that the slope decreases when h/g is higher than 5 and is almost flat from a h/g value equal to 10. As with the w/g effect, a channel height lower than the electrode width does not let the potential gradient in the solution be created all along the electrode width. As w/g is equal to 5 in this case, h/g has to be higher than 5 for the potential gradient to be established all along the electrode width.

Figure 3.18 further explains this phenomenon using a 20 μm electrode width, and a 10 μm gap value. For h/g lower than 1, the displacement current is almost entirely due to the inner edge effects. A displacement current appears in the solution from h/g=1, with a low intensity at the outer part of the electrode and a few outer edge effects. From a h/g value of 5, the displacement current takes place in the solution all along the electrode width.

3.4.6 Edge effects

The evolution of the capacitance with or without edge effects was studied at 10 MHz by simulating a variation of w/g with the value of the e/g parameter set to 0 or 1.5 (Figure 3.19). The edge effects have a strong influence on the capacitance when the

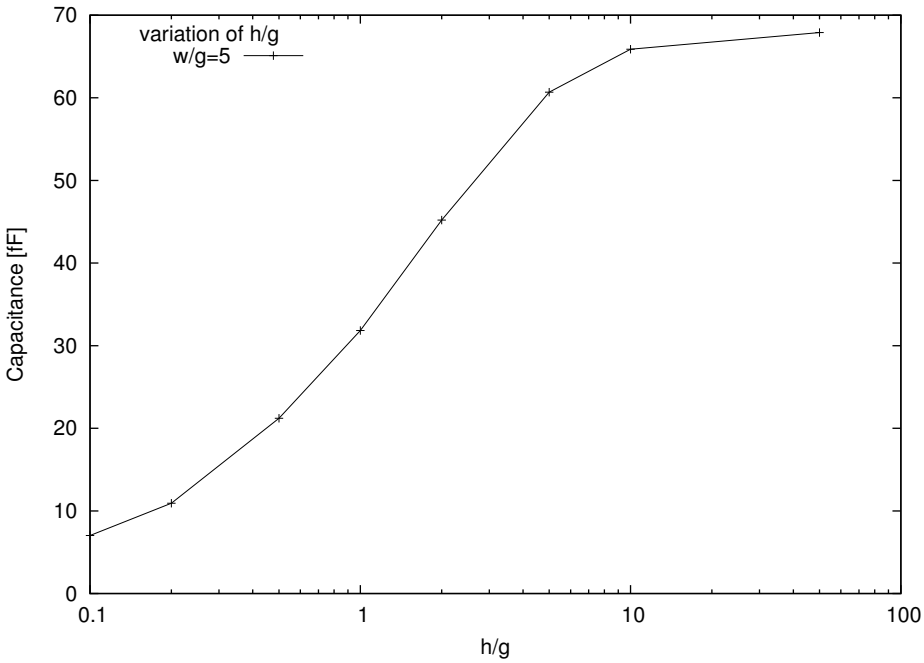

Figure 3.17: Capacitance against a h/g variation.

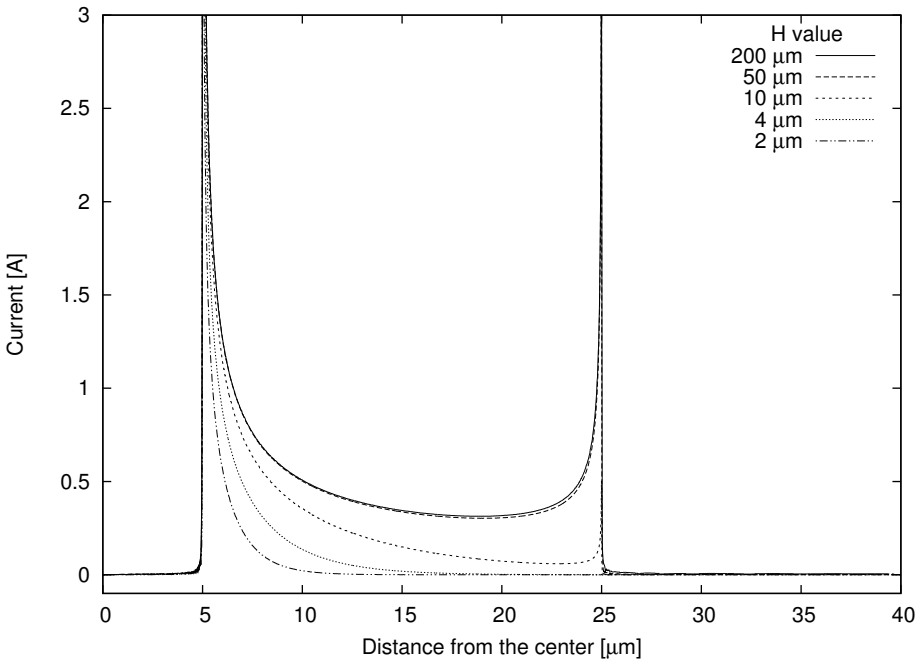

Figure 3.18: Current with respect to the distance from the symmetry axis

width of the electrode is small, as the capacitance is improved by 38 % when w/g=0.1 (difference of capacitance of 1.35 fF). However, this influence decreases when the value of w/g increases, as the relative part of the capacitance due to the edge effects decreases

when the width of the electrodes increases (the difference in capacitance still being constant). From w/g=5 the difference of capacitance is reduced and no difference can be observed from w/g=10. As h/g=5, the height of the channel is too low and the value of the displacement current is lowered on the outer part region of the electrode width. Thus, the outer edge effects cannot take place when w/g is at least twice higher than h/g.

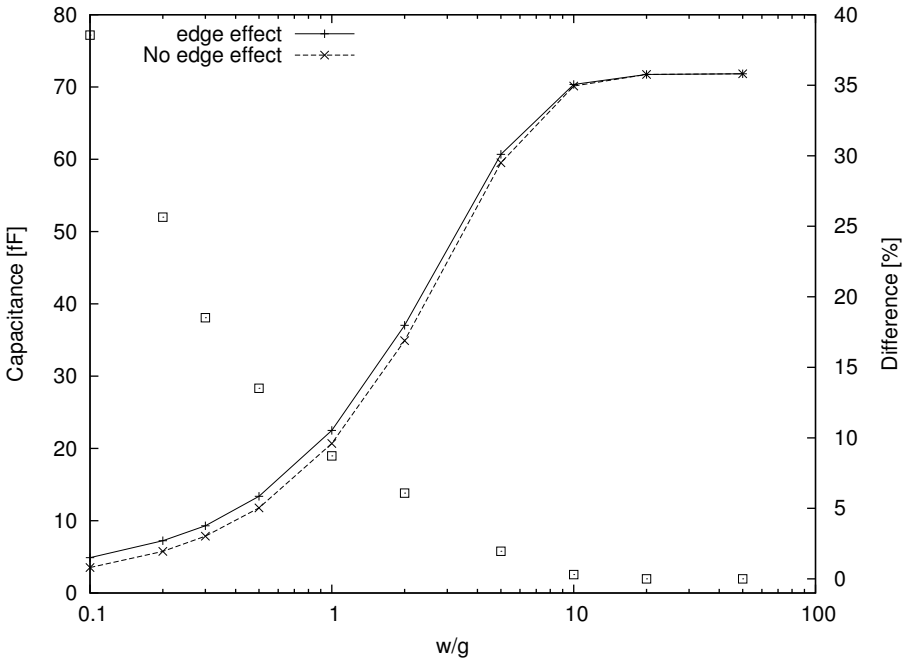

Figure 3.19: Capacitance with respect to w/g for a variation of e/g

3.4.7 High-Frequency design rules

In order to insure a good level of high frequency capacitance, a Gq parameter that should be equal or higher than 1 is introduced.

Definition of Gq

It was previously observed that the displacement current cannot take place in the solution along all the electrode width when h/w <1. However, h/g equal to w/g is

not enough to ensure that the gradient of potential into the solution takes place along all the electrode width, as the gap is not taken into account. Taking the full width of the electrode plus half of the gap value might ensure a good level of capacitance. We can then introduce the Geometry Quality (Gq) dimensionless number as:

$$Gq : \frac{h}{\frac{g}{2} + w} \geqslant 1 \tag{3.19}$$

Design rules

It was observed in this study that the displacement current took place at high frequencies. The design behaviour was then simulated at 10 MHz, with a w/g and h/g variation while the gap was fixed to 10 μm and the insulator thickness to 1 μm (Figure 3.20).

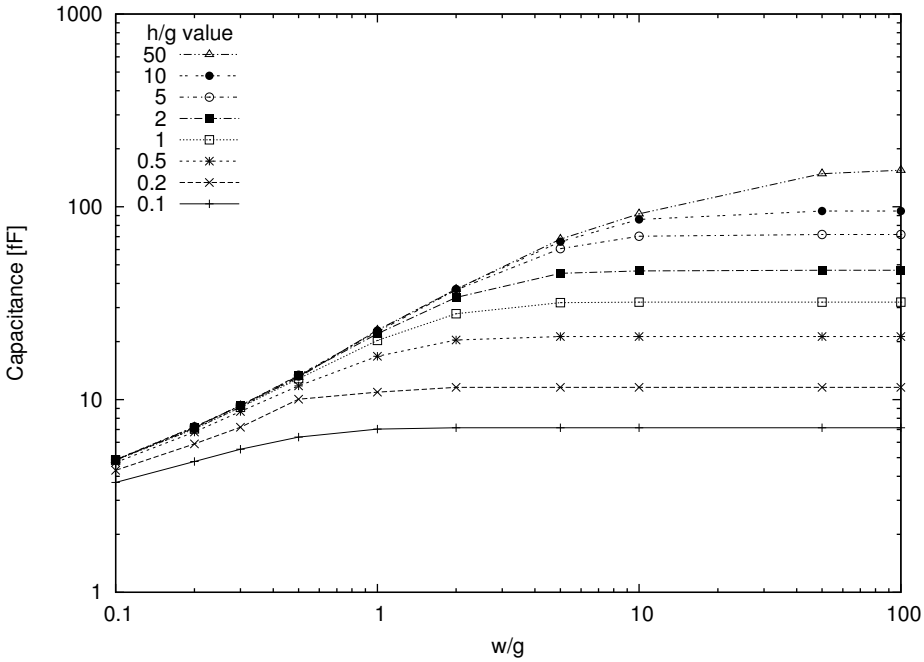

Figure 3.20: Capacitance against the frequency for a w/g variation using different h/g values, with a 1 μm insulator thickness

For high w/g values, the capacitance is limited by the channel height, until $h/g = w/g$. However, it can be noted that for a w/g value of 10, the capacitance for a h/g ratio of 50 is 286 fF while those of a h/g ratio of 10 is 257 fF (Figure 3.21). Thus a h/g ratio of 10 (Gq=0.95) provides 90 % of the maximum possible capacitance. A h/g value equal to 10.5 (Gq=1) would provide a capacitance of 818 fF, 91 % of the maximum possible capacitance. This is not a great increment as the electrode width is relatively high.

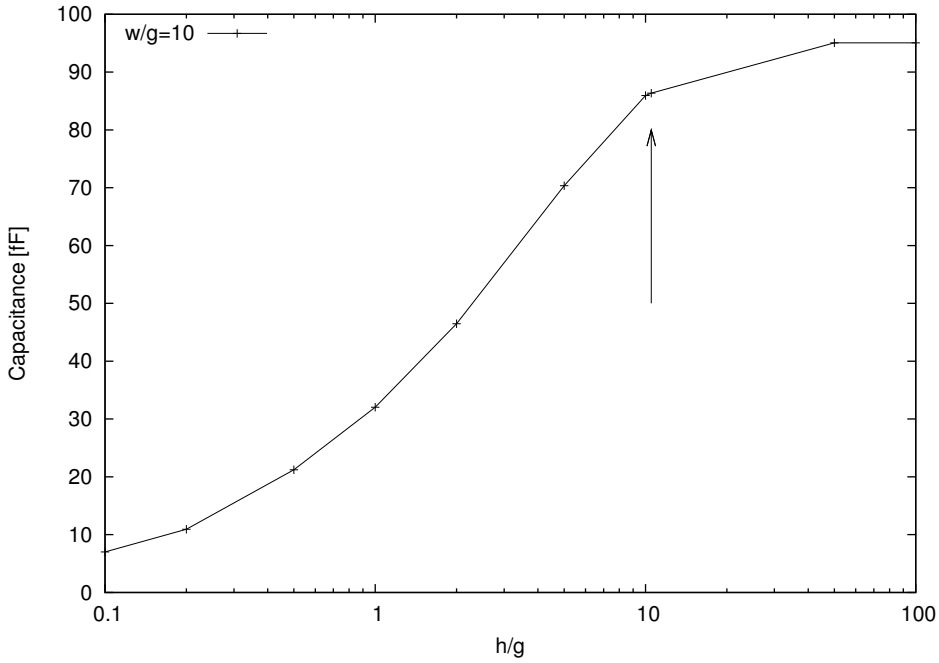

Figure 3.21: Capacitance against h/g for $w/g = 10$. The capacitance value with h/g respecting Gq=1 can be found on top of the arrow.

On the other side, for small w/g values, a h/g ratio equal to w/g is far to provide the maximum capacitance. For a w/g value of 0.2, a h/g value of 0.2 (Gq=0.29) provides a capacitance of 5.9 fF, 81 % of the maximum possible capacitance (Figure 3.22). A h/g value equal to 0.7 (Gq=1) provides a capacitance of 6.6 fF, 97 % of the maximum possible capacitance.

Thus, a good design rule to obtain a reasonable amount of capacitance would be to design a channel that would satisfy a Gq number equal to at least 1.

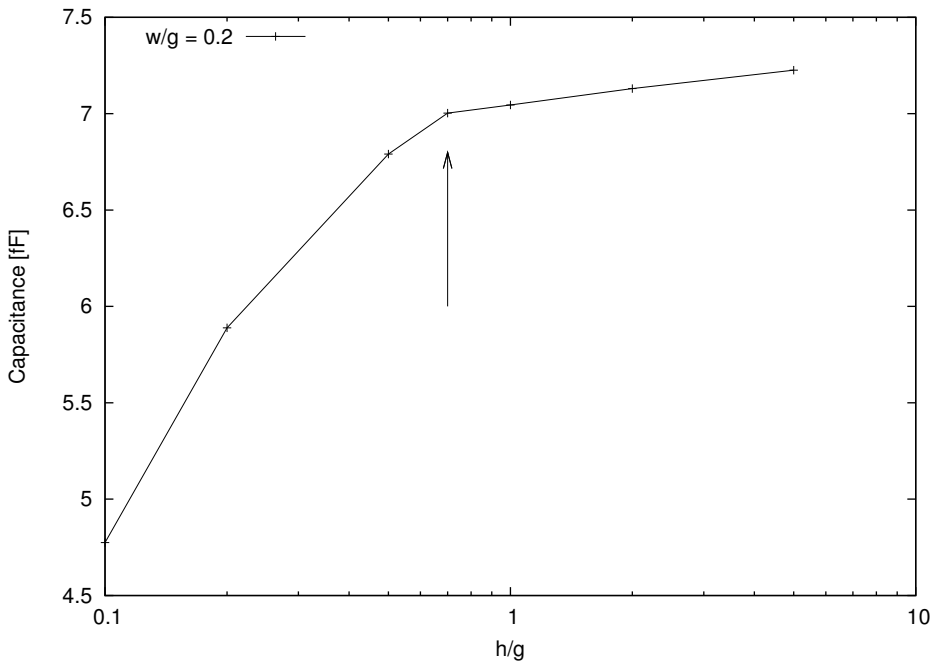

Figure 3.22: Capacitance against h/g for w/g = 0.2. The value of the capacitance with h/g respecting Gq=1 can be found on top of the arrow.

3.5 Conclusion

Numerical simulations were carried out for a face-to-face and a coplanar design using an insulating layer between the simulated electrode and the solution. A harmonic signal was applied for a frequency ranging from 100 Hz to 10 MHz. Two levels of capacitance were observed. At low frequencies, two capacitances were created by the PET insulating layers, in series with the resistance of the solution. At high frequencies, the displacement current took place in the solution and the resulting capacitance was due to the capacitance created by the solution in series with those created by the PET layers.

The variation of the solution conductivity led to a time constants variation for both designs. Decreasing the channel height lowered the value of the high frequency capacitance while keeping the low frequency capacitance unchanged. For the coplanar design, the decrease in height of the channel also led a decreased value of the cut-off

frequency between the low and high capacitance. It was shown that both designs were sensitive to the insulating layer thickness, which modified the low frequency capacitance value, and then also those of the high frequency.

Dimensionless parameters were set for the coplanar design relative to the value of the gap between the two electrodes. It was observed that the response of this design at high frequencies was dependent on the relationship between the channel height and the electrode width. The dimensionless number Gq was defined to check the quality of the geometry at high frequencies.

Bibliography

[1] S. Erpicum et al. "2D numerical flow modeling in a macro-rough channel". In: *International Journal for Numerical Methods in Fluids* 61.11 (2009), pp. 1227–1246.

[2] T. Knacke and F. Thiele. *Time-resolved 3D simulation of an aircraft wing with deployed high-lift system*. Vol. 110. 2010.

[3] R. Hart, R. Lec, and H.. Noh. "Enhancement of heterogeneous immunoassays using AC electroosmosis". In: *Sensors and Actuators, B: Chemical* 147.1 (2010), pp. 366–375.

[4] Y. Varol et al. "CFD modeling of heat transfer and fluid flow inside a pent-roof type combustion chamber using dynamic model". In: *International Communications in Heat and Mass Transfer* 37.9 (2010), pp. 1366–1375.

[5] F.D. Molina-Aiz et al. "Comparison of finite element and finite volume methods for simulation of natural ventilation in greenhouses". In: *Computers and Electronics in Agriculture* 72.2 (2010), pp. 69–86.

[6] F. Zhou, D. Su, and Y.-H. Peng. "Contrast simulation of aluminum extrusion process with FEM and FVM". In: *Shanghai Jiaotong Daxue Xuebao/Journal of Shanghai Jiaotong University* 37.7 (2003), pp. 1072–1076.

[7] J. Olofsson et al. "A microfluidics approach to the problem of creating separate solution environments accessible from macroscopic volumes". In: *Analytical Chemistry* 76.17 (2004), pp. 4968–4976.

[8] C.G. Xie et al. "Design of capacitance electrodes for concentration measurement of two-phase flow". In: *Measurement Science and Technology* 1.1 (1990), pp. 65–78.

[9] P. Osterberg et al. "Self-consistent simulation and modeling of electrostatically deformed diaphragms". In: *Proceedings of the IEEE Micro Electro Mechanical Systems* (1994), pp. 28–32.

[10] S. Catalan-Izquierdo et al. *Capacitance evaluation on parallel-plate capacitors by means of finite element analysis*. ICREPQ.

[11] J. Cheng, J. Zhe, and X. Wu. "Analytical and finite element model pull-in study of rigid and deformable electrostatic microactuators". In: *Journal of Micromechanics and Microengineering* 14.1 (2004), pp. 57–68.

[12] N.Y. Abed and O.A. Mohammed. "Physics-based high-frequency transformer modeling by finite elements". In: *IEEE Transactions on Magnetics* 46.8 (2010), pp. 3249–3252.

[13] William H. Press et al. *Numerical Recipes: The Art of Scientific Computing*. 3rd Revised edition. Cambridge University Press, Sept. 2007. ISBN: 0521880688.

[14] Richard Feynman et al. *Le Cours de physique de Feynman : Electromagnetisme, tome 1*. Ed. en format de poche. Dunod, Oct. 1999. ISBN: 2100048619.

[15] A. Bansal, B.C. Paul, and K. Roy. "An analytical fringe capacitance model for interconnects using conformal mapping". In: *IEEE Transactions on Computer-Aided Design of Integrated Circuits and Systems* 25.12 (2006), pp. 2765–2774.

[16] Kemal Nisancioglu and John Newman. "CURRENT DISTRIBUTION ON A ROTATING SPHERE BELOW THE LIMITING CURRENT." In: *Journal of the Electrochemical Society* 121.2 (1974), pp. 241–246.

[17] C. Belmont and H.H. Girault. "Coplanar interdigitated band electrodes for synthesis Part I: Ohmic loss evaluation". In: *Journal of Applied Electrochemistry* 24.6 (1994), pp. 475–480.

[18] Y.-C. Lin, M. Li, and C.-C. Wu. "Simulation and experimental demonstration of the electric field assisted electroporation microchip for in vitro gene delivery enhancement". In: *Lab on a Chip - Miniaturisation for Chemistry and Biology* 4.2 (2004), pp. 104–108.

Chapter 4

PET microchips

4.1 Introduction

These last years saw the emergence of the system-on-chip philosophy [1–6] and thus of the microfluidic era. Using a microchannel design has multiple advantages. It reduces the diffusion length, but also the reactants quantity. This globally leads to faster adsorption times and lower costs. Microfluidics has been used in many fields such as mass spectrometry[7–11], capillary electrephoresis[12–15], or biosensing[16–20]. However a microchannel also means a reduced electrode size. In the case of a capacitive biosensor that deals with a low surface capacitance, the signal-to-noise ratio becomes worrying. In our laboratory, Gamby et al tried before to monitor the adsorption of antibodies using contactless electrodes in a microchip[21, 22]. The microchip presented in this work is inspired from their electrode design, keeping the PET as basic material for both chip and insulating layer construction. An optimization work of both holder and microchip design was done to limit the noise sources as much as possible, and find the most efficient electrode design.

4.2 Material and methods

4.2.1 Material

Chips were made from a 100 μm thickness PolyEthylene Terephthalate (PET) sheet (Goodfellow, UK). Channels was drilled in the PET sheet by an excimer laser (Lambda Physik, Germany). Some channels were filled with a silver paste (Ercon R431, USA). The chip was cured at 80 degrees in an oven (Heraeus, Germany). A one-way syringe-pump (KD Scientific, USA) was used to inject the fluid contained in a 1 mL plastic syringe (BD-Plastipak, UK). An adapter (Upchurch, USA) was used between the syringe and a 100 μm inner diameter capillary of 30 cm length. The capillary was connected to a holder using a fluidic connector (Upchurch, USA) and a sleeve. Impedance measurements were realised using a 1296A Dielectric Interface (Solartron, UK) coupled to a Frequency Response Analyser 1255B (Solartron, UK).

4.2.2 Solutions

Various KCl concentration solutions were diluted from KCl 1 M, made from KCl powder (Sigma Aldrich, Switzerland) diluted in ultrapure water (MilliQ, USA).
Phosphate Buffered Saline (PBS) solution was prepared from 137 mM NaCl (Sigma Aldrich, Switzerland), 2.7 mM KCl (Sigma Aldrich, Switzerland), and 10 mM Na_2HPO_4 (Sigma Aldrich, Switzerland). The solution was then adjusted to pH 7.4 with NaOH (Sigma Aldrich, Switzerland). BSA solutions differently concentrated were diluted from a 40 mg.mL^{-1} BSA mother solution, made from 400 mg of BSA (Sigma-Aldrich, Switzerland) diluted in 10 mL of PBS.

4.2.3 Methods

A 0 V DC and 3 V AC peak to peak potential were applied. The frequency ranged from 1 Hz to 1 MHz with 5 points per decade. As the signal recorded by the spectrometer was unstable below 100 Hz due to the low capacitance values considered, the data were plotted from 100 Hz to 1 MHz.

4.3 Design

4.3.1 Chip

A channel was drilled in the PET sheet by an excimer laser (Lambda Physik, Germany) (Figure 4.1). Its length was 20 mm, its width 200 μm and its depth 50 μm. Two reservoirs were drilled at each side of the channel for the input and the output of the fluid. On the other side of the PET sheet were drilled two other channels of 10 mm length, 1 mm width, and 40 μm depth. A reservoir was drilled again at each side of the channel to obtain the desired depth on the whole channel.

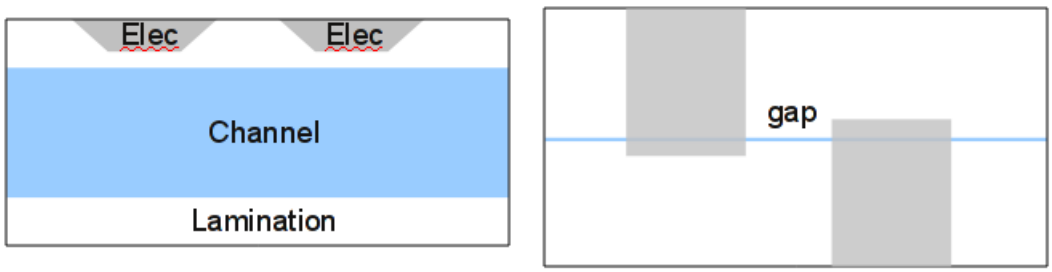

Figure 4.1: Scheme of the chip. Front view at the left and top view at the right.

These two last channels were filled with a silver paste (Ercon R431, USA). The chip was then cured in an oven at 80°C for 30 minutes. Then the chip was laminated on the fluidic channel side and cured again for 30 minutes in the oven.

Figure 4.2: Picture of a PET microchip

4.3.2 Holder

Each holder containing the chip was composed of PEEK material for the top part, and of Plexiglas material for the bottom part. The first and original holder (Figure 4.3a) recovered the top and the bottom part of the chip, from the input fluidic connector to the electrodes, just keeping the chip output fluidic connector free. An input fluidic connector was drilled in the top part of the holder in a way that an Upchurch connector could be plugged in. A 2 mm inner diameter toric gasket was placed between the connector and the reservoir to avoid fluid leackage. Two electrical connectors mounted on springs were installed in the holder to create an electrical connection between the chip electrodes and the Solartron instrument. The top and bottom parts were maintained with two screws at each side of the holder.

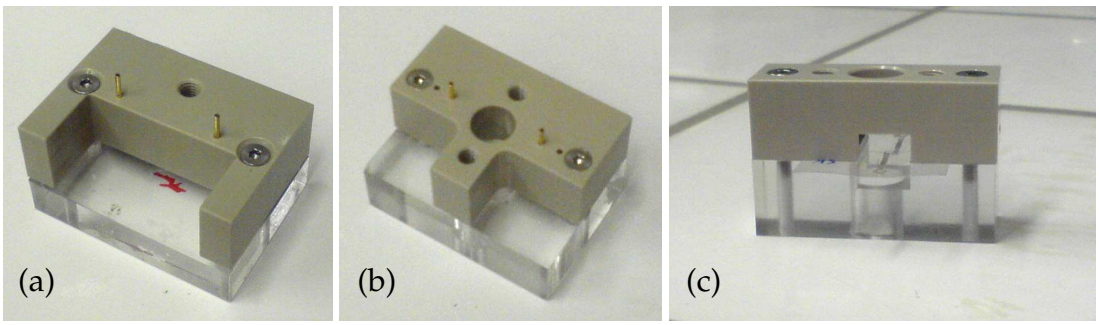

Figure 4.3: Pictures of the holders. Holder 1 can be observed on (a), holder 2 on (b) and holder 3 with a chip in (c)

A second holder (Figure 4.3b) was made with the same dimensions than the first one. The top part recovered the whole chip length. Two fluidic connections were realized in the holder top part, for each chip fluidic connector. A 6 mm diameter hole was drilled in both top and bottom holder parts at the chip electrodes positions. Like with the first holder, two electrical connectors mounted on springs were installed in the holder top part.

The goal of the third holder (Figure 4.3c) was only to connect the chip with the fluidic elements. For this purpose, the chip electrodes remained free while the input and output reservoirs were connected to the holder top part. Two 5 mm depth grooves were drilled respectively in the top and bottom parts of the holder. These grooves were drilled as the electrodes position.

4.4 Optimization of the holder design

The chip channel needs to be connected to a source. This can be done by sticking a fluidic connector to the channel input. However for a large amount of chips, a better solution might be to install the chip into a holder equipped with at least one fluidic connection. As the capacitance recorded from the chip is really low (hundreds of fF), the holder influence has to be as weak as possible.

The void capacitance (Figure 4.4) was recorded with the Solartron instrument not connected to anything. The connectors were spaced each other from 4 cm. In that case the capacitance was 144 fF at 100 KHz. The chip capacitance was measured by plugging the chip to the instrument. The chip was let as far as possible than any other material to get rid of the dielectric effects on the electric field around the chip. The measured capacitance was 250 fF at 100 KHz. The holders capacitance was measured by

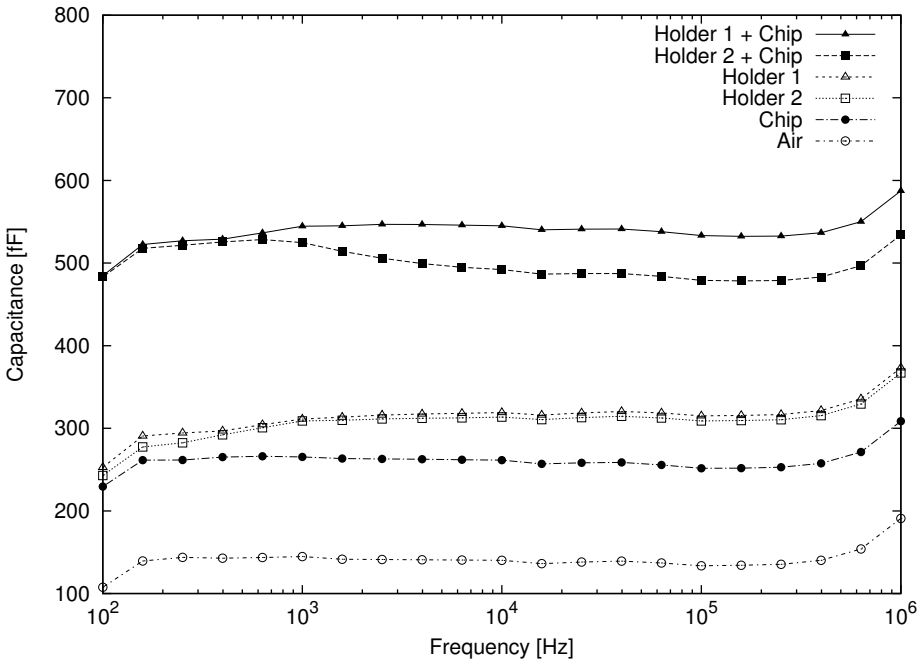

Figure 4.4: Capacitance of the air, of a chip and of the holders 1 and 2

connecting the Solartron to the holders electrical connectors without any chip mounted in. The capacitance value for the holders 1 and 2 was almost the same, about 320 fF.

However, when mounted in a holder, the chip capacitance values are not the same for the two holders (Figure 4.4). At 100 KHz, the capacitance value for the chip in the holder 1 is 340 fF, while it is 280 fF for the chip in the holder 2. In both cases it is higher than the expected capacitance for the chip added to the capacitance of one of the holders, measured on Figure 4.4, its value being 170 fF. The expected value is far lower than the measured value of the chip into the holder 2, which is even lower than for the chip into the holder 1. The main difference between the first and second holders is the hole in the top and bottom parts of the second holder. The relative permittivities of the PEEK and the Plexiglas are close to 3 F.m^{-1}, those of the air to 1 F.m^{-1}. In the holder 1 the holder top and the bottom parts are in contact with the chip. This creates two capacitances in parallel with those of the chip. The first one is created by the electrodes

directly in contact with the PEEK material, which is used as a dielectric material. The second one is also created by the electrodes, but using the chip PET and the Plexiglas material as a dielectric. The holes in the holder top and bottom parts replaces a part of the PEEK and Plexiglas materials by air. The relative permittivity in the hole is then around 1 F.m^{-1}, which reduces the capacitance using the second holder. Nevertheless, the capacitance is still higher than what can be expected for the chip in one of the two holders. As the rest of the electrodes is still covered by the PEEK and the Plexiglas material, the volume capacitances are still higher than the expected value.

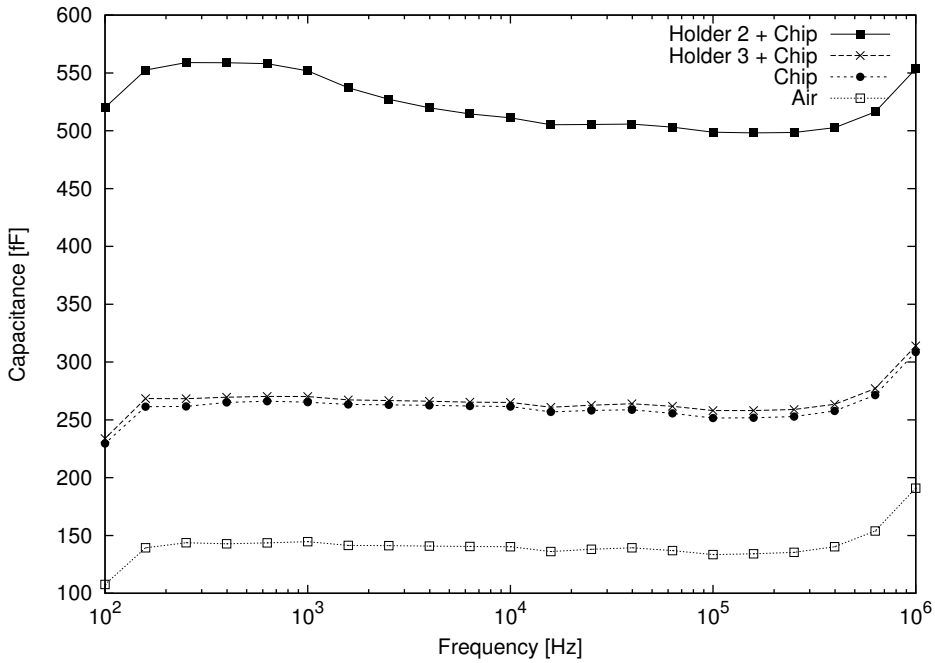

Figure 4.5: Capacitance of the air, of a chip and of a the chip in the second and third holders.

The holder effect is confirmed on Figure 4.5, where it can be seen that the capacitance of the chip mounted in the holder 3 is just 5 fF higher than those of the chip alone. Two phenomena can explain this result. The first one deals with the first and second holders connectors. As the third holder lacks these connectors, we can conclude that the capacitance difference between the first and the second holder without the chip is due to these connectors. The second phenomenon is due to the device design. No

part of the electrode is in contact with the holder top or bottom parts. The holder itself also offers a 5 mm gap above and below the chip. As a consequence most of the capacitance generated by the electrodes around the chip uses the air as a dielectric. The slight increase in capacitance between the chip alone and in the holder is due to a small part of the previous stray capacitance using the PEEK and the Plexiglas material. Nevertheless, the influence of the holder 3 on the stray capacitance can be considered negligible.

4.5 Chip design optimization

After studying the holder influence on the stray capacitance, the chip design was investigated to maximize the useful capacitive signal while keeping the noise and the stray capacitance at the lowest possible levels. The channel was filled with water and the acquisition was launched (Figure 4.6). If the capacitance spectra of the chip using a dry channel was relatively flat, the capacitance spectra with a channel filled with water can be divided in two sections. The first area (Low frequency plateau) ranging from 100 Hz to 3 KHz has a higher capacitance value than the second area (high frequency plateau) above 3 KHz.

4.5.1 Electrode's width and gap variation

A 100 μm , 200 μm , and 1 mm electrode width was used with, in each case, 200 μm , 500 μm and 1 mm between the electrodes. Each chip was mounted in the holder 3. Capacitance spectra were recorded without and later with water in the channel.

The capacitance of the two electrodes unconnected but separated from 3 cm (capacitance of the air) was 132 fF. Thus, the capacitance of a chip in the holder 3, recorded at 282 fF, was actually 150 fF. All the chip capacitance values were corrected to take into

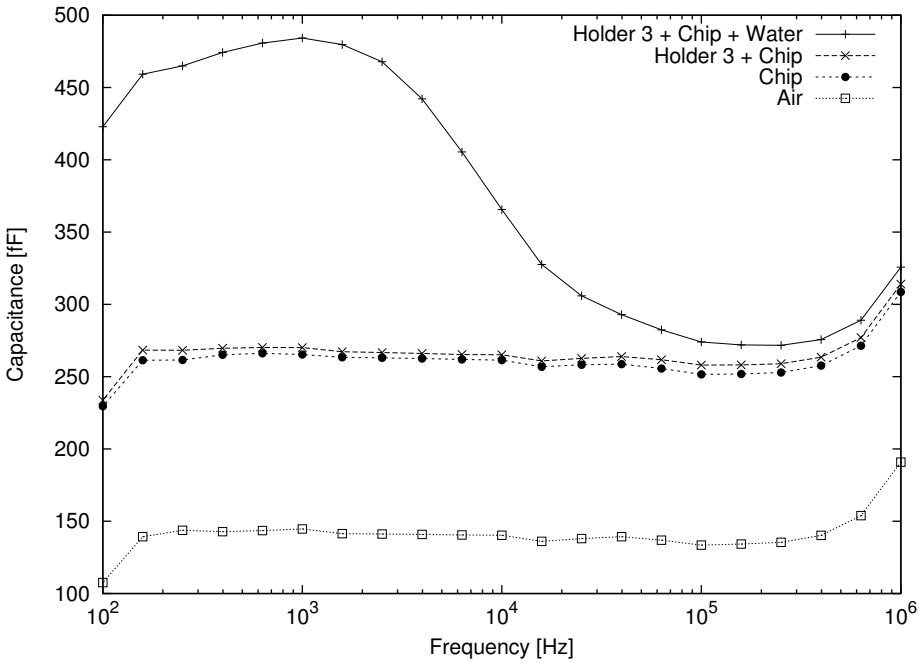

Figure 4.6: Capacitance of the air, of a chip in and out of the holder 3, and in with water

account the unconnected capacitance influence.

100 μm electrode width

The "Air" plots refer to a dry channel. In this case, the capacitance is created by the electrodes using PET or air as dielectric material. These values can be considered as a noisy baseline. The noise value increases when the gap decreases, as reducing the inter-electrodes distance increases the stray capacitance.

The low plate capacitance also increases when the gap decreases. This phenomenon is directly due to the noise levels : The noise level difference between a 200 μm and 500 μm gap is 24.5 fF, while it is 28 fF for the low plateau. The difference between a 500 μm and 1000 μm gap is also 18 fF for Air and 25 fF for the low plateau. The capacitance difference between the low plateau and the air can then be attributed to the capacitance created by the electrode and the water, using the PET as dielectric.

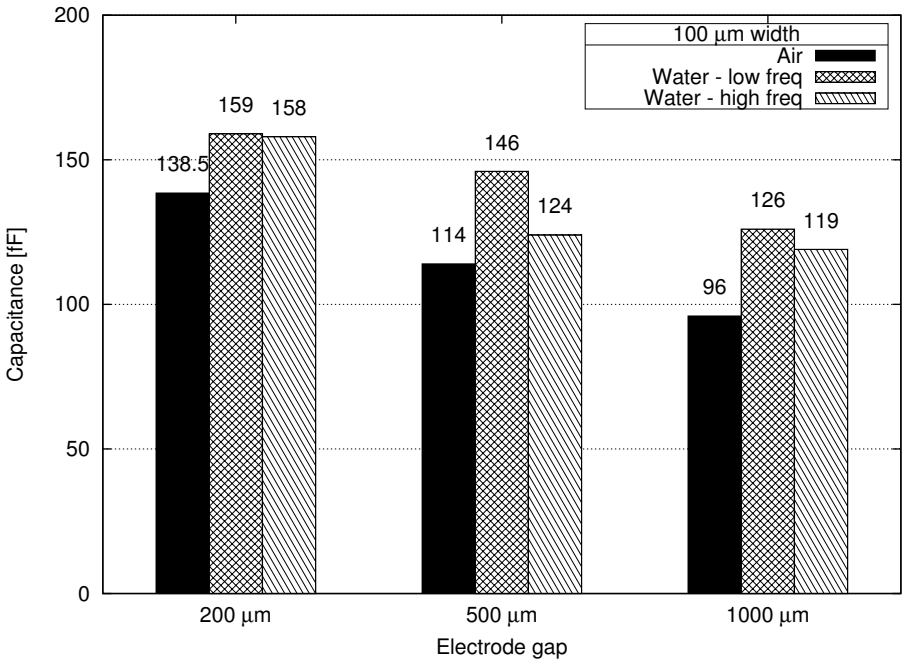

Figure 4.7: Capacitance of a chip with a 100 μm electrode width, with and without water in the channel for various electrode gap.

The value of this capacitance is around 30 fF, while the value predicted by numerical simulations (Appendix D), is about 31 fF.

The high plateau value also increases when the gap decreases. The value of this capacitance is around 20 fF for 200 μm and 1000 μm gap values, while it decreases to 10 fF for a 500 μm gap, almost reaching the medium plateau value. Numerical simulations predict a value of 7 nF for a 1000 μm gap and 16 nF for a 200 μm gap. This capacitance is then the result of the two surface capacitors being in series with the volume capacitance using the solution as dielectric.

200 μm electrode width

A 200 μm electrode width gave a global increase in capacitance, both in noise and signal with water in the channel. It can be observed (Figures 4.8 and 4.9) that the noise value increases when the gap decreases, as with a 100 μm electrode width chip. When

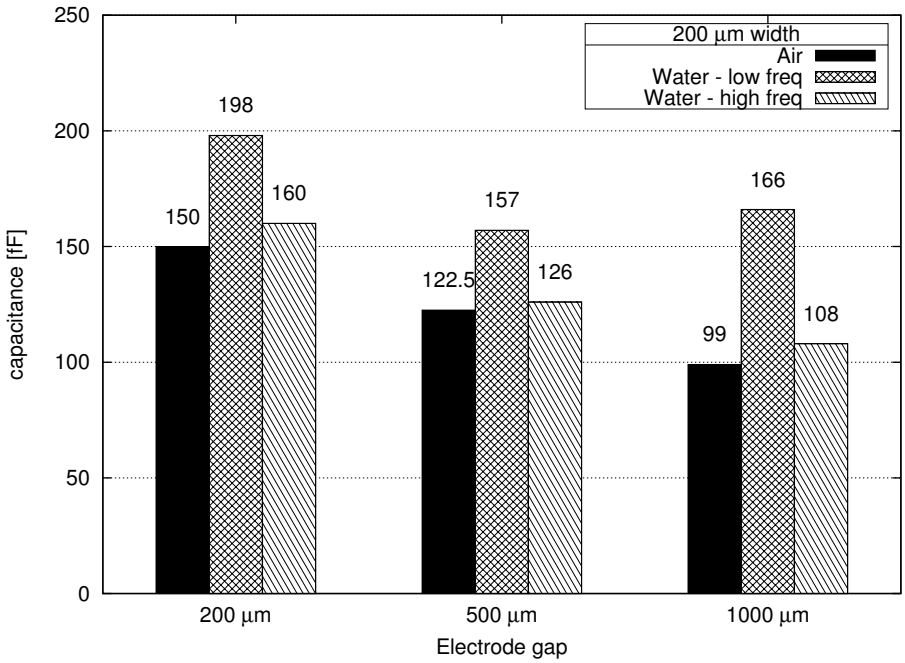

Figure 4.8: Capacitance of a chip with a 200 μm electrode width, with and without water in the channel.

the gap equals 1 mm, the noise capacitance increases by 3 fF (3 %) while it is increased by 11.5 fF (8.3 %) for a 200 μm gap. With a 1 mm gap, the capacitance created by the electrodes around the chip and using air as dielectric might be negligible (with such a little electrode width) compared to the capacitors created inside the chip and using the PET as dielectric. However, with a lower gap value, the value of the capacitance around the chip increases and takes benefit of the added electrode width, whereas the electrode area of the capacitors inside the chip does not change.

Comparing the capacitances of the noise and low plateau for the three values of the gap, it can be deducted that the surface capacitance would have a value between 48 fF and 67 fF. The value calculated by numerical simulations was of 59 fF. The capacitance of the high plateau should be around 10 fF. Values computed with numerical simulations were of respectively 20 fF and 7.6 fF for a 200 μm and 1 mm electrode width. These differences can be attributed to the measurement errors.

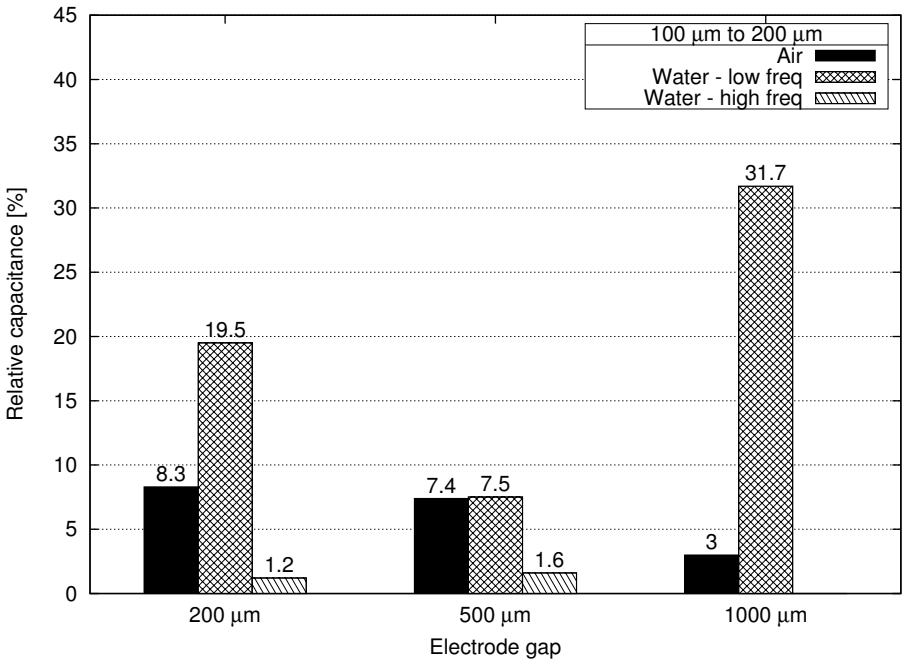

Figure 4.9: Relative capacitance of a chip with an electrode width from 100 μm to 200 μm , with and without water in the channel.

When comparing the low plateau values with the 100 μm electrode width chip (Figure 4.9), it can be observed that the capacitance improvements are higher with high gap values, with an exception at 500 μm which might result from measurement errors. As the noise does not increase much for a 1 mm gap, the capacitance improvement due to the electrode width is directly noticeable. This improvement is diluted in the noise when the electrodes get closer. In this case and when working with the surface capacitance, the best signal amplitude is achieved with a high gap value. It can be observed that the high plateau capacitance is not improved, and is even worse for a 1 mm gap. Some measurement errors have to be taken into account. Nevertheless, considering the geometry, the height/gap ratio is lower than 1 for all the electrodes width and gap values. Thus only the inner edge effects and a little part of the electrode area can be used by the volume capacitance. In this case, the capacitance of the high plateau does not increase much.

1000 μm electrode width

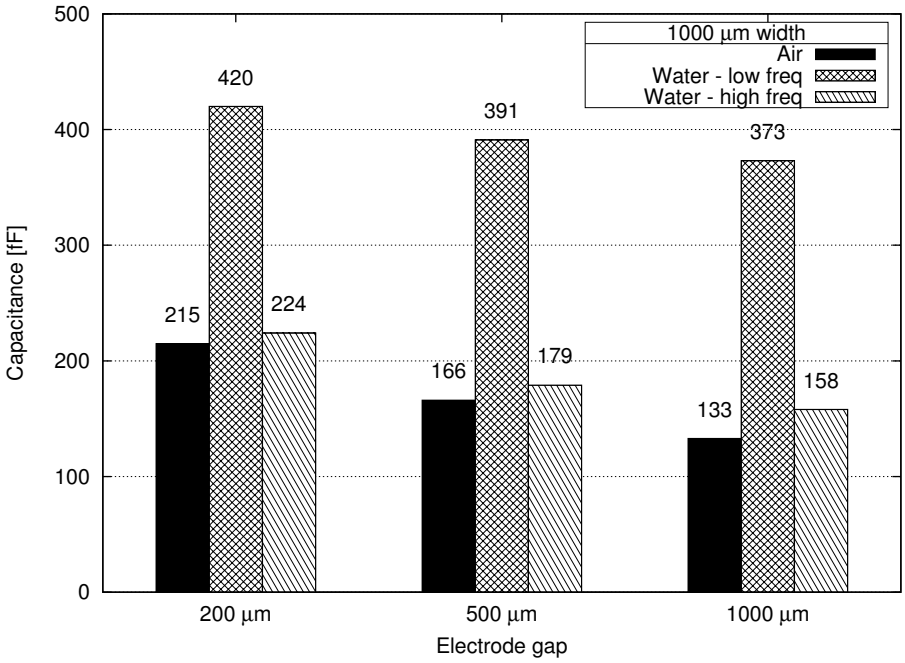

Figure 4.10: Capacitance of a chip with a 1000 μm electrode width, with and without water in the channel.

A 1 mm width electrode has 5 times the surface of a 200 μm one. Nevertheless, the noise increment is well contained with just 33 fF and 65 fF more for gap values of respectively 200 μm and 1 mm (Figure 4.10), so an increment of respectively 33 % and 43 % (Figure 4.11). As the electrodes thickness is unchanged from the previous electrodes width, the major part of the added noise comes from the added surface, which increases the capacitance using PET as dielectric and the capacitance around the chip.

According to the difference between the low plateau and the noise capacitance levels, the surface capacitance value should be around 230 fF. A value of 260 fF was found with some numerical simulations. Interestingly, the high plateau value relative to the low plateau is severely reduced compared to the previous electrodes width, with a

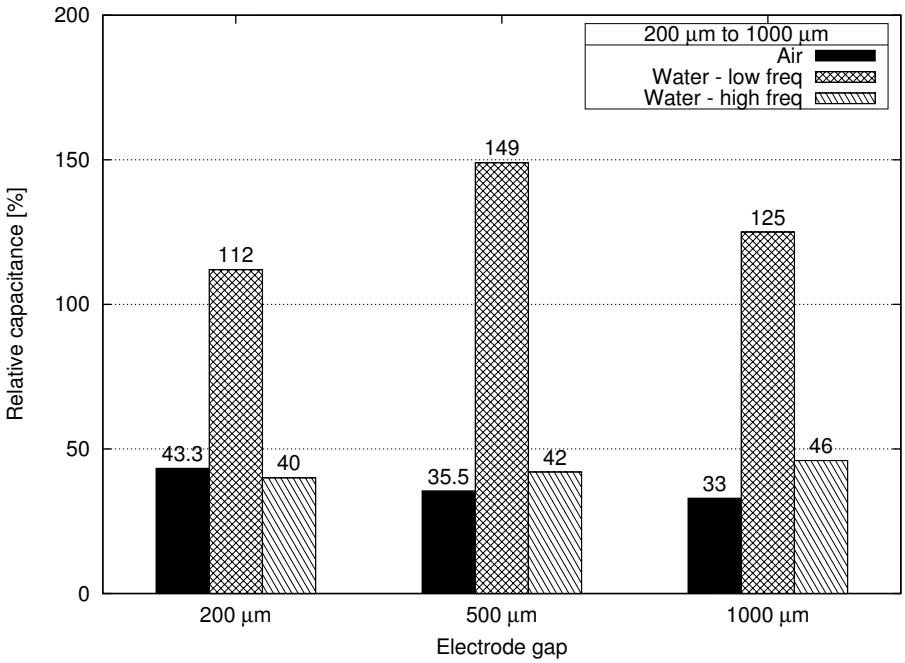

Figure 4.11: Relative capacitance of a chip with an electrode width from 200 μm to 1000 μm , with and without water in the channel.

high plate value from 9 to 25 fF. Values computed by numerical simulations were respectively 7.8 fF and 21 fF for 200 μm and 1 mm gap values. These values are close to the experimental and theoretical values found for a 200 μm electrode width, as the height/gap ratio does not evolve.

The comparison of the low and high plateaus values with the 200 μm electrode width values is a little more flat. Both ratios decrease when the gap value decreases, as the capacitance improvement is diluted in the noise. An exception occurs with the low plateau capacitance for a 500 μm gap, which is higher due to the low capacitance level recorded with the 200 μm electrode width. It can be noted that the high plateau values are improved by at least 40 % relatively to a 200 μm electrode width, while it did not improve from 100 μm to 200 μm . This improvement is directly the result of the noise increment, as no improvement in capacitance can be observed. A 500 μm gap value seems to be a good compromise between surface and volumic effects.

4.5.2 Insulator thickness

The insulator thickness between the electrode and the channel influences directly the surface capacitance value. The chip was traditionally built using a 15 μm electrode thickness and a 10 μm insulator layer. It was possible to drill the electrode deeper to reach a 18 μm thickness, reducing the insulating layer thickness to 7 μm .

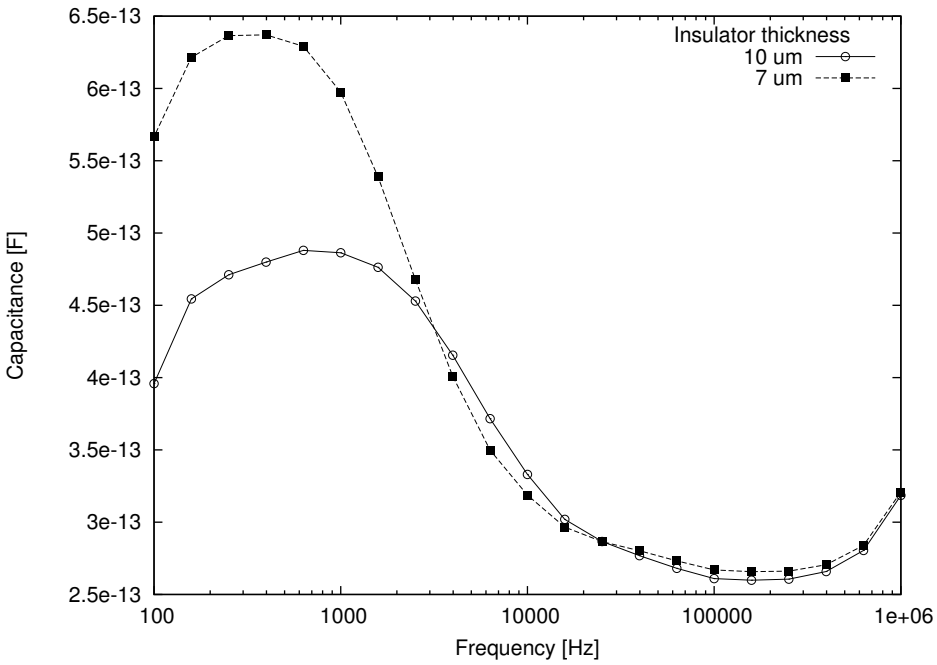

Figure 4.12: Influence of the insulating layer thickness on the chip capacitance.

From 355 fF with a 10 μm insulator thickness, the low plateau value was improved to a 505 fF capacitance level (Figure 4.12). An improvement of 42 %, in perfect agreement with the theoretical values.

The high plateau value capacitance increases of 6 fF. This increment is directly due to the surface capacitance increment, as the surface and volume capacitors are in series.

4.5.3 Cross section length variation

The section length has a responsibility for the chip noise level. The cross section length is usually 900 μm , including the 200 μm channel width. Two chips with a 5

mm cross section were built, one with a 1 mm electrode width, the other with a 200 μm electrode width. Both chips had a 200 μm electrode gap. Capacitance spectra were recorded using a dry channel, from 1 Hz to 1 MHz.

Electrode width	Air	lamination	ratio
200 μm	150	256	70.7 %
1 mm	215	307	42.8 %

Table 4.1: Noise capacitance due to the cross section length

The increment in capacitance is around 100 fF, whatever the electrode's width (Table 4.1). The inter-electrode capacitance using PET as dielectric, independent from the electrode width, seems to dominate. The capacitance around the chip might also increase, but has less influence as the relative permittivity of the air is 3 times lower than those of the PET. The value of this capacitance with a 1mm electrode width might also not be much higher than with a 200 μm electrode. As the noise level is lower with a 200 μm electrode width than with a 1 mm one, the added noise impact is more important (70.7 % instead of 42.8 % for the 1 mm width). The cross section length should then be reduced as much as possible.

4.5.4 Lamination layer on top of the electrodes

Two chips, one with a 200 μm electrode width and the other with 1 mm, were laminated on the electrode side. The electrode gap of both chip was 200 μm . Capacitance spectra were recorded with a dry channel, from 1 Hz to 1 MHz.

The capacitance increment is respectively 32 fF and 26 fF for a 200 μm and 1 mm electrode width. The added capacitance comes from the capacitance around the chip, as a portion of dielectric adds a little capacitance. It also comes from the edge effect of the inter-electrode capacitance using the PET as dielectric. As the electrodes thickness is only 15 μm , the edge effects influence on the global capacitance is important.

Electrode width	900 μm CS	5 mm CS	ratio
200 μm	150	182	21.3 %
1 mm	215	241	12.1 %

Table 4.2: Noise capacitance due to the lamination layer

Adding a PET layer instead of air contributes to this edge effect. The effect of the added capacitance on small electrodes (21 %) is not negligible. The surface of the electrodes should then not be laminated.

4.5.5 Solution conductivity variation

The effects of various solutions conductivity injected into the channel were evaluated using deionized water and several KCl concentrations. Data were acquired across frequencies ranging from 1 kHz to 1 MHz. It can be observed on Figure 4.13 that the Real part of the impedance presents a plateau for lower frequencies and then a slope when acquiring to higher frequencies. Increasing the solution conductivity decreases the Real part of the impedance value on the plateau (Figure 4.13).

It also increases the cut-off frequency as the plateaus are shifted to higher frequencies with the solution concentration. Real part of the impedance values are summarized in Table 4.3, while the reverse values are presented on Figure 4.14. The standard deviation was evaluated at 4.1%, too small to be presented on Figure 4.14.

Data were fitted by the linear relation $ax + b$ with a=7x10^4 and b=1.13x10^{-7}. b corresponds to the inverse of the measured resistance of the water. a is equal to the solution conductivity multiplied by the cell constant. From Kohlrausch's law (5.4.4), a KCl 5 mM solution conductivity is equal to 72.5 mS. The cell constant value was then found to be equal to 48.8 m^{-1}.

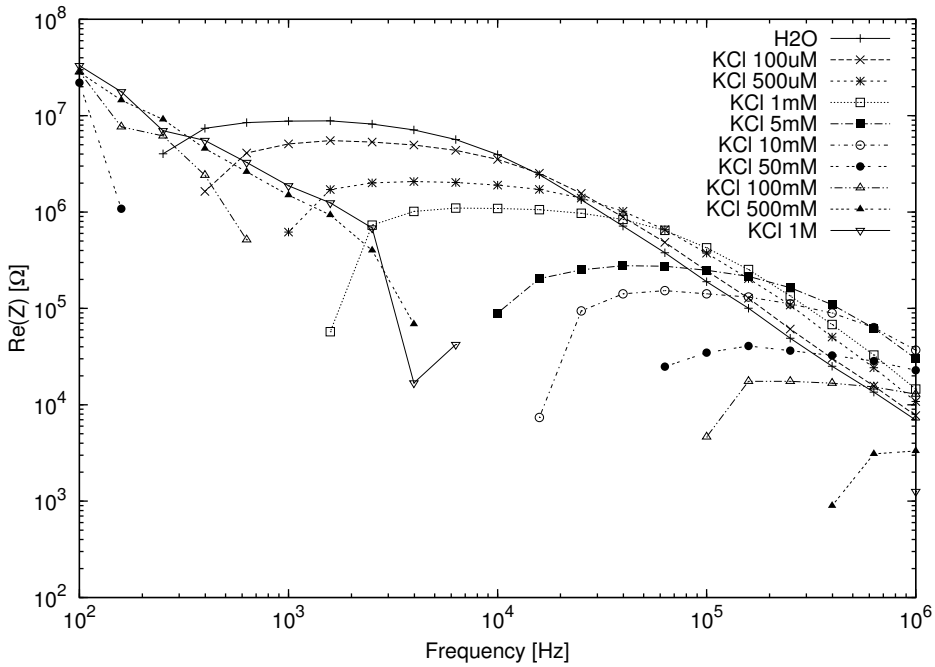

Figure 4.13: Bode plots of the Real part of the impedance for Water and various KCl concentrations in the chip channel.

Solution	Resistance [Ω]	Frequency
Water	8.87x10^6	1300 Hz
KCl 100 μM	5.44x10^6	1800 Hz
KCl 500 μM	2.05x10^6	4 kHz
KCl 1 mM	1.09x10^6	7 kHz
KCl 5 mM	282885	42 kHz
KCl 10 mM	154792	63 kHz
KCl 50 mM	37908	160 kHz
KCl 100 mM	16966	200 kHz
KCl 500 mM	3208	1 MHz
KCl 1 M	1280	1 MHz

Table 4.3: Resistance of the channel measured by the sensor for various solutions.

4.6 BSA detection

4.6.1 Single BSA concentration detection

Capacitive detection

The chip was mounted in the holder 3. The flow was established by using a 5 mL volume syringe (ONCE, Spain) mounted in aspiration to avoid the dead volume ef-

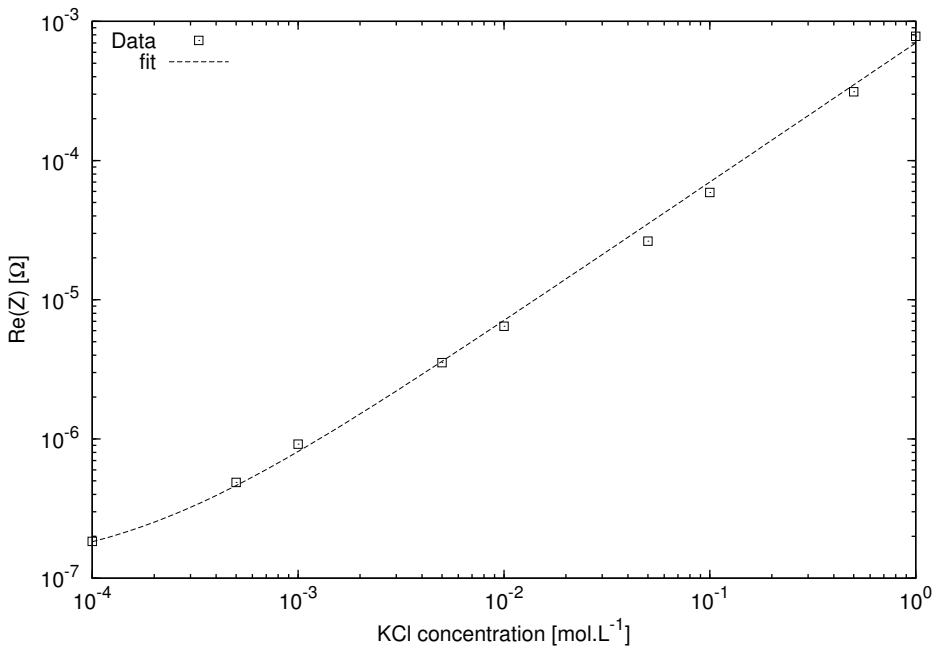

Figure 4.14: Inverse of the Real part of the impedance with respect to the frequency

fects. A drawback of this technique is that the flow rate was unknown. The baseline was set using a solution of Acetic Acid 1 %. First attempts to detect the BSA were carried out in the low frequency range, that is to say the surface capacitance. No deviation was observed in this frequency range. This is likely due to the low capacitance created by the PET insulating layer.

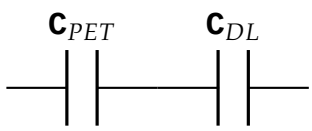

Figure 4.15: Equivalent circuit of the capacitance created by the PET insulating layer in serial with the electrical double layer capacitance.

The electrical double-layer capacitance is reported to be between 10 and 50 μF.cm^{-2} with an electrolyte[23]. The capacitance created by the PET layer, with a value of 27 nF.cm^{-2}, is about 1000 times lower. The electrical double-layer capacitance variation (C_{DL} in Figure 4.15) with such a low insulating capacitance could theoretically be mon-

itored. However this variation would be very tiny, and despite all the optimization work done on both holders and microchip design, the electrical double-layer capacitance variations were masked by the baseline noise.

Conductivity detection

The other possibility to detect BSA using the microchip would be to monitor the solution conductivity variations. The tests were then carried out in the high plateau frequency range (the channel), with a frequency fixed to 200 KHz. Acetic Acid 1 % containing some BSA is more resistive than just Acetic Acid 1%. This tendancy is confirmed by conductimetric mesurements carried out with a Metrohm 711 conductimeter. Acetic acid 1% conductivity was 664 μS.cm^{-1}, while the conductivity of the same solution including 100 μM BSA was 557 μS.cm^{-1}. An hypothesis would be that, despite being positively charged at the considered pH, the BSA conductivity would be lower than the acetic acid conductivity. Adding BSA in acetic acid would then give a less conductive solution than acetic acid alone. The sensogram was then recorded in resistance to clearly observe the resistance differences.

The sensor was able to detect a BSA solution concentrated at 25 μM in Acetic Acid 1 % (Figure 4.16). The first peak around 50 s after the acquisition launch is due to the capillary switching from Acetic Acid to BSA + Acetic Acid. 12 s after the switch, the channel resistance increased by 4.2 %. The second peak around 105 s is due to the switching from BSA + Acetic Acid to Acetic Acid only. The baseline was recovered 15 s after the switch. This behaviour is comparable to other conductivity sensors [24, 25].

4.6.2 Multiple BSA concentrations

Various BSA concentrations in Acetic Acid 1 % were injected in the channel, from 3 μM to 50 μM. For each injection, the channel resistance was recorded at a 200 kHz frequency.

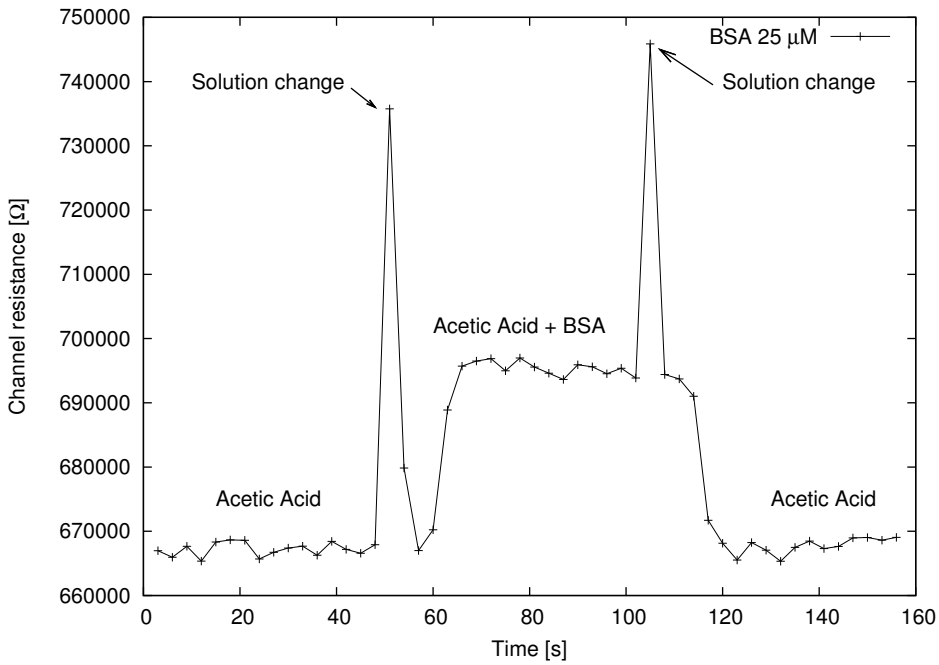

Figure 4.16: Detection of a solution of BSA concentrated at 25 μM in a solution of Acetic Acid 1 %

BSA concentration	Resistance kΩ
50 μM	701
25 μM	696
12 μM	686
6 μM	676
3 μM	672
Baseline	668

Table 4.4: Values of the channel resistance for various BSA concentrations in Acetic Acid 1% injected in the channel

Table 4.4 present the results of the channel resistance for various BSA concentrations in Acetic Acid 1 %. These values can be expressed relative to the baseline (bulk Acetic Acid 1 %) (Figure 4.17). It can be observed that the resistance increases until a concentration of 12 μM where the slope begin to decrease, and decreases again after 25 μF, trending to saturate with a solution more concentrated in BSA.

The lowest detectable concentration was 3 μM. Below this concentration, the signal was not distinguishable from the noise. Conductivity detection has also been carried

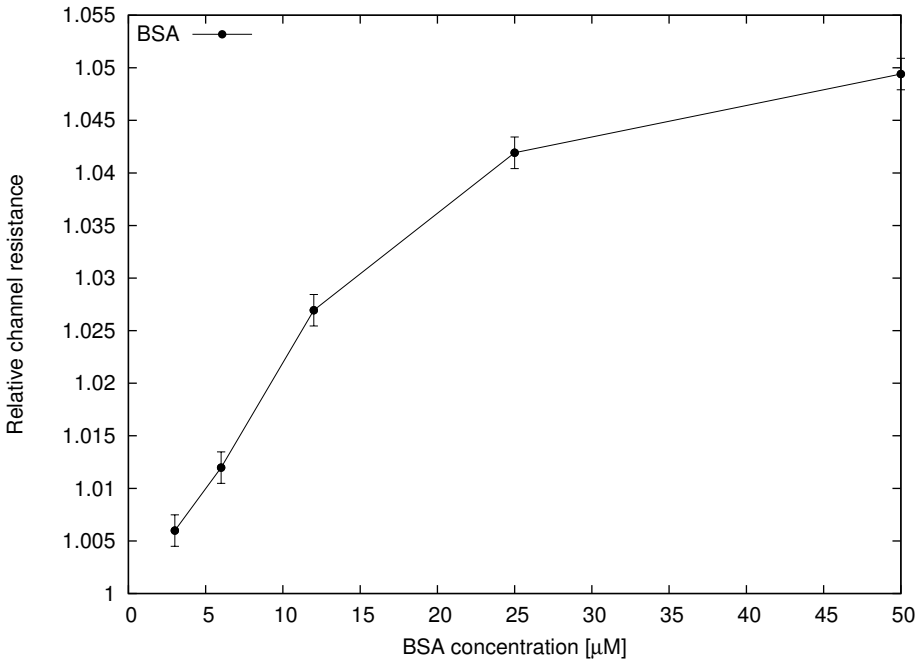

Figure 4.17: Detection of 25 μM BSA in Acetic Acid 1%.

out with success in microchips capillary electrophoresis[26]. To improve the detection limit, a ground electrode might be integrated to the system [27, 28]. However, the purpose of the sensor was to detect an adsorption and not a channel conductivity variation. The adsorption of the BSA went undetected due to the relatively high insulator thickness: A dielectric thickness of 7 μm , with a 3 F.m^{-1} relative permittivity cannot create a high surface capacitance. This low capacitance therefore masked the double-layer capacitance variations when adsorbing species.

4.7 Conclusion

Optimizing the signal quality is critical when dealing with weak capacitances. To achieve such a task, the holder and microchip designs were studied in detail. Removing the connectors from the holder and moving away the plastic elements as far as possible from the microchip made the influence of the holder on the signal quality almost negligible.

The influence of the electrodes width and the distance between them was studied to maximize the useful capacitance over noise ratio. The electrode width had a strong influence at low frequencies but not at high frequencies, where the signal was mostly due to the inner edge effects. In this way, it was found that a 1 mm electrode width separated by a distance of 500 μm was a good compromise. The influence of various parameters like the insulating layer thickness, the lamination layer on top of the electrodes and the cross section length were also examinated.

Finally, the sensor ability to detect BSA was studied. It was found that the sensor was not able to detect any BSA adsorption in the low frequency range. However, it was able to detect conductivity variations of various BSA concentrations in the high frequency range.

Bibliography

[1] J. Tanyanyiwa et al. "Microfluidic lab-on-a-chip systems based on polymers - fabrication and application". In: *Chemical Engineering Journal* 101.1-3 (2004), pp. 447–453.

[2] C.D. Chin, V. Linder, and S.K. Sia. "Lab-on-a-chip devices for global health: Past studies and future opportunities". In: *Lab on a Chip - Miniaturisation for Chemistry and Biology* 7.1 (2007), pp. 41–57.

[3] C.-C. Lin et al. "Microfluidic Immunoassays". In: *JALA - Journal of the Association for Laboratory Automation* 15.3 (2010), pp. 253–274.

[4] L. Yobas et al. "A self-contained fully-enclosed microfluidic cartridge for lab on a chip". In: *Biomedical Microdevices* 11.6 (2009), pp. 1279–1288.

[5] L. Nyholm. "Electrochemical techniques for lab-on-a-chip applications". In: *Analyst* 130.5 (2005), pp. 599–605.

[6] B.C. Heinze et al. "Microfluidic immunosensor for rapid and sensitive detection of bovine viral diarrhea virus". In: *Sensors and Actuators, B: Chemical* 138.2 (2009), pp. 491–496.

[7] Y. Jiang et al. "Integrated plastic microfluidic devices with ESI-MS for drug screening and residue analysis". In: *Analytical Chemistry* 73.9 (2001), pp. 2048–2053.

[8] T.C. Rohner, J.S. Rossier, and H.H. Girault. "Polymer microspray with an integrated thick-film microelectrode". In: *Analytical Chemistry* 73.22 (2001), pp. 5353–5357.

[9] W.-C. Sung et al. "Poly(dimethylsiloxane)- based microfluidic device with electrospray ionization-mass spectrometry interface for protein identification". In: *Electrophoresis* 24.21 (2003), pp. 3648–3654.

[10] N. Lion et al. "Microfluidic systems in proteomics". In: *Electrophoresis* 24.21 (2003), pp. 3533–3562.

[11] M. Abonnenc et al. "Electrospray micromixer chip for on-line derivatization and kinetic studies". In: *Analytical Chemistry* 80.9 (2008), pp. 3372–3378.

[12] Y. Liu et al. "Microfabricated polycarbonate CE devices for DNA analysis". In: *Analytical Chemistry* 73.17 (2001), pp. 4196–4201.

[13] J. Lichtenberg, N.F. de Rooij, and E. Verpoorte. "A microchip electrophoresis system with integrated in-plane electrodes for contactless conductivity detection". In: *Electrophoresis* 23.21 (2002), pp. 3769–3780.

[14] R. Bharadwaj, J.G. Santiago, and B. Mohammadi. "Design and optimization of on-chip capillary electrophoresis". In: *Electrophoresis* 23.16 (2002), pp. 2729–2744.

[15] R.S. Foote et al. "Preconcentration of proteins on microfluidic devices using porous silica membranes". In: *Analytical Chemistry* 77.1 (2005), pp. 57–63.

[16] J.S. Rossier et al. "Microfluidic based immunoassay". In: *Nanobiotechnology* 1.3 (2005), pp. 311–312.

[17] R. Kurita et al. "On-chip enzyme immunoassay of a cardiac marker using a microfluidic device combined with a portable surface plasmon resonance system". In: *Analytical Chemistry* 78.15 (2006), pp. 5525–5531.

[18] J.P. Golden et al. "Target delivery in a microfluidic immunosensor". In: *Biosensors and Bioelectronics* 22.11 (2007), pp. 2763–2767.

[19] H. Wang et al. "Microfluidic immunosensor based on stable antibody-patterned surface in PMMA microchip". In: *Electrochemistry Communications* 10.3 (2008), pp. 447–450.

[20] Y. Liu et al. "Microchip-based ELISA strategy for the detection of low-level disease biomarker in serum". In: *Analytica Chimica Acta* 650.1 (2009), pp. 77–82.

[21] J. Gamby, J.-P. Abid, and H.H. Girault. "Supercapacitive admittance tomoscopy". In: *Journal of the American Chemical Society* 127.38 (2005), pp. 13300–13304.

[22] J. Gamby et al. "Nanowires network for biomolecular detection using contactless impedance tomoscopy technique". In: *Analytical Chemistry* 78.15 (2006), pp. 5289–5295.

[23] Mark E. Orazem and Bernard Tribollet. *Electrochemical Impedance Spectroscopy*. Wiley-Interscience, Sept. 2008. ISBN: 0470041404.

[24] A.J. Zemann et al. "Contactless Conductivity Detection for Capillary Electrophoresis". In: *Analytical Chemistry* 70.3 (1998), pp. 563–567.

[25] W.K.T. Coltro, J.A.F. da Silva, and E. Carrilho. "Fabrication and integration of planar electrodes for contactless conductivity detection on polyester-toner electrophoresis microchips". In: *Electrophoresis* 29.11 (2008), pp. 2260–2265.

[26] K.A. Mahabadi et al. "Capacitively coupled contactless conductivity detection with dual top-bottom cell configuration for microchip electrophoresis". In: *Electrophoresis* 31.6 (2010), pp. 1063–1070.

[27] J.G. Alves Brito-Neto et al. "Understanding capacitively coupled contactless conductivity detection in capillary and microchip electrophoresis. Part 2. Peak

shape, stray capacitance, noise, and actual electronics". In: *Electroanalysis* 17.13 (2005), pp. 1207–1214.

[28] P. Kuban and P.C. Hauser. "Contactless conductivity detection in capillary electrophoresis: A review". In: *Electroanalysis* 16.24 (2004), pp. 2009–2021.

Chapter 5

Aluminium chips : Design

5.1 Introduction

Most immunoassays are nowadays performed on gold surfaces, may it be SPR [1–4], electrochemical based ELISA tests [5], or impedance based immunoassays [6–9]. In impedance detection, gold has been extensively used in contact mode, thanks to its good biocompatibility properties. However, the contact mode is affected by electrode oxydation and faradic currents that can alter the integrity of the biological elements present in the solution. Contactless electrodes provide a good solution to these problems. When using gold, these electrodes can be realized by adsorbing one or several layers of species (thiols,...) to create an insulating layer. This offers a good sensitivity but is delicate to use in a mass market configuration. Another possible configuration would be to use a metal covered with a metallic oxyde, such as aluminium covered by an alumina layer. Aluminium is a strong reductor, and then reacts very easily with oxygen. A thin layer of alumina (about 3 nm thickness) is naturally formed around the metal when exposed to air. The geometry of an electrode, but also the design of a reservoir (or of a channel) influences directly the frequency response of the sensor. This dependance of the response on the geometry is even more true for a contactless

design, which adds an insulating parameter to the geometry.

5.2 Materials

5.2.1 Measurement

Impedance data were recorded with a Solartron 1296 Dielectric interface (Ametek, UK) coupled to a Solartron 1255B Frequency Response Analyser (FRA).

5.2.2 Holders

The holders were made of two parts, both composed of PEEK material. The top part was 40 mm long, 20 mm wide and 10 mm high. These dimensions were the same for the bottom part. One hole was drilled at each corner of the holder to maintain the top and the bottom part firmly screwed. A reservoir was drilled in the center of the holder top part. For the first holder, the diameter of this reservoir was 12 mm. For the second holder, the reservoir diameter was 6 mm. A toric gasket of 14 mm inner diameter was integrated to the top part of the first holder (8 mm diameter for the second holder).
A small rectangular plastic petribox 50 mm long, 35 mm wide and 10 mm high was also used.

5.2.3 Solutions

KCl solutions of various concentrations were diluted from a 1M KCl solution (Sigma Aldrich, Switzerland).
Phosphate Buffered Saline (PBS) solution was prepared from 137 mM of NaCl (Sigma Aldrich, Switzerland), 2.7 mM of KCl (Sigma Aldrich, Switzerland), and 10 mM of

Na_2HPO_4 (Sigma Aldrich, Switzerland). The solution was then adjusted to pH 7.4 with a solution of NaOH (Sigma Aldrich, Switzerland).

5.3 Coplanar and face-to-face design in a rectangular plastic box

5.3.1 Methods

Two experiments were carried out using a plastic box. The first one dealt with the study of the face-to-face design. Two aluminium electrodes 32 mm wide and 10 mm high were cut from an aluminium foil 30 μm thick (Universal, TWR). The electrodes were stuck on the smaller edge of the box with a double face adhesive tape (Scotch, 3M) (Figure 5.1a). The distance between the electrodes was 50 mm. To study the edge effects, the electrodes were cut to 16 mm wide and cut in the middle of the longer side of the box (Figure 5.1b). The distance between the two electrodes was then 35 mm.

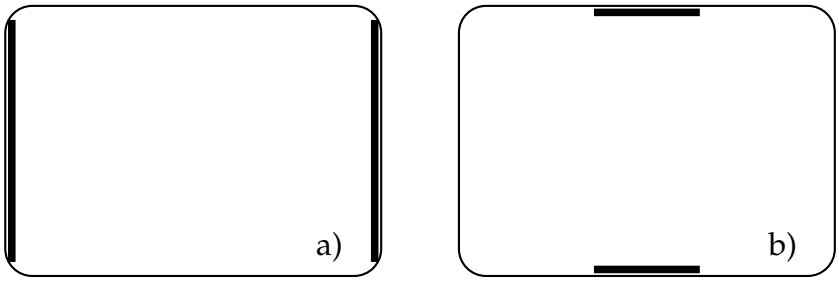

Figure 5.1: Scheme of the aluminium electrodes stuck in the rectangular plastic box using a face to face design.

The second deals with the differences between the face-to-face design and the coplanar design using the same electrodes than the Figure 5.1. These electrodes were stuck to the same side of the box with a gap between each other being respectively 1 mm, 4 mm and 8 mm(Figure 5.2).

For both experiments, the box was entirely filled with a 10 mM PBS solution. A 10

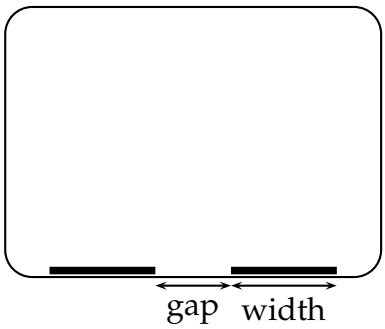

Figure 5.2: Scheme of the aluminium electrodes stuck to the rectangular plastic box.

mV peak-to-peak AC potential difference was applied between the electrodes. Spectra were recorded for frequences ranging from 1 Hz to 1 MHz with 5 points per decade.

5.3.2 Results : Face-to-face design

32 mm wide electrode (No edge effects)

The first experiment dealt with the two aluminium electrodes covering completely two sides of the plastic box as shown in Figure 5.1a, the latter being fully filled with a PBS solution.

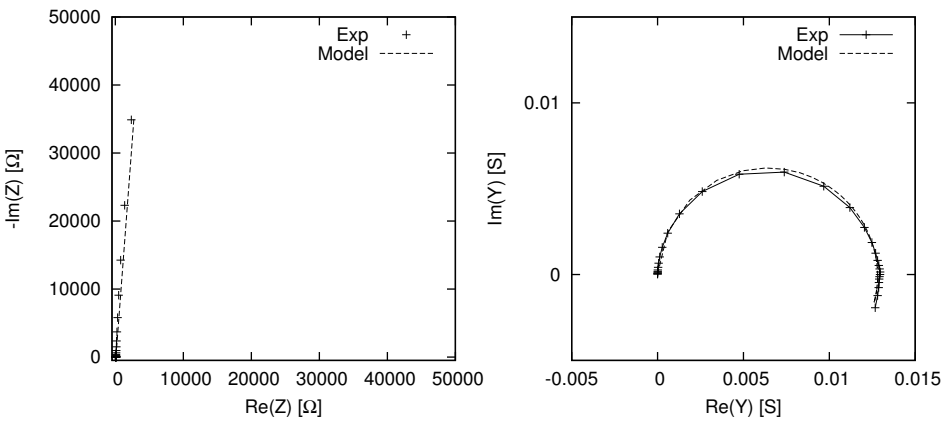

Figure 5.3: Nyquist plots of the impedance and admittance of the face-to-face electrodes covering the whole width of the box (no edge effect).

The real part of the impedance at low frequency on the Nyquist plot in impedance (Figure 5.3) is not constant. As the different points are all aligned, this might be the

result of a CPE behaviour. The Nyquist plot in admittance describes a perfect semi-circle, meaning that the edge effects are negligible.

Modelling

The experiment studies two aluminium electrodes separated by a solution. In that case, the circuit can be modeled as two capacitors created by the aluminium electrode and the solution, separated by the alumina layer as a dielectric. The surface of the aluminium electrodes is not perfectly smooth, involving a CPE behaviour. These capacitors are in series with the resistance R_{sol} created by the solution between the two electrodes. The impedance of two inductors are added in series with the previous elements to take into account the self-inductance created by each wires and the electrodes pair. The capacitance due to the solution being far lower than those due to the alumina/electrical double-layer interface, it was not included in the model. The resistance R_{alu} of the alumina layer is in parallel with the CPE, although not being present on Figure 5.4. The impedance of the model is then:

$$Z = 2jL\omega + \frac{2R_{alu}}{1 + (j\omega)^{\alpha} R_{alu} C} + R_{sol} \tag{5.1}$$

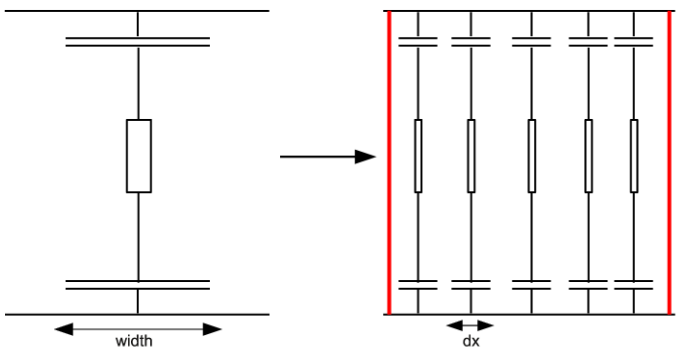

Figure 5.4: Discretization of the elements of the model

However, this model can be discretized, as seen on Figure 5.4. Discretizing the

model on the x-axis leaves a piece of capacitance in series with a piece of resistance, creating what can be called a transmission line[10, 11] or **RC line**. The admittance of a RC line can be expressed as follows :

$$Y_{line} = \left(\frac{2R_{alu}}{1 + (j\omega)^{\alpha} R_{alu} C} \times \frac{width}{dx} + \frac{\rho D}{dx \times H} \right)^{-1} \tag{5.2}$$

with $width$ being the electrode width, H the electrode height, D the distance between the two electrodes, ρ the solution resistivity, and dx a fraction of the electrode width on the x-axis. These RC lines are in parallel one from each other. The admittance previously calculated at each point of the x-axis can then just be added to create what can be called a **distribution of time constants**. The final impedance of the discrete model in the case of a face-to-face design is then :

$$Z_{discrete} = 2jL\omega + \left(\sum_{0}^{width} \left(\frac{2R_{alu}}{1 + (j\omega)^{\alpha} R_{alu} C} \times \frac{width}{dx} + \frac{\rho D}{dx \times H} \right)^{-1} \right)^{-1} \tag{5.3}$$

In the case of a face-to-face design and not taking into account the edge effects, the values calculated by the discrete model are the same as those calculated by the general model described by Equation 5.1. This is due to the fact that the distance between the two electrodes does not change at all. It can be observed on Figure 5.5 that the discrete model fits perfectly the data of a face-to-face experiment free of edge effects (Figure 5.1a).

The fit parameters (Table 5.1) were taken equal to the electrode and box dimensions. R_{alu} was fitted using the model. The real of the impedance value at high frequencies was equal to 78 Ω. Using Equation 2.2 with the solution conductivity but also the width and height of the electrodes and the distance between them, we find a 78 Ω resistance for the solution. The real part of the admittance is not constant at low frequencies. This is directly due to the resistance R_{alu} being in parallel with the capacitance C. A

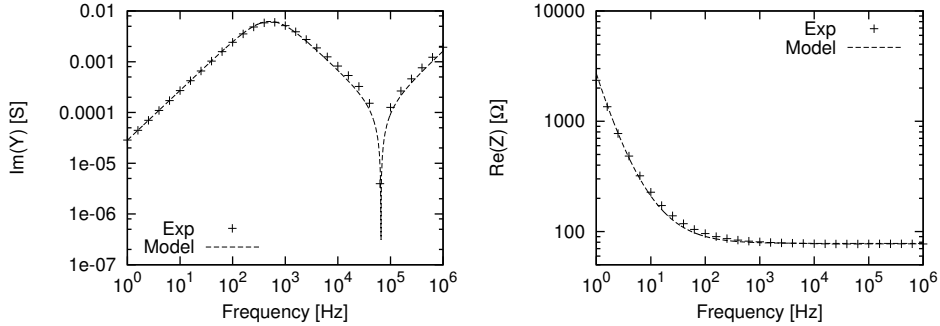

Figure 5.5: Bode plots of the imaginary part of the admittance and of the real part of the impedance of the face-to-face electrodes covering the whole width of the box (no edge effect).

R_{alu}	$4\times10^{5}\ \Omega$
C	9.4×10^{-6} F
L	8×10^{-7} H
D	5×10^{-2} m
H	10^{-2} m
$width$	3.2×10^{-2} m
dx	10^{-4} m
ρ	$0.5\ \Omega$.m
α	0.98

Table 5.1: Summary of the various parameters used in the model described in Equation 5.3, using a face-to-face design in a box with a 32 mm wide electrode.

resonance similar to the one observed in Figure 2.16 can be observed on the imaginary part of the admittance plot. Using Equation 2.41, the resonance peak frequency was found equal to 58 kHz. This value is close to the resonance peak frequency observed on Figure 5.5.

16 mm wide electrode (Edge effects)

As the model does not take into account the edge effects, it cannot fit the data of an experiment where these effects are important (Figure 5.1b).

In the case of this experiment, there is no edge effect from 1 Hz to 1 KHz (low frequency), as the model fits perfectly the left part of the Nyquist plot in impedance(Figure

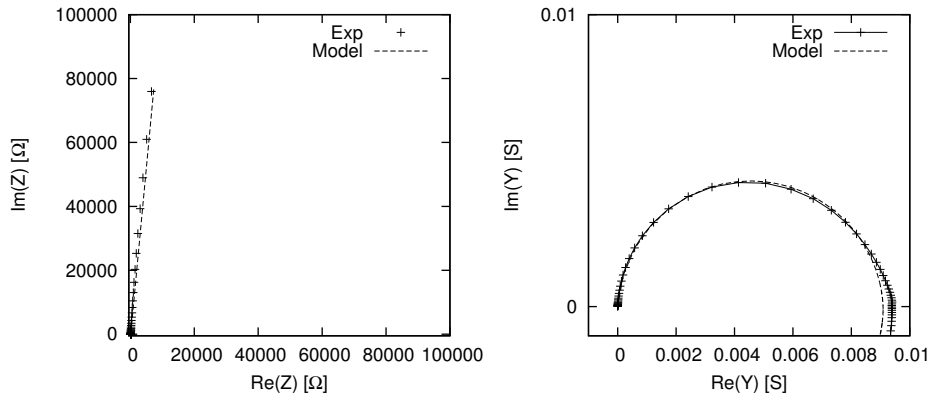

Figure 5.6: Nyquist plots of the impedance and admittance of the face-to-face electrodes covering a third of the width of the box. The edge effects are important in this case.

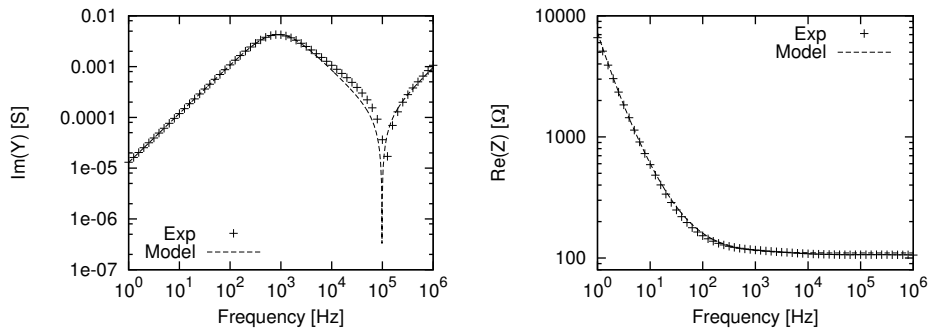

Figure 5.7: Bode plots of the imaginary part of the admittance and of the real part of the impedance of the face-to-face electrodes covering the third of the width of the box. The edge effects are important and the resonance is not fitted by the model.

5.6). However, these effects are important from 1 KHz to 1 MHz (high frequencies), as the imaginary part of the admittance, real part of the impedance and Nyquist plot in admittance all differ from the model. The real part of the impedance value is 106.6 Ω for the experiment and 110 Ω for the model (Figure 5.7).

The edge effects produce supplementary transmission lines compared to a perfect device (Figure 5.8). These supplementary transmission lines produce a larger virtual section for the resistance. In consequence the resistance is lower than for a device with no edge effects.

The R_{alu} and C values, fitted from the model (fit parameters in Table 5.2), are in

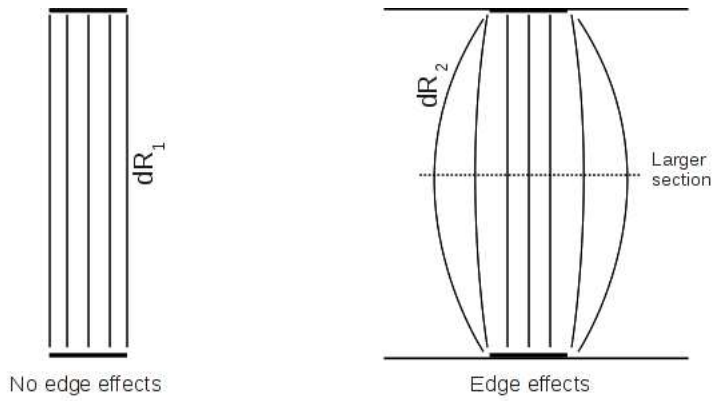

Figure 5.8: Supplementary transmission lines due to the edge effects. These supplementary lines produce a larger section but also a larger amount of greater RC time constants

R_{alu}	10^6
C	4.4×10^{-6} F
L	8×10^{-7} H
D	3.5×10^{-2} m
H	10^{-2} m
$width$	1.6×10^{-2} m
dx	10^{-4} m
ρ	0.5 Ω.m
α	0.965

Table 5.2: Summary of the various parameters used in the model described in Equation 5.3, using a face-to-face design in a box with a 16 mm wide electrode.

good agreement with a half-sized electrode (compared to 5.3.2). Using Equation 2.41, the resonance peak frequency value of the model was 93 kHz. This value is 24 % lower than the resonance peak frequency observed on Figure 5.5, which was estimated at 115 kHz. As the length of the transmission lines on the edges is higher than those between the two plates, the local RC time constants at the edge of the electrode differ from the center of the electrode, and more RC time constants are introduced. The consequence is a capacitance dispersion, leading to a virtual capacitance loss at high frequencies and so a higher resonance peak frequency.

5.3.3 Results : Coplanar design

Figure 5.9 presents the results of an experiment involving two aluminium electrodes with a gap variation between each electrode starting from 1 mm to 10 mm.

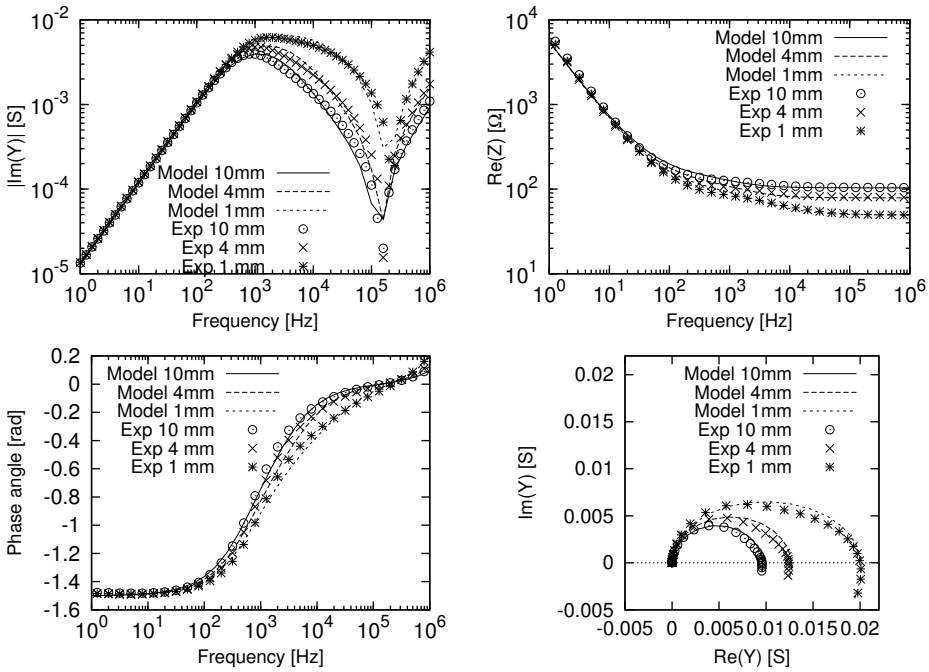

Figure 5.9: Spectra of the imaginary part of the admittance, the real part of impedance and phase against the frequency for a gap value between the two electrodes of 1, 4 and 10 mm. The Nyquist plot in admittance is also represented.

It can be observed that the imaginary part of the admittance values are equal for frequencies ranging from 1 Hz to 200 Hz. However, the resonance peak frequencies are close to each other for a gap between the electrodes equal to 4 mm and 10 mm, but not for a 1 mm gap where the resonance peak frequency is much higher. Moreover, although the resonance peak is close for 4 and 10 mm gaps, the values of the imaginary part of the admittance are not equal between 200 Hz and the resonance peak for these two distances, with the values for the 10 mm gap being much lower than for 4 mm, itself lower than for 1 mm. Three semi-circles can be observed on the Nyquist plot, the 10 mm distance being the smallest one while the 1 mm is the bigger. This seems logical as the resistance decreases when the electrodes get closer. However, it can be noted

that a second semi-circle increases at the right of the first circle as the distance between the electrodes decreases. As seen with the face-to-face design, this second semi-circle might be the result of the length variation of the transmission lines along the electrodes width.

Modelling

The discrete model presented in the face-to-face design analysis can be adapted to the coplanar design. Figure 5.10 illustrates the principle of a discrete model adapted to

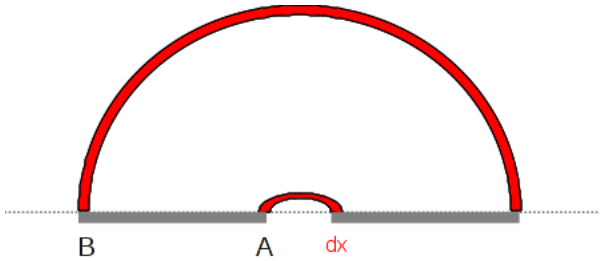

Figure 5.10: Adaptation of the principles of the discrete model to coplanar design.

a coplanar design. The basis is still to consider a RC line between the two electrodes. However, the distance between the two electrodes for a RC line at point A on the x-axis is far from being the same as the distance at point (B). This means that the value of the resistance at point (B) is much higher than at point (A). The effect is that the RC time constant at point (B) is higher than at point (A).

This case is similar to coplanar interdigitated band electrodes, so the distribution of the electrical field lines is elliptic[12]. Using a $f(z)$=$cos(z)$ conformal mapping[13, 14], we can transform the xy coordinates into uv coordinates by writing:

$$x + \imath y = cos(z) = cosh(u)cos(v) - \imath sinh(u)sin(v) \tag{5.4}$$

From Equation 5.4, we can write:

$$x = cosh(u)cos(v) \tag{5.5}$$

$$y = -sinh(u)sin(v) \tag{5.6}$$

As $cos^2(v) + sin^2(v) = 1$, the distribution of the electric field is:

$$\frac{x^2}{cosh^2(u)} + \frac{y^2}{sinh^2(u)} = 1 \tag{5.7}$$

The value of the parameter u can be calculated from the value of the semi-major axis a. Then the value of y is 0 and, from Equation 5.7, the value of u is:

$$u = acosh(a) \tag{5.8}$$

Then the value of the semi-minor axis b can be found as x=0 on this axis. Combining Equations 5.7 and 5.8, we get:

$$b = sinh(acosh(a)) \tag{5.9}$$

The half-perimeter HP of the ellipse for each RC line can then be calculated using Ramanujan's approximation of the ellipse perimeter [15].

$$HP = \frac{\pi}{2}\left((a+b) + \frac{3(a-b)^2}{10(a+b) + \sqrt{a^2 + 14ab + b^2}}\right) \tag{5.10}$$

The admittance for a RC line adapted to the coplanar design is :

$$Y_{line} = \left(\frac{2R_{alu}}{1 + (j\omega)^{\alpha} R_{alu} C} \times \frac{width}{dx} + \frac{\rho HP}{dx \times h}\right)^{-1} \tag{5.11}$$

R_{alu}	$2\times10^{6}\ \Omega$
C	4.5×10^{-6} F
h	10^{-2} m
L	8×10^{-7} H
$width$	1.6×10^{-2} m
dx	5×10^{-7} m
ρ	$0.5\ \Omega$.m
α	0.955

Table 5.3: Summary of the various parameters used in the coplanar discrete model described in Equation 5.12, for the three gap values (A=0.5, 2 and 5). Experiment done with a coplanar design using a 16 mm wide electrode

with x being the value of the considered point on the x-axis. Calculating from A to B, the impedance of the coplanar design using the discrete coplanar model and ignoring the edge effects is :

$$Z_{discrete} = jL\omega + \left(\sum_{x=A}^{B} \left(\frac{2R_{alu}}{1+(j\omega)^{\alpha} R_{alu} C} \times \frac{width}{dx} + \frac{\rho HP}{dx \times h} \right)^{-1} \right)^{-1} \tag{5.12}$$

The fits presented on Figure 5.9 are all plotted with a B-A value equal to *width* (16 mm) and A = 0.5, A = 2, A = 5 respectively for a distance between the two electrodes equal to 1 mm, 4 mm and 10 mm. The values fitted by the model, presented in Table 5.3, are globally in good agreement with the data, although the fit could be better taking into account the edge effects.

The electrodes were the same 16 mm width electrode used in the face-to-face experiment with edges effects (5.3.2. The *width* and h values were then the same while the C value was very close (2% variation). R_{alu} and α variations can be attributed to the electrode manipulation from the face-to-face design to the coplanar design in the box. The behaviour due to the edge effects observed in a 16 mm width electrode face-to-face design is exacerbated with the coplanar design, especially for a 1 mm gap. This is particularly visible on the real part of impedance plot of Figure 5.9, as one plateau appears around 1 kHz, to let place to a less resistive one after 10 kHz. The resonance observed

in the imaginary part of the admittance plot also presents the same behaviour than with the face-to-face experiment. The difference in RC time constant values between the beginning and the end of the electrode is higher for a 1 mm gap than for a 4 mm gap. A bigger time constant difference between the beginning and the end of the electrode increases the capacitance dispersion and so the virtual capacitance loss, resulting in a higher resonance peak frequency for smaller gap values.

5.4 Face-to-face design in reservoir

5.4.1 Experiment

Two aluminum band electrodes 4 cm long and 3 mm wide were cut from an aluminum foil and sticked in a 6 mm reservoir using a double-face adhesive rubber (Scotch, 3M) (Figure 5.11).

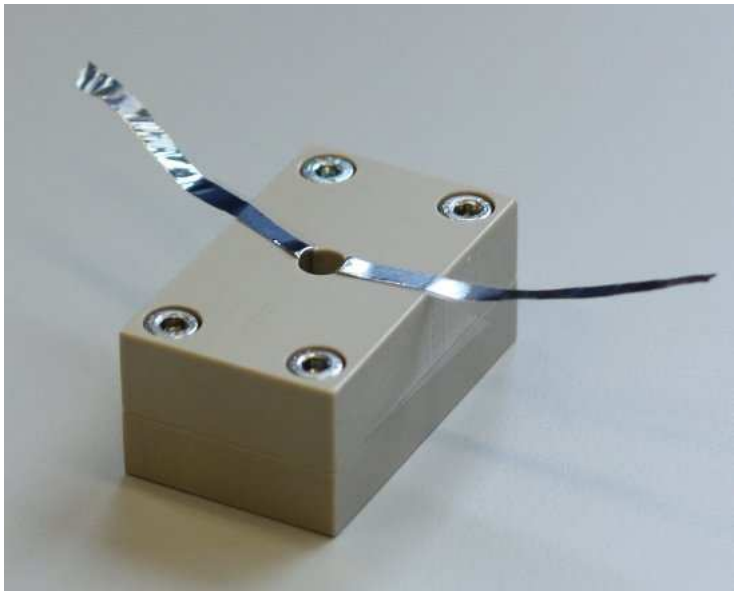

Figure 5.11: Picture of a face-to-face design using a 6 mm diameter reservoir

A 10 mV peak-to-peak AC potential difference was applied between the electrodes. Spectra were recorded for frequencies ranging from 1 Hz to 1 MHz with 5 points per

decade. 300 μL of 10 mM PBS were injected in the reservoir.

5.4.2 Spectra

The sensor relies on impedance signals to measure the variations of capacitance. This is done by applying an AC potential at each electrode composing the sensor. Figure 5.12 presents some spectra recorded for a face-to-face design in a reservoir : Absolute value of the Imaginary part of admittance, Capacitance calculated from the former, Argument of impedance, Real part of impedance, all recorded from 1 Hz to 1 MHz.

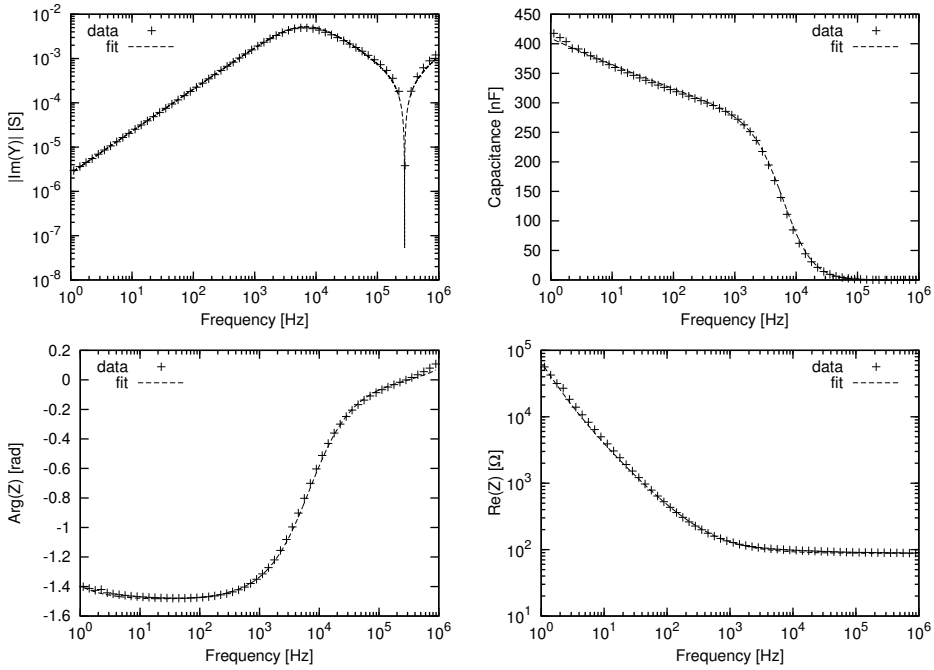

Figure 5.12: Four plots of the frequency response of a face-to-face sensor from 1 Hz to 1 MHz. Are represented on the plot the Absolute value of the Imaginary part of admittance, the Capacitance, the Argument of the impedance and the Real part of impedance for a face-to-face design in a reservoir using 3 mm width electrodes.

The signal is capacitive below 1 KHz, as the phase value is close to $-\pi/2$. Around 1 KHz the signal begins to become resistive, and is effectively resistive at 1 MHz. However, it can be seen on the Imaginary part of admittance that a resonance appears between 100 KHz and 1 MHz. The creation of this resonance depends on the value of the solution resistivity. The position of the resonance depends on the inductance and

capacitance values. Here, the inductors are for the major part created by the wires connecting the Solartron instrument to the sensor, and for the minor part by the aluminium electrodes composing the sensor. The capacitance relies, for this design, on the capacitance created by the aluminium electrode and the solution, using the thin alumina layer as a dielectric. This capacitance englobes the electrical double-layer interface. It can be seen on the capacitance plot that the capacitance at low frequencies is not constant, and so depends on the frequency. In this way, the phase is not equal to $-\pi/2$. This means that the capacitance is not a true capacitance but could rather be modelised as a Constant Phase Element (CPE). This CPE might be due to the surface roughness of the aluminium electrode[16], as can be observed on Figure 5.13. The real

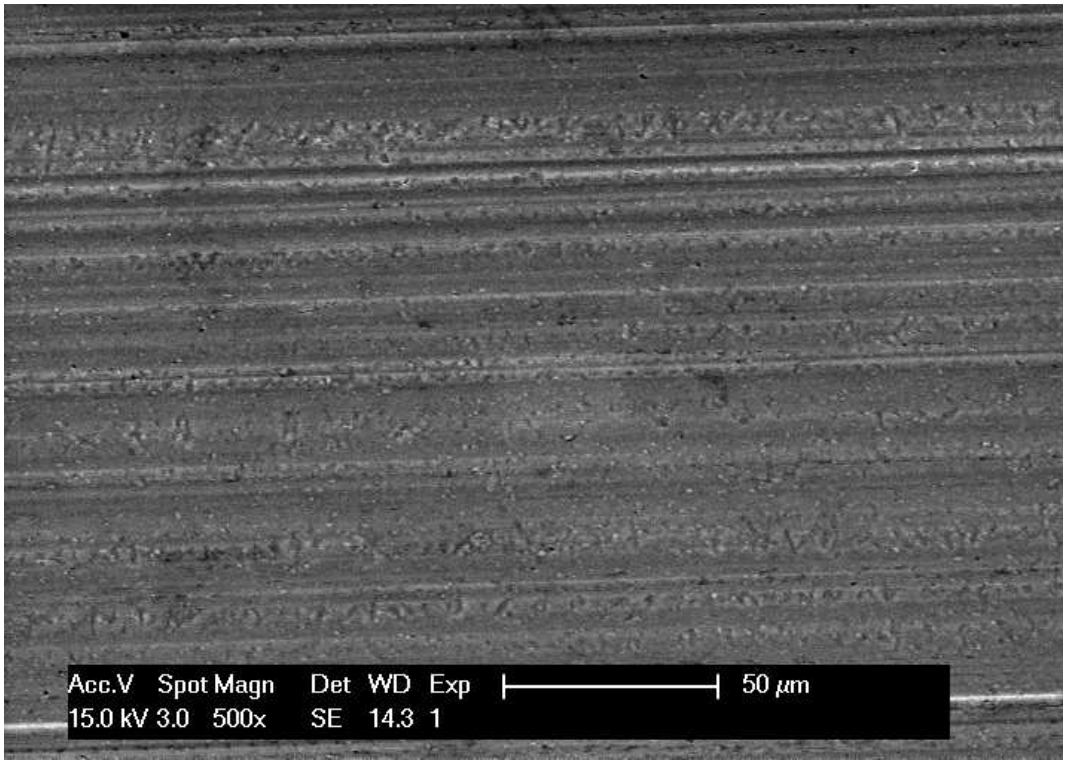

Figure 5.13: SEM image of the surface of an aluminium sheet. Note the large amount of lines, illustrating the fact that the surface is not smooth.

part of the impedance plot is quite interesting. At high frequencies, where the signal is resistive, the value of the impedance is due to the resistance of the solution in the reservoir. That is to say, in this design, the resistance between the two electrodes at

each side of the channel.

5.4.3 Modelling

The design of this sensor is very similar to the face-to-face design studied in 5.3.2. Thus, the model describing the face-to-face design of this sensor (Figure 5.14) was largely inspired from Equation 5.1.

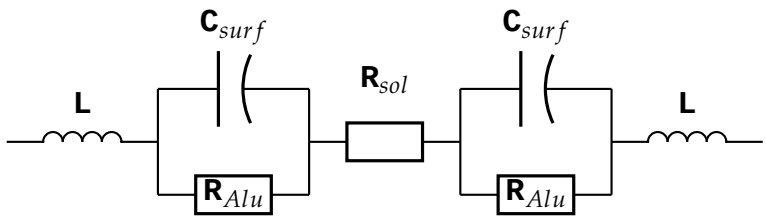

Figure 5.14: Model of a circuit composed of a face-to-face design using a reservoir.

The interface aluminium/alumina/solution is modeled as a resistor R_{Alu} in parallel with a CPE (C_{surf}). The resistor R_{Alu} represents the resistance of the alumina layer. The CPE includes for one part the capacitance created by the aluminium and the solution using the alumina layer as a dielectric (C_{Alu}), and for the other part the capacitance of the electrical double layer(C_{edl}) like:

$$C_{surf} = \left(\frac{1}{C_{Alu}} + \frac{1}{C_{edl}}\right)^{-1} \tag{5.13}$$

Two of the elements are included in the model, one for each electrode. The following elements are the inductors, created by the wires connecting the spectrometer to the sensor, and by the aluminium electrodes themselves. Two inductors are included in the model, representing each wire/electrode. Finally, a resistor R_{sol} is added to the model. As indicated by its name, this resistor represents the resistance created by the solution between the two electrodes.

As seen in Chapter 2, the impedance of a resistor is equal to R. The impedance of a capacitor of value C is equal to $1/jC\omega$. The impedance of an inductor of value L is equal

to $jL\omega$. We can calculate that the impedance of the resistor and the CPE describing the aluminium/alumina/solution interface is:

$$Z_{interface} = \left(\frac{1}{Z_R} + \frac{1}{Z_{surf}}\right)^{-1} = \frac{R_{alu}}{1 + (j\omega)^{\alpha} R_{alu} C_{surf}}$$

Injecting the impedance of the interface in the model, we find :

$$Z_{model} = \frac{R_{alu}}{1 + (j\omega)^{\alpha} R_{alu} C_{surf}} + 2j\omega L + R_{sol} \tag{5.14}$$

It is then possible, from Equation 5.14, to calculate the admittance of the circuit, and also various parameters like the real and imaginary parts, the phase or the capacitance. Experimental data was fitted with the model (fit parameters summarized in Table 5.4). A value of 900 nF was found for C_{surf}. Considering a 6 mm diameter reservoir filled with 300 μL PBS, the immersed height of the electrode is 1 mm. The useful electrode surface is then 5.3 times lower than in the 16 mm face-to-face design presented in 5.3.2, the capacitance ratio being 4.9.

The resistance R_{alu} in parallel with C_{surf} was found to be equal to 10^6 Ω. Each inductor was fitted at 700 nH. The solution resistance R_{sol} was fitted at 88 Ω. We apply the Ohm law to the electrodes and the reservoir, ignoring the edge effect of the electrodes and the curvature of the reservoir to calculate the resistivity of the solution in the reservoir :

$$\sigma_{sol} = \frac{L}{RS} \tag{5.15}$$

with L being the radius of the reservoir (6 mm), S the surface of the electrodes and R the fitted value. We find σ_{sol} equals to 2.27 S.m^{-1}. However, with such a distance between the electrodes with respect to the electrodes width, the edge effects have to be taken into account. Considering Feynman's approximation and assuming that the distance between the electrodes is constant and equal to 6 mm, the surface due to the

R_{alu}	$2\times10^{6}\ \Omega$
C_{surf}	9×10^{-7} F
L	7×10^{-7} H
R_{res}	$88\ \Omega$
α	0.95

Table 5.4: Summary of the various parameters used in the model described in Equation 5.14, and using a face-to-face design with a 3 mm wide electrode

edge effects is 52.5 mm^2 instead of 30 mm^2 The solution conductivity calculated with the edge effects is then 1.29 S.m^{-1}. The solution in the reservoir is a 10 mM PBS solution with a conductivity equal to 1.3 S.m^{-1}.The values found for the conductivity are then close to the theory.

5.4.4 Variations of parameters

Solution conductivity

The resistance of the reservoir is linked to the conductivity of the solution present in it, following equation 5.16

$$R_{channel} = \frac{L}{\sigma_{sol} S} \tag{5.16}$$

with

$$\sigma_i = \Lambda_i [C]_i \tag{5.17}$$

Λ_i represents the molar conductivity and $[C]_i$ the concentration of the solution i. Λ_i can be calculated by the Kohlrausch's law (equation 5.18)

$$\Lambda_i = \Lambda_i^0 - K\sqrt{[C]} \tag{5.18}$$

Λ^0 corresponds to the limiting molar conductivity of the solution[17]. In the case of a KCl solution, $\Lambda^0 = \Lambda_{K^+} + \Lambda_{Cl^-}$. Then theoretically $\Lambda^0 = (73.5 + 76.3) \times 10^{-4} = 149.8 \times 10^{-4}\ S.cm^2.mol^{-1}$. The value of the K constant was determined to be 1.2×10^{-4}

M^2.

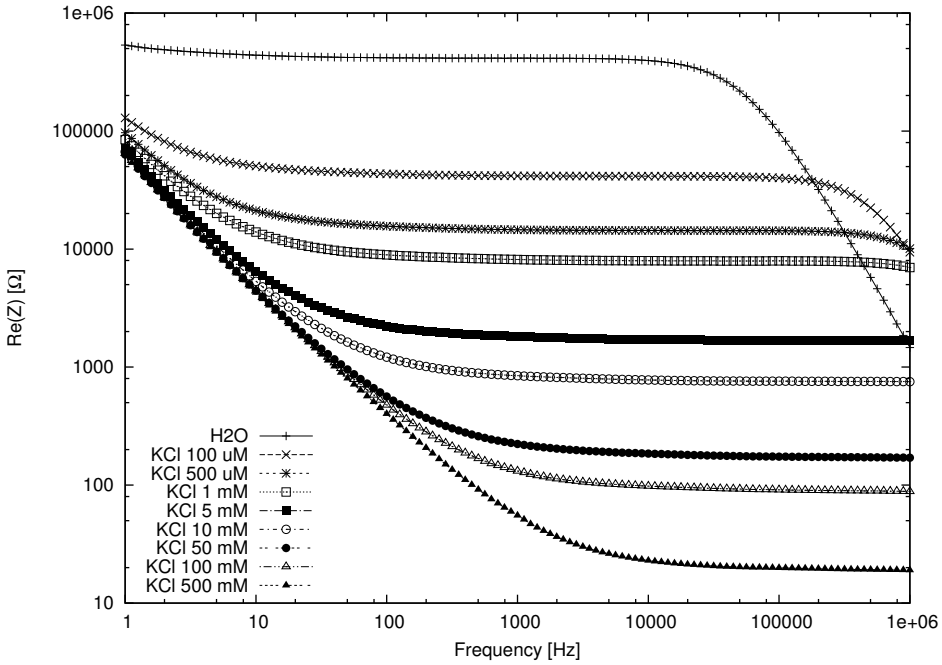

Figure 5.15: Resistance of the normal face-to-face sensor for different solution conductivities

Figure 5.15 presents the resistance (Real part of impedance) of the sensor when submitted to water and then to different KCl concentrations. The sensor is mostly capacitive at low frequencies and resistive at high frequencies. That is why the resistance of the sensor has to be measured at a 1 kHz frequency for water and at higher frequencies as the conductivity of the solution increases. The resistance of the channel measured by the sensor decreases as the solution conductivity increases.
This is illustrated by the values collected in Table 5.11. The resistance of the reservoir is 408 KHz with water. It can be observed that the resistance decreases almost 10 times when the KCl concentration increases in the same proportion.

When taking the inverse of equation 5.16 combined with equation 5.17 , we obtain:

$$\frac{1}{R_{channel}} = \frac{S\Lambda[C]}{L} \tag{5.19}$$

Solution	Resistance [Ω]
Water	408000
KCl 100 μM	41655
KCl 500 μM	14600
KCl 1 mM	7870
KCl 5 mM	1631
KCl 10 mM	754
KCl 50 mM	171
KCl 100 mM	90
KCl 500 mM	19

Table 5.5: Resistance of the channel measured by the sensor for various solutions.

The inverse of the measured resistance should then be a straight line when the concentration of the solution varies (low influence of the Kohlrausch's law at the considered concentrations). Figure 5.16 shows the plot representing the values of the inverse of the resistance collected in Table 5.11 for KCl concentrations ranging from 500 μM to 500 mM.

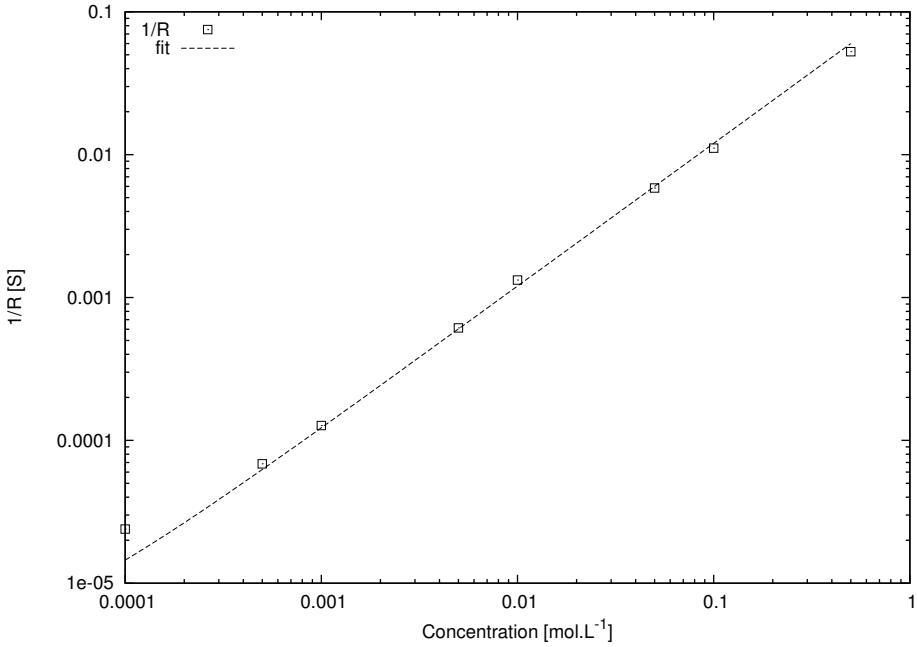

Figure 5.16: Resistance of the normal face-to-face sensor for different solution conductivities

The plot is presented in logarithmic scale for both x and y axis to make the lowest concentrated solution points visible. The standard deviation, evaluated at 1.4%, was not presented on Figure 5.16 as it was too small. As predicted, the inverse of the resistances measured with the sensor fits a straight line. This line was fitted with by $y = A \times x + B$ with A=0.12 S.L.mol^{-1} and B=2.5 $\times$ 10^{-6} S. This B factor means that the fitted resistance has a value of 4 $\times$ 10^5 Ω when the solution is totally free of KCl. This value is in good agreement with the value found when the reservoir is filled with water (408 kΩ). The A coefficient is useful to calculate the L/S ratio as Λ is calculated with the Kohlrausch's law. The point with an abscissa corresponding to 5 mM KCl is located on the fitted line. So this concentration will be used to calculate the L/S ratio. The molar conductivity of a KCl 5 mM concentrated solution calculated by the Kohlraush's law is equal to 147.1 S.cm^2.mol^{-1}. The L/S ratio is then equal to 122 m^{-1}. Assuming that the distance between the two electrodes is equal to 6 mm, the value of S is 4.92$\times$10^{-5} m^2. Knowing that the height of the fluid in the reservoir is equal to 1 cm, we find that the width of one electrode is equal to 4.92 mm. Taking into account the edge effects using Feynman's approximation, we find an electrode width of 2.8 mm. Considering that the distance between the electrodes is globally lower than 6 mm, the value of the edge effects is overestimated. The physical width of one electrode, equal to 3 mm, can then be considered true.

The surface capacitance fitted by the model is equal to 900 nF. The relative permittivity of alumina was found ranging from 9 to 10 F.m^{-1}[18–20]. Considering that the relative permittivity of the alumina is about 9 F.m^{-1}, and with the electrode dimensions previously found, the thickness of the alumina layer calculated by equation 2.5 was found to be equal to about 2.7 nm. Aluminium is a strong reductor, and a thin layer of about 3 nm thickness is created when exposed to the air. A value of about 2.7 nm is in good agreement with a naturally created alumina layer [21].

Electrode surface

Figure 5.17 presents the spectra of two different electrode sizes in a reservoir filled with a 10 mM PBS solution. The largest electrode width was 3 mm, giving a real surface of 30 mm^2. The width of the smallest electrode was 2 mm. Its physical surface was then 20 mm^2. The surface of the electrode decreases from one sensor to the other, and

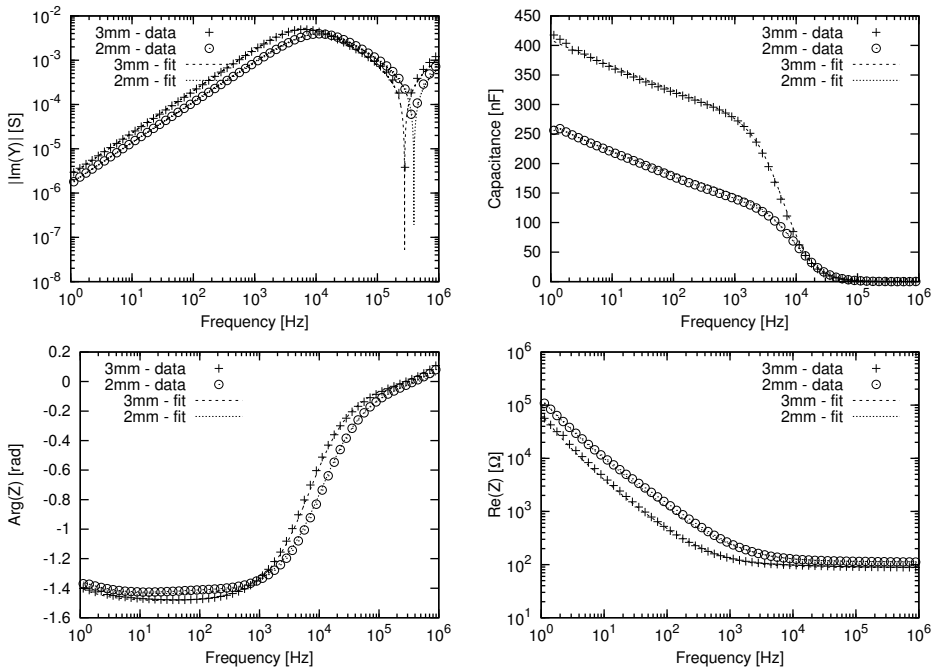

Figure 5.17: Spectra of two different surfaces of electrodes.

so does the capacitance. As the capacitance decreases, the resonance peak frequency increases too, as predicted by equation 2.41. It can also be seen that the real part of impedance increases when the surface of the electrode decreases. As predicted by equation 2.2, the resistance $R_{channel}$ increases in this case. At low frequencies the phase does not evolve, as it is dependent on the state of the alumina surface. But a shift can be observed around 10 KHz at the transition from the capacitive signals to the resistive signals. This is in fact a variation of a time constant of the circuit which relies on R_{sol} and C_{surf}.

The capacitance variation due to the reduced surface of the electrodes can be simulated

Solution	Resistance [Ω]
Water	562000
KCl 100 μM	50663
KCl 500 μM	17560
KCl 1 mM	9620
KCl 5 mM	2082
KCl 10 mM	950
KCl 50 mM	211
KCl 100 mM	111
KCl 500 mM	24

Table 5.6: Resistance of the channel measured by the sensor for various solutions.

with the model.

The conductivity experiments previously run on the normal electrode were also run on the smaller electrode. The results of the measured resistances are listed in Table 5.6.

The standard deviation was evaluated at 1%. As for Figure 5.16, the deviation was too small to be presented. The A coefficient on the fitted line on Figure 5.18 is equal to 0.095 S.L.mol^{-1}. When chosing 5 mM KCl as a reference, which has a molar conductivity of 147.1 S.cm^2.mol^{-1}, the value of the L/S ratio is equal to 145 m^{-1}. With the same assumptions as for the normal electrode, that is to say a distance of 6 mm between the two electrodes and a height of 10 mm, the width of the reduced size electrode is equal to 4.1 mm. The width found taking the edge effects into account is 1.85 mm. The edge effects being overestimated by considering a flat electrode, the real width of the electrode might then be 2 mm.

The capacitance C_{surf} of the reduced size electrode (Figure 5.17) was fitted at 620 nF (fit parameters in Table 5.7). Taking equation 2.7 and injecting the specific surface previously found for the reduced size electrode, it can be calculated that the alumina layer thickness is around 2.6 nm, close to the previously found value. As the resonance position relies on the surface capacitance, the peak shifts to lower frequencies when the capacitance increases.

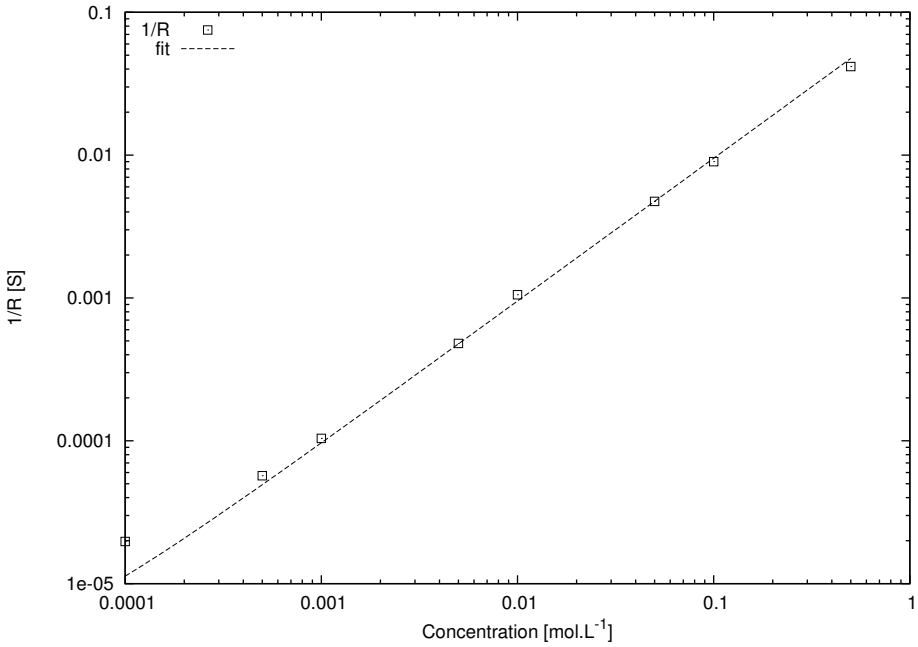

Figure 5.18: Resistance of the reduced size face-to-face sensor for solutions of different concentrations.

R_{alu}	$3\times10^{6}\ \Omega$
C_{surf}	6.2×10^{-7} F
L	7×10^{-7} H
R_{res}	$113\ \Omega$
α	0.92

Table 5.7: Summary of the various parameters used in the model described in Equation 5.14, and using a face-to-face design with a 2 mm wide electrode

Volume in the reservoir

The variation of the solution volume in the reservoir directly changes the height of the fluid in the reservoir. A variation of the solution height involves a variation of the electrode surface. Figure 5.19 presents the evolution of the capacitance when the volume of the fluid injected in the reservoir increases by steps of 5 μL .

It can be observed that the capacitance increases at each step, particularly at low frequencies. Figure 5.20 presents the evolution of this capacitance taken at 100 Hz with respect to the volume of solution injected in the reservoir.

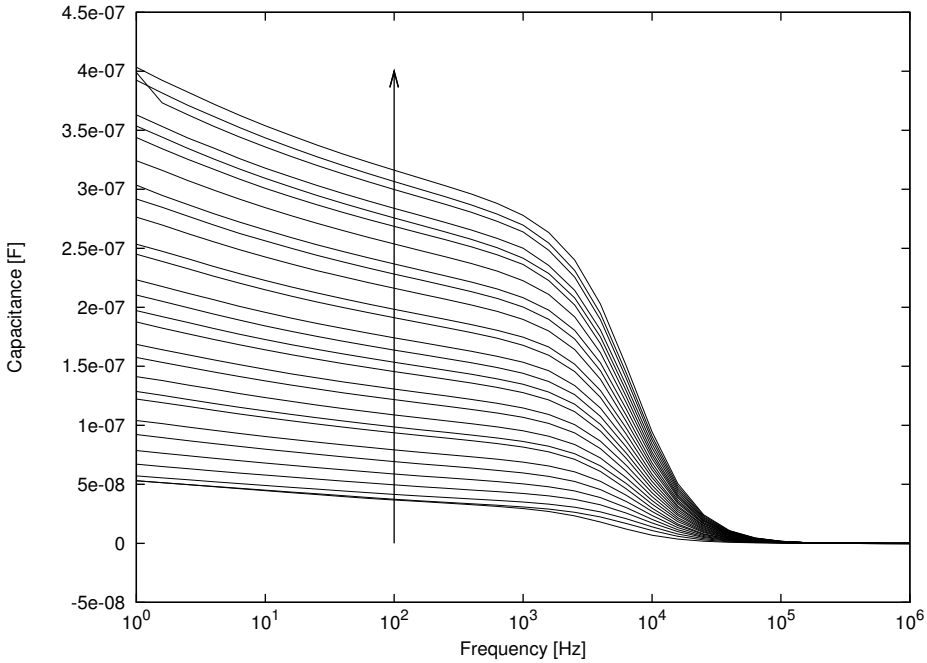

Figure 5.19: Capacitance against the frequency when increasing the volume of solution in the reservoir.

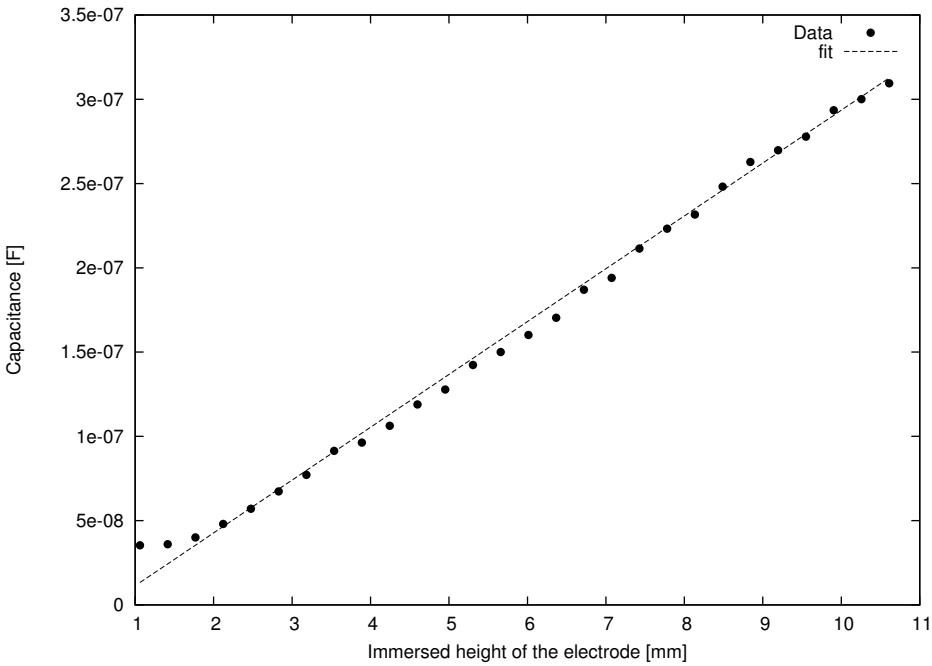

Figure 5.20: Capacitance against the immersed height of the electrode when increasing the volume of the solution in the reservoir.

The data is fitted using Equation 2.5, with the surface being equal to the electrode width multiplied by the height of the fluid in the reservoir. The equation fits the data, meaning that the evolution is linear. However, the capacitance between an 1 mm and 1.75 mm immersed height is not linear. This can be due to the signal coming from the edge effects being greater than the signal coming only from the surface of the electrode.

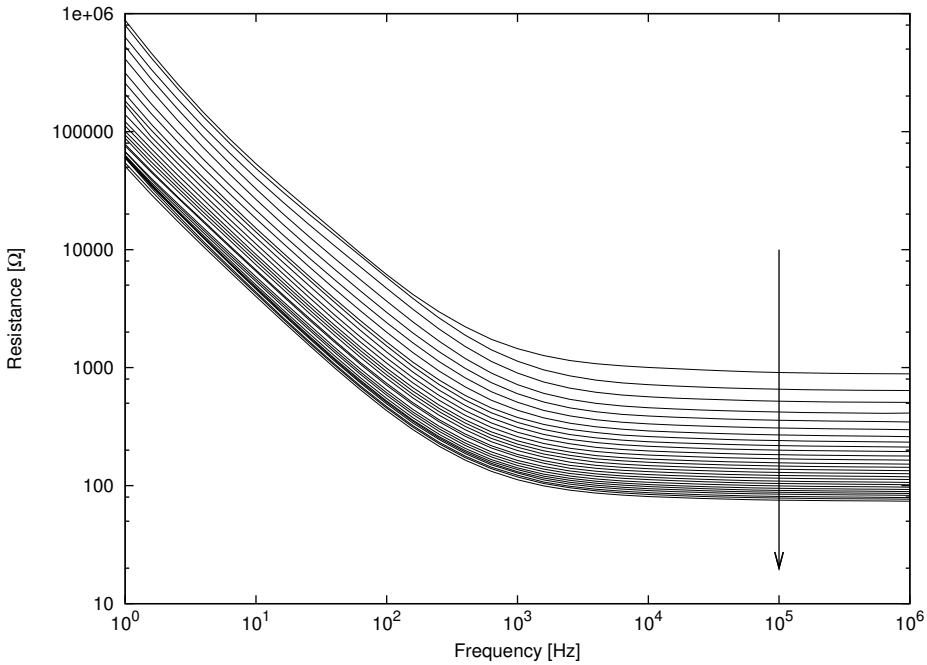

Figure 5.21: Resistance against the frequency when increasing the volume of the solution in the reservoir using a face-to-face design.

The evolution of the real part of the impedance is presented on Figure 5.21. The real part of the impedance decreases on all the frequency range from 1 Hz to 1 MHz when the immerged surface of the electrode increases. Figure 5.22 presents the evolution of the real part of the impedance with respect to the immerged electrode height, taken at 1 MHz. Contrary to the capacitance, the evolution of the real part of the impedance does not look linear at first sight on Figure 5.21 and 5.22. However a data fit with Equation 2.2 (fit parameters presented in Table 5.8) confirms that the evolution is actually linear, as it obeys to Ohm's law. The electrode width value was fitted larger than the real width due to the constant interelectrode distance hypothesis.

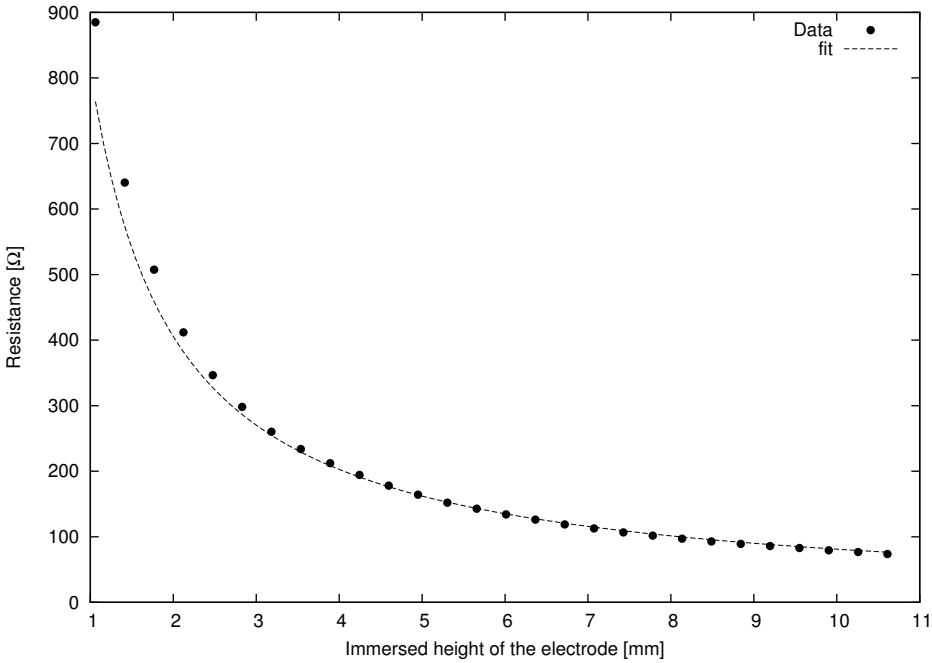

Figure 5.22: Resistance against the immersed height of the electrode when increasing the volume of the solution in the reservoir using a face-to-face design.

ρ	0.5 Ω.m
L	6×10^{-3} m
S	h$\times3.3\times10^{-6}$ m^2

Table 5.8: Summary of the parameters used to fit Figure 5.22

5.5 Coplanar design in reservoir

5.5.1 Design

Despite its qualities like a certain ease of modelling and scalability, the face-to-face design is delicate to build. Actually, it needs two independant electrodes to be placed as precisely as possible in front of each other. This drawback can be solved by using a rectangular reservoir, but this implies some engineering work to avoid water leakage that was feasible in this work. Placing the electrodes on the same plane, one near the other, just allows to consider one parameter when building the sensor : The spacing between the two electrodes.

The coplanar sensor is built in three steps:

- A 100 μm thick PET sheet composes the support of the sensor.
- A line of glue is deposed on the PET sheet with a Pritt roller (Henkel, Germany).
- Two aluminium electrodes are cut from an aluminium foil and sticked on the glue. The spacing between the electrodes can be adapted to the required sensor behaviour.

The sensor is then placed in a 6 mm or 12 mm diameter reservoir. The center of the chip is placed at the center of the reservoir in order to have the same surface for each electrode exposed to the solution.

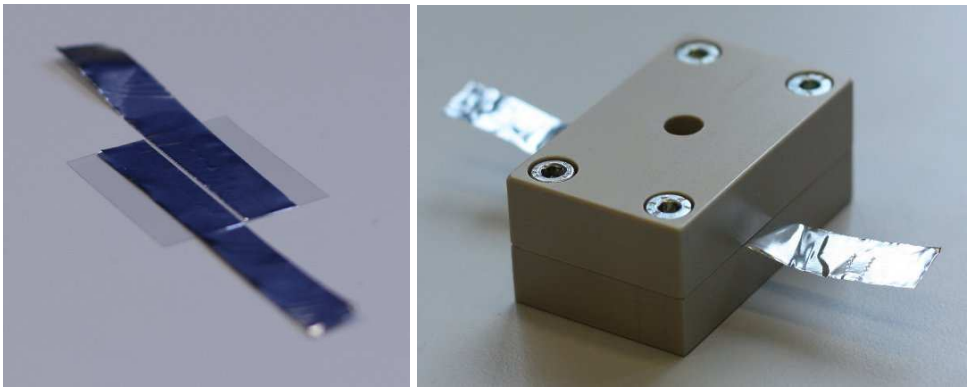

Figure 5.23: Picture of a coplanar design chip and of a coplanar chip using a 6 mm diameter reservoir

5.5.2 Experiment

A 10 mV peak-to-peak AC potential difference was applied between the electrodes. Spectra were recorded for frequences ranging from 1 Hz to 1 MHz with 5 points per decade.

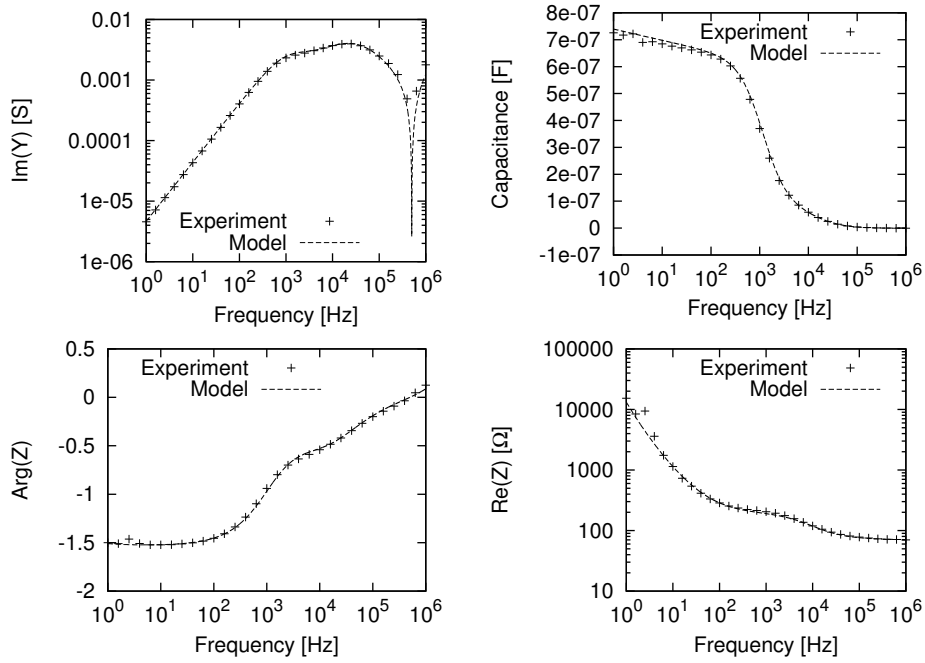

Figure 5.24: Spectra of the sensor using a coplanar design

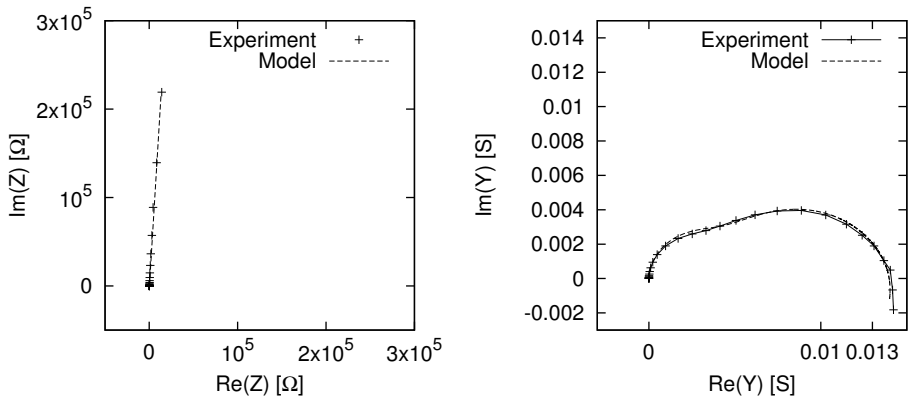

Figure 5.25: Nyquist plots of the sensor reponse.

5.5.3 Spectra

Figure 5.24 presents a spectrum recorded using a coplanar chip in a 6 mm diameter reservoir. The general behaviour of the coplanar design is the same as the face-to-face design. However, it can be seen that the resonance peak sets at a higher frequency than for the face-to-face design. A reservoir filled with 160 μL of PBS does not give a semi-circle for the Nyquist plot in admittance (Figure 5.25), but instead two semi-circles.

5.5.4 Modelling

The coplanar design in a reservoir is different from the coplanar design in the box in two principal points. The first point deals with the geometry itself, as in the reservoir the electrodes are semi-circular and not rectangular. The second point deals with the height of fluid. The box was large enough to let the maximum of the signal going from one electrode to the other. In the reservoir, the height of the fluid might be as low as possible to limit the effects of the diffusion as much as possible. Thus, the geometry of a reservoir is much more complicated than for a box, and the discrete model elaborated in 5.3.3 would have to take into account this added complexity. At this step it would be more convenient to use Finite Element computations to model the response of the sensor, as the discrete model established for a box is already time consuming, and would be unusable with an added complexity. However, due to technical limitations of the Solartron interface (explained in further details in Chapter 6), an analytical model is required. The most time consuming part of the algorithm is the calculation of the volumic transmission lines. As a CPE is a distribution of time constants, the transmission lines used in the model described in 5.3.3 can be replaced by a CPE.

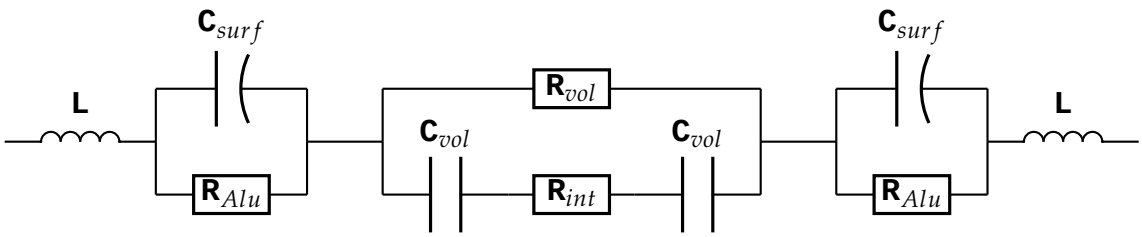

Figure 5.26: Equivalent circuit of the model taking into account the transmission lines by using CPE elements.

As two semi-circles on a Nyquist plot (Figure 5.25) likely represent two *RC* circuits in serial, the proposed model (Figure 5.26) is composed of two serial *RC* circuits. The first one, at low frequencies, is represented by the two C_{surf} CPE in serial with R_{vol}. The second one, at high frequencies, is the resultant of the volumic transmission lines.

As the resistance R_{vol} is constant in this model, in parallel with this resistor are combined two C_{vol} CPE in serial with a resistor R_{int}. These C_{vol} CPE represent the volumic time constants distribution at high frequencies while R_{int} represents a surface resistance between the two electrodes and the edge effects between the two electrodes. The impedance Z_{cop} of the global model is:

$$Z_{cop} = 2\left(\frac{1}{R_{alu}} + Y^{\alpha}_{C_{surf}}\right)^{-1} + 2Z_L + \left(\frac{1}{R_{vol}} + \frac{Y^{\beta}_{C_{surf}}}{2 + R_{int}Y^{\beta}_{C_{surf}}}\right)^{-1} \tag{5.20}$$

with:

$$Y^{\alpha}_{C_{surf}} = C_{surf}(j\omega)^{\alpha}$$

and

$$Y^{\beta}_{C_{vol}} = C_{surf}(j\omega)^{\beta}$$

The model fits the experimental data of a 12 mm diameter reservoir coplanar design, whose reservoir is filled with 160 μL of PBS (Figure 5.25). The hypothesis about the low frequency and high frequency parts can be checked by deactivating the surface or the volumic part of the model (Figure 5.27)

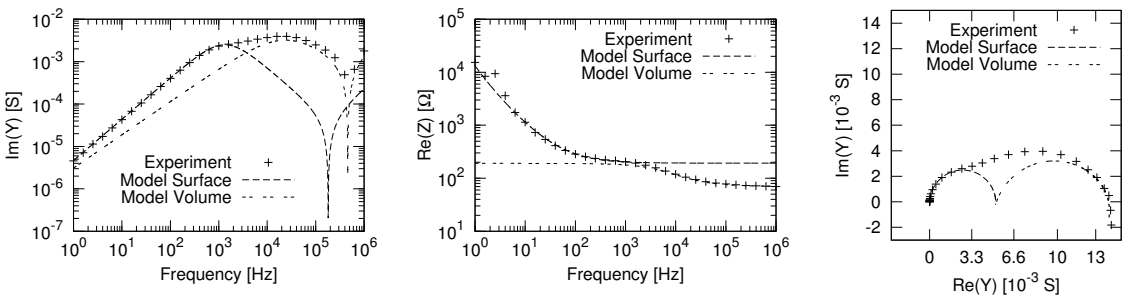

Figure 5.27: Bode plot of the Imaginary part of the admittance and resistance, and Nyquist plot in admittance of the experimental data of 6 mm diameter reservoir.

R_{alu}	$5\times10^{6}\ \Omega$
R_{vol}	$193\ \Omega$
R_{int}	$110\ \Omega$
C_{surf}	1.55×10^{-6} F
L	7×10^{-7} H
α	0.975
β	0.785

Table 5.9: Summary of the various parameters used in the model described in Equation 5.20

When considering only the surface part (low frequencies) of the model, only one matching semi-circle appears at low frequencies. It can also be observed that the surfacic part of the model fits the imaginary part of the admittance and the real part of the impedance until 1 KHz. Above this frequency, the resonance is well predicted by the model as the frequency predicted by the surface part is much lower than observed, and the value of the resistance is fixed to 193 Ω. On the other side, the volumic part of the model fits the resonance and matches the values of the resistance after 1 KHz. It also fits the second semi-circle (high frequency) part of the Nyquist plot in admittance. Thus, the volume part of the model can successfully fit the transmission lines distribution involved in a coplanar design, even with more complicated geometries than the plastic box. The fit parameters used to fit the data presented in Figures 5.24, 5.25 and 5.27 can be found in Table 5.9

5.5.5 Variation of parameters

Variation of the electrodes surface

The variation of the electrodes surface was studied by acquiring the signal from chips mounted in 6 mm and 12 mm diameter reservoir holders. The experimental data (Figure 5.28) were fitted with the model fit parameters in Table 5.10 to extract the values of various parameters.

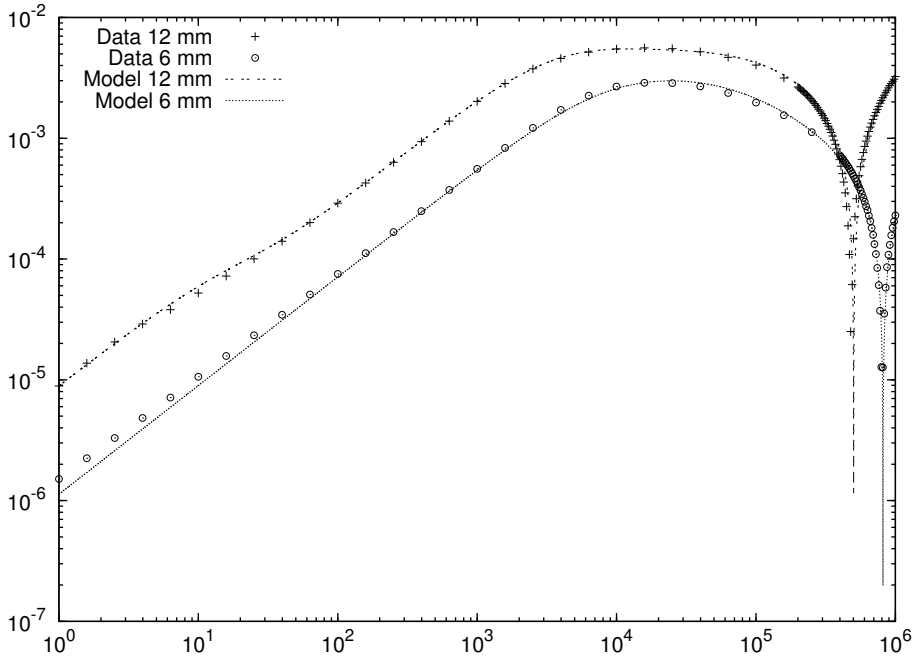

Figure 5.28: Spectra of the sensor using a 12 mm and 6 mm diameter reservoir.

Diameter	C_{surf} [nF]	α	β	R_{vol} [Ω]	R_{int} [Ω]
6 mm	437	0.90	0.755	170	360
12 mm	1750	0.90	0.72	90	106

Table 5.10: Values fitted with the model

The electrode surface created by a 12 mm reservoir is 4 times bigger than the one created with a 6 mm reservoir. The model agrees with this fact with C_{surf} being equal to 1750 nF for the first one and 4 times less for the second. The α factor was the same between the two reservoirs, meaning that only geometrical effects are involved. This is illustrated by the β factor being higher for the 6 mm diameter reservoir, as the time constant difference between the beginning and the end of an electrode is lower for a smaller electrode. It can also be observed that the resonance peak position is located at 478 KHz for the chip in 12 mm diameter reservoir and 823 KHz for the 6 mm diameter one. The ratio is then 1.73, a bit far from the expected 2. This is mainly due to volumic geometrical effects. When setting a β coefficient of 0.755 to the 12 mm diameter reservoir, the value of its resonance peak shifts to 426 KHz, giving a ratio of 1.93.

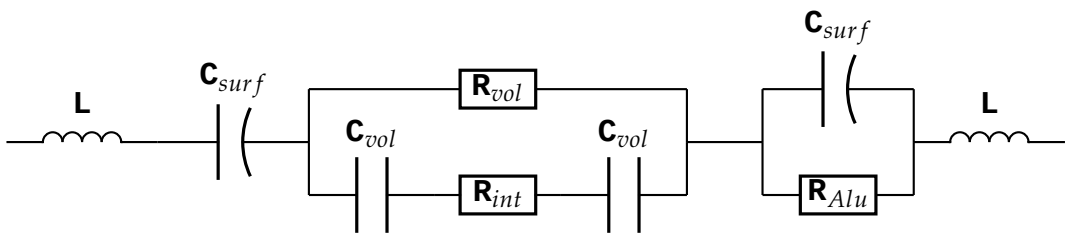

Figure 5.29: Model of a circuit taking into account the time constant effect resulting in the appearance of only one capacitor around 1 Hz. One R_{Alu} component is removed to take into account the very low frequency effects

A deviation can be observed between 1 and 10 Hz especially on the 12 mm diameter reservoir. The amplitude of this deviation matches the value of only one capacitor, and might be due to a time constant effect. The model can be modified to take into account this time constant effect, by removing one R_{alu} resistor in one of the surface elements (Figure 5.29). The only capacitor C_{surf} then fits the extremely low frequencies, is later in serial with the other surface capacitor in the low/medium frequencies, and let place to the volumic effects in the high frequency range. However, this case happened only a few times, and moreover, as will be seen in details in Chapter 6, the working part of the sensor is located at high frequencies. As a consequence, this modified model can be useful, but the vast majority of the cases can be studied with the former model.

Resistance of the solution

Changing the solution conductivity has a strong influence on the response of the sensor. This response is illustrated on Figure 5.30, where a water solution and different KCl concentrations are introduced in the reservoir. The surface effects at low frequencies are more pronounced than for the face-to-face design, and the spectra are much less regular. The level of resistivity has to be taken for different frequencies, along the whole frequency range. It has to be noted that for a low KCl concentration, the behaviour of the sensor is different from the face-to-face design, as the real part of the impedance does not evolve as much as with higher concentration solutions.

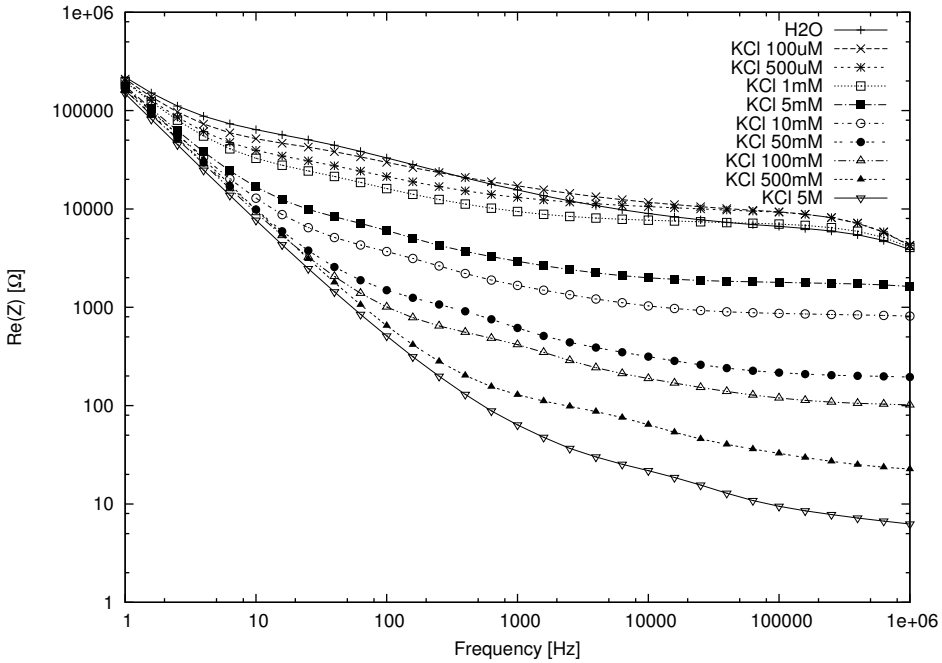

Figure 5.30: Bode plot of the real part of the impedance against the frequency for various KCl concentrations.

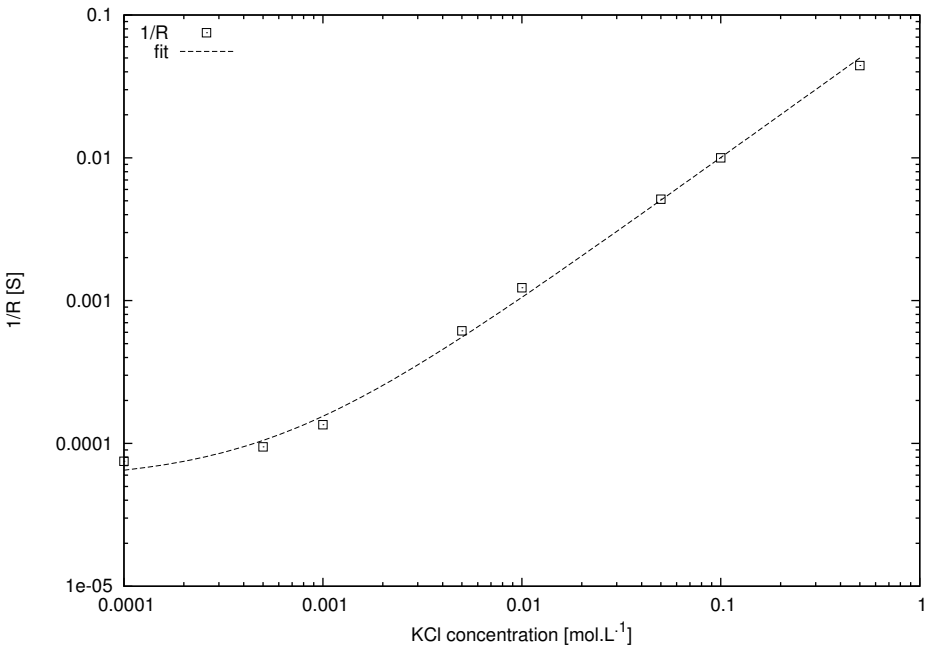

Figure 5.31: Reverse of the resistance against the concentration of a KCl solution, presented in logarithmic scale on x and y axis.

Solution	Resistance [Ω]	Frequency
Water	20700	400 Hz
KCl 100 μM	13321	400 Hz
KCl 500 μM	10575	10 KHz
KCl 1 mM	7400	25 KHz
KCl 5 mM	1626	1 MHz
KCl 10 mM	813	1 MHz
KCl 50 mM	195	1 MHz
KCl 100 mM	100	1 MHz
KCl 500 mM	22.6	1 MHz

Table 5.11: Resistance of the reservoir using a coplanar design measured by the sensor for various solutions.

The values of the resistance are similar to those of the face-to-face design for highly concentrated KCl solutions. However, as noted before, the resistance does not increase when the concentration of the solution decreases below 1 mM. The plot presenting the reverse of the resistance against the KCl concentration is similar to the one of the face-to-face design, as can be seen on Figure 5.31.

The evolution of the resistance against the KCl concentration is linear from 1 mM to 500 mM. However, the value of the resistance becomes constant as the concentration of the solution in KCl decreases. The data are fitted using the equation 2.2 previously used with the face-to-face design. The A coefficient was fitted at A = 0.1 and with B coefficient of 5.5×10^{-5} S. The coefficient is close to the coefficient found with the face-to-face design. The value of the reverse of B is 18181, which is close to the value of the resistance found with deionized water in the reservoir.

Variation of the volume in the reservoir

The variation of the volume for the coplanar design was realized in the same way as for the face-to-face design. A coplanar design chip fixed in a holder of 12 mm diameter was used.

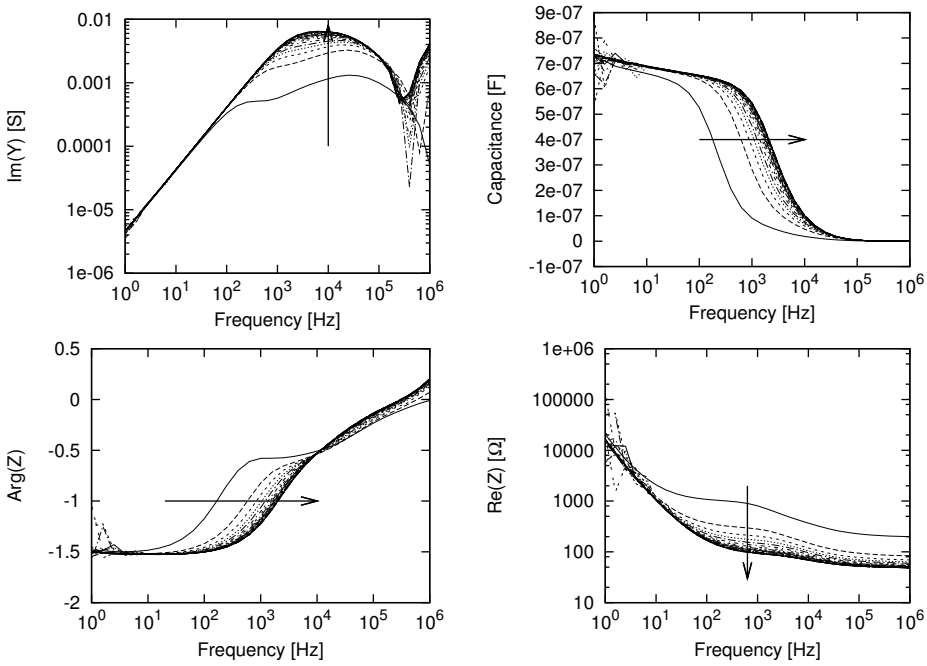

Figure 5.32: Bode plots of the addition of fluid in the reservoir with 40 μL steps.

Figure 5.32 describes the evolution of the imaginary part of the admittance, the capacitance, the phase and the real part of the impedance against the frequency, when the volume of the solution in a reservoir of 12 mm diameter increases by steps of 40 μL. Like with the face-to-face design, the value of the real part of the impedance decreases when the volume of the solution in the reservoir increases. However the variation of this value seems to decrease when the volume increases.

Following this variation of resistance, a variation of a RC time constant can be observed on the phase and the capacitance plots from 100 Hz to 10 KHz. Like with the real part of the impedance, the intensity of this variation seems to decrease as the volume in the reservoir increases. The value of the imaginary part of the admittance also increases between 1 KHz and 100 KHz. It can be observed that the resonance shifts to lower frequencies when the volume of solution injected in the reservoir increases.

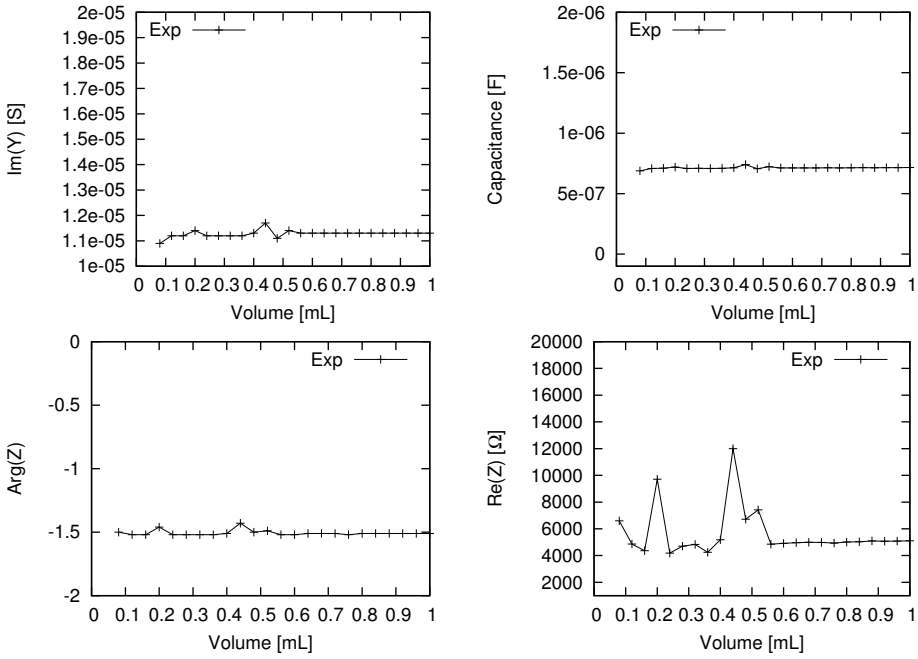

Figure 5.33: Imaginary part of admittance, capacitance, phase and real part of impedance after addition of fluid in the reservoir with 40 μL steps at low frequency.

Nevertheless, these effects do not seem to happen for each frequency. At 1 Hz (Figure 5.33), all the parameters (capacitance, resistance, real part of impedance and imaginary part of admittance) observed on Figure 5.32 do not evolve when the volume of solution injected in the reservoir increases. This means that the effects at low frequencies are related to the surface of the electrodes, as the size of the aluminium electrode in contact with the solution does not increase when the volume of the solution increases.
However, these effects are important for a 1 MHz frequency (Figure 5.34).

It can be observed that the values of the capacitance and the imaginary part of the admittance increase when the volume of the solution in the reservoir increases until a total of 800 μL .
In the same way, increasing the solution volume in a 6 mm diameter reservoir using a coplanar design produces the same effect for a 1 MHz frequency (Figure 5.35).

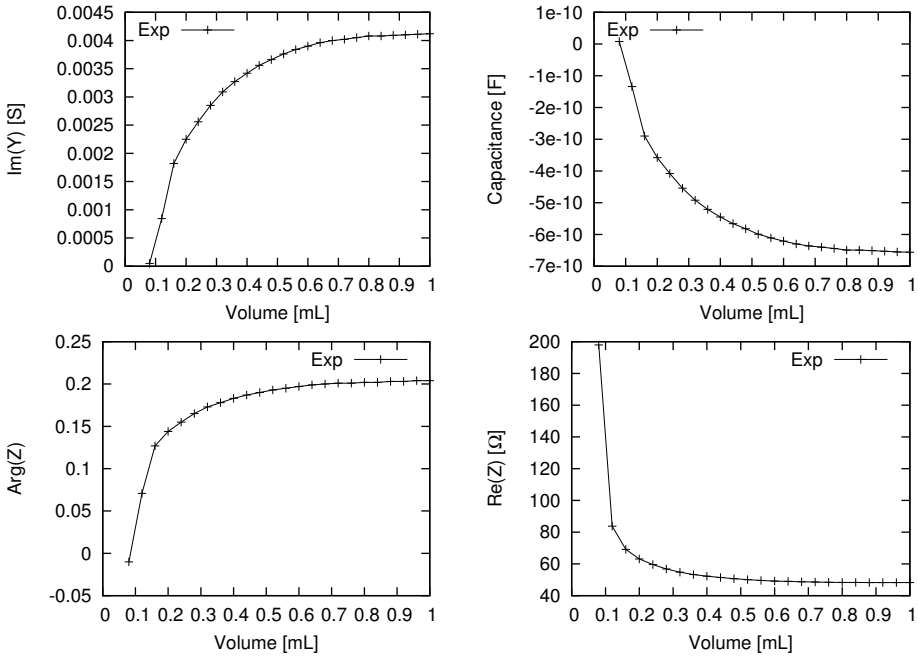

Figure 5.34: Imaginary part of admittance, capacitance, phase and real part of impedance after addition of fluid in the reservoir with 40 μL steps at high frequency.

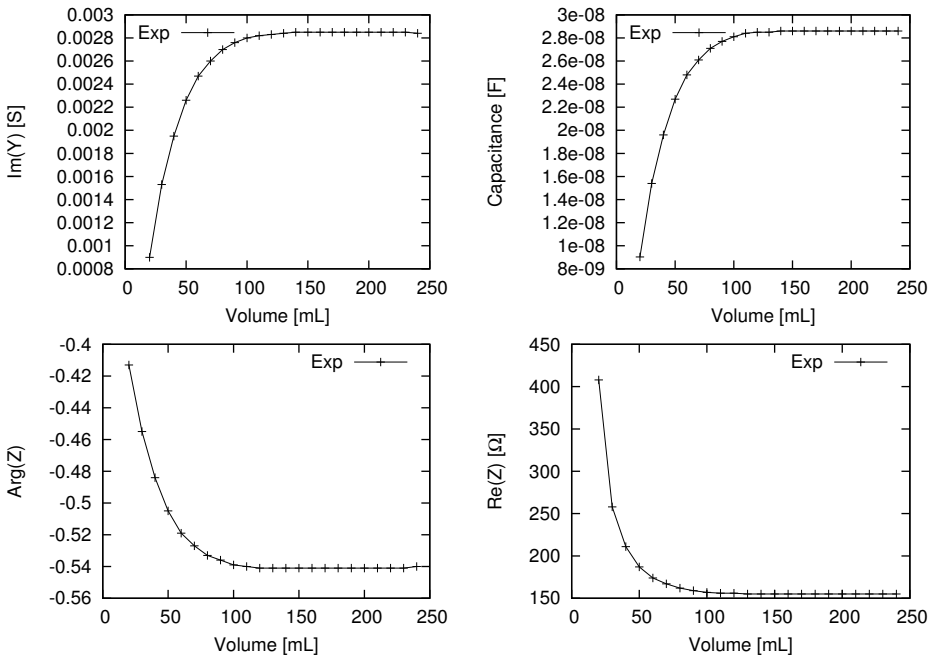

Figure 5.35: Imaginary part of admittance, capacitance, phase and real part of impedance after addition of fluid in the reservoir with 10 μL steps at high frequency.

The imaginary part of the admittance and the capacitance do not increase when injecting a volume greater than 120 μL in the reservoir.
In a reservoir of 12 mm diameter, a volume of 800 μL gives a fluid height of 7 mm. This height is 4 mm for a reservoir of 6 mm diameter filled with 120 μL of solution. These heights are in both cases close to the radius of the reservoir.
This result has previously been observed in the Chapter 3, where the channel capacitance at high frequencies stops increasing when the Gq number is higher than 1. This behaviour also applies to the resistance of the channel, as both effects are based on the electric field repartition in the reservoir. The reservoir surface resistance will then increase as the volume of the solution in the reservoir increases, lowering the global resistance of the reservoir. As seen on Figure 5.32, the resonance position is related to the channel resistance value as it depends on the distribution of time constants produced by the latter. As the resistance surface of the reservoir increases, the resistance lines get longer and so the local resistance increases. So even if the global resistance of the reservoir decreases, the global RC time constant increases.

Variation of the distance between the electrodes

The distance between the two electrodes was set to 150 μm , 400 μm , and finally 800 μm . The chip was each time mounted in a holder drilled with a 6 mm diameter reservoir. 60 μL of KCl 100 mM were injected in the reservoir. Spectra were recorded from 1 Hz to 1 MHz with 5 points per decade, except from 500 KHz to 1 MHz with 100 points per decade.

The resonance peak frequency (Figure 5.36) increases when the distance between the electrodes decreases. This result is close to what was observed with the coplanar design in a plastic box (5.3.3), as the difference of resistance between the transmission lines at the beginning (center side) and the end (reservoir side) of the electrode

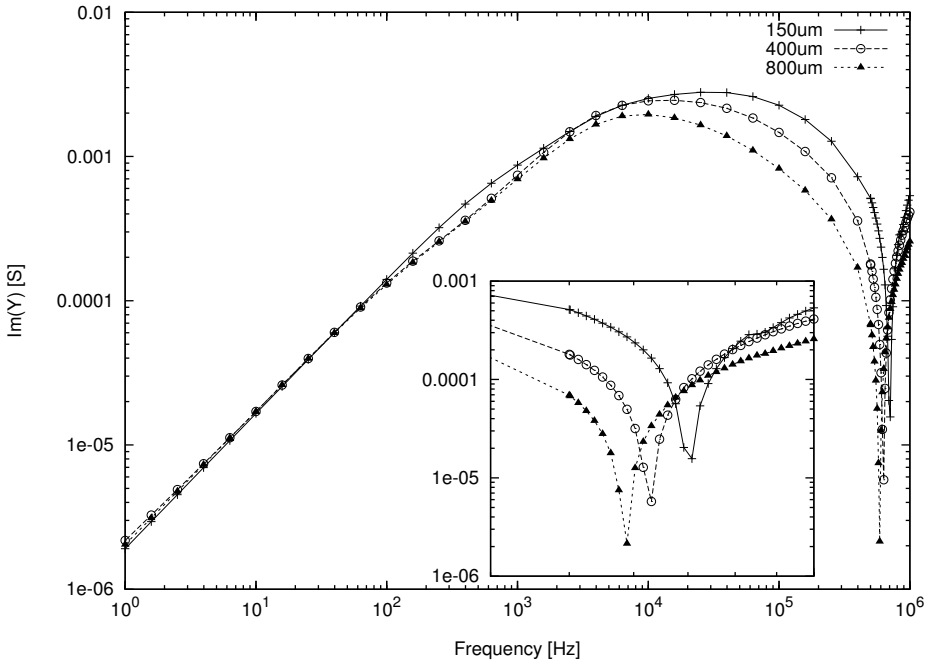

Figure 5.36: Bode plot of the imaginary part of the admittance against the frequency for a distance between the electrodes equal to 150 μm , 400 μm and 800 μm for a reservoir of 6 mm diameter.

increases when the distance between the electrodes decreases.

5.6 Coplanar design in channel

Adsorbing in a microchannel reduces the time needed to reach the equilibrium, as the diffusion length is strongly reduced due to the smaller channel dimensions compared to the reservoir, but also as the species are continuously renewed by the flow. However adsorption in a microchannel has some constraints : The fluidic system needs to be reinforced to support the fluid pressure and the design of the chip needs to be adapted.

Channel design

A flow cell was created in two parts. The top part is made of teflon material to avoid adsorption on the holder elements, while the bottom part is made of plexiglas material

to have the possibility to install the chip correctly in the holder (Figure 5.37).

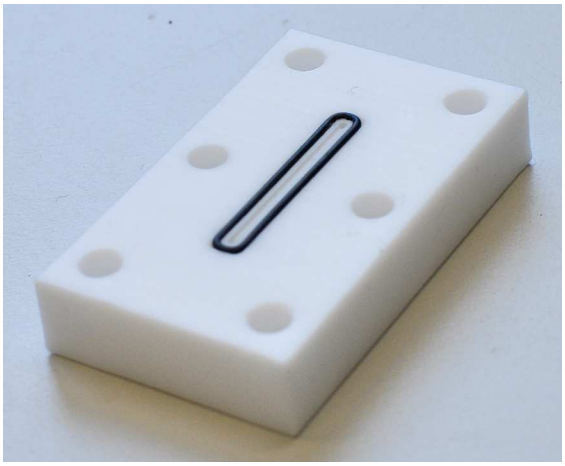

Figure 5.37: Top part of the teflon holder. The channel and the toric gasket can be observed.

A channel 1 mm wide, 20 mm long and 300 μm high was drilled in the top part of the flow cell. A second channel was drilled all around the first one to insert a toric gasket in order to avoid any leakage. The spacing between the first and the second channel was 1 mm. Two holes were drilled in the holder at each end of the channel to introduce and maintain the fluidic connectors (Upchurch, USA). Finally, six holes were drilled on the edges of both the top and the bottom part of the holder to maintain the top and the bottom parts firmly screwed.

Chip design

Two possibilities are let for the chip design, both based on the coplanar design previously studied (Figure 5.38).

The first design is called the *Reservoir design*. It is actually the same chip that was used in the reservoir experiments. Due to the channel drilled in the holder, the useful size of one electrode is 1 mm wide and 10 mm long, which gives a surface area of 10 μm^2 per electrode.

The second design is called the *Channel design*. In this design, the electrodes are placed

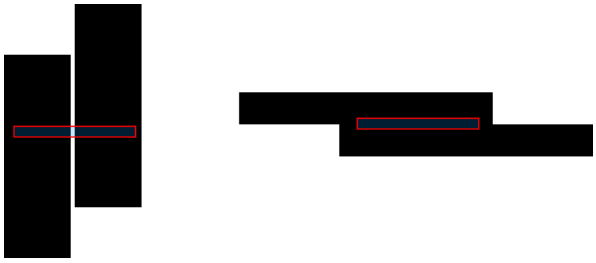

Figure 5.38: Design of the chips. Reservoir chip on the left and Channel chip on the right. In the Reservoir chips the electrodes are separated by 1 mm, whereas they are separated from about 200 μm in the Channel chips. The channel is represented by the grey rectangle

parallel to the channel. The distance between the two electrodes is about 200 μm . The useful size of one electrode is then 22 mm by 400 μm , which gives a surface area of about 9 μm^2. The useful electrode surface between the two designs is then similar.

Frequency response

The frequency response of the different designs was measured with the channel filled with PBS 10 mM, for frequencies ranging from 1 Hz to 1 MHz.

Figure 5.39 presents the absolute value of the imaginary part of the admittance for the channel design, the reservoir design in channel and the reservoir design in a 6 mm reservoir filled with 90 μL of PBS. It can be seen at low frequencies that the values of the imaginary part of the admittance are similar for all the chips, as the electrode area is comparable between each chip. The surface capacitance of all the chips is then roughly the same. However, the behaviour of each design differs notably at high frequencies, as the resonance of the reservoir chip in channel is not as much defined as the resonance of the two other designs. The value of the imaginary part of the admittance from 1 KHz to 1 MHz for the channel chip is also higher than those of the reservoir chip in a reservoir. The resonance appearance depends on the resistance of the reservoir or of the channel. These facts would mean that the channel resistance of the reservoir chip in channel is very high.

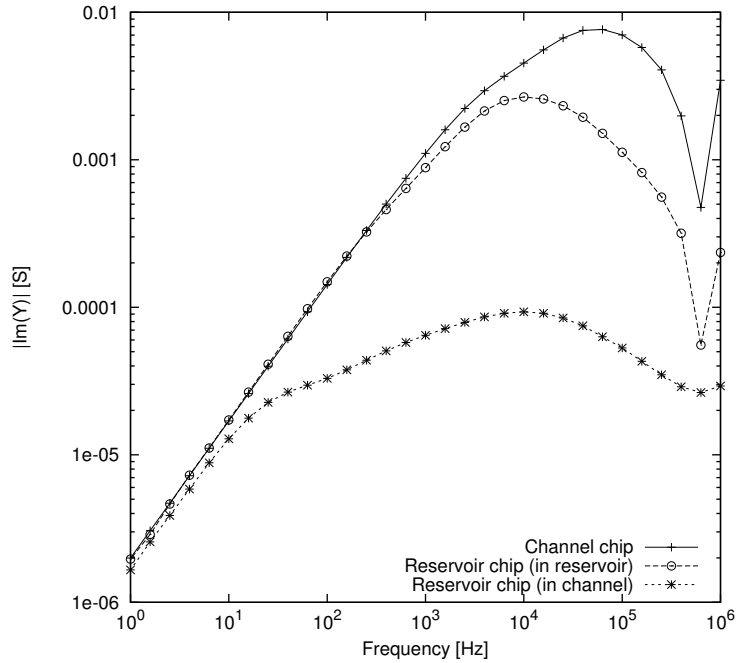

Figure 5.39: Imaginary part of the admittance spectra against the frequency for three different design : A chip design, a reservoir design in a channel and a reservoir design in a reservoir of 6 mm diameter.

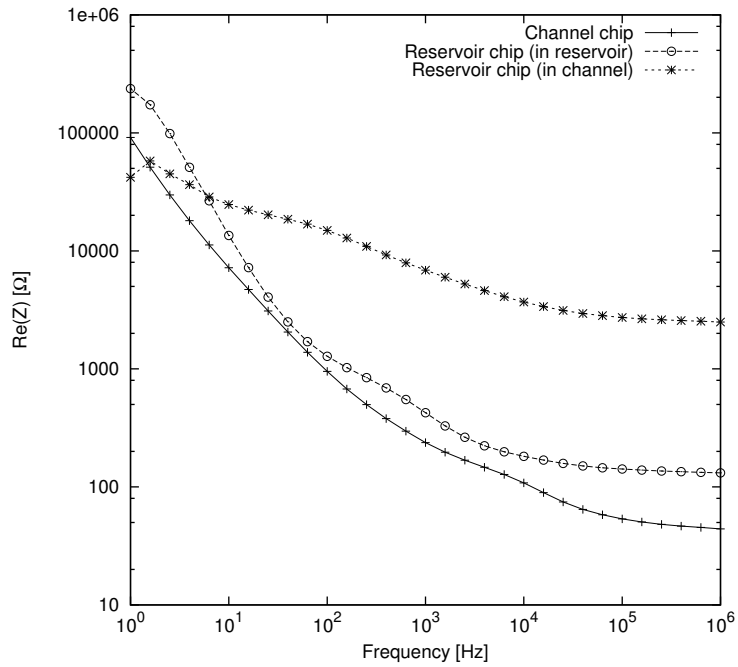

Figure 5.40: Real part of the impedance spectra against the frequency for three different designs : A chip design, a reservoir design in a channel and a reservoir design in a reservoir of 6 mm diameter.

This fact is confirmed by Figure 5.40, where the resistance value for the reservoir chip in channel is 2 kΩ at 1 MHz. This value is in the same order as for a reservoir of 6 mm filled with 5 mM KCl. The channel being filled with a 10 mM PBS solution, the high resistance value is due to the design. The channel height being 300 μm and the electrode width being 10 mm, the Gq number value is 2.8x10^{-2}, meaning that a huge part of the electrode has no effect at high frequencies. These facts mean that the channel resistance area is extremely small and leads to a very high channel resistance.

The resistance value for the channel chip design is on the contrary lower than those for the reservoir chip in a 6 mm diameter reservoir. The value of Gq is equal to 0.6, which results in the electrode signal being much more used than in the reservoir in channel design. The channel length being equal to 22 mm instead of 1 mm for the reservoir in channel design, the channel design resistance is extremely low.

5.7 Conclusion

Aluminium electrodes covered by a nanometric alumina layer provide a strong capacitance that might be used to detect the adsorption of species such as proteins. In a first step, the face-to-face and coplanar designs of the electrodes were studied in a small plastic box to get rid of the perturbations induced by the holders. A discrete model based on transmission lines was developed to understand the response of the sensor across frequencies ranging from 1 Hz to 1 MHz. As with the microchip, it could be observed that the behaviour of the sensor was mostly capacitive at low frequencies and resistive at high frequencies. However, contrary to the microchip, the presence of a resonance could be observed at high frequencies, dependant on the capacitance created by the electrodes, the reservoir resistance and the value of inductance created by the connectors and the electrodes. The resonance peak position was also influenced

by the distance between the electrodes in the case of the coplanar design, as the time constant at high frequencies are dependant on the electrodes geometry.

In a second step, the electrodes were mounted in a holder equipped with a 6 mm or 12 mm diameter reservoir for the coplanar design. The influence of parameters such as the solution conductivity in the reservoir, the electrode surface area, and the volume of solution in the reservoir were studied for the face-to-face design. Both face-to-face and coplanar designs were found to have a linear response with respect to the solution conductivity and their response was proportional to the electrode surface area. The face-to-face design response was also proportionnal to the volume of the solution present in the reservoir for the whole frequency range. However, in the case of the coplanar design, the capacitance created by the electrodes at low frequencies did not change when increasing the volume of solution in the reservoir. This was not the case at high frequencies where the reservoir resistance was found to decrease when increasing the volume, until a solution height equal to the reservoir diameter was reached. As the discrete model could not be used to describe the coplanar design behaviour in a reservoir, a new model using CPE elements was proposed.

Finally, the coplanar design in a channel was studied. A new design of the electrodes was developed, as the electrodes needed to be placed parallel to the channel rather than perpendicular to it in order to maximize the quality of the signal at high frequencies.

Bibliography

[1] S. Kumbhat et al. "Surface plasmon resonance based immunosensor for serological diagnosis of dengue virus infection". In: *Journal of Pharmaceutical and Biomedical Analysis* 52.2 (2010), pp. 255–259.

[2] S. Scarano et al. "Surface plasmon resonance imaging for affinity-based biosensors". In: *Biosensors and Bioelectronics* 25.5 (2010), pp. 957–966.

[3] S.D. Mazumdar et al. "Surface plasmon resonance (SPR) as a rapid tool for serotyping of Salmonella". In: *Biosensors and Bioelectronics* 25.5 (2010), pp. 967–971.

[4] H. Li et al. "Continuous immunoassay for sulfamethazine by surface plasmon resonance-based biosensor". In: *Analytical Letters* 43.3 (2010), pp. 499–507.

[5] J.S. Rossier et al. "Microfluidic based immunoassay". In: *Nanobiotechnology* 1.3 (2005), pp. 311–312.

[6] Y.-H. Yun et al. "A label-free electronic biosensor for detection of bone turnover markers". In: *Sensors* 9.10 (2009), pp. 7957–7969.

[7] O. Laczka et al. "Detection of Escherichia coli and Salmonella typhimurium using interdigitated microelectrode capacitive immunosensors: The importance of transducer geometry". In: *Analytical Chemistry* 80.19 (2008), pp. 7239–7247.

[8] N. Puri et al. "Electrochemical characterization of surface modified gold electrode for the detection of C-reactive protein". In: *International Journal of Integrative Biology* 9.1 (2010), pp. 1–5.

[9] M.B. Mejri et al. "Electrochemical impedance spectroscopy for specific detection of enterovirus". In: *Sensor Letters* 7.5 (2009), pp. 896–899.

[10] Digby D. Macdonald and Mirna Urquidi-Macdonald. "Kramers-kronig transformation of constant phase impedances". In: *Journal of the Electrochemical Society* 137.2 (1990), pp. 515–518.

[11] J. Bisquert et al. "Impedance of constant phase element (CPE)-blocked diffusion in film electrodes". In: *Journal of Electroanalytical Chemistry* 452.2 (1998), pp. 229–234.

[12] C. Belmont and H.H. Girault. "Coplanar interdigitated band electrodes for synthesis Part I: Ohmic loss evaluation". In: *Journal of Applied Electrochemistry* 24.6 (1994), pp. 475–480.

[13] B. Chaoudhary. *The Elements of Complex Analysis, 2nd Edition*. 2nd ed. Wiley-Interscience, Oct. 1993. ISBN: 047022116X.

[14] A. Bansal, B.C. Paul, and K. Roy. "An analytical fringe capacitance model for interconnects using conformal mapping". In: *IEEE Transactions on Computer-Aided Design of Integrated Circuits and Systems* 25.12 (2006), pp. 2765–2774.

[15] M. Villarino. "A note on the accuracy of Ramanujan's approximative formula for the perimeter of an ellipse". In: *Journal of Inequalities in Pure and Applied Mathematics* 7.1 (2006), pp. 1–10.

[16] J.-B. Jorcin et al. "CPE analysis by local electrochemical impedance spectroscopy". In: *Electrochimica Acta* 51.8-9 (2006), pp. 1473–1479.

[17] Girault. *Electrochimie physique et analytique*. PPUR, 2007.

[18] Y. Kobayashi and M. Katoh. "Microwave Measurement of Dielectric Properties of Low-Loss Materials by the Dielectric Rod Resonator Method". In: *Microwave Theory and Techniques, IEEE Transactions on* 33.7 (1985), pp. 586–592. ISSN: 0018-9480. DOI: 10.1109/TMTT.1985.1133033.

[19] V. Mikhaelashvili et al. "Electrical characteristics of metal-dielectric-metal and metal-dielectric-semiconductor structures based on electron beam evaporated Y2O3, Ta2O5 and Al2O3 thin film". In: *Journal of Applied Physics* 84.12 (1998), pp. 6747–6752.

[20] J. Krupka et al. "A dielectric resonator for measurements of complex permittivity of low loss dielectric materials as a function of temperature". In: *Measurement Science and Technology* 9.10 (1998), pp. 1751–1756.

[21] A. Charlesby. "Ionic current and film growth of thin oxide layers on aluminium". In: *Proceedings of the Physical Society. Section B* 66.4 (1953), pp. 317–329.

Chapter 6

Aluminium chips : Immunosensor

6.1 Introduction

Despite having optimized both holder and chip designs in Chapter 4, the microchip was not able to detect any adsorption, but only channel conductivty. Thus, the PET microchip was dropped to move to aluminium chips, whose design was studied in Chapter 5. The thin alumina layer may enable the detection of an adsorption[1–3], as the relatively high capacitance of the alumina layer might let the electrical-double-layer capacitance variations observable. Most of the geometry effects were studied in Chapter 5. The sensor response was found to be dependent on the applied frequency. It is mostly capacitive at low frequencies and resistive at high frequencies. A resonance was found at high frequencies. This resonance relies on the surface capacitance, the inductance of the wires and the resistance of the channel. The adsorption process might theoreticaly be observed at a low frequencies or around the resonance. Keeping the goal of the Allergy Card project, the development was aimed at a low cost device that would be used only once. In this context, the adsorption of species was studied, but the adsorption reversibility was not. The research of the best frequency to monitor the adsorption, but also the ability of the sensor to monitor an adsorption, is studied.

6.2 Theory

6.2.1 Langmuir isotherm

In most biosensors, the recognition event, such as an antigen-antibody reaction, occurs between a molecule in the sample solution and the receptor adsorbed on a solid support. The relation between the adsorbate surface concentration Γ [mol.m^{-2}] and the bulk concentration C^0 [mol.L^{-1}] is called the adsorption isotherm [4]. The most used isotherm in immunosensing is the Langmuir isotherm, based on the following hypothesis:

- The adsorption is reversible
- The properties of the molecules are constant, even after the adsorption.
- The surface is defined by a number of adsorption sites, whose concentration is defined by Γ_{max} [mol.m^{-2}].
- The adsorption sites have the same affinity for the adsorbate molecules.
- Each active site adsorbs only one molecule.
- No lateral interaction between the adsorbed molecules.

The reaction of adsorption can be written as:

$$\text{Free site + molecule in solution} \underset{k_{off}}{\overset{k_{on}}{\rightleftharpoons}} \text{Adsorbed molecule}$$

with k_{on} [m^3.mol^{-1}.s^{-1}] and k_{off} [s^{-1}] being the rate of adsorption and desorption of the adsorbate onto the active sites. At a time t, the surface concentration of free sites is $\Gamma_{max} - \Gamma(t)$. The system kinetics can then be described as:

$$\frac{d\Gamma(t)}{dt} = k_{on}C(t)(\Gamma_{max} - \Gamma(t)) - k_{off}\Gamma(t) \tag{6.1}$$

The adsorption equilibrium constant K can be defined by:

$$K = \frac{k_{on}}{k_{off}} = \frac{\Gamma_{eq}}{(\Gamma_{max} - \Gamma_{eq})} \tag{6.2}$$

with Γ_{eq} being the adsorbate surface concentration at the equilibrium, when $\frac{d\Gamma}{dt}$=0. Equation 6.2 can also be written as follows[5] :

$$\frac{\Gamma_{eq}}{\Gamma_{max}} = \frac{KC^0}{1 + KC^0} = \frac{\psi}{1 + \psi} \tag{6.3}$$

where $\psi = KC^0$ can be seen as an indicator of the capacity of the system to reach the maximum surface coverage.

6.2.2 Kinetic controlled adsorption

The surface coverage ratio θ can be described as:

$$\theta = \frac{\Gamma(t)}{\Gamma_{max}} \tag{6.4}$$

The law for adsorption (Equation 6.1) can then be described as the difference between the adsorption and the desorption, such as:

$$\frac{d\theta}{dt} = k_{on}C^0(1 - \theta) - k_{off}\theta \tag{6.5}$$

which leads to:

$$\frac{d\theta}{dt} + \theta(k_{on}C^0 + k_{off}) = k_{on}C^0 \tag{6.6}$$

Solving Equation 6.6, we get:

$$\theta = \frac{k_{on}C^0}{k_{on}C^0 + k_{off}} \left[1 - exp[-(k_{on}C^0 + k_{off})t]\right] \tag{6.7}$$

As $K = k_{on}/k_{off}$ and $\psi = KC^0$, Equation 6.7 becomes:

$$\theta = \frac{\psi}{1+\psi}\left[1 - exp(-t/\tau)\right] \tag{6.8}$$

with τ the adsorption time constant, defined by:

$$\tau = \frac{1}{k_{on}C^0 + k_{off}} \tag{6.9}$$

As the goal of this work is to create an immunosensor, the desorption process will not be studied.

6.2.3 Diffusion controlled adsorption

Damkohler number

The Damkohler number caracterizes the regime of the adsorption . It is defined by Da such as

$$Da = \frac{k_{on}\Gamma_{max}\delta}{D} \tag{6.10}$$

with δ being the diffusion length [m]. δ can be defined as[6]:

$$\delta = (Dt)^{1/2} \tag{6.11}$$

When $Da >>1$, the kinetic is diffusion controlled. When $Da <<1$, the kinetic is reaction controlled.

Fick's laws

The first Fick's law is:

$$J = -D\frac{\partial c}{\partial x} \tag{6.12}$$

While Fick's second law is:

$$\frac{\partial c}{\partial t} = D\frac{\partial^2 c}{\partial x^2} \tag{6.13}$$

When the adsorption process is limited by the diffusion (Da >1), we have to solve Fick's second law. To solve this equation analytically, the Langmuir isotherm has to be linearized, leading to the assumption that $\Gamma_{eq} << \Gamma_{max}$ (small surface coverage). Thus, ψ <<1 and Equation 6.2 can be linearized as[4] :

$$\Gamma_{eq} = KC^0\Gamma_{max} \tag{6.14}$$

Fick's second law can then be solved analytically [4], leading to :

$$\frac{\Gamma(t)}{\Gamma_{eq}} = 1 - exp\left(\frac{Dt}{K^2\Gamma_{max}^2}\right) erfc\left(\frac{(Dt)^{1/2}}{K\Gamma_{max}}\right) \tag{6.15}$$

where $erfc$ is the complementary error function. Equation 6.15 might ideally be used when ψ <<1. Nevertheless this equation can be used as an approximation in the case of a full surface coverage adsorption limited by the diffusion. More details about the resolution of this equation can be found in Appendix F.

6.3 Materials

6.3.1 Measurement

Impedance data were recorded with a Solartron 1296 Dielectric interface (Ametek, UK) coupled to a Solartron 1255B Frequency Response Analyser (FRA).

6.3.2 Holders

The holders were made of two parts, both composed of PEEK material (Figure 5.11). The dimensions of the top part were of 40 mm length, 20 mm width and 10 mm height. These dimensions were the same for the bottom part. One hole was drilled at each corner of the holder to maintain the top and the bottom part firmly screwed. A hole of 6mm diameter was drilled in the center of the top part of the holder. A 8 mm inner diameter toric gasket was integrated in the top part of the first holder.

6.3.3 Solutions

KCl solutions of various concentrations were diluted from a stock 1 M KCl solution made from KCl powder (Sigma Aldrich, Switzerland), diluted in 500 mL of ultrapure water (MilliQ, USA).
Phosphate Buffered Saline (PBS) solution was prepared from 137 mM of NaCl (Sigma Aldrich, Switzerland), 2.7 mM KCl (Sigma Aldrich, Switzerland), and 10 mM Na_2HPO_4 (Sigma Aldrich, Switzerland). The solution was then adjusted to pH 7.4 with a solution of NaOH (Sigma Aldrich, Switzerland). BSA solutions were prepared from a mother solution concentrated of 400 mg of BSA (Sigma-Aldrich, Switzerland) diluted on 10 mL of solution of PBS. Anti-Milk IgG (Abcam GmBH, Germany) were directly injected in the reservoir. Anti-β-lactoglobulin IgG (Acris GmBH, Germany) were diluted in the PBS solution, at various concentrations depending on the experiment. The IgG concentration of the mother solution was unknown. β-lactoglobulin (Sigma-Aldrich, Switzerland) solution was prepared by diluting the mother solution of β-lactoglobulin in the PBS solution.

6.4 First layer detection

6.4.1 One step adsorption

It was shown in Chapter 5 that surface phenomena were located at low frequencies. As adsorption is a surface phenomenon, the best way to measure it should be to work at low frequencies. The problem with low frequencies is that the capacitance does not have the same behaviour from one chip to another : This comes from the electrodes surface and from the chip construction that is not always exactly the same for each chip. The result is that at a given frequency, the measured signal can be a capacitance for one chip and a transition from one capacitance to an other one, or a resistance, for another chip. In the other way, the resonance can be exploited to monitor the surface capacitance of the sensor, as its behaviour is always the same.

Face-to-face

The first step before recording an adsorption is to choose at which frequency to record. Two choices can be done to record an adsorption :

- The first one is to record a frequency spectrum from 1 Hz to 1 MHz with 5 points per decade and repeat it until the end of the experiment. The advantage of this approach is to have all the information about the sensor behaviour at every frequency. The main drawback is that one point is recorded every minute at the same frequency. This leads to a poor temporal resolution that can be acceptable for very slow phenomena but is not suited for quick phenomena like the beginning of the adsorption, or some adsorptions where the equilibrium is quickly reached.

- The second choice is to record the adsorption at a fixed frequency previously

determined from some frequency spectra. The advantage and the drawbacks are inverted from the previous choice : The temporal resolution is 2 seconds, but the information about the behaviour of the sensor at all the other frequencies is lost.

The first choice is certainly the best to discover the properties of a sensor and find the right parameters to record an adsorption. The second choice is the best to monitor an adsorption when the parameters are known. It permits a better time resolution and signal dynamics.

For this experiment, the spectra were recorded from 1 Hz to 1 MHz with 5 points per decade.

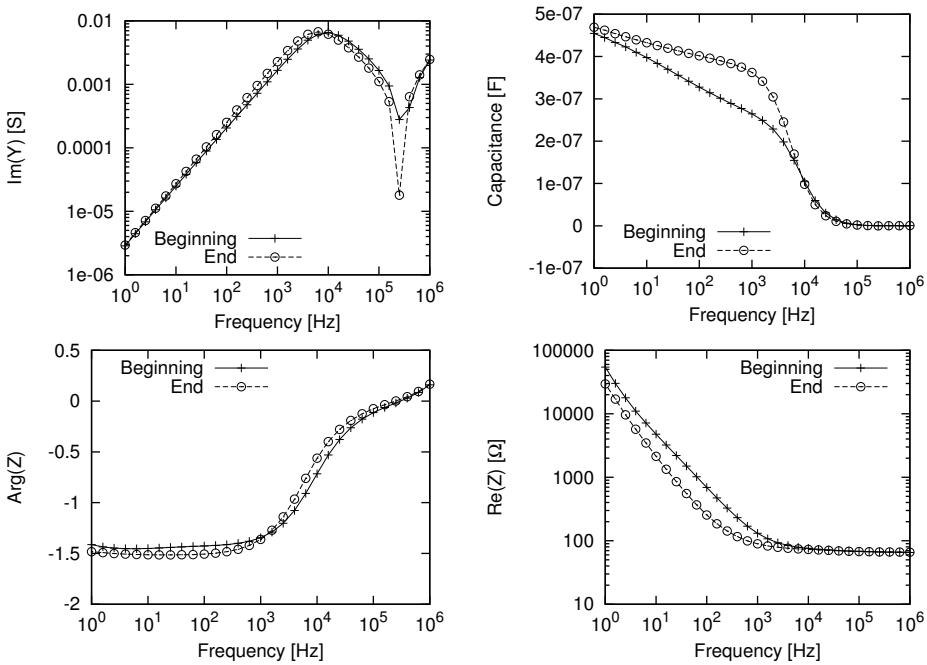

Figure 6.1: Spectra of the beginning and the end of an adsorption experiment of a 13.3 mg.mL^{-1} BSA solution in a reservoir using a face-to-face design.

Figure 6.1 describes the sensor state at the beginning and at the end of a BSA adsorption experiment. 300 μL of 10 mM PBS were injected in the reservoir. After acquiring for 5 minutes, 100 μL of PBS were removed and replaced by 100 μL PBS + 40 mg.mL^{-1} BSA, giving a final 13.3 mg.mL^{-1} BSA concentration. Normally, the pH 7.4

of the PBS solution might enable the BSA to adsorb on the alumina [7].

At the beginning of the experiment, the sensor is not completely capacitive at low frequencies as the phase value is -1.45 rad. This observation is confirmed by the fact that the capacitance seen on the capacitance diagram from 1 Hz to 1 KHz is far to be flat. The resonance frequency peak can be determined to be around 400 KHz.
At the end of the adsorption, the phase has decreased to -1.5 rad at 100 Hz. The sensor is then globally more capacitive. This is illustrated on the capacitance plot between 1 Hz and 1 KHz : Its value is higher and its slope closer from an horizontal curve. The resonance peak position also moved to a lower frequency. This is due to an increment of the effective capacitance, that might be directly linked to the phase value variation. The variation of the resonance peak frequency was also observed by Moreno & al when adsorbing DNA on interdigitated aluminum/alumina electrodes [8].

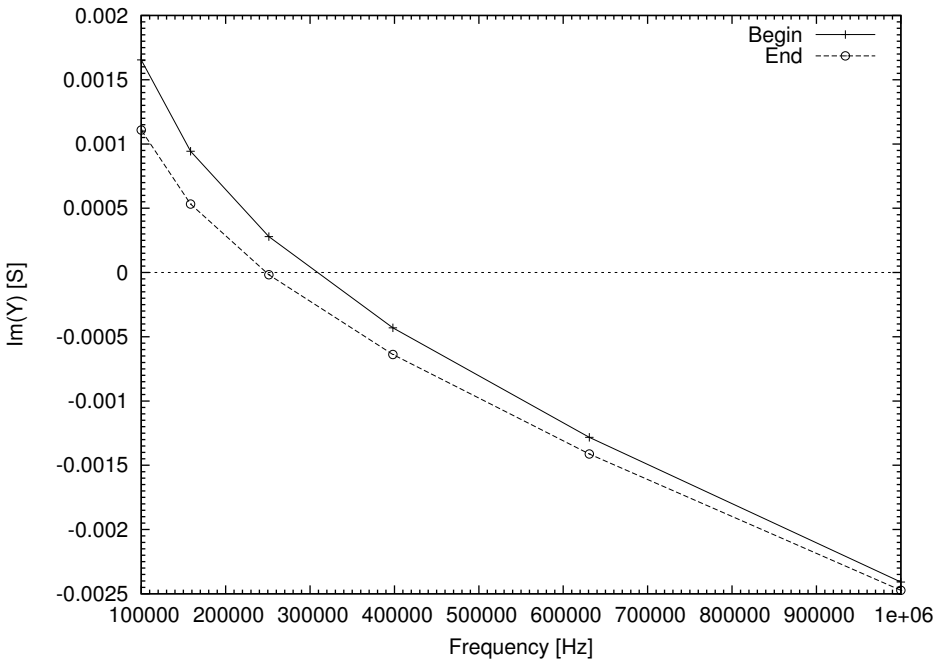

Figure 6.2: Imaginary part of the admittance with respect to the frequency from 100 kHz to 1 MHz, presenting the beginning and the end of an adsorption of BSA. The plots are close to be linear.

The resonance frequency shift may also be observed on Figure 6.2, which only

shows the imaginary part of the admittance around the resonance. It can be observed that contrary to the absolute imaginary part of the admittance plotted on Figure 6.1, the evolution around the resonance is close to be linear. However, the absolute imaginary part of the admittance is prefered. It is actually more convenient to directly observe a peak shift than finding a zero. Figure 6.1 also has the advantage of presenting the low frequency capacitance on the same plot than the resonance, thus offering the possibility to observe all the capacitance shifts generated by an adsorption. Many different plots are presented in Appendix E. From all these plots, the most relevant might be the imaginary part of the admittance, the capacitance, the phase angle and the real part of the impedance. The other plots were considered redondant to the formers or presenting less interest.

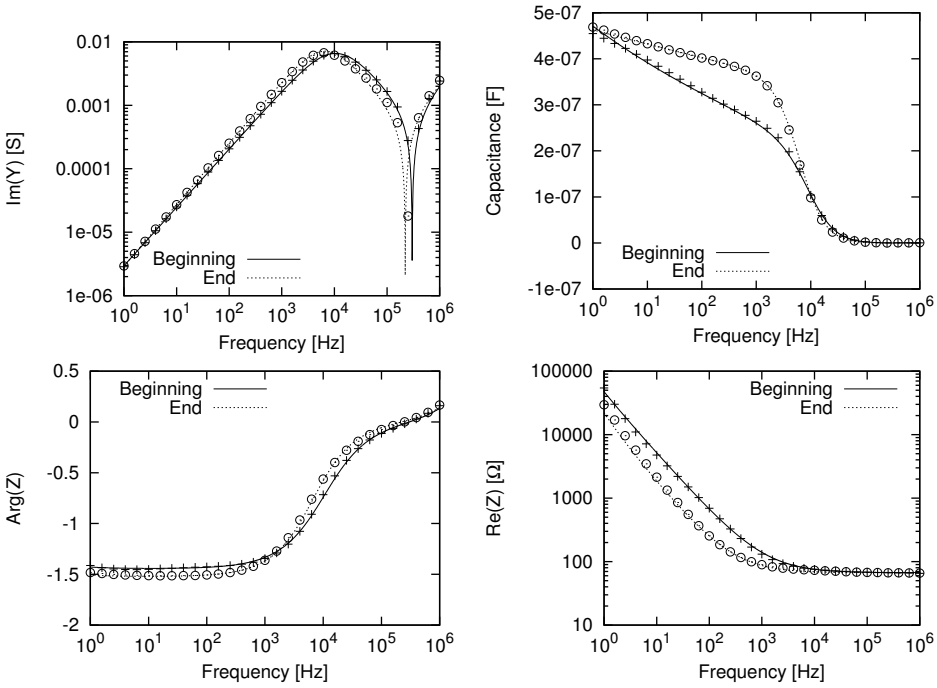

Figure 6.3: Fits of the spectra of the beginning and the end of an adsorption experiment of a 13.3 mg.mL^{-1} concentrated solution of BSA in a reservoir using a face-to-face design. The power coefficient of the CPE increases while the capacitance decreases a few. Compared to Figure 6.1, the fit shows precisely the resonance peak, which is a crucial parameter.

Fitting the experimental data (Figure 6.1) with the model defined in 5.14 gives a

Parameter	Beginning	End
α	0.92	0.97
C_{surf} [nF]	1100	980
R_{Alu} [Ω]	10^7	10^7
R_{sol} [Ω]	67	67
L [μH]	0.8	0.8

Table 6.1: Fit parameters between the beginning and the end of the adsorption of 13.3 mg.mL^{-1} BSA using a face-to-face design in reservoir.

good understanding of the sensor behaviour when adsorbing species. The fit parameters can be found in Table 6.1. The main differences between the beginning and the end of the experiment are phase value and capacitance variations at low frequencies, but also a lower resonance peak frequency. It can be found from the fit a variation of the CPE power parameter α, from 0.92 to 0.97, but also a variation of the capacitive term of the CPE, decreasing from 1100 nF to 980 nF. The power coefficient variation is responsible for the lower value of the phase at low frequencies, but also for the less pronounced slope of the capacitance at low frequencies. The lower capacitive term value of the CPE might be the result of a lower relative permittivity of the electrical double-layer when adsorbing the species. Capacitance has been found to change through the relative permittivity variation of the electrical double-layer.[8–11]. Following the buffer and the species, this variation can be positive or negative. The higher CPE value could be due to a distribution of local RC time constants modified by the adsorption of the species[12, 13]. Despite a lower capacitive coefficient, the increment of the CPE power parameter (α) makes the effective capacitance value higher. This results in a global higher capacitance value at low frequencies, but also by the resonance peak shift to lower frequencies.

One frequency has to be chosen among the frequency range to plot the result of the adsorption. Figure 6.4 presents the adsorption taken at a 100 Hz. This frequency was

chosen among all the other frequencies from 1 Hz to 1 KHz : It is preferable to take the frequency where the difference between the beginning and the end of the experiment is the most important. However it is also important for this frequency to be in the range where the sensor is capacitive, that is to say from 1 Hz to 300 Hz. The capacitance variation is less important at 100 Hz than at 1 kHz, however the phase variation being maximum at 100 Hz, this frequency might be the best to record the adsorption among all the low frequency range. The adsorption begins at the 5th minute and follows a rate limited by the diffusion.

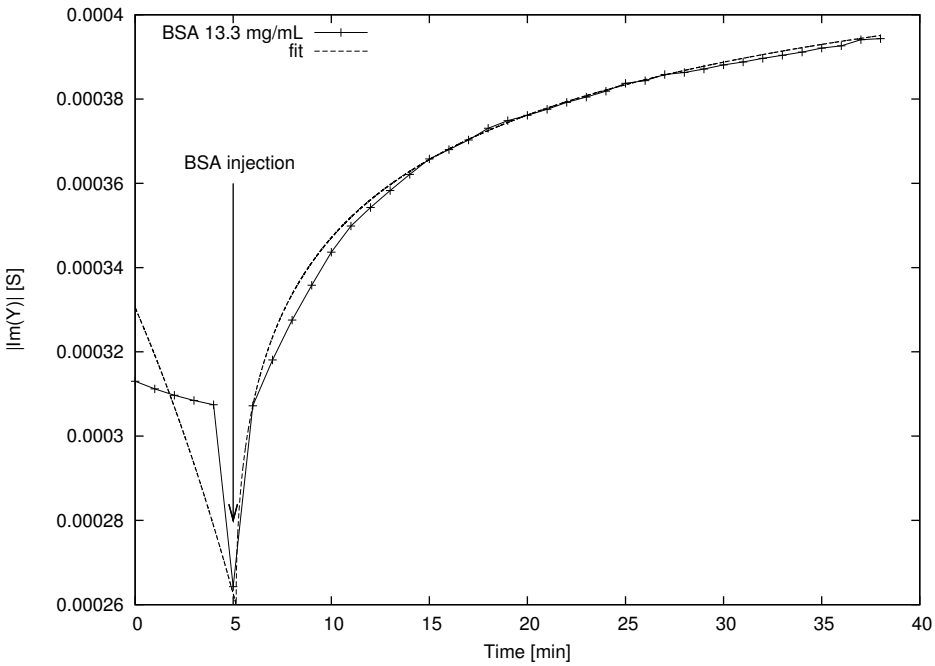

Figure 6.4: Sensogram of an adsorption of 13.3 mg.mL^{-1} BSA recorded at 100 Hz.

From the K value found in 6.4.3, ψ was equal to 17.3. However, data were fitted with Equation 6.15. The diffusion constant of the BSA goes from 3.4×10^{-11} m^2.s^{-1}[14] to 6.9×10^{-11} m^2.s^{-1}[15], depending on the temperature and the solution concentration. Given a room temperature of about 300 K and the solution concentration, a diffusion constant of 6×10^{-11} m^2.s^{-1} was taken. $K\Gamma_{max}$ was fitted as 2x10^{-4} m. Using the k_{on} constant found in 6.4.3, the Γ_{max} value found in 6.4.3, and the diffusion length cal-

culated at 10 minutes using Equation 6.11 with D=6$\times$10$^{-11}m^2.s^{-1}$, Da was evaluated equal to 652. The kinetic is then diffusion controlled and the use of Equation 6.15 is justified, although this high ψ value might result in an important error of the $K\Gamma_{max}$ value.

The adsorption can also be monitored at a higher frequency, using the resonance. The best and simple way to monitor the adsorption using the resonance would be to monitor the resonance peak frequency. As the Solartron interface is not fast enough to work with this method, the adsorption has to be monitored at a fixed frequency to improve the temporal resolution. This frequency might be fixed at a point where the capacitance variation does not make this frequency being out of the resonance frequency range. The ideal point to record the adsorption is around the resonance peak, as the imaginary part of the admittance variation with respect to the frequency is the highest. A comfortable method is to fix the frequency at a higher frequency than the resonance peak. Taking the absolute value of the imaginary part of admittance will make the sensogram looking like those obtained with the SPR technique[16, 17]. However to reach the best sensitivity it might be more advised to fix the frequency at a lower value than the resonance peak. On Figure 6.5 the frequency was fixed at 250 KHz. Like on Figure 6.4 the adsorption begins after the injection of the BSA at the 5th minute. It can be observed that the value of the imaginary part of the admittance decreases. As can be seen on Figure 6.3, the effective capacitance increases when the BSA adsorbs on the sensor, shifting the resonance to lower frequencies. So the value of the imaginary part of the admittance when monitoring at a frequency lower than those of the resonance peak will decrease.

Unfortunatelly, Figure 6.5 cannot be fitted by Equation 6.15. It nevertheless shows that monitoring the adsorption using the resonance provides the same information than using the surface capacitance.

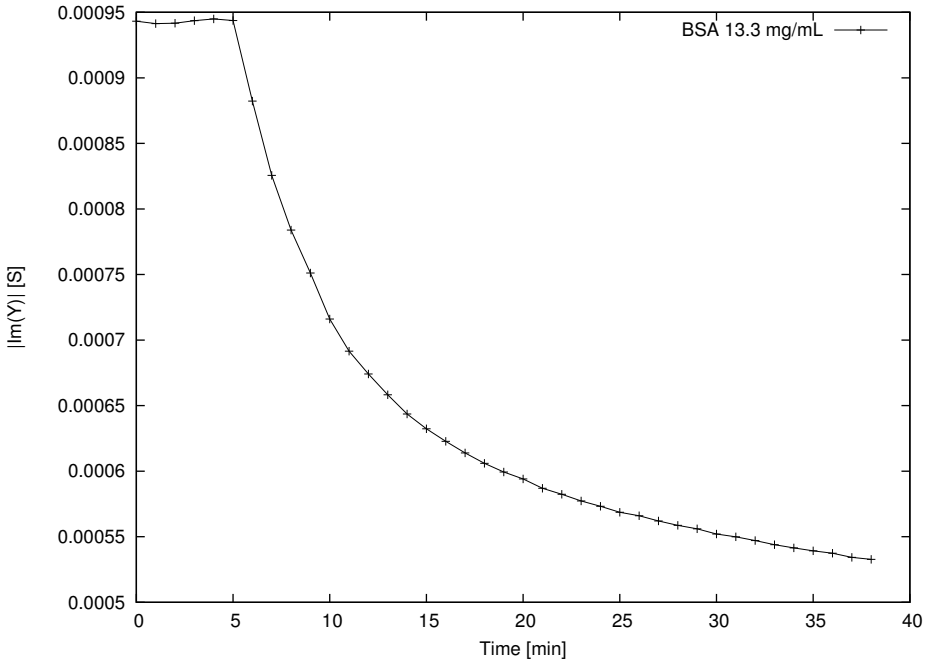

Figure 6.5: Sensogram of an adsorption of 13.3 mg.mL^{-1} concentrated BSA solution recorded at 250 kHz.

Coplanar design in reservoir

The experiments using a coplanar design in reservoir are similar to those running a face-to-face design. The main differences are involved by the supplementary effects due to the coplanar design itself. The influence of the edge effects between the inner part of the electrodes is more pronounced.

The first kind of experiment run on the coplanar design sensor was BSA experiments to study the sensor behaviour when adsorbing some species on it.

60 μL of a PBS 10 mM were injected inside the reservoir. A spectrum was recorded from 1 Hz to 1 MHz with 5 points per decade. Then another spectrum was recorded from 400 KHz to 1 MHz with 100 points per decade to gain some resolution around the resonance, and was assembled with the first spectrum. Contrary to the face-to-face design, the experiments were run at a fixed frequency chosen from the latest spectrum in order to improve the temporal resolution. The acquisition was launched at a frequency of 980 KHz and after two minutes, the PBS was replaced by 60 μL of BSA concentrated

at 40 mg.mL^{-1} . The BSA was adsorbed for 2 hours and 45 minutes.

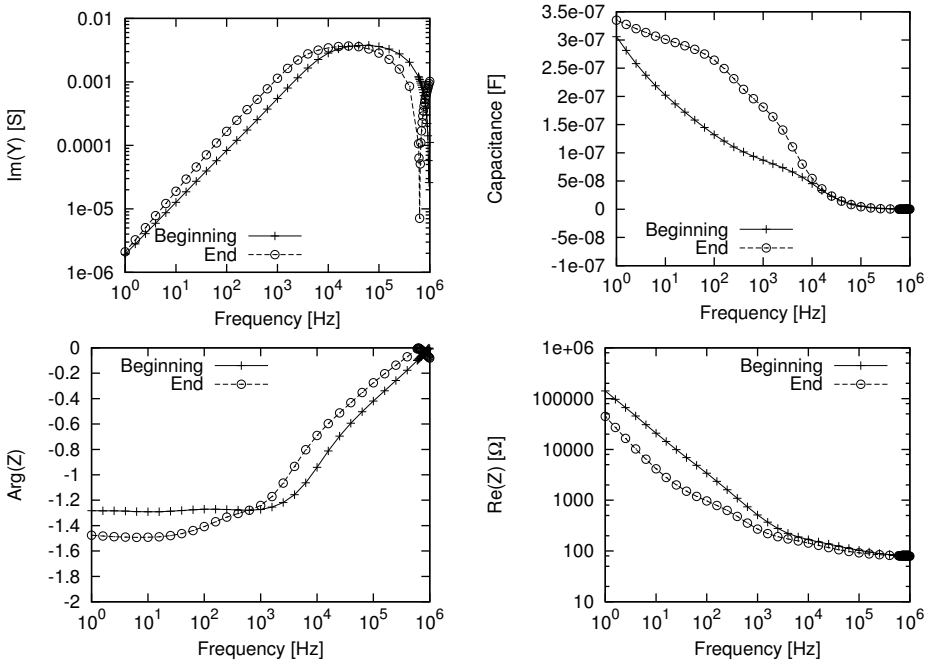

Figure 6.6: Adsorption of BSA 40 mg.mL^{-1} using a coplanar design.

Figure 6.6 presents the spectra of the beginning and the end of a 40 mg.mL^{-1} BSA adsorption. Like with the face-to-face design, the resonance peak was shifted from more than 1 MHz to 631 KHz. As the volume of solution in the reservoir was the same between the beginning and the end of the adsorption, the variation does not come from the geometry of the sensor (including the solution). The resonance peak frequency variation is, like with the face design, due to the variation of the surface CPE power coefficient. It can be observed that the signal at low frequency is far less perfect than for the face-to-face design.

The BSA adsorption sensogram was plotted on Figure 6.7. To get a more accurate $K\Gamma_{max}$ value that those found fitting Figure 6.4, the data were linearized using a home-made linearizer program (Appendix B) : When adsorbing species, the resonance shifts to lower frequencies. As the resonance evolution at one frequency is not absolutely linear, the sensogram presents the same error and would preferably be corrected to fit an adsorption law. The linearizer transposes each recorded point position in resonance

peak frequency, using the model described in 5.5.4. This gives the effective capacitance for each point. The reaction being diffusion controlled like in 6.4.1, the corrected points were fitted using Equation 6.15, illustrated by the dashed line, with D=6$\times$10$^{-11}m^2.s^{-1}$ and $K\Gamma_{max}$ = 7.14x10^{-4} m.

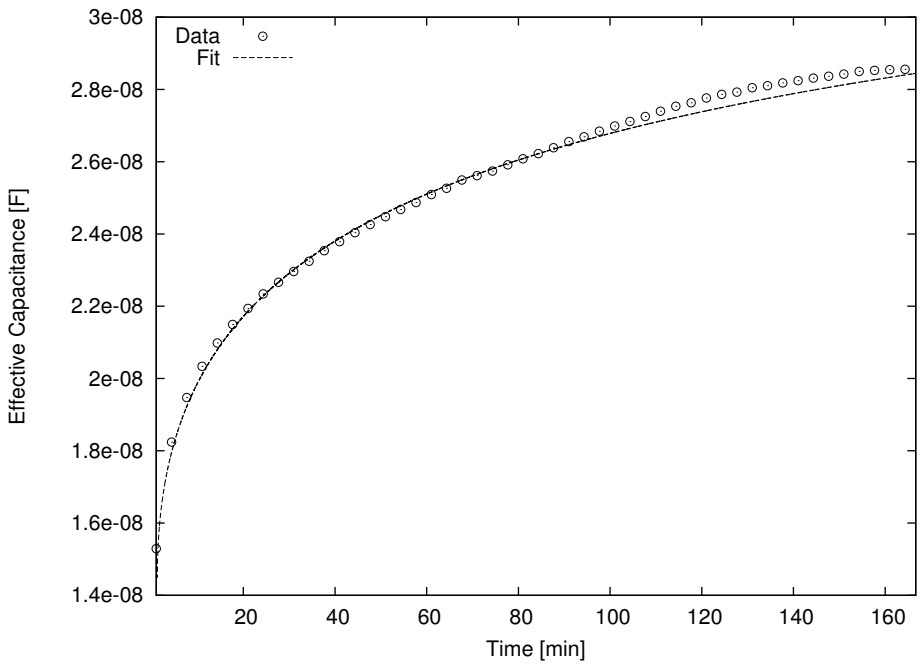

Figure 6.7: Plot of a BSA 40 mg.mL^{-1} adsorption with data matched to the adsorption peak using the program presented in Appendix B.

Inter-electrodes gap variation

Figure 6.8 presents the result of a BSA 40 mg.mL^{-1} adsorption on three sensors with a different distance between the electrodes. It can be seen that the signal amplitude increases with a reduced gap value. However, this gain sacrifices the acquisition stability as the imaginary part of the admittancediverges after 10000 s for a 400 μm and lower gap, instead of reaching an equilibrium.

The amplitude gain might be due to the edge effect between the two electrodes becoming stronger when the gap between the two electrodes decreases. This increases

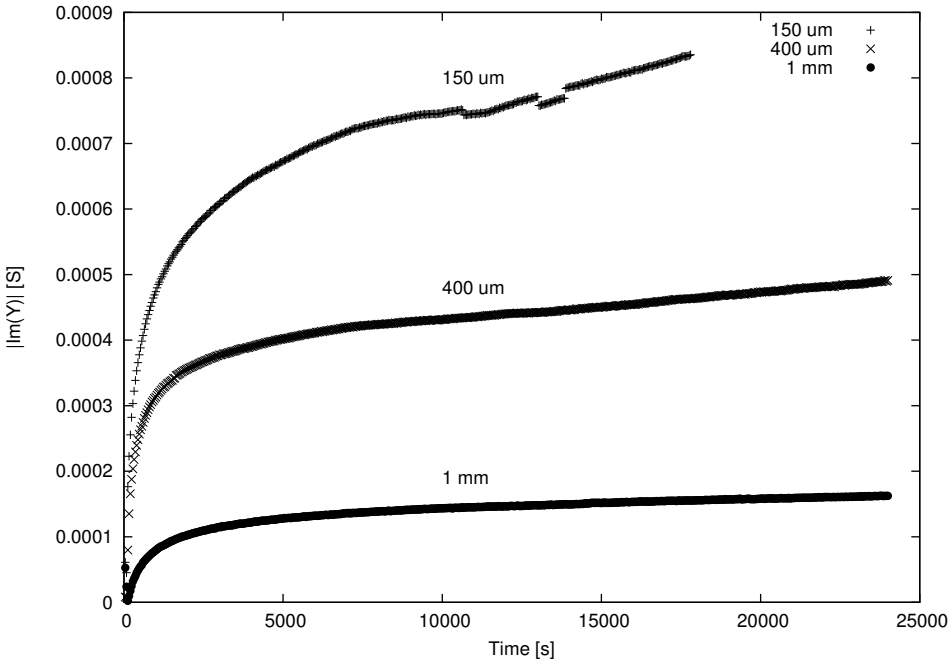

Figure 6.8: Adsorption of BSA 40 mg.mL^{-1} on three sensors with a different distance between the electrodes

the value of the inter-electrodes capacitance and thus the sensitivity.

6.4.2 Multistep adsorption

One adsorption step has been shown to work, as BSA was detected. However this could likely just be a species deposition on the surface that could be cleaned by washing the reservoir. In that case, it is important to study the adsorption of a diluted BSA solution after several washes. Figure 6.9 presents the results of multiple 0.67 mg.mL^{-1} BSA adsorptions in a 12 mm diameter reservoir. 300 μL of PBS were injected in the reservoir. After acquiring a baseline during 30 minutes, 100 μL of PBS was removed and replaced by 2 mg.mL^{-1} BSA, resulting in a 0.67 mg.mL^{-1} BSA solution. The acquisition continued for 200 minutes. The reservoir was washed three times with PBS. Like before, a baseline was acquired for 30 minutes, then 100 μL of BSA was injected for 950 minutes after having removed 100 μL of PBS. The reservoir was washed again three times with PBS and 100 μL of BSA was injected like before after 40 minutes of

baseline acquisition.

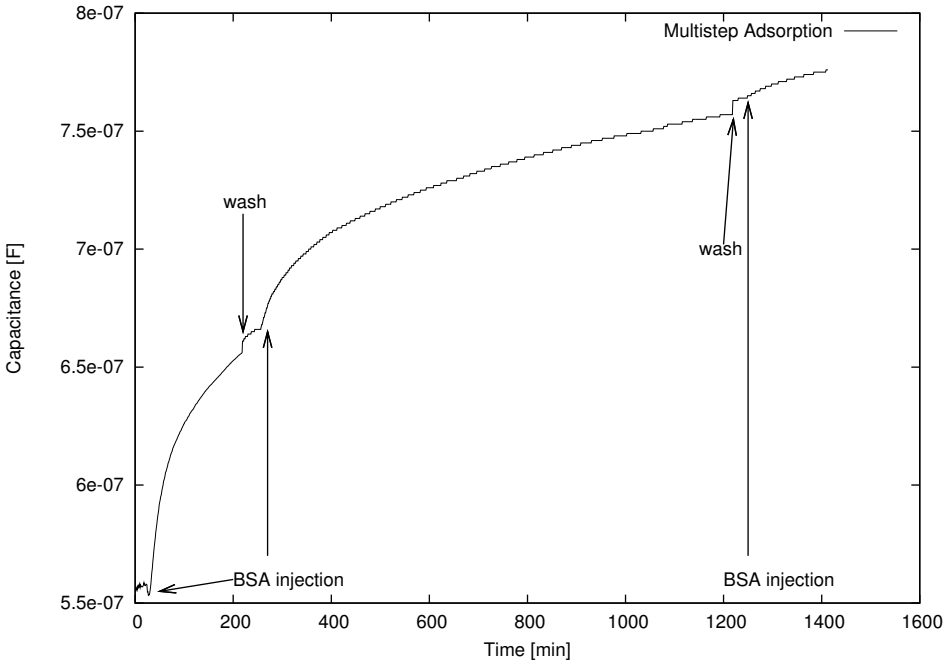

Figure 6.9: Multistep adsorption of BSA 0.67 mg.mL^{-1} , recorded at 40 Hz . Three steps are presented. The reservoir is washed three times with PBS between each step. A 30 minutes baseline is recorded before each BSA injection. It can be seen that the adsorption rate decreases at each BSA adsorption step.

Figure 6.9 was made by combining the data of three steps into one datafile, without changing anything to the data. A 40 Hz frequency was chosen among all the others, as the sensor was always capacitive in this frequency range. It is interesting to note that the imaginary part of the admittance is almost the same between the end of an adsorption of BSA and the beginning of the following baseline. This fact proves that the BSA does not desorb from the sensor surface even after three PBS washes. The second interesting fact is that the adsorption slope curve decreases at the beginning of each step. This tells that as the BSA does not desorb from the sensor surface, the density of free sites for a new step is lower than for the previous steps. As a consequence, the adsorption speed is reduced for the new steps compared to the previous ones.

6.4.3 Different concentrations

It has been proved that the BSA adsorbs on the sensor surface and does not desorb after three PBS washes. However the sensor behaviour could not be determined from the previous experiment for different concentrations of BSA. Tests were run using both face-to-face and coplanar design.

Face-to-face design

300 μL of PBS was injected in the reservoir. The acquisition was launched, recording data from 1 Hz to 1 MHz with five points per decade. Only one point per minute per frequency could be recorded when acquiring on the whole frequency range. As each chip was different, the properties of each chip in the low frequency range working domain were different and not really reproducible. As mentioned in Chapter 5, the resonance situated at high frequencies has the same general behaviour from one chip to the other. It is then preferable to work in the resonance frequency range rather than at low frequencies

Figure 6.10 presents the bulk results of this experiment from 133 μg.mL^{-1} to 13 mg.mL^{-1} , in logarithmic values. The bulk baselines do not have the same value for each chip, but are all flat, meaning that no adsorption phenomena is happening initially. However from log(time)=1.6, the horizontal line tranforms into a line whose slope changes with the BSA concentration: The more concentrated the solution the more negative the slope. Multiplying the whole data at a given frequency changes the value of the baseline but not the adsorption slope line. The peak visible at log(time)=3.3 for 13 mg.mL^{-1} BSA is only due to the logarithmic conversion.

Figure 6.11 presents the same data as Figure 6.10 with all the experiments baselines scaled to the experiment baseline running 333 μg.mL^{-1} BSA. As expected the adsorption slope curve does not change. Considering the data this way can be justified by the

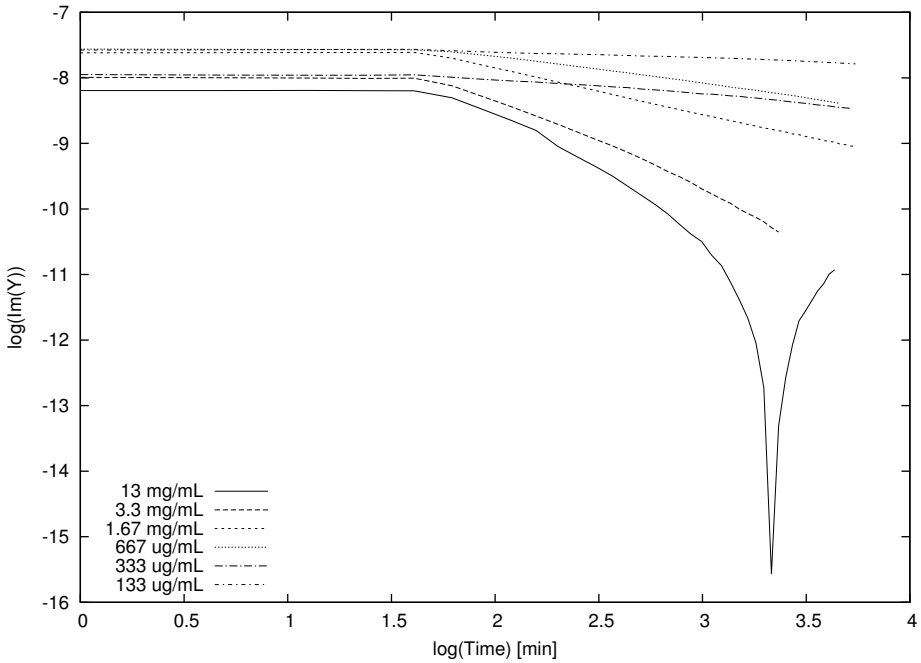

Figure 6.10: Logarithmic values of the result and of different concentrations of BSA using a face-to-face design. The adsorption plots are taken at 250 KHz.

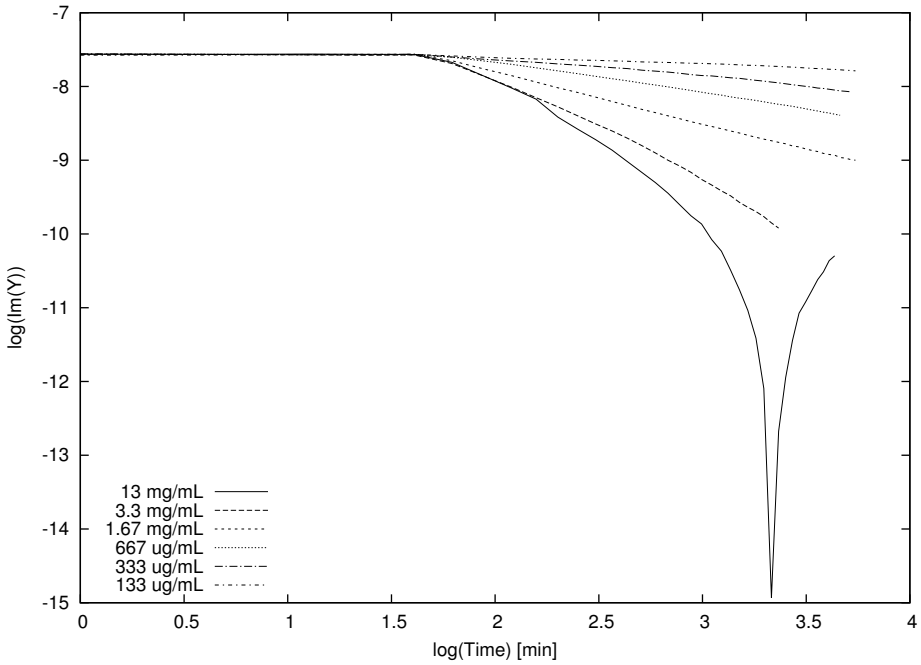

Figure 6.11: Logarithmic values of the result and of different concentrations of BSA in a face-to-face design. The adsorption plots are taken at 250 KHz. The data are scaled in order to align the baselines. The BSA adsorption slopes are unchanged by the scaling.

resonance origin. In a face-to-face design the resonance peak frequency is directly the result of the surface capacitance. This surface depends on the electrode geometry and on the surface roughness of the electrode. An assumption can be made that the signal generated by the adsorption of species is directly proportional to the electrode surface. As each experiment baseline is directly the result of the resonance position at a given frequency, the different experiment data can then be multiplied to match a reference value.

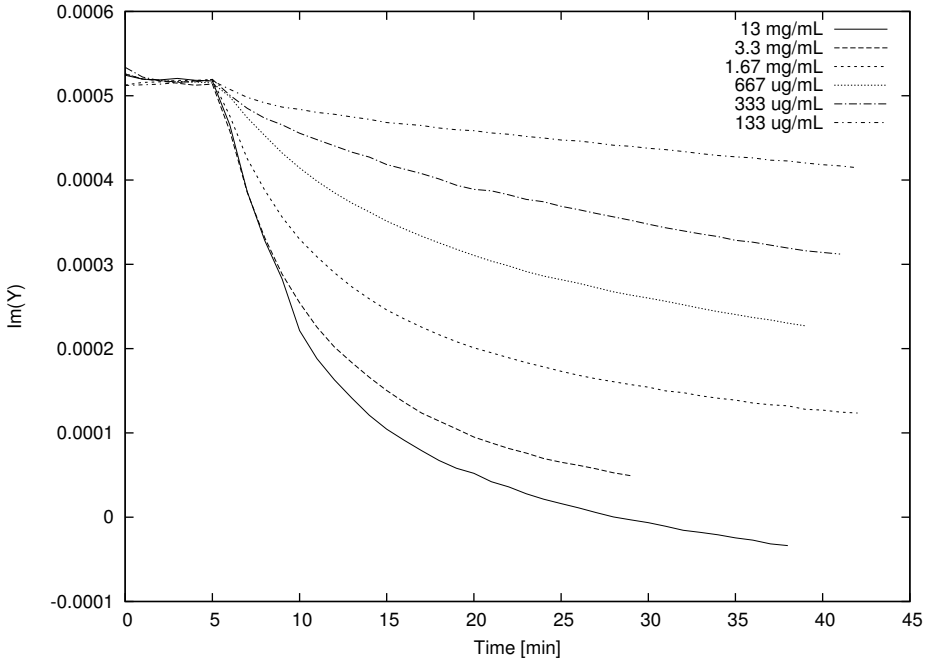

Figure 6.12: Imaginary part of admittance for different concentrations of BSA in a face-to-face design. Each plot is scaled to the same baseline. The adsorption plots are taken at 250 kHz.

The variation of the signal when plotting the results in a linear scale (Figure 6.12) is then higher when the BSA concentration increases. The signal decreases when the species adsorb on the electrodes. This can be explained by the fact that these points were recorded at 250 kHz, before the resonance peak. As the capacitance increases when BSA adsorbs on the electrode, the resonance peak moves to lower frequencies. This means that for a given frequency, the signal decreases as the resonance shifts.

Figure 6.13 presents the plot of these points with respect to the BSA concentration after 30 minutes of adsorption. The ideal way to compare different concentrations would be to reach the equilibrium for each one. Unfortunately these experiment were not run long enough to reach the quilibrium. However, after 30 minutes the adsorption can be estimated to be close to 90% of the equilibrium. Taking this position offers then a fair comparison between all the concentrations. The data presented on Figure 6.13 can be fitted by a Langmuir isotherm using Equation 6.3. As ψ was equal to 17.3 for 13.3 mg.mL^{-1} BSA, the coverage was then 95%. However for practical reasons, it was assumed to be 100% at this concentration.

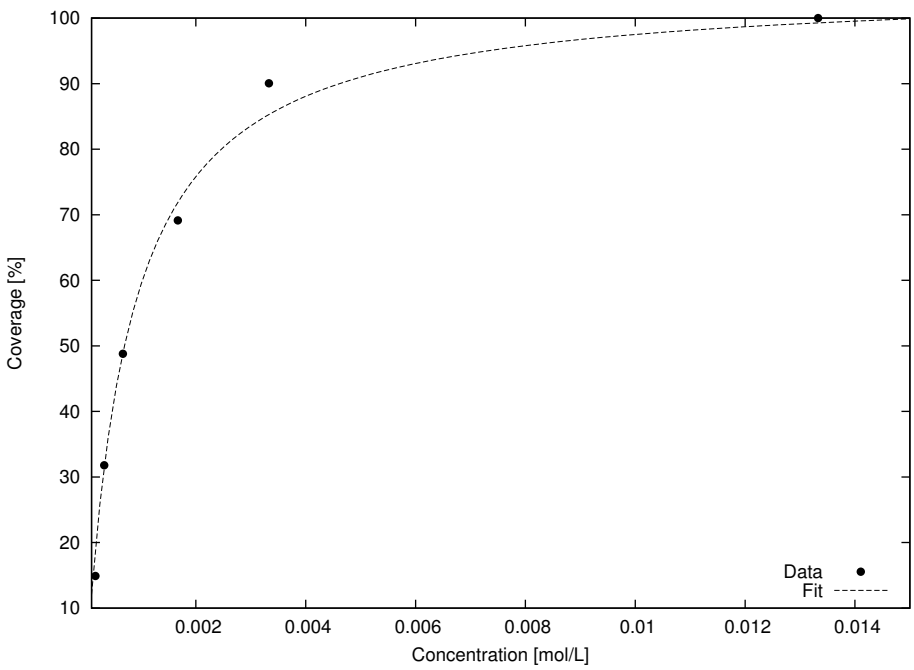

Figure 6.13: Langmuir isotherm fitted from the values of Figure 6.12 after 30 minutes of adsorption

The K constant value was fitted at 8.4×10^{4} M^{-1}. From the Equation 6.15 parameters, fitted in 6.4.1 using a coplanar design, a Γ_{max} value equal to 8.3×10^{-6} mol.m^{-2} was found, while this value was 2.4×10^{-6} mol.m^{-2} using the face-to-face design (Figure 6.4). This gives a surface concentration equal to 0.2 nm^2 per molecule (0.45 nm by 0.45 nm per molecule) for the coplanar design experiment. The surface concentra-

tion was 0.69 nm^2 per molecule (0.83 nm by 0.83 nm per molecule) for the face-to-face experiment.

In the litterature, the Γ_{max} value for BSA adsorbing on gold was found equal to 6.1×10^{-8} mol.m^{-2} with a K value equal to 10^3 M^{-1}[18]. BSA adsorption at alumina/water interface was described by Urano and Fukuzaki[19]. They found a surface concentration equal to 25 nm^2 per molecule (5 nm by 5 nm per molecule) (Γ_{max}=6.67×10^{-8} mol.m^{-2}). The values found with both face-to-face and coplanar designs are low compared to the one found by Urano and Fukuzaki. The size of BSA was found equal to 4 nm by 4 nm (and 14 nm height)[20]. This error could result of multiple factors:

- The Equation 6.15 not well suited for ψ >1 for both designs
- A frequency not matching the best parameters for the coplanar design experiment.
- The K value was not fitted in the best conditions.

As the Γ_{max} values found are not accurate, the value found by Urano and Fukuzaki will be used for the rest of this work.

Coplanar design in reservoir

60 μL of PBS was injected in a 6 mm diameter reservoir. The acquisition was launched and after one minute the reservoir was emptied and filled with 60 μL of BSA solution to get rid of the diffusion effect as much as possible. A new chip was used for each BSA concentration.

Figure 6.14 presents the Imaginary part of the admittance with respect to time for BSA concentrations of 10 mg.mL^{-1}, 2 mg.mL^{-1}, 500 μg.mL^{-1}, 50 μg.mL^{-1} and 10 μg.mL^{-1}, recorded at various frequencies (Table 6.4). The values were shifted to the same baseline. The variation amplitude decreases with the BSA concentration in the so-

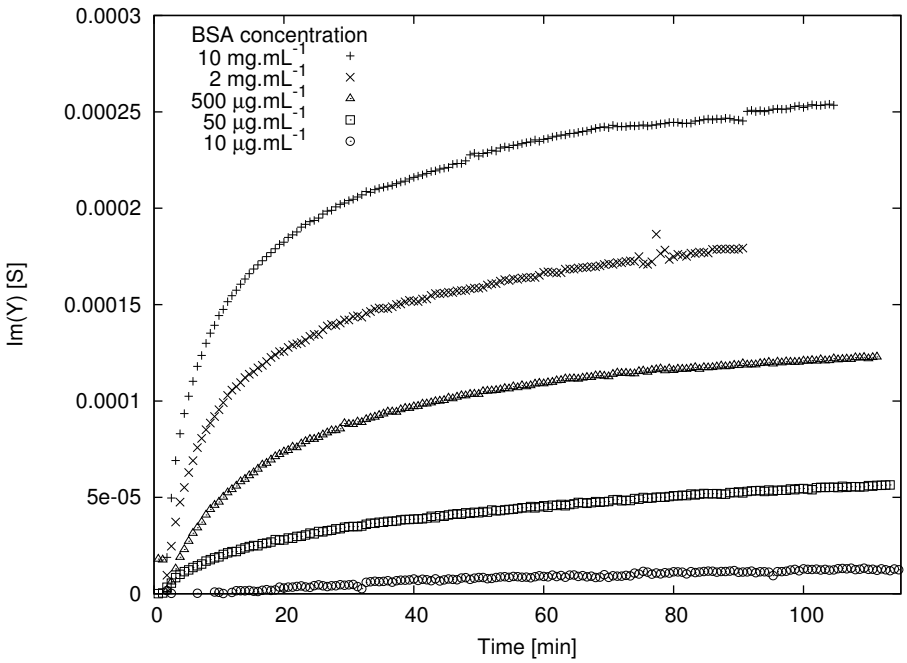

Figure 6.14: Imaginary part of admittance for different BSA concentrations in a coplanar design. Each plot is shifted to a baseline of 0.

BSA concentration	Acquisition Frequency
10 mg.mL^{-1}	840 kHz
2 mg.mL^{-1}	770 kHz
500 μg.mL^{-1}	740 kHz
50 μg.mL^{-1}	770 kHz
10 μg.mL^{-1}	771 kHz

Table 6.2: Acquisition frequency for each BSA concentration.

lution, on par with the kinetics. The reliable detection limit was reached at 10 μg.mL^{-1} (150 nM). This limit might be pushed back by reducing diffusional effects.

Coplanar design in channel

The sensor is able to monitor an adsorption in a reservoir. However adsorbing in a reservoir requires a long time due to diffusion effects. Using a flow can in this case greatly reduce the time needed to reach the equilibrium. A channel coplanar design was mounted in the teflon holder presented on Figure 5.37. The holder height being

300 μm , the effects due to the diffusion are limited compared to the reservoir. A 10 mg.mL^{-1} BSA solution was injected at a 10 μL .min^{-1} flow rate and later 30 μL .min^{-1} with a new chip.

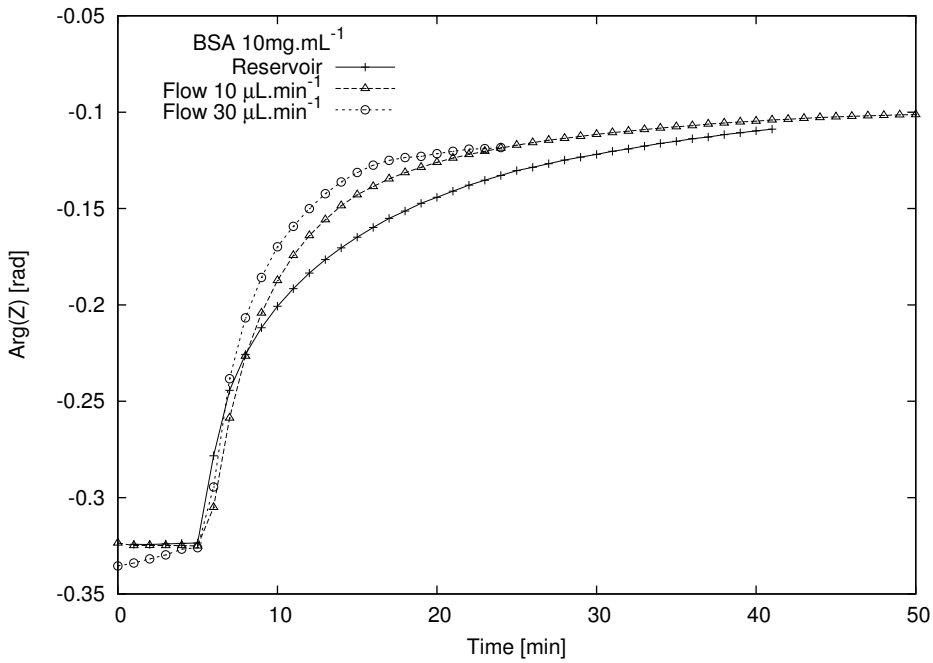

Figure 6.15: 10 mg.mL^{-1} BSA adsorption in a reservoir sensor and in a channel sensor using two different flow rates.

The results were compared to the same solution injected in a 6 mm diameter reservoir (Figure 6.15). The plots amplitude were scaled for the beginning and the end of each plot to match the other presented plots, as the data is by far too complicated to correct in a way able to compare with any other experiment. It can be observed that the equilibrium was not reached after 50 minutes when using the reservoir. However the equilibrium was reached with a 10 μL .min^{-1} flow rate after 40 minutes of adsorption. With a 30 μL .min^{-1} flow rate, the equilibrium was reached after 20 minutes of adsorption.

The system behaviour when going back to the buffer could not be studied due to a lack of robustness of the fluidic system. The desorption process could then unfortunately

not be studied, nor k_{off} could be determined empirically.

The channel section being rectangular, the hydraulic diameter D_h [21] of the channel can be defined by:

$$D_h = \frac{4S}{P} = \frac{4HW}{2H + 2W} \tag{6.16}$$

with S [m^2] being the channel section, and P [m] the channel perimeter. The hydraulic diameter value was found equal to 462 μm . The Reynolds number [21] Re can then be defined by:

$$Re = \frac{U_0 D_h}{\nu} \tag{6.17}$$

with U_0 [m.s^{-1}] the fluid linear velocity and ν [m^2.s^{-1}] the fluid kinematic viscosity. In the case of water, ν=10^{-6} m^2.s^{-1}. The Reynolds number was found equal to 0.25 for a 10 μL .min^{-1} flow rate and 0.77 for a 30 μL .min^{-1} flow rate. Consequently the flow is laminar in both cases. The Peclet number Pe can be calculated using the Reynolds and the Schmidt (Sc) number [21]:

$$Pe = ReSc \tag{6.18}$$

with the Schmidt number representing the ratio between the fluid viscosity and the mass diffusivity:

$$Sc = \frac{\nu}{D} \tag{6.19}$$

Taking a 6^{-11} m^2.s^{-1} diffusion coefficient, the Schmidt number was found equal to 1.67$\times$10^4. The Peclet number was then equal to 2.5x10^3 for a 10 μL .min^{-1} flow rate and 7.7x10^3 for a 30 μL .min^{-1} flow rate. These relatively high Peclet values means that the transport is assured by convection instead of diffusion. We can then assume that for a 30 μL .min^{-1} flow rate, the convection is important enough so that the kinetic is

K	8.4×10^{4} M^{-1}
k_{on}	2.7×10^{1} M^{-1}.s^{-1}
k_{off}	3.1×10^{-4} s^{-1}
C^{0}	1.52×10^{-4} M

Table 6.3: Values used to fit the data presented on Figure 6.16, using a 30 μL .min^{-1} flow rate in channel.

reaction limited. With a K value equal to 8.4×10^{1} and 10 mg.mL^{-1} BSA, ψ was found equal to 12.7. Using Equation 6.3, this leads to a 93% surface coverage. The 30 μL .min^{-1} flow rate adsorption data were then normalized and scaled to 0.93 (Fig 6.16).

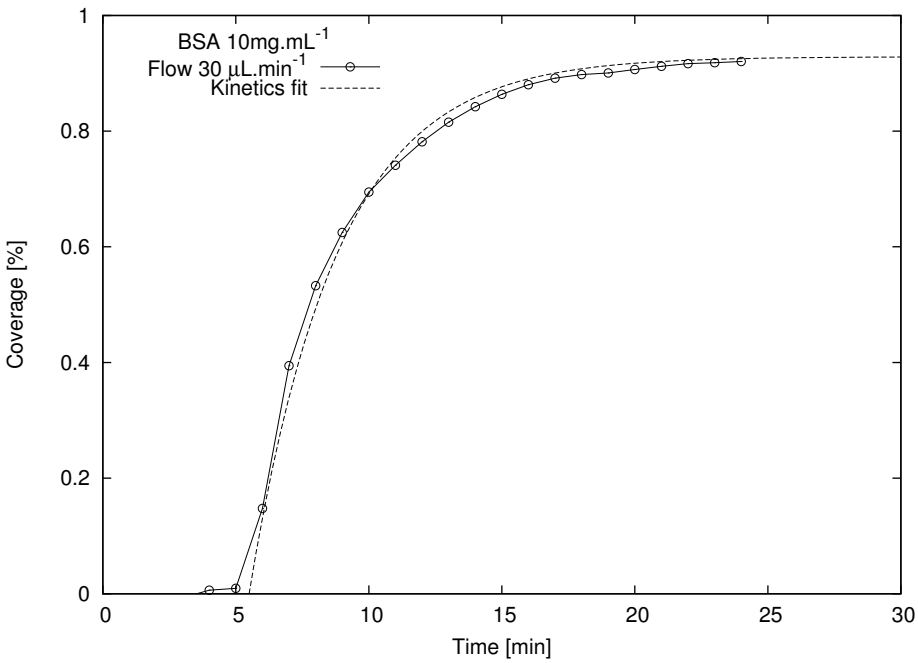

Figure 6.16: Fit of the normalized 30 μL .min^{-1} flow rate adsorption.

The plot was then fitted using Equation 6.8, fitting k_{on} while k_{off} was calculated from k_{on}/K (fit values in Table 6.3). k_{on} was found equal to 2.7×10^{1} M.s^{-1} while k_{off} was deducted equal to 3.1×10^{-4}.s^{-1}. As the BSA did not desorb during reservoir washing, and as the kinetic seems slow compared to a BSA adsorption on gold (data not shown), these k_{on} and k_{off} values seem acceptable.

6.5 Second layer detection

6.5.1 Goals

It has been demonstrated that a BSA adsorption on the electrodes can be detected by the sensor. Moreover, this adsorption follows the Langmuir isotherm. However, the original goal of this work was to create a contactless, label-free immunosensor. An immunologic reaction generally involves that a species binds to another one. An immunosensor has to detect this binding. In a sandwich ELISA test, this is done by adsorbing an antibody on the substrate, inject the patient sample and after that inject a enzyme-linked antibody that binds to the antigene[22, 23]. Then a substrate that reacts with the enzyme is injected to detect if the first adsorbed antibodies reacted with the patient antigenes, if these antigenes were present in the patient blood.
Only the two first steps are considered when running a label-free immunologic test. This detection can be realized in SPR, and shall be realized by the currently studied electrochemical sensor. The second layer (the antigene in the ELISA second step) has then to be detected as the first layer was.

6.5.2 Design and detection

As seen in the last section, the sensor design has its importance in its ability to detect the first adsorbed layer. In this way it should be appropriate to consider that the design should be a key question for the detection of the second adsorbed layer.

The experiments involving the face-to-face design were run in a 6 mm diameter reservoir. No second layer adsorption could be detected. This might be due to the huge distance between the electrodes that greatly increases the importance of the diffusional effects, diluting a weak signal in the noise. A face-to-face design with a greatly reduced distance between the electrodes should make the second adsorbed layer de-

tectable.

The coplanar design is far more complicated than the face-to-face design. However with the current use of a reservoir, it offers the possibility to reduce the volumes used and so the effects of the diffusion. All the coplanar experiments were carried out using a 6 mm diameter reservoir. The recording frequency was fixed around the resonance, as no second layer adsorption could be detected at low frequencies. An hypothesis could be that the low frequencies concern only surface measurements. Thus, the signal may only be provided by the aluminium/alumina/Stern layer interface, meaning that only the first layer would be detected. When monitoring around the resonance, the signal goes from one electrode to the other through the solution, The second layer might then be detected.

6.5.3 Specific interaction detection

A key question with the first experiments is the sensor ability to detect the second adsorbed layer. Even if detected, it has to be checked whether the signal is due to the binding of the injected species onto the species adsorbed as the first layer, or just to some species reaching the surface but not reacting or adsorbing. This means that the sensor ability to detect specific interactions is as important, if not more, than just the detection of the second adsorbed layer.

The specific interaction detection was studied using a coplanar design coupled to a 6 mm diameter reservoir where 40 mg.mL^{-1} BSA was left overnight to saturate the surface (Figure 6.7 in 6.4.1) Two tests were then performed. The first one consisted in injecting 5 μL of 2 mg.mL^{-1} β-lactoglobulin in the reservoir. The second one consisted in injecting several steps of Anti-Milk antibodies in the reservoir.

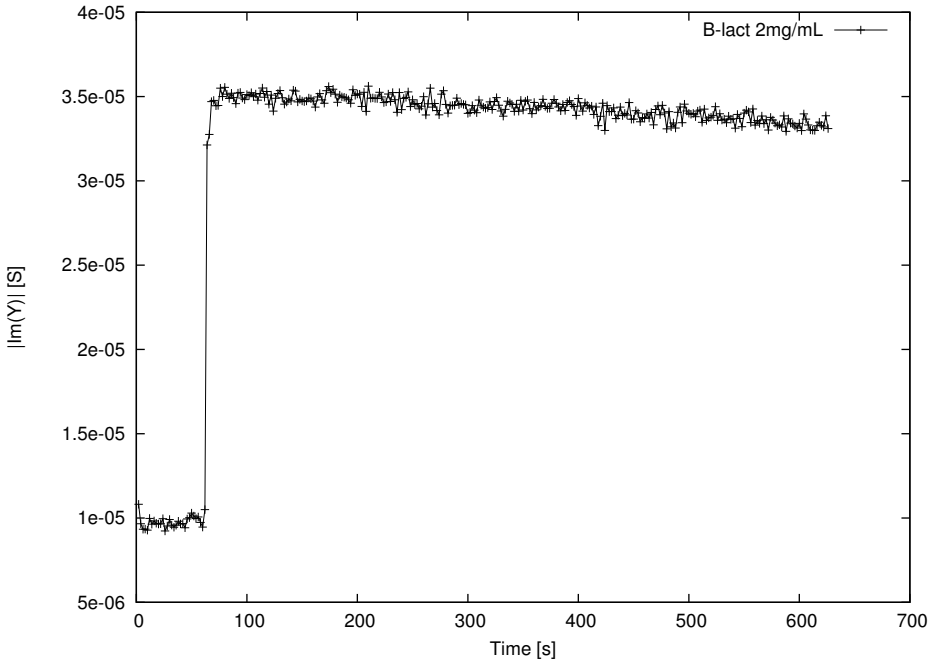

Figure 6.17: Addition of β-lactoglobulin into the reservoir after an overnight BSA 40 mg.mL^{-1} adsorption . Nothing happens after the β-lactoglobulin injection

Figure 6.17 describes the first experiment. 60 μL of PBS solution was injected in the reservoir. The acquisition was launched at a 630 kHz frequency and 5 μL of2 mg.mL^{-1} β-lactoglobulin were injected in the reservoir. The signal increases suddenly after the β-lactoglobulin injection. This increment is due to the β-lactoglobulin injection, which increases the solution volume present in the reservoir, and so its height. The volume capacitance increases when the liquid quantity present in the reservoir increases. This behaviour results in a resonance shifts to a lower frequency, forcing the signal to increase as the acquisition is fixed at a frequency higher than those of the resonance peak. If an adsorption occurs, the signal should evolve quickly after the injection, as the concentration of β-lactoglobulin in the injected solution is important. However, in the considered conditions, the β-lactoglobulin should not interact with the BSA, and so the signal should be unchanged. As it does not evolve during 10 minutes after the injection, the theory is respected as no adsorption is detected.

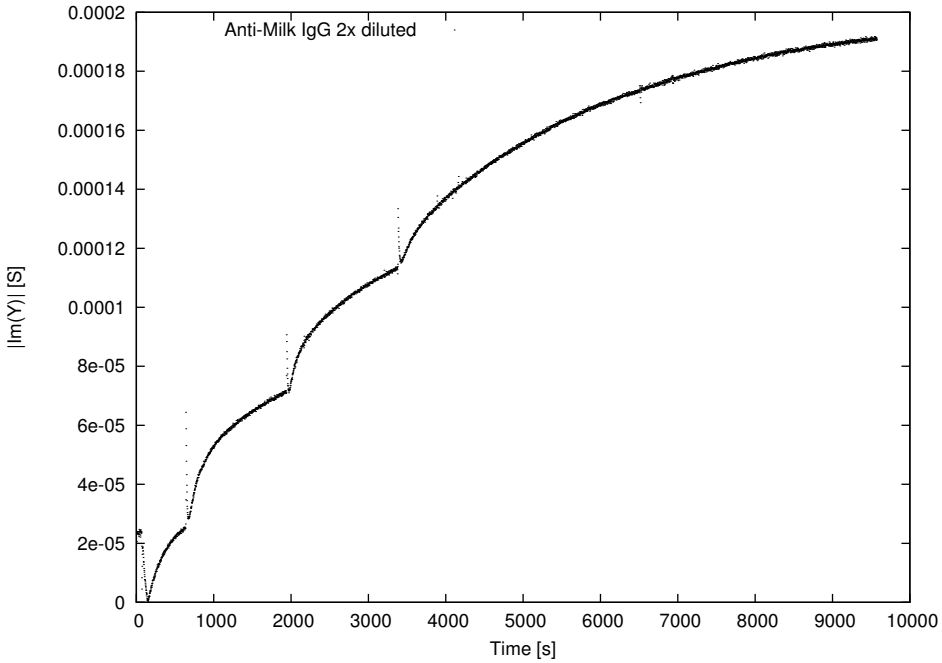

Figure 6.18: Several Anti-Milk antibodies injections after a BSA adsorption and the previous β-lactoglobulin injection. Four Anti-Milk antibodies injections are performed one after the other without washing between each injection. The response intensity slows down at each injection. However the surface is not saturated even at the end of the fourth injection.

The reservoir was washed three times with PBS after the first experiment. The acquisition was launched at the same frequency as before and a first Anti-Milk antibodies injection was performed after 2 minutes (Figure 6.18). The immediate and significant signal increment proves that the Anti-Milk antibodies reacts with the previously adsorbed BSA. Considering the K value found in 6.4.3 and the BSA concentration, ψ was equal to 0.98. As the BSA solution was left overnight in the reservoir, we will assume full surface coverage. Considering the Γ_{max} value found by Urano and Fukuzaki[19], the quantity of adsorbed BSA was 4×10^{16} molecules. One injection of Anti-Milk antibodies adds 4×10^{13} molecules in the reservoir. As this value is in large default to interact with all the adsorbed BSA, three more injections of 5 μL of Anti-Milk antibodies were performed. The slope of the curve at each injection is slower than for the previous one, which is logical as the quantity of free BSA sites on the surface de-

creases. However the plot slope at the beginning of each injection if far higher than the plot slope before the injection : The solution depletes rapidly.

6.5.4 Immunosensor

It has been proved that the sensor could detect the adsorption of two layers. It was also demonstrated that the sensor was able to detect specific interactions. The next step is then the immunologic test. The processes required to make such an experiment are more complicated than for the previous experiments.

First immunologic test

The immunologic test can be run with a Anti-β-lactoglobulin antibodies / β-lactoglobulin system. The first step consists in adsorbing the antibodies on the electrodes. 60 μL of 10 mM PBS was injected in a 6 mm diameter reservoir, and then replaced by 60 μL of Anti-β-lactoglobulin antibodies diluted 128 times from the mother solution. The Anti-β-lactoglobulin antibodies concentration in the solution, being a serum, was unknown. The adsorption was monitored during 4h30 and the solution was left in the reservoir overnight to fill the surface in Anti-β-lactoglobulin antibodies as much as possible. Data were recorded at 970 KHz, below the resonance peak (Figure 6.19).

The second step consists in blocking the surface with a highly concentrated BSA solution. This ensures that no β-lactoglobulin can adsorb on the alumina when it is injected in the reservoir during the third step. After being washed three times, 60 μL of 10 mM PBS was injected in the reservoir and replaced after one minute of acquisition by 60 μL of 40 mg.mL^{-1} BSA. The adsorption was monitored during two hours at 910 kHz (Figure 6.20) and left in the reservoir during 7 hours.

It has to be noted that in 250 minutes, the imaginary part of the admittance variation when adsorbing the Anti-β-lactoglobulin was 4x10^{-5} S. This variation is 25x10^{-5} S in 120 minutes when adsorbing the BSA : Although the Anti-β-lactoglobulin solution

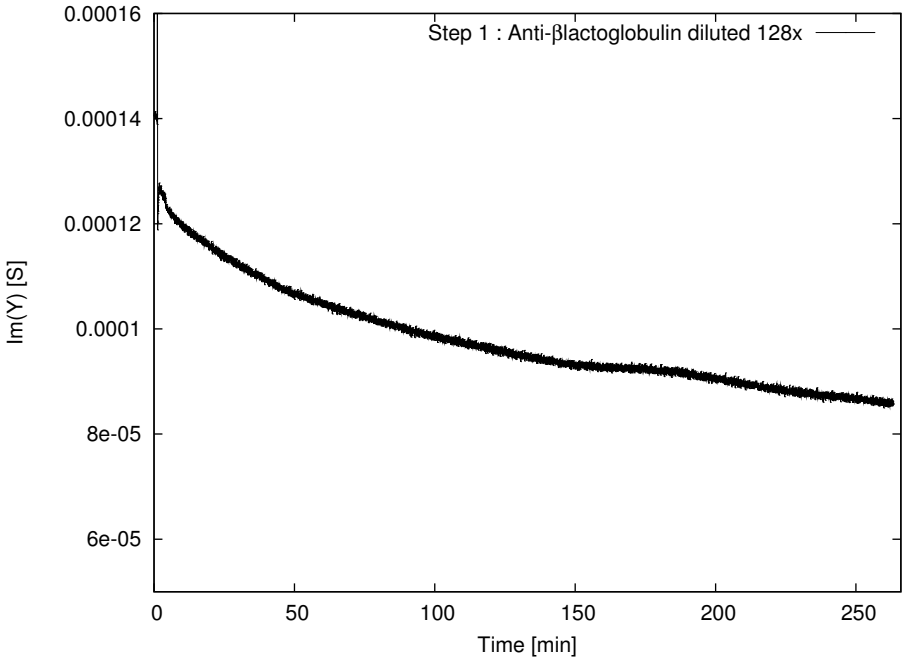

Figure 6.19: Imaginary part of the admittance of Anti-β-lactoglobulin antibodies adsorbed (diluted 128 times) as a first layer.

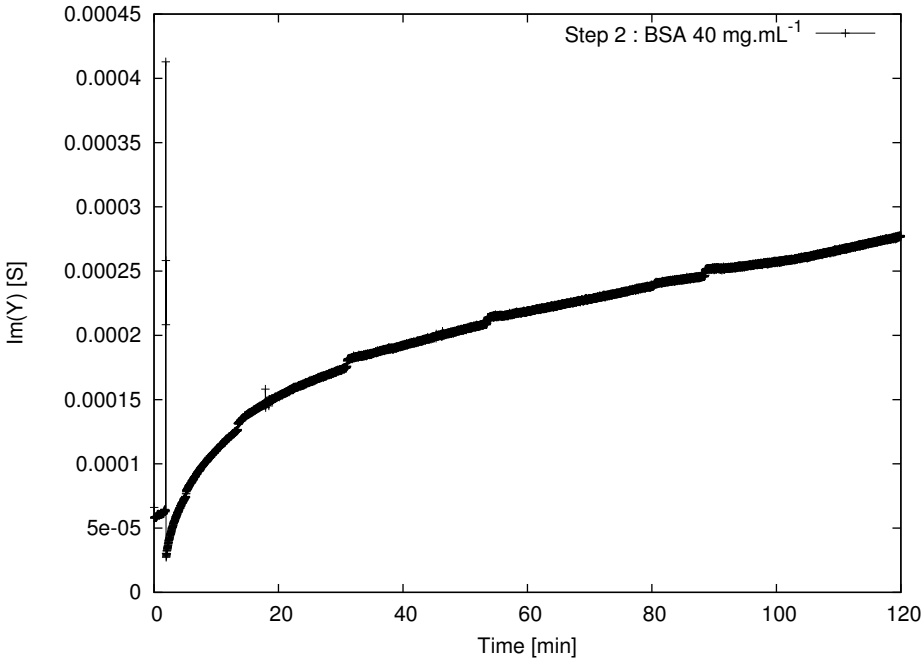

Figure 6.20: Imaginary part of the admittance of the adsorption of BSA concentrated at 40 mg.mL^{-1} as a first blocking layer.

was left overnight, the low concentration of the solution did not saturate the electrode surface. Thus, the latter still owns a good quantity of free sites available for the BSA.

The reservoir was washed three times with the PBS solution. 60 μL of PBS 10 mM was injected in the reservoir, and after one minute of acquisition at 730 kHz, 10 μL of 3 mg.mL^{-1} β-lactoglobulin was injected in the reservoir (Figure 6.21).

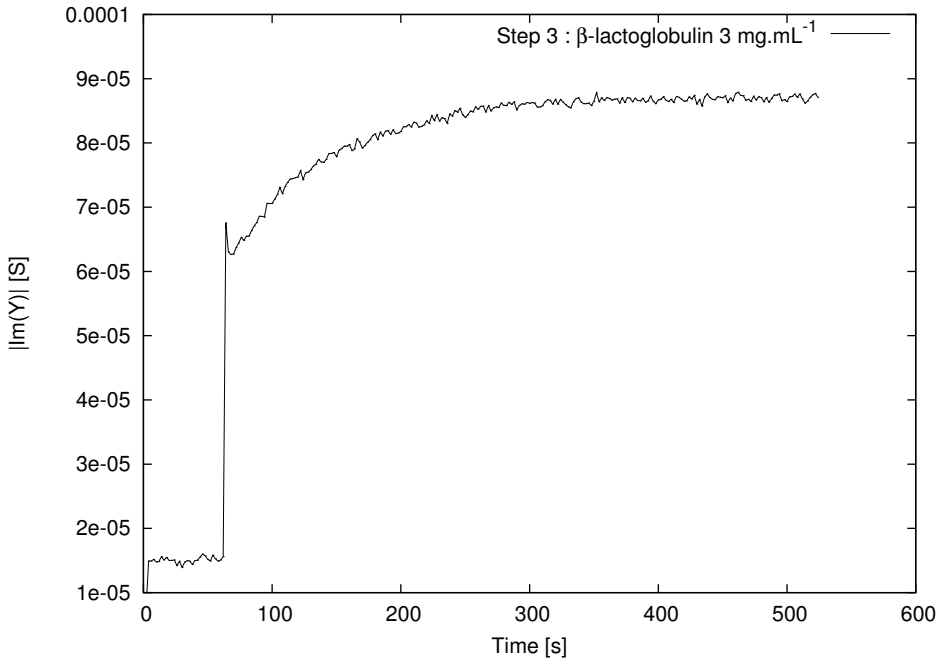

Figure 6.21: Imaginary part of the admittance when injecting the β-lactoglobulin concentrated at 3 mg.mL^{-1} as a second layer.

The signal increases which means that the β-lactoglobulin reacts with the Anti-β-lactoglobulin antibodies. The signal variation is roughly 2x10^{-5} S, and increases during about 200 s.

Differently concentrated antibodies solutions

The sensor can be used as an immunosensor that is able to say if a species is present or not. A good progress would be to be able to quantify the amount of adsorbed species. The Anti-β-lactoglobulin solution was diluted twice, 8 times, 32 times and 128 times from the mother solution. 60 μL of each solution was injected in a 6 mm

IgG dilution	Acquisition Frequency
Twice	680 kHz
8 times	850 kHz
32 times	612 kHz
128 times	610 kHz

Table 6.4: Acquisition frequency for each of the four sensors.

diameter reservoir with one chip integrated in each holder during 5 hours instead of almost 20 hours in the previous immunoassay. After washing the reservoir with 10 mM PBS, 40 mg.mL^{-1} BSA was injected overnight. The reservoir was then washed three times and after one minute of acquisition, 10 μL of 3 mg.mL^{-1} β-lactoglobulin was added to the 60 μL of PBS present in each reservoir. Each acquisition was performed at a frequency higher than the resonance peak. These frequencies are listed in Table 6.4.

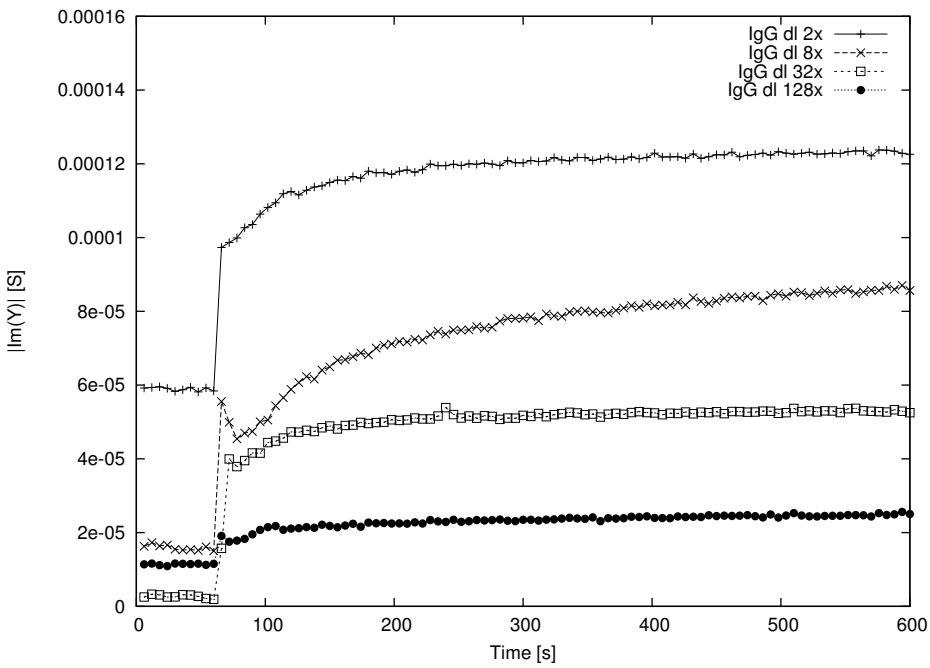

Figure 6.22: Different concentrations of Anti-β-lactoglobulin was adsorbed as a first layer during 1h30. 40 mg.mL^{-1} BSA was let overnight to block the surface. These plots represent the β-lactoglobulin injection in the reservoir after washing. The amplitude of the signal decreases as the adsorbed antibodies concentration decreases.

The imaginary part of the admittanceevolution when the β-lactoglobulin was injected in the reservoir is plotted on Figure 6.22. The different baseline levels are due to the different recording frequencies. The baseline variation after the β-lactoglobulin injection is likely due to small construction differences between each sensor which affect the electric field distribution when adding solution in the reservoir. This static effect might not be taken into account when comparing the different concentrations. As the Anti-β-lactoglobulin concentration is unknown, this comparison can only be qualitative. The evolution of Anti-β-lactoglobulin diluted 8 times has not the same shape than for the other concentrations, and might be due to the far higher acquisition frequency compared to the other concentrations. Nevertheless the evolution amplitude is on the same order than for the twice diluted concentration. It can be noted that the variation amplitude is lower when the Anti-β-lactoglobulin solution is diluted 32 times. This variation is even lower and almost null when the Anti-β-lactoglobulin solution is diluted 128 times, which contrasts with the previous case when the Anti-β-lactoglobulin antibodies were let adsorbing overnight.

6.6 Conclusion

The adsorption of species using aluminium electrodes covered with a nanometric alumina layer was studied using both face-to-face and coplanar designs. The sensor ability to monitor the adsorption of a first layer of species on the electrodes was tested using a highly concentrated BSA solution. The sensor was able to monitor the BSA adsorption due to capacitance variation created by the electrodes. It was observed that this adsorption was better monitored using the resonance shifting to lower frequencies (due to the surface admittance increment), rather than monitoring at low frequencies whose behaviour was less reliable from one chip to another. Using the coplanar design, the influence of the distance between the electrodes was studied. A small distance

increased the signal dynamic but resulted in a less reliable behaviour of the sensor during the time. The adsorption was also studied using a fluid flow. It was observed that the equilibirum was reached faster as the flow rate value increased.

As a single step adsorption was successfully monitored by the sensor, a multistep adsorption of 2 mg.mL^{-1} BSA was successfully monitored using a coplanar design. The adsorption of differently concentrated BSA solutions was studied using face-to-face and coplanar designs. The Langmuir isotherm could be plotted from the recorded data and an adsorption constant value could be extracted. Using a channel flow, some kinetic parameters (k_{on} and k_{off}) of the adsorption could be extracted. The detection limit was reached for a 10 μg.mL^{-1} BSA solution using a coplanar design.

The second layer detection was then investigated. The ability of the sensor to detect biological interations was studied by blocking the surface with a 40 mg.mL^{-1} BSA solution. No adsorption was detected when injecting β-lactoglobulin into the reservoir. However, the sensor was able to monitor an adsorption when injecting Anti-Milk antibodies in the reservoir An immunologic test was then performed, using Anti-β-lactoglobulin antibodies as a first layer and blocking the surface with a 40 mg.mL^{-1} BSA solution. The β-lactoglobulin injection was detected by the sensor. Repeating the operation for four differently concentrated solutions of Anti-β-lactoglobulin antibodies gave a strong second layer detection for the most concentrated solution and almost no detection for the most diluted solution.

The results reproducibility mainly depends on the sensor construction reproducibility. As this sensor is hand made, the resonance peak initial frequency variation can sometimes be important. The reproducibility could be enhanced by building the sensor with microfabrication techniques.
The desorption process and the adsorption reversability might also be studied. The fi-

nal immunoassay may be performed using a constant IgG concentration on the surface and various concentrations of β-lactoglobulin in the reservoir.

Bibliography

[1] K. Rezwan et al. "Bovine serum albumin adsorption onto colloidal Al2O3 particles: A new model based on zeta potential and UV-Vis measurements". In: *Langmuir* 20.23 (2004), pp. 10055–10061.

[2] J. Dai, G.L. Baker, and M.L. Bruening. "Use of porous membranes modified with polyelectrolyte multilayers as substrates for protein arrays with low nonspecific adsorption". In: *Analytical Chemistry* 78.1 (2006), pp. 135–140.

[3] M. Karlsson and L. Tang. "Surface morphology and adsorbed proteins affect phagocyte responses to nano-porous alumina". In: *Journal of Materials Science: Materials in Medicine* 17.11 (2006), pp. 1101–1111.

[4] Andrea Lionello. *Controlled Protein Adsorption for Microimmunoassays*. Lausanne, 2006.

[5] K.R. Hall et al. "Pore- and solid-diffusion kinetics in fixed-bed adsorption under constant-pattern conditions". In: *Industrial and Engineering Chemistry Fundamentals* 5.2 (1966), pp. 212–223.

[6] T.M. Squires, R.J. Messinger, and S.R. Manalis. "Making it stick: Convection, reaction and diffusion in surface-based biosensors". In: *Nature Biotechnology* 26.4 (2008), pp. 417–426.

[7] S. Fukuzaki, H. Urano, and K. Nagata. "Adsorption of bovine serum albumin onto metal oxide surfaces". In: *Journal of Fermentation and Bioengineering* 81.2 (1996), pp. 163–167.

[8] L. Moreno-Hagelsieb et al. "Electrical detection of DNA hybridization: Three extraction techniques based on interdigitated Al/Al2O3 capacitors". In: *Biosensors and Bioelectronics* 22.9-10 (2007), pp. 2199–2207.

[9] J. Rickert et al. "A 'mixed' self-assembled monolayer for an impedimetric immunosensor". In: *Biosensors and Bioelectronics* 11.8 (1996), pp. 757–768.

[10] M. Yi, K.-H. Jeong, and L.P. Lee. "Theoretical and experimental study towards a nanogap dielectric biosensor". In: *Biosensors and Bioelectronics* 20.7 (2005), pp. 1320–1326.

[11] S.-W. Wang et al. "A CMOS capacitive dopamine sensor with Sub-nM detection resolution". In: *Proceedings of IEEE Sensors*. 2009, pp. 400–404.

[12] Q. Xie et al. "A novel dual-impedance-analysis EQCM system - Investigation of bovine serum albumin adsorption on gold and platinum electrode surfaces". In: *Journal of Colloid and Interface Science* 262.1 (2003), pp. 107–115.

[13] T. Pajkossy. "Impedance spectroscopy at interfaces of metals and aqueous solutions - Surface roughness, CPE and related issues". In: *Solid State Ionics* 176.25-28 (2005), pp. 1997–2003.

[14] M.R. Rodriguez Nino and J.M. Rodriguez Patino. "Effect of the aqueous phase composition on the adsorption of bovine serum albumin to the air-water interface". In: *Industrial and Engineering Chemistry Research* 41.6 (2002), pp. 1489–1495.

[15] A.K. Gaigalas et al. "Diffusion of bovine serum albumin in aqueous solutions". In: *Journal of Physical Chemistry* 96.5 (1992), pp. 2355–2359.

[16] D.J. O Shannessy et al. "Determination of rate and equilibrium binding constants for macromolecular interactions using surface plasmon resonance: Use of non-linear least squares analysis methods". In: *Analytical Biochemistry* 212.2 (1993), pp. 457–468.

[17] E. Stern et al. "Label-free immunodetection with CMOS-compatible semiconducting nanowires". In: *Nature* 445.7127 (2007), pp. 519–522.

[18] S.H. Brewer et al. "Probing BSA binding to citrate-coated gold nanoparticles and surfaces". In: *Langmuir* 21.20 (2005), pp. 9303–9307.

[19] H. Urano and S. Fukuzaki. "Conformation of adsorbed bovine serum albumin governing its desorption behavior at alumina-water interfaces". In: *Journal of Bioscience and Bioengineering* 90.1 (2000), pp. 105–111.

[20] K. Hirayama et al. "Rapid confirmation and revision of the primary structure of bovine serum albumin by ESIMS and Frit-FAB LC/MS". In: *Biochemical and Biophysical Research Communications* 173.2 (1990), pp. 639–646.

[21] Andrej Dmitrievic Poljanin. *Hydrodynamics, Mass and Heat Transfer in Chemical Engineering*. London: Taylor & Francis, 2002. ISBN: 0-415-27237-8.

[22] U.B. Nielsen and B.H. Geierstanger. "Multiplexed sandwich assays in microarray format". In: *Journal of Immunological Methods* 290.1-2 (2004), pp. 107–120.

[23] E. Eteshola and D. Leckband. "Development and characterization of an ELISA assay in PDMS microfluidic channels". In: *Sensors and Actuators, B: Chemical* 72.2 (2001), pp. 129–133.

Chapter 7

Conclusions and perspectives

In the present work, a label-free, contactless and capacitive immunosensor was developed using impedance spectroscopy, in the aim to perform low-cost immunoassays. The primary objective was to demonstrate the ability of the sensor to monitor the adsorption of species on the surface of the electrodes. This goal was reached, as it was found that the adsorption followed a Langmuir isotherm. An equilibrium constant was also extracted. The second objective of the sensor was to recognize and monitor the second adsorbate layer. This objective was reached by studying the interactions between β-lactoglobulin and Anti-β-lactoglobulin which opens the way for achieving immunoassays.

To obtain this a result, numerical simulations were carried out for a face-to-face and a coplanar design using an insulating layer between the simulated electrode and the solution. A harmonic signal was applied for a frequency ranging from 100 Hz to 10 MHz and two levels of capacitance were observed. At low frequencies, two capacitances were created by the insulating layers, in series with the resistance of the solution. At high frequencies, the displacement current took place in the solution and the resulting capacitance was due to the capacitance created by the solution in series with those cre-

ated by the PET layers.
The variation of the conductivity of the solution led to a variation of the time constants for both designs. Decreasing the channel height lowered the high frequency capacitance value while keeping the low capacitance unchanged. For the coplanar design, the decrease in channel height also led to a decreased value of the cut-off frequency between the low and high capacitance. It was shown that both designs were sensitive to the insulating layer thickness, which modified the low frequency capacitance value, but also the high frequency ones.
Dimensionless parameters were set for the coplanar design relative to the gap value between the two electrodes. It was observed that the response of this design at high frequencies was dependent on the relationship between the channel height and the electrode width. The dimensionless number Gq was defined to check the quality of the geometry at high frequencies.

The results of the numerical simulations were exploited to optimize the signal quality of a microchip/holder system. To achieve such a task, both holder and microchip designs were studied in detail. Removing the connectors of the holder and moving away the plastic elements from the microchip as far as possible made the influence of the holder on the signal quality almost negligible.
The influence of the electrode width and the distance between them was studied to maximize the useful capacitance over noise ratio. The electrode width had a strong influence at low frequencies but not at high frequencies, where the signal was mostly due to the inner edge effects. In this way, it was found that a 1 mm electrode width separated by a distance of 500 μm was a good compromise. The influence of various parameters like the insulating layer thickness, the lamination layer on top of the electrodes and the cross section length were also examinated.
Finally, the sensor ability to detect BSA was studied. It was found that the sensor was

not able to detect any adsorption of BSA in the low frequency range. However, it was able to detect conductivity variations of various BSA solutions in the high frequency range.

As no adsorption could be monitored using the microchips due to the high thickness value of the PET layer, a material that would have a relatively important relative permittivity but also permit a low insulating layer thickness was needed. Aluminium electrodes covered by a nanometric alumina layer provide this strong capacitance and were used to detect the adsorption of proteins. In a first step, the face-to-face and coplanar electrode designs were studied in a small plastic box to get rid of the perturbations involved by the holders. A discrete model based on transmission lines was developed to understand the sensor response across frequencies ranging from 1 Hz to 1 MHz. As with the microchip, it could be observed that the sensor behaviour was mostly capacitive at low frequencies and resistive at high frequencies. However, contrary to the microchip, the presence of a resonance could be shown at high frequencies, dependant on the capacitance created by the electrodes, the resistance of the reservoir and the inductance value created by the connectors and the electrodes. The resonance peak position was also influenced by the distance between the electrodes in the case of the coplanar design, as the time constants at high frequencies are dependant on the electrodes geometry.

In a second step, the electrodes were mounted in a holder equipped with a 6 mm or 12 mm diameter reservoir for the coplanar design. The influence of parameters like the conductivity of the solution injected in the reservoir, the electrode surface area, and the volume of solution in the reservoir were studied for the face-to-face design. Both face-to-face and coplanar designs were found to have a linear response with respect to the solution conductivity, and their response was proportionnal to the electrode surface area. The face-to-face design response was also proportional to the volume of the

solution present in the reservoir for the whole frequency range. However, in the coplanar design case, the capacitance created by the electrodes at low frequencies did not change when increasing the volume of the solution in the reservoir. This was not the case at high frequencies, where the resistance of the reservoir was found to decrease when increasing the volume, until a solution height equal to the diameter of the reservoir was reached. As the discrete model could not be used to describe the behaviour of the coplanar design in a reservoir, a new model using CPE elements was proposed. Finally, a new electrode design was developed to enable the use of the coplanar design in a channel.

Adsorption was monitored using a shift of the resonance peak frequency. The ideal way to follow such a shift would be to record the resonance peak position for each time step. The Solartron dielectric interfaces and frequency response analyzer available for this work provided an excellent performance regarding the impedance spectra recording, the signal-to-noise ratio of both spectrometers being strong. However, this equipment was to slow to monitor the resonance peak frequency variation in real time, and a choice had to be made between the time resolution or the frequency resolution. To compensate this weakness, the homemade software Plotgen was developed and permitted to find the best frequency range for monitoring the adsorption. The linearizer program was then written to correct the data. Nevertheless, these corrections rely on an imperfect model that needs to be fitted for each experiment. Thus, a fast spectrometer, with a high signal to noise ratio would be required to extract the full potential of the sensor. Using a channel flow, some kinetic parameters (k_{on} and k_{off}) of the adsorption could be extracted. The detection limit was reached for a 10 μg.mL^{-1} BSA solution using a coplanar design.

The face-to-face design was not able to detect the second adsorbed layer. This fact is mainly due to important diffusion effects in the reservoir. On the other side, the coplanar design was able to detect the second layer when monitoring around the resonance, but its behaviour is far more complicate than the face-to-face design. After having demonstrated the sensor ability to detect the second layer adsorption, an immunologic test was performed, using Anti-β-lactoglobulin antibodies as a first layer and blocking the surface with a 40 mg.mL^{-1} BSA solution.

The results reproducibility could be improved by manufacturing the chips in an industrial way, or by using microfabrication facilities.
The latter point would require a miniaturized version of the chip that would permit to control every parameter, and so may achieve a very good reproducibility. It would in the same time reduce the diffusional effects.

From the previous perspectives, we can conclude that this technique is still very young and would require some work to be improved. The full caracterization of the technique may be done by studying the desorption process and the adsorption reversability. The final immunoassay may be performed using a constant IgG concentration on the surface and various concentrations of β-lactoglobulin in the reservoir. The technique presents a good developement potential and may be able to challenge SPR techniques when cost and space are critical. Moreover, the miniaturization potential is relatively high and it is not impossible to imagine a credit card format of this device in a near future.

Appendix A

Discrete model program

A.1 Description

The discrete model program is used to generate the data from the model defined in 5.3.3 The frequency list are loaded from the freq.csv file. The model and its functions are then loaded. Later, the model calculate a value for each loaded function.

A.2 Code

```
/*-----------------------------------------------------------------
            Coplanar Discrete-model 0.8

            Brice Perruche
            LEPA - 2009
-----------------------------------------------------------------*/

#include <stdio.h>
#include <math.h>
#include <stdlib.h>
#include <complex.h>

#define PI 3.14159
#define w 2.0*PI
```

```
#define freq_plot 1

double freqtable[31];

double complex freq( int num ) {
     return (double complex) freqtable[num-2];
}

// Loading frequencies
void init_freq() {
     FILE *gp;
     char buffer[30];
     int i;
     gp = fopen("freq.csv","r");
     for( i=0; i<31; i++) {
          fscanf(gp,"%s",buffer);
          freqtable[i] = atof(buffer);
     }
     fclose(gp);
}


// Definition of the double parallel function
double complex para( double complex a , double complex b) {
     return 1.0/( 1.0/a + 1.0/b );
}

// Definition of the triple parallel function
double complex para3( double complex a , double complex b,
   double complex c) {
     return 1.0/( 1.0/a + 1.0/b + 1.0/c );
}

// Definition of the CPE function
double complex Zcps( double complex Csurf, double complex x,
   double complex powc )  {
     return (double complex) 1.0/(Csurf*cpow(I*w*x,powc));
}

// Definition of the  function
double complex Zj( double complex induct , double complex x) {
     return induct * I *w * x;
}
```

```
// Calculation of the y-axis coordinate function
double complex f(double x,double u) {
     return sinh(u)*sqrt(1.0-x*x/(cosh(u)*cosh(u)));
}


// Definition of the model
double complex Zc_cpe2(double gap, double width, double complex
    prof, double complex rho, double complex x, double capa,
   double Ralu, double powc ) {
     double complex y_glob = 0.0;
     double step=5e-7;
     double begin;
     double a,b;
     double length;
     begin = gap+width;
     while (  begin > (gap+step) ) {
          a = begin;
          b = gap*sinh( acosh(begin/gap) );
          // Calculation of the perimeter of the ellipse
          length = PI/2.0*( (a+b) + 3.0*pow((a-b),2.0)/( 10.0*(
             a+b) + sqrt(  pow(a,2.0)+ 14.0*a*b + pow(b,2.0)))
             );
          // Definition of the model admittance
          y_glob += para3( prof*step/(rho*length) , para(cpow(I
             *w*x,powc)*capa*step/width , Ralu*step/width) ,
             para(cpow(I*w*x,powc)*capa*step/width , Ralu*step/
             width) );
          begin-=step;
     }
     return 1.0/y_glob;
}


// Injection of the parameters into the model
double complex Zmodel( double x, double Csurf, double powc,
   double induct, double Ralu, int cpe ) {
     double gap = 0.5e-3;
     double width = 16e-3;
     double prof = 10.0e-3;
     double rho = 0.5;
```

```
        return Zc_cpe2( gap, width, prof, rho, x, Csurf, Ralu,
           powc )  +
        Zj(induct,x);
}

// Model caller
double complex Z(int num, int cpe) {
        return Zmodel( freq(num), 4500e-9, 0.955, 1.6e-6, 2e6, cpe
            );
}



// Calculation of the values from the model
double ReY( double complex z) {
        return  creal( 1.0/z);
}

double ImY( double complex z) {
        return  cimag( 1.0/z );
}

double ArgZ( double complex z) {
        return  carg( z);
}

double ReZ( double complex z) {
        return  creal( z);
}

double ImZ( double complex z) {
        return  cimag( z);
}



int main() {

int i;
double time=0.0, result;
init_freq();
FILE * gp;
double complex zmodel;
```

```
gp = fopen("sim-data-cpe1.csv","w");
for(i=2;i<33; i+=1) {
        time+=0.1;
        printf("Freq %e\n", (double) freq(i));
        zmodel = Z(i,1);
        fprintf(gp,"%e %e %e %e %e %e\n", (double) freq(i),ReY(
            zmodel),ImY(zmodel),ReZ(zmodel),ImZ(zmodel),ArgZ(zmodel
            ));
}
fclose(gp);



return 0;
}
```

Appendix B

Linearizer program

B.1 Description

When adsorbing to a single frequency in the resonance range, the evolution of the recorded data is not linear, as the the resonance shifts to lower frequencies. The linearizer program uses a model based on the CPE at high frequency to get the data and traduce it in an effective capacitance. The data are loaded using the load-file function. Then the data is fitted using the power parameter of the CPE. When the data and the model match, the frequency of the peak of the resonance is found using the dedicated ffreq model. As the value of the inductance has been previsouly fitted, the frequency can be directly traduced by in effective capacitance.

B.2 Code

```
/*-----------------------------------------------------------------
            Linearizer 1.0

            Brice Perruche
            LEPA - 2009
-----------------------------------------------------------------*/

#include <stdio.h>
#include <stdlib.h>
#include <string.h>
#include <complex.h>

#define PI 3.14159
#define w 2.0*PI

char param[20][500];
```

```
typedef struct datas {
     double *data, *dcorr, *values;
     char name[200];
     double ratio;
     int numdata;
     int lines;
     double capa;
} Datas;

double complex para( double complex a , double complex b) {
     return 1.0/( 1.0/a + 1.0/b );
}


double complex Zcps( double complex Csurf, double complex x,
   double complex powc )  {
     return (double complex) 1.0/(Csurf*cpow(I*w*x,powc));
}


double complex Zj( double complex induct , double complex x) {
     return induct * I *w * x;
}


double complex Zparam( double complex nb_elec, double complex x
   , double complex Csurf,
          double complex powc, double complex powe, double
             complex induct,
          double complex Rchannel, double complex rmisc)  {
     return    nb_elec*Zcps(Csurf,x,powc) +
     para( Rchannel , rmisc+nb_elec*Zcps(Csurf,x,powe) )
     + 2.0*Zj(induct,x);
}

double fpo(double powa, char p[20][500]) {
     return cimag( 1.0/Zparam(atof(p[7]), atof(p[5]), atof(p
        [9])
          , powa, atof(p[11]), atof(p[13]), atof(p[15]), atof(p
             [17])) );
}

double ffreq(double x, double value, char p[20][500] ) {
```

```
    return cimag( 1.0/Zparam(atof(p[7]), x, atof(p[9]), value,
        atof(p[11]),
         atof(p[13]), atof(p[15]), atof(p[17])) );
}

double * load_file(char * name, int * num ) {
    int rows, i=0, j=0, dt=28;
    FILE *gp;
    double * data;
    char filename[500];
    char *pcharbuffer;
    char buffer[50];

    //Counting number of elements in the file
    i=0;
    gp = fopen(name,"r");
    while (!feof(gp)) {
        fscanf(gp,"%s",buffer);
        i++;
    }
    fclose(gp);


    //Declare a tmp char buffer
    data = malloc (sizeof(data)*i*2 );


    //Loading data in general char table
    i=0;
    gp = fopen(name,"r");
    while (!feof(gp)) {
        fscanf(gp,"%s",buffer);
        data[i] = atof(buffer);
        i++;
    }
    fclose(gp);
    *num = i-1;
    return data;
}


void load_param(char * pfile[]) {
    FILE *gp;
    int i;
```

```
        printf("\n%s",pfile[1]);
        gp = fopen(pfile[1],"r");
        for( i=0; i<18; i++ ) {
                fscanf(gp,"%s",param[i]);
        }
        fclose(gp);
}



int main( int argc, char * argv[] ) {

FILE *gp;
int i;
int b,e,f;
double value, lb, step;
char buffer[1000];
load_param(argv);
sprintf(buffer,"%s/%s",param[1],param[3]);
printf("\n%s\n",buffer);

Datas f10;
strcpy(f10.name,buffer);
f10.numdata = 0;
f10.data = load_file( f10.name, &f10.numdata);

f10.dcorr = malloc( sizeof(f10.dcorr)*(f10.numdata-12)/12 );
f10.values = malloc( sizeof(f10.dcorr)*(f10.numdata-12)/12 );

b=0;

//---------- Fit of power ----------------------------------
for(i=28; i<f10.numdata-12; i+=12) {
        value = f10.data[i+9];
        f10.values[b]=value;
        step = 0.01;
        lb = 0.999;
        while (step > 1e-8) {
                while ( fpo(lb-step,param) < value ) {
                        lb -=step;
                }
                step /=2.0;
        }
```

```
        f10.dcorr[b] = lb;
        printf("\n Line %d : Val : %e    fit : %e  pow : %f",
              (i-28)/12,f10.data[i+9],fpo(lb,param),lb);
        b++;
}
f10.lines = b-1;

//———— Resonance peak frequency search ————————
b = 0;
gp = fopen(argv[2],"w");
for(i=0; i<f10.lines; i++) {
        value = f10.dcorr[i];
        step = 50000.0;
        lb = 100000.0;
        while (step > 1e-2) {
              while ( ffreq(lb+step, value, param) > 0 ) {
                    lb +=step;
              }
              step /=2.0;
        }
        f10.capa = lb;
        fprintf( gp, "%d %f %e %f %e\n",b, lb, 1.0/(2.0*atof(param
           [13])
              *(w*lb)*(w*lb)),f10.dcorr[i], f10.values[i] );
        printf( "\n%d %f %e",b, lb, 1.0/(2.0*9e-7*(w*lb)*(w*lb)) )
           ;
        b++;
}
fclose(gp);

return 0;
}
```

Appendix C

Plotgen

C.1 Description

Plotgen is used to extract and reorganize the data recorded by the Solartron device using the SMaRT software. Values like real and imaginary part of both admittance and impedance, phase, modulus, capacitance and Nyquist plots can be generated against the time or the frequency. The interface of Plotgen is written around the GTK+ library and uses Gnuplot to plot the data.

C.2 plotgen.c

```
/*********************************************************
                        PlotGen 2.1

                        Brice Perruche
                        LEPA - 2007


plotgen.c
_____________

This file is the main source code of PlotGen 2.1
*********************************************************/


#include <stdlib.h>
#include <string.h>
#include <gtk/gtk.h>
#include <pthread.h>
```

```
#include <unistd.h>
#include "plotgen2.h"
#include "plotgen-pdf.h"

void plot_update (  float *data, float *param, int *list, char
   *filename );
void export_plot();
void modify_huge_list(GtkWidget *pBtn, gpointer data);
void modify_list(GtkWidget *pBtn, gpointer data);
void modify_freq(GtkWidget *pBtn, gpointer data);
void export_data_csv();


int list[20000], slots_list[20000][3];
int leftcount, leftstate[2000], slots_leftstate[2000][3];
int slots_sel;
float freq_table[31];
float data[20000][12], slots_data[20000][12][3];
float param[50], slots_param[20000][3];
char buffer[40], slots_filename[3][500];
int intdata = 0, slots[3];
int radiosel=1;
pthread_t th_plot[10];
int state_plot[20] = {0,0,0,0,0,0,0,0,0,0,0,0,0,0,0,0,0,0,0,0};

GtkWidget *pcheck[2000];
GtkWidget *leftcheck[200];
GtkWidget *radio[31];
GtkWidget *entry[4];
GtkWidget *measure;
GtkWidget *h_main_panel;
GtkWidget *create_measure( void );


void plotgen_close() {
int i;
FILE * gp;
for ( i=2 ; i<12 ; i++ ) {
     param[i] = 0;
}

system("rm plotparam-rez.plt");
system("rm plotparam-rez_t.plt");
system("rm plotparam-imz.plt");
```

```
system("rm plotparam-imz_t.plt");
system("rm plotparam-rey.plt");
system("rm plotparam-rey_t.plt");
system("rm plotparam-imy.plt");
system("rm plotparam-imy_t.plt");
system("rm plotparam-argz.plt");
system("rm plotparam-argz_t.plt");
system("rm plotparam-nyz.plt");
system("rm plotparam-nyy.plt");
system("rm plotparam-capa.plt");
system("rm plotparam-capa_t.plt");
system("rm plotparam-absz.plt");
system("rm plotparam-absz_t.plt");
system("rm plotparam-absy.plt");
system("rm plotparam-absy_t.plt");
gtk_main_quit();
}


void file_radio_select( GtkWidget *radio, char *charsel ) {
int rows, i=0, j=0, dt=28;
FILE *gp;
char filename[500];
char * pcharbuffer;
radiosel=-radiosel;
int sel;

if ( radiosel >0 ) {
sel = atoi(charsel);



// Backuping active leftlist and list
for(i=0; i<2000 ; i++) {
slots_leftstate[i][(int) param[14]] = leftstate[i];
}
for(i=0; i<20000 ; i++) {
slots_list[i][(int) param[14]] = list[i];
}
param[14] = sel;

if ( (slots[sel]==0) || ((slots[sel]==1) && (strcmp(
   slots_filename[sel], gtk_entry_get_text(GTK_ENTRY(entry[sel
   ])) )) )) {
```

```
slots[sel]=1;
printf("\n\nSlot␣%d␣:␣%d␣->␣New␣file", sel, slots[sel]);
strcpy( filename, gtk_entry_get_text(GTK_ENTRY(entry[sel])));
strcpy ( slots_filename[sel] , filename);

i=0;
//Counting number of elements in the file
gp = fopen(filename,"r");
while (!feof(gp)) {
      fscanf(gp,"%s",buffer);
      i++;
}
fclose(gp);

//Declare a tmp char buffer

pcharbuffer = (char *) malloc (sizeof(pcharbuffer)*2*i*50 );

//Loading data in general char table
i=0;
gp = fopen(filename,"r");
while (!feof(gp)) {
      fscanf(gp,"%s",&pcharbuffer[i*50]);
      i++;
}
fclose(gp);

//Calculate row quantity
rows = (int) (i-dt)/12;


//Copying and converting data into rectangular table
for(j=0 ; j<rows ; j++) {
      for(i=0 ; i<12 ; i++) {
                  if ( strcmp(&pcharbuffer[ (dt+j*12+i)*50 ] , "-
                     ") ) {
                  data[j][i] = (float) atof(&pcharbuffer[ (dt+j
                     *12+i)*50 ]);
                  }
      }
}
free(pcharbuffer);

//Exporting table data to file and reserve RAM table
```

```
sprintf( buffer, "data%d.csv", sel );
gp = fopen(buffer,"w");
for(j=0 ; j<rows ; j++) {
      for(i=0 ; i<12 ; i++) {
            fprintf(gp,"%e ",data[j][i]);
            slots_data[j][i][sel] = data[j][i];
      }
      fprintf(gp,"\n");
}
fclose(gp);

// Generating list[20000] == 0
for ( i=0 ; i<20000 ; i++) {
      list[i] = 0;
      slots_list[i][sel] = 0;
}

// Generating leftlist
for(i=0; i<2000 ; i++) {
leftstate[i]=0;
slots_leftstate[i][sel] = 0;
}

//Calculating block quantity
param[13] = rows/31;
slots_param[13][sel] = param[13];

// Generating leftlist
for(i=0; i<((int) param[13])/10+1 ; i++) {
slots_leftstate[i][sel] = 1;
leftstate[i]=1;
}

// Putting checkers to 1
for ( i=0 ; i<(int) param[13] ; i++) {
      list[i] = 1;
      slots_list[i][sel] = 1;
}
} // end of if
else {// if slot = 1
printf("\n\nSlot %d : %d -> Same file", sel, slots[sel]);
for ( i=0 ; i<20000 ; i++) {
      list[i] = slots_list[i][sel];
}
```

```
for(i=0; i<2000 ; i++) {
      leftstate[i] = slots_leftstate[i][sel];
}
for(j=0 ; j<(int) param[13]*31 ; j++) {
      for(i=0 ; i<12 ; i++) {
            data[j][i] = slots_data[j][i][sel];
      }
}
param[13] = slots_param[13][sel];
} // end of else

// Generating plot quantity
param[16] = param[13];

// Updating measures panel
gtk_container_remove (GTK_CONTAINER (h_main_panel), measure);
measure = create_measure();
gtk_container_add (GTK_CONTAINER (h_main_panel), measure);
gtk_widget_set_usize(h_main_panel,-2,300);

// Reploting
//plot_init ( data, param, NULL, NULL );


// Threading
th_init( *data );
plot_update ( (float *) data, param, list, NULL );
}
}


void modify_time ( GtkWidget *radio, char *charsel  ) {
param[0] = atof(charsel);
plot_update ( (float *) data, param, list, NULL );
}


void modify_plt ( GtkWidget *radio, char *charsel  ) {
int i;
printf("\n%d", atoi(charsel));
param[atoi(charsel)] = -param[atoi(charsel)];
for(i=2 ; i<12 ; i++) {
      if(param[i]<0)
            state_plot[i-2]=0;
```

```
      printf("\nParam %d : %d   -> sp %d", i, (int) param[i],
         state_plot[i-2] );
}
param[15]=1;
plot_update ( (float *) data, param, list, NULL );
}


static void file_ok_sel( GtkWidget *w, GtkWidget *fs) {
gtk_entry_set_text(GTK_ENTRY(entry[3]) ,
   gtk_file_selection_get_filename (GTK_FILE_SELECTION (fs)) );
gtk_widget_destroy(fs);
gtk_entry_set_text(GTK_ENTRY(entry[intdata]) ,
   gtk_entry_get_text(GTK_ENTRY(entry[3])));
}


int file_selection( GtkWidget *widget, char *data ) {

intdata = atoi(data)-1;
GtkWidget *fselect;

fselect = gtk_file_selection_new( "Pick a file" );

g_signal_connect (G_OBJECT (fselect), "destroy", G_CALLBACK (
   gtk_widget_destroy), NULL);
g_signal_connect (G_OBJECT (GTK_FILE_SELECTION (fselect)->
   ok_button), "clicked", G_CALLBACK (file_ok_sel), (gpointer)
   fselect);
g_signal_connect_swapped (G_OBJECT (GTK_FILE_SELECTION (fselect
   )->cancel_button), "clicked", G_CALLBACK (gtk_widget_destroy
   ), G_OBJECT (fselect));
gtk_widget_show_all (fselect);
g_main_context_iteration (NULL, TRUE);
return 0;
}


GtkWidget *create_control ( void ) {
GtkWidget *vbox;
GtkWidget *separator;
GtkWidget *export_button;
GtkWidget *export_data;
GtkWidget *hbox[7];
```

```
GtkWidget *control_radio[3];
GtkWidget *file_button[3];
GtkWidget *file_radio[3];
GtkWidget *control_check[10];

vbox = gtk_vbox_new(FALSE, 0);

hbox[0] = gtk_hbox_new(FALSE, 0);
gtk_widget_show (hbox[0]);
gtk_container_add(GTK_CONTAINER(vbox),hbox[0]);

control_radio[0] = gtk_radio_button_new_with_label(NULL, "Both"
   );
gtk_box_pack_start(GTK_BOX (hbox[0]), control_radio[0], FALSE,
   FALSE, 25);
gtk_widget_show (control_radio[0]);

control_radio[1] = gtk_radio_button_new_with_label_from_widget(
   GTK_RADIO_BUTTON (control_radio[0]), "Freq");
gtk_box_pack_start(GTK_BOX (hbox[0]), control_radio[1], FALSE,
   FALSE, 0);
gtk_widget_show (control_radio[1]);
control_radio[2] = gtk_radio_button_new_with_label_from_widget(
   GTK_RADIO_BUTTON (control_radio[0]), "Time");
gtk_box_pack_start(GTK_BOX (hbox[0]), control_radio[2], FALSE,
   FALSE, 0);
gtk_widget_show (control_radio[2]);
g_signal_connect (G_OBJECT (control_radio[0]), "clicked",
   G_CALLBACK (modify_time), "0");
g_signal_connect (G_OBJECT (control_radio[1]), "clicked",
   G_CALLBACK (modify_time), "1");
g_signal_connect (G_OBJECT (control_radio[2]), "clicked",
   G_CALLBACK (modify_time), "2");

separator = gtk_hseparator_new ();
gtk_box_pack_start(GTK_BOX(vbox), separator, FALSE, FALSE, 0);

hbox[1] = gtk_hbox_new(FALSE, 0);
gtk_container_add(GTK_CONTAINER(vbox),hbox[1]);
gtk_widget_show (hbox[1]);
control_check[0] = gtk_check_button_new_with_label("ReZ");
gtk_box_pack_start(GTK_BOX (hbox[1]), control_check[0], FALSE,
   FALSE, 2);
```

```
gtk_toggle_button_set_active( GTK_TOGGLE_BUTTON(control_check
    [0]), 0 );
control_check[1] = gtk_check_button_new_with_label("ImZ");
gtk_box_pack_start(GTK_BOX (hbox[1]), control_check[1], FALSE,
    FALSE, 5);
gtk_toggle_button_set_active( GTK_TOGGLE_BUTTON(control_check
    [1]), 0 );
control_check[2] = gtk_check_button_new_with_label("ReY");
gtk_box_pack_start(GTK_BOX (hbox[1]), control_check[2], FALSE,
    FALSE, 5);
gtk_toggle_button_set_active( GTK_TOGGLE_BUTTON(control_check
    [2]), 0 );
control_check[3] = gtk_check_button_new_with_label("ImY");
gtk_box_pack_start(GTK_BOX (hbox[1]), control_check[3], FALSE,
    FALSE, 5);
gtk_toggle_button_set_active( GTK_TOGGLE_BUTTON(control_check
    [3]), 0 );

hbox[2] = gtk_hbox_new(FALSE, 0);
gtk_container_add(GTK_CONTAINER(vbox),hbox[2]);
gtk_widget_show (hbox[2]);
control_check[4] = gtk_check_button_new_with_label("ArgZ");
gtk_box_pack_start(GTK_BOX (hbox[2]), control_check[4], FALSE,
    FALSE, 2);
gtk_toggle_button_set_active( GTK_TOGGLE_BUTTON(control_check
    [4]), 0 );
control_check[5] = gtk_check_button_new_with_label("NyZ");
gtk_box_pack_start(GTK_BOX (hbox[2]), control_check[5], FALSE,
    FALSE, 0);
gtk_toggle_button_set_active( GTK_TOGGLE_BUTTON(control_check
    [5]), 0 );
control_check[6] = gtk_check_button_new_with_label("NyY");
gtk_box_pack_start(GTK_BOX (hbox[2]), control_check[6], FALSE,
    FALSE, 7);
gtk_toggle_button_set_active( GTK_TOGGLE_BUTTON(control_check
    [6]), 0 );
control_check[7] = gtk_check_button_new_with_label("Capa");
gtk_box_pack_start(GTK_BOX (hbox[2]), control_check[7], FALSE,
    FALSE, 2);
gtk_toggle_button_set_active( GTK_TOGGLE_BUTTON(control_check
    [7]), 0 );

hbox[3] = gtk_hbox_new(FALSE, 0);
gtk_container_add(GTK_CONTAINER(vbox),hbox[3]);
```

```
gtk_widget_show (hbox[3]);
control_check[8] = gtk_check_button_new_with_label("|Z|");
gtk_box_pack_start(GTK_BOX (hbox[3]), control_check[8], FALSE,
   FALSE, 2);
gtk_toggle_button_set_active( GTK_TOGGLE_BUTTON(control_check
   [8]), 0 );
control_check[9] = gtk_check_button_new_with_label("|Y|");
gtk_box_pack_start(GTK_BOX (hbox[3]), control_check[9], FALSE,
   FALSE, 14);
gtk_toggle_button_set_active( GTK_TOGGLE_BUTTON(control_check
   [9]), 0 );
export_button = gtk_button_new_with_label ("PDF");
gtk_box_pack_start(GTK_BOX (hbox[3]), export_button, FALSE,
   FALSE, 0);
export_data = gtk_button_new_with_label ("CSV");
gtk_box_pack_start(GTK_BOX (hbox[3]), export_data, FALSE, FALSE
   , 0);
g_signal_connect (G_OBJECT (control_check[0]), "clicked",
   G_CALLBACK (modify_plt), "2");
g_signal_connect (G_OBJECT (control_check[1]), "clicked",
   G_CALLBACK (modify_plt), "3");
g_signal_connect (G_OBJECT (control_check[2]), "clicked",
   G_CALLBACK (modify_plt), "4");
g_signal_connect (G_OBJECT (control_check[3]), "clicked",
   G_CALLBACK (modify_plt), "5");
g_signal_connect (G_OBJECT (control_check[4]), "clicked",
   G_CALLBACK (modify_plt), "6");
g_signal_connect (G_OBJECT (control_check[5]), "clicked",
   G_CALLBACK (modify_plt), "7");
g_signal_connect (G_OBJECT (control_check[6]), "clicked",
   G_CALLBACK (modify_plt), "8");
g_signal_connect (G_OBJECT (control_check[7]), "clicked",
   G_CALLBACK (modify_plt), "9");
g_signal_connect (G_OBJECT (control_check[8]), "clicked",
   G_CALLBACK (modify_plt), "10");
g_signal_connect (G_OBJECT (control_check[9]), "clicked",
   G_CALLBACK (modify_plt), "11");
g_signal_connect (G_OBJECT (export_button), "clicked",
   G_CALLBACK (export_plot), NULL);
g_signal_connect (G_OBJECT (export_data), "clicked", G_CALLBACK
    (export_data_csv), NULL);


separator = gtk_hseparator_new ();
```

```
gtk_box_pack_start(GTK_BOX(vbox), separator, FALSE, FALSE, 0);


hbox[4] = gtk_hbox_new(FALSE, 0);
gtk_container_add(GTK_CONTAINER(vbox),hbox[4]);
file_radio[0] = gtk_radio_button_new_with_label(NULL, "");
gtk_box_pack_start(GTK_BOX (hbox[4]), file_radio[0], FALSE,
   FALSE, 0);
g_signal_connect (G_OBJECT (file_radio[0]), "clicked",
   G_CALLBACK (file_radio_select), "0");
gtk_widget_show (file_radio[0]);
entry[0] = gtk_entry_new();
gtk_box_pack_start(GTK_BOX(hbox[4]), entry[0], FALSE, FALSE, 2)
   ;
gtk_widget_show(entry[0]);
gtk_widget_set_usize (entry[0], 170, -2);
file_button[0] = gtk_button_new_with_label ("File");
g_signal_connect (G_OBJECT (file_button[0]), "clicked",
   G_CALLBACK (file_selection), "1");
gtk_box_pack_start(GTK_BOX (hbox[4]), file_button[0], FALSE,
   FALSE, 0);
gtk_widget_show(file_button[0]);

hbox[5] = gtk_hbox_new(FALSE, 0);
gtk_container_add(GTK_CONTAINER(vbox),hbox[5]);
file_radio[1] = gtk_radio_button_new_with_label_from_widget(
   GTK_RADIO_BUTTON (file_radio[0]), "");
gtk_box_pack_start(GTK_BOX (hbox[5]), file_radio[1], FALSE,
   FALSE, 0);
g_signal_connect (G_OBJECT (file_radio[1]), "clicked",
   G_CALLBACK (file_radio_select), "1");
gtk_widget_show (file_radio[1]);
entry[1] = gtk_entry_new();
gtk_box_pack_start(GTK_BOX(hbox[5]), entry[1], FALSE, FALSE, 2)
   ;
gtk_widget_show(entry[1]);
gtk_widget_set_usize (entry[1], 170, -2);
file_button[1] = gtk_button_new_with_label ("File");
g_signal_connect (G_OBJECT (file_button[1]), "clicked",
   G_CALLBACK (file_selection), "2");
gtk_box_pack_start(GTK_BOX (hbox[5]), file_button[1], FALSE,
   FALSE, 0);
gtk_widget_show(file_button[1]);
```

```
hbox[6] = gtk_hbox_new(FALSE, 0);
gtk_container_add(GTK_CONTAINER(vbox),hbox[6]);
file_radio[2] = gtk_radio_button_new_with_label_from_widget(
   GTK_RADIO_BUTTON (file_radio[0]), "");
gtk_box_pack_start(GTK_BOX (hbox[6]), file_radio[2], FALSE,
   FALSE, 0);
g_signal_connect (G_OBJECT (file_radio[2]), "clicked",
   G_CALLBACK (file_radio_select), "2");
gtk_widget_show (file_radio[2]);
entry[2] = gtk_entry_new();
gtk_box_pack_start(GTK_BOX(hbox[6]), entry[2], FALSE, FALSE, 2)
   ;
gtk_widget_show(entry[2]);
gtk_widget_set_usize (entry[2], 170, -2);
file_button[2] = gtk_button_new_with_label ("File");
g_signal_connect (G_OBJECT (file_button[2]), "clicked",
   G_CALLBACK (file_selection), "3");
gtk_box_pack_start(GTK_BOX (hbox[6]), file_button[2], FALSE,
   FALSE, 0);
gtk_widget_show(file_button[2]);

entry[3] = gtk_entry_new();
gtk_widget_show_all (vbox);

return vbox;
}


GtkWidget *create_measure( void ) {

int i;
int rows = (int) param[13];
GtkWidget *scrolledwindow;
GtkWidget *viewport1;
GtkWidget *pVBox[1];
GtkWidget *LeftBox;
GtkWidget *hpaned;
GtkWidget *viewport2;

//
   ____________________________________________________________

// Declaration of the windowing interface
```

```
//
   ____________________________________________________________________


hpaned = gtk_hpaned_new ();
  gtk_widget_show (hpaned);

viewport2 = gtk_viewport_new (NULL, NULL);
gtk_widget_show (viewport2);
gtk_paned_pack1 (GTK_PANED (hpaned), viewport2, FALSE, FALSE);

LeftBox = gtk_vbox_new(FALSE, 0);
gtk_widget_show (LeftBox);
gtk_container_add(GTK_CONTAINER(viewport2),LeftBox);


scrolledwindow = gtk_scrolled_window_new (NULL, NULL);
gtk_widget_show (scrolledwindow);
gtk_paned_pack2 (GTK_PANED (hpaned), scrolledwindow, TRUE, TRUE
   );
gtk_scrolled_window_set_policy (GTK_SCROLLED_WINDOW (
   scrolledwindow), GTK_POLICY_NEVER, GTK_POLICY_AUTOMATIC);


viewport1 = gtk_viewport_new (NULL, NULL);
gtk_widget_show (viewport1);
gtk_container_add (GTK_CONTAINER (scrolledwindow), viewport1);

pVBox[0] = gtk_vbox_new(FALSE, 0);
gtk_widget_show (pVBox[0]);
gtk_container_add(GTK_CONTAINER(viewport1),pVBox[0]);

//
   ____________________________________________________________________

// Declaration of checkbuttons
//
   ____________________________________________________________________


leftcount = -1;
for (i=0 ; i<rows ; i++) {
     sprintf( buffer, "%d", i+1 );
     pcheck[i] = gtk_check_button_new_with_label(buffer);
```

```
        gtk_box_pack_start(GTK_BOX (pVBox[0]), pcheck[i], FALSE,
           FALSE, 0);
        if ( list[i] == 1 )
             gtk_toggle_button_set_active( GTK_TOGGLE_BUTTON(
                pcheck[i]), 1 );

        if ( (int) (i+1)/10  > leftcount ) {
             leftcount++;
             sprintf( buffer, "%d", leftcount*10 );
             leftcheck[leftcount] =
                gtk_check_button_new_with_label(buffer);
             gtk_box_pack_start(GTK_BOX (LeftBox), leftcheck[
                leftcount], FALSE, FALSE, 0);
             if ( leftstate[leftcount] == 1 )
                  gtk_toggle_button_set_active( GTK_TOGGLE_BUTTON(
                     leftcheck[leftcount]), 1 );
        }

}

gtk_widget_show_all(hpaned);

//
   ------------------------------------------------------------------

// Connection of buttons to signal
//
   ------------------------------------------------------------------


for (i=0 ; i<rows ; i++) {
g_signal_connect(G_OBJECT(pcheck[i]), "clicked", G_CALLBACK(
   modify_list), NULL);
}
for (i=0 ; i<rows/10+1 ; i++) {
g_signal_connect(G_OBJECT(leftcheck[i]), "clicked", G_CALLBACK(
   modify_huge_list), NULL);
}

return hpaned;
}


GtkWidget *create_freq( void ) {
```

```
int i;
float frequency;
GtkWidget *scrolledwindow;
GtkWidget *viewport;
GtkWidget *pVBox2;
FILE *gp;

scrolledwindow = gtk_scrolled_window_new (NULL, NULL);
gtk_widget_show (scrolledwindow);
gtk_scrolled_window_set_policy (GTK_SCROLLED_WINDOW (
   scrolledwindow), GTK_POLICY_NEVER, GTK_POLICY_AUTOMATIC);

viewport = gtk_viewport_new (NULL, NULL);
gtk_widget_show (viewport);
gtk_container_add (GTK_CONTAINER (scrolledwindow), viewport);

pVBox2 = gtk_vbox_new(FALSE, 0);
gtk_widget_show (pVBox2);
gtk_container_add(GTK_CONTAINER(viewport),pVBox2);


//Cr ation d'un fichier de fr quences
gp = fopen("freq.csv","r");

fscanf(gp,"%f",&frequency);
sprintf( buffer, "%f", frequency );
radio[0] = gtk_radio_button_new_with_label(NULL, "1000000");
gtk_box_pack_start(GTK_BOX (pVBox2), radio[0], FALSE, FALSE, 0)
   ;
gtk_widget_show (radio[0]);
freq_table[0] = 1000000;

for(i=1 ; i<31 ; i++) {
     fscanf(gp,"%f",&frequency);
     sprintf( buffer, "%f", frequency );
     freq_table[i] = frequency;
     radio[i] = gtk_radio_button_new_with_label_from_widget(
        GTK_RADIO_BUTTON (radio[0]), buffer);
     gtk_box_pack_start(GTK_BOX (pVBox2), radio[i], FALSE,
        FALSE, 0);
     gtk_widget_show (radio[i]);
}
fclose(gp);
```

```
gtk_toggle_button_set_active (GTK_TOGGLE_BUTTON (radio[0]),
   TRUE);
for(i=0 ; i<31 ; i++) {
g_signal_connect(G_OBJECT(radio[i]), "clicked", G_CALLBACK(
   modify_freq), radio[0]);
}

gtk_widget_show (scrolledwindow);
return scrolledwindow;
}


void modify_huge_list(GtkWidget *pBtn, gpointer data) {
     int i , j, rows;
     rows = (int) param[13];
     for( i=0 ; i<(int) param[13]/10+1 ; i++) {
        /* Le bouton est il selectionne */
          if(gtk_toggle_button_get_active(GTK_TOGGLE_BUTTON(
             leftcheck[i]))) {
               if ( leftstate[i] == 0 ) {
                    leftstate[i] = 1;
                    for ( j=i*10; (( j<i*10+10) && (j<=rows));
                       j++) {
                         if (j>0)
                         gtk_toggle_button_set_active(
                            GTK_TOGGLE_BUTTON(pcheck[j-1]), 1 )
                            ;
                    }
                    modify_list(NULL, NULL);
               }
          }
          else {
               if ( leftstate[i] == 1 ) {
                    leftstate[i] = 0;
                    for ( j=i*10; ( (j<i*10+10) && (j<=rows));
                       j++) {
                         if (j>0)
                         gtk_toggle_button_set_active(
                            GTK_TOGGLE_BUTTON(pcheck[j-1]), 0 )
                            ;
                    }
                    modify_list(NULL, NULL);
               }
```

```
            }
        }
        g_main_context_iteration (NULL, FALSE);
}


void modify_list(GtkWidget *pBtn, gpointer data) {

int i;
printf("\nRows quantity");
param[16] = 0.0;
for( i=0 ; i<(int) param[13] ; i++) {

            list[i]=0;
            /* Le bouton est il selectionne */
if(gtk_toggle_button_get_active(GTK_TOGGLE_BUTTON(pcheck[i])))
    {
            list[i]=1;
        param[16] = param[16] + 1.0;
}
}
param[15]=0;
plot_update ( data, param, list, NULL );
}


void modify_freq( GtkWidget *pBtn, gpointer data ) {

GSList *rlist;
rlist = gtk_radio_button_get_group(GTK_RADIO_BUTTON(data));
int i = 0, freq = 0;;
while (rlist) {
        if(gtk_toggle_button_get_active(GTK_TOGGLE_BUTTON(rlist->
            data))) {
                freq=30-i;
                rlist=NULL;
        }
        rlist = g_slist_next(rlist);
        i++;
}
param[1] = freq;
plot_update ( data, param, list, NULL );
}
```

```
void main_init()  {

int i;
FILE * gp;
char names[18][500] = {"rez", "imz", "rey", "imy", "argz", "nyz
   ", "nyy", "capa", "absz", "absy", "rez_t", "imz_t", "rey_t",
    "imy_t", "argz_t", "capa_t", "absz_t", "absy_t"};

for( i=0 ; i<18 ; i++) {
      sprintf(buffer, "loader-%s.plt", names[i] );
      gp = fopen(buffer, "w");
      fprintf(gp,"load \"plotparam-%s.plt\"\n",names[i]);
      fprintf(gp,"reread");
      fclose(gp);
}

for ( i=0; i<3; i++ )
      slots[i] = 0;

param[0] = 0;
param[1] = 0;
for ( i=2; i<12; i++ )
      param[i]=-1;
//param[5] = 1;
//param[6] = 1;
param[12] = 0.0;
param[13] = 40;
param[14] = 0;
}


void export_data_csv() {

      system("mkdir csv");
      system("cp rez.csv csv");
      system("cp imz.csv csv");
      system("cp rey.csv csv");
      system("cp imy.csv csv");
      system("cp absz.csv csv");
      system("cp absy.csv csv");
      system("cp nyz.csv csv");
      system("cp nyy.csv csv");
```

```
    system("cp argz.csv csv");
    system("cp capa.csv csv");
    system("cp rez_t.csv csv");
    system("cp imz_t.csv csv");
    system("cp rey_t.csv csv");
    system("cp imy_t.csv csv");
    system("cp absz_t.csv csv");
    system("cp absy_t.csv csv");
    system("cp nyz_t.csv csv");
    system("cp nyy_t.csv csv");
    system("cp argz_t.csv csv");
    system("cp capa_t.csv csv");
}



int main(int argc, char **argv) {
printf("\nFinal launch OK");
GtkWidget *window;
GtkWidget *vpanel;
GtkWidget *freq;
GtkWidget *control;


gtk_init(&argc, &argv);

main_init();




window = gtk_window_new (GTK_WINDOW_TOPLEVEL);
    gtk_window_set_title (GTK_WINDOW (window), "PlotGen 2.1");
    g_signal_connect (G_OBJECT (window), "destroy",
                      G_CALLBACK (plotgen_close), NULL);
    gtk_widget_set_size_request (GTK_WIDGET (window), 250, 600)
       ;

vpanel = gtk_vpaned_new ();
    gtk_container_add (GTK_CONTAINER (window), vpanel);
    gtk_widget_show (vpanel);

control = create_control();
gtk_paned_pack1 (GTK_PANED (vpanel), control, TRUE, TRUE);
```

```
gtk_widget_show (control);

h_main_panel = gtk_hpaned_new ();
gtk_paned_pack2 (GTK_PANED (vpanel), h_main_panel, TRUE, TRUE);
gtk_widget_set_usize(h_main_panel,-2,300);
gtk_widget_show (h_main_panel);

measure = create_measure();
gtk_paned_pack2 (GTK_PANED (h_main_panel), measure, TRUE, TRUE)
    ;
gtk_widget_show (measure);

freq = create_freq();
gtk_paned_pack1 (GTK_PANED (h_main_panel), freq, TRUE, TRUE);
gtk_widget_set_usize(freq,90,-2);
gtk_widget_show (freq);

gtk_widget_show (window);

gtk_main();

return 0;

}
```

Appendix D

Microchip mesh

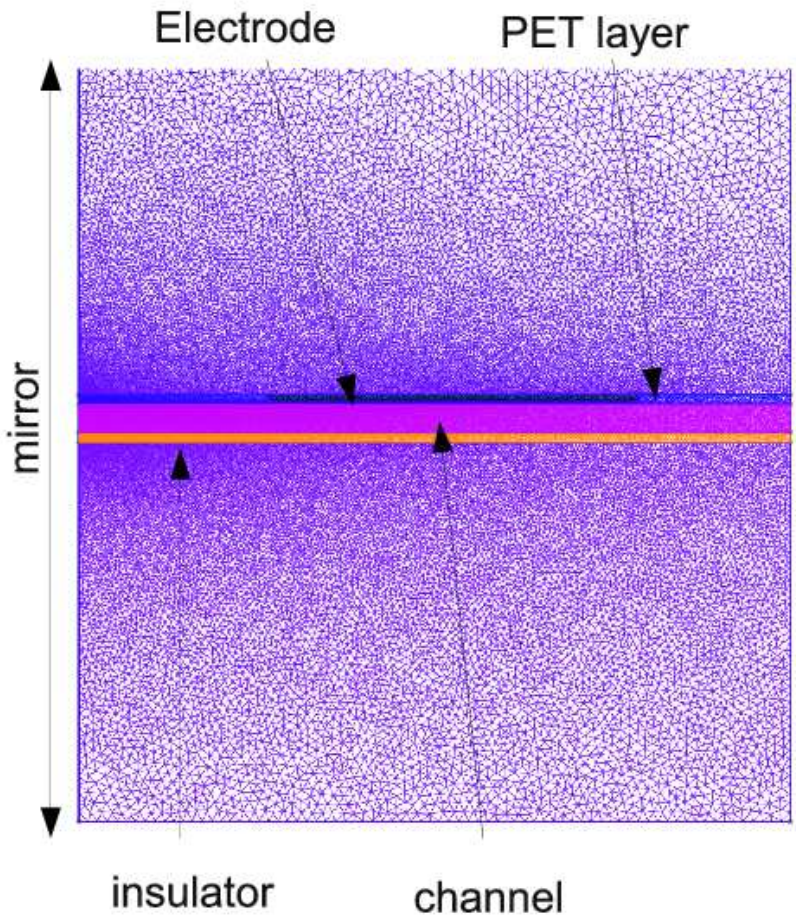

Figure D.1: Mesh of microhip using a coplanar design

Appendix E

Adsorption in 6 mm reservoir using a face-to-face design

Up to eleven different parameters can be considered to analyse the behaviour of the sensor.

Figure E.1 presents the imaginary part of the sensor ranging from 100 kHz to 1 MHz for an adsorption experiment of BSA (State of the sensor at the beginning and at the end of the experiment). It can be observed thst the signal is shifted to lower frequencies after an adsorption.

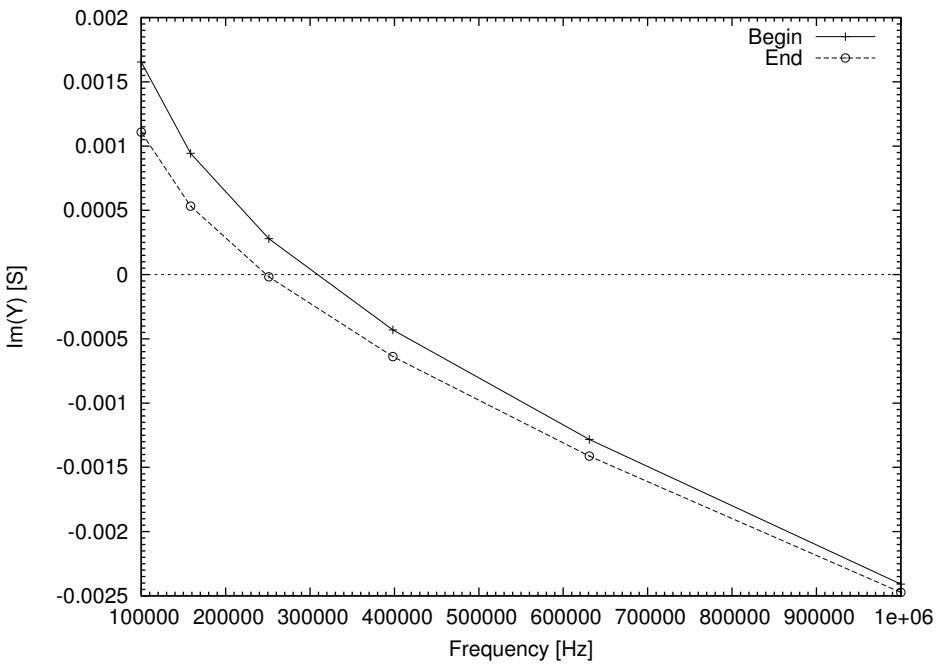

Figure E.1: Imaginary part of the admittance with respect to the frequency from 100 kHz tp 1 MHz, presenting the beginning and the end of an adsorption of BSA. The plots are close to be linear.

The same plot can be observed in logarithmic scale on Figure E.2, ranging from 1

Hz to 1 MHz. This figure presents the absolute value of the imaginary part of the admittance. This time the resonance appears as a peak, which shifts to lower frequencies after an adsorption. It can also be observed at low frequencies that the value of the admittance increases after the adsorption. This plot gives a more complete information than Figure E.1 and might then be prefered.

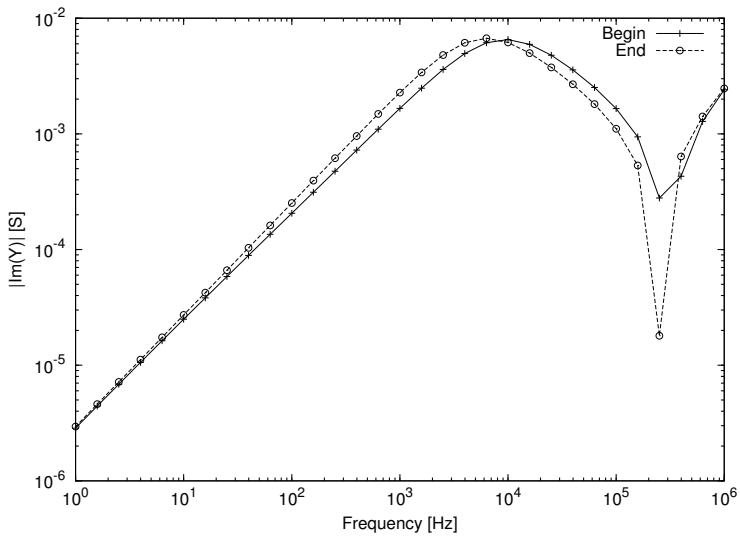

Figure E.2: Absolute value of the Imaginary part of the admittance with respect to the frequency from 1 Hz tp 1 MHz, presenting the beginning and the end of an adsorption of BSA.

Additionnal information on the behaviour of the imaginary part of the admittance sensor can be found on the capactance plot. The increment seen on Figure E.2 is presented here with finer details. The variation of the slope between the beginning and the end of the adsorption is due to a modification of the power coefficient of the Constant Phase Element. This directly traduces a modification of the surface state of the sensor.

The Real part of the impedance is presented on Figure E.4. As seen in the Chapter 5, the constant part seen at high frequencies represents the resistance of the reservoir. This part, only due to the solution in the reservoir, does not evoluate between the beginning and the end of the adsorption. The evolution of the low frequency part if directly due to the variation of the Constant Phase Element during the adsorption. As its power coefficient increases, the value of the real part of the impedance decreases, as described by Equation 2.27

The Real part of the admittance (Figure E.5) is the reverse of the real part of the impedance for high frequencies (1.3×10^{-2} S against 70 Ω). However this is not the case for lower frequencies. As the circuit is RC serial at low frequencies, the values of the capacitance and the resistance are mixed, giving a different value from the Real part of the impedance.

The Imaginary part of the impedance is the reverse of the imaginary part of the impedance, and so is not of much interest.

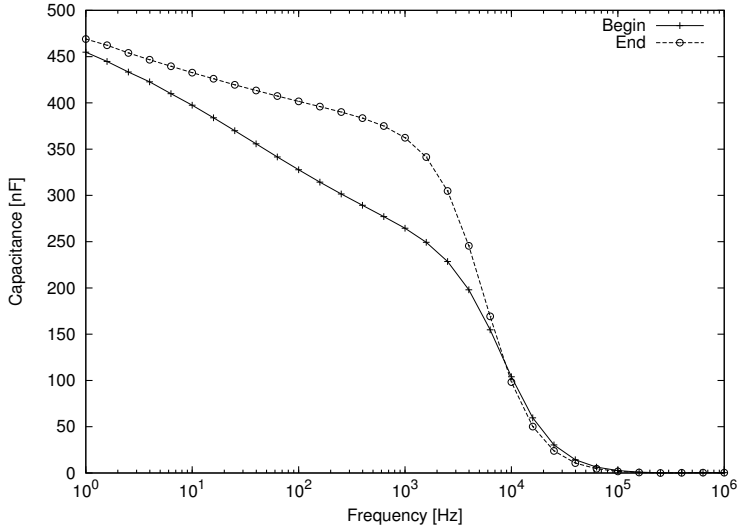

Figure E.3: Capacitance of the sensor with respect to a frequency ranging from 1 Hz to 1 MHz. The beginning and the end of an adsorption of BSA are presented.

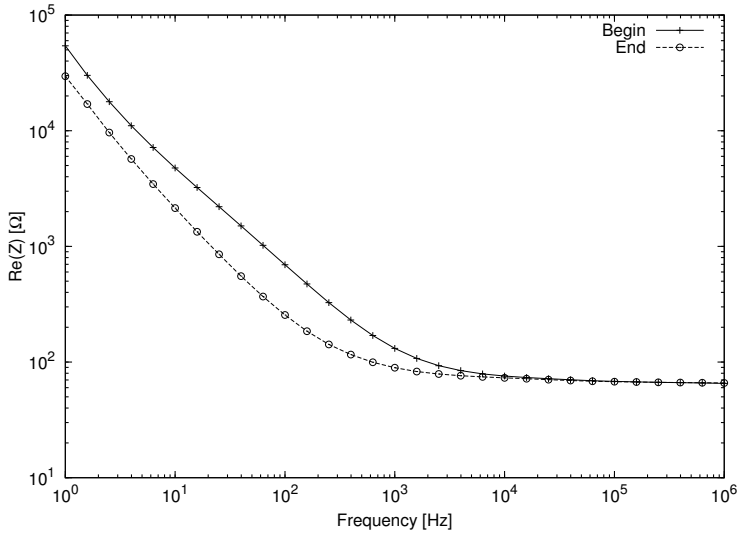

Figure E.4: Real part of the impedance with respect to a frequency ranging from 1 Hz to 1 MHz. The beginning and the end of an adsorption of BSA are presented.

The phase angle plot presents the behaviour regime (capacitive, resistive, inductive) of the sensor for a frequency ranging from 1 Hz to 1 MHz. As observed in Chapter 5, the sensor is capacitive at low frequencies and resistive at high frequencies, tending to become inductive after 1 MHz. It can be observed that the value of the pahse at low frequencies decreases when the BSA adsorbs on the electrodes.

The Absolute values of the impedance and admittance present a mix behavior between the real and imaginary parts. This behaviour obey to the state of the sensor determied by the phase angle plot. The resistive aspect of the sensor at high frequencies is found on the former plots to be equal to the behaviour of the real parts. The

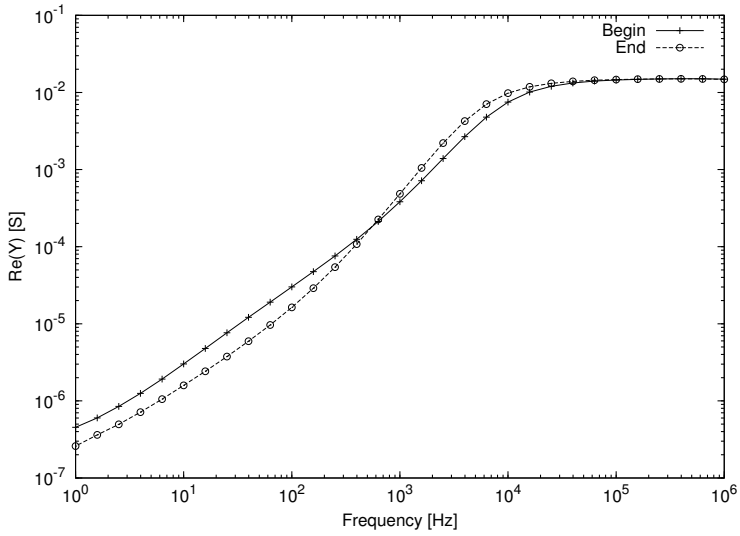

Figure E.5: Real part of the admittance with respect to a frequency ranging from 1 Hz to 1 MHz. The beginning and the end of an adsorption of BSA are presented.

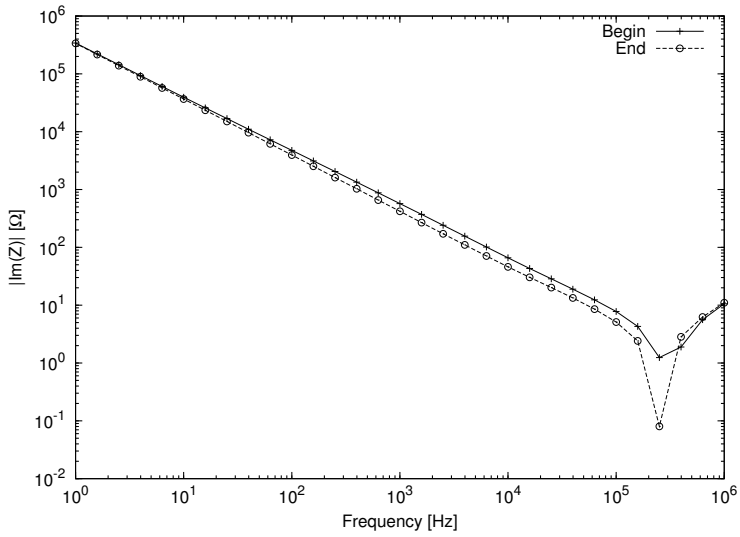

Figure E.6: Imaginary part of the impedance with respect to a frequency ranging from 1 Hz to 1 MHz. The beginning and the end of an adsorption of BSA are presented.

capacitive aspect at low frequencies present the same values than the imaginary parts. These plots could be useful, but in the goal to monitor an adsorption, the imaginary part of the admittance and the capacitive plots provide more information.

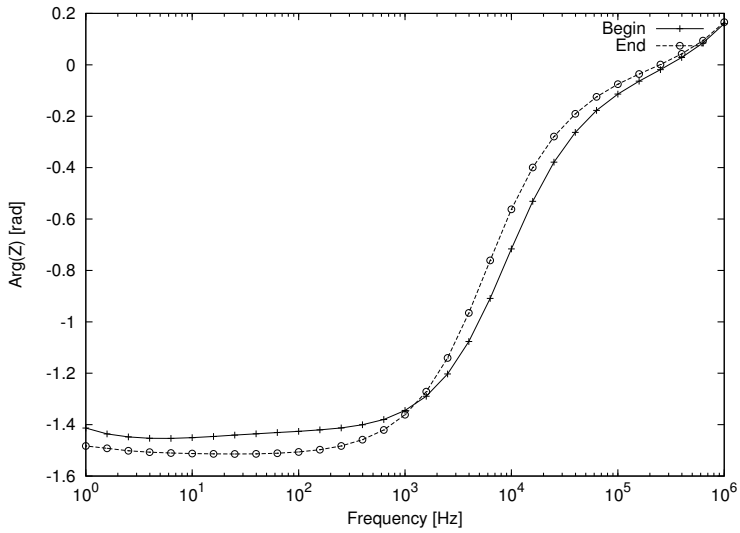

Figure E.7: Phase angle of the sensor with respect to a frequency ranging from 1 Hz to 1 MHz. The beginning and the end of an adsorption of BSA are presented.

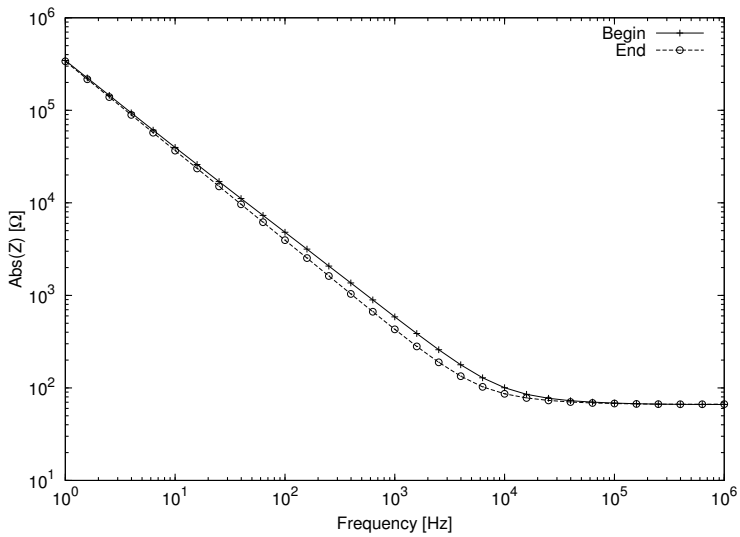

Figure E.8: Absolute value of the impedance with respect to a frequency ranging from 1 Hz to 1 MHz. The beginning and the end of an adsorption of BSA are presented.

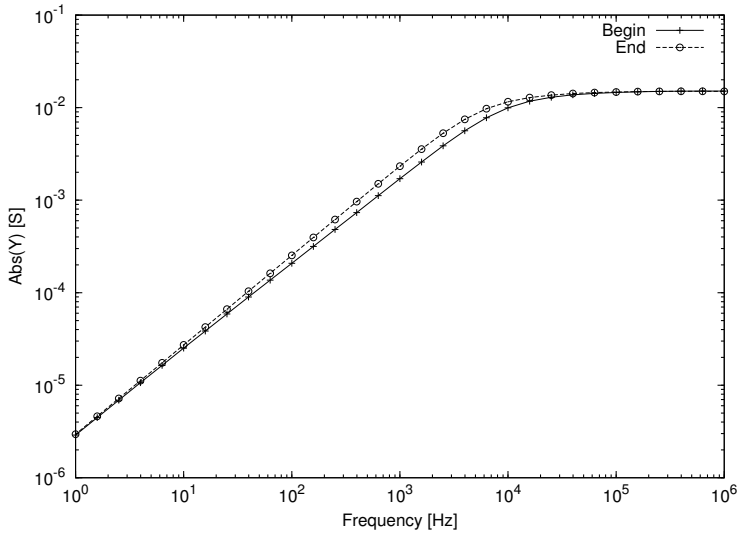

Figure E.9: Absolute value of the admittance with respect to a frequency ranging from 1 Hz to 1 MHz. The beginning and the end of an adsorption of BSA are presented.

Appendix F

Fick's equations

The Laplace transform of the first Fick Equation is:

$$\bar{J}(s) = D\left[A(s)\sqrt{\frac{s}{D}}\right] \tag{F.1}$$

while the Laplace transform of the second Fick Equation is:

$$\bar{c}(x,s) = \frac{c(x,0)}{s} + A(s)exp^{\sqrt{\frac{s}{D}}x} \tag{F.2}$$

Injecting $A(s)$ from Equation F.1 into Equation F.2, we obtain:

$$\bar{c}(x,s) = \frac{c(x,0)}{s} + \bar{J}(s)\sqrt{\frac{1}{Ds}}exp^{\sqrt{\frac{s}{D}}x} \tag{F.3}$$

$$-\bar{J}(s) = s\bar{\Gamma}(s) - \bar{\Gamma}(0) \tag{F.4}$$

Taking the assumption that all the sites are free at the beginning of the adsorption, Equation F.5 becomes:

$$-\bar{J}(s) = s\bar{\Gamma}(s) \tag{F.5}$$

Injecting $\bar{J}(s)$ from Equation F.5 into Equation F.3 gives:

$$\bar{c}(x,s) = \frac{c^0}{s} - \bar{\Gamma}(s)\sqrt{\frac{s}{D}}exp^{\sqrt{\frac{s}{D}}x} \tag{F.6}$$

Assuming that ψ <<1, the Langmuir Equation 6.3 can be linearized. Its Laplace transform is:

$$\bar{\Gamma}(s) = \Gamma_{max}Kc(0,s) \tag{F.7}$$

Taking $\bar{c}(0,s)$ from Equation F.7 into Equation F.6 on the surface (x=0), we obtain:

$$\frac{\bar{\Gamma}(s)}{K\Gamma_{max}} = \frac{c^0}{s} + \bar{\Gamma}(s)\sqrt{\frac{s}{D}} \tag{F.8}$$

which gives:

$$\bar{\Gamma}(s) = \frac{c^0}{s\left(\frac{1}{K\Gamma_{max}} + \sqrt{\frac{s}{D}}\right)} \tag{F.9}$$

Injecting Equation F.9 into Equation F.6, we get:

$$\bar{c}(x,s) = \frac{c^0}{s} - \frac{c^0}{s\left(\frac{1}{K\Gamma_{max}} + \sqrt{\frac{s}{D}}\right)}\sqrt{\frac{s}{D}}exp^{\sqrt{\frac{s}{D}}x} \tag{F.10}$$

The concentration transform at the surface (x=0) is then:

$$\bar{c}(x,s) = \frac{c^0}{s} - \frac{c^0}{\sqrt{s}\left(\frac{\sqrt{D}}{K\Gamma_{max}} + \sqrt{s}\right)} \tag{F.11}$$

Taking the following reverse transform:

$$L\left\{exp(u^2t)erfc(u\sqrt{t}\right\} = \frac{1}{\sqrt{s}(\sqrt{s}+u)} \tag{F.12}$$

we obtain:

$$c_{surf}(t) = c^0\left[1 - exp(a^2Dt)erfc(a\sqrt{Dt})\right] \tag{F.13}$$

or

$$\Gamma_{eq} = \Gamma_{eq}\left[1 - exp(a^2Dt)erfc(a\sqrt{Dt})\right] \tag{F.14}$$

with

$$a = \frac{1}{K\Gamma_{max}} \tag{F.15}$$

Brice PERRUCHE 16/09/1982
Chemin des Plaines 11
1007 Lausanne
+41 78 800 71 16
brice.perruche@gmail.com

- **Physicist (Fluidic, Thermic, Nanotechnologies, Electromagnetism)**
- **Expertise in Numerical simulations- HPC / Software Development**

Physicist

Professional Experience

2005 - 2010 Laboratory of Physical and Analytical Chemistry (LEPA - EPFL)
PhD in Physics : Development of a **label-free**, **real-time** monitoring, **contactless capacitive immunosensor** to perform immunoassays. Realization of **numerical simulations** (finite elements) and **analytical models**, **microfabrication** of electrodes and fluidic channels in **clean room**.

2005 - 2009 Ecole Polytechnique Fédérale de Lausanne (EPFL)
Assistantship in FTIR-ATR practical work.
Administration of the computers devoted to the numerical simulations of the laboratory.

2005 Diagnoswiss – Monthey – Switzerland (Master's internship)
Determination of the optimal parameters for coupling a **surface acoustic wave** device with an immunoassay device to increase its sensitivity. The goals were reached within the 5 months imparted.

2003 and 2004 Laboratoire Gestion des Risques et Environnement (GRE) – Mulhouse – France (Maîtrise's internship, then summer job)
Realization of two **numerical models** (finite differences) for the adsorption of particles (nitrogen oxides) in a car exhaust to find the kinetic constants of the system. An optimization of the **solver** increased the solving speed by 100 times. This work was pursued during summer 2004 on a similar project.

Education

2005 - 2010 PhD thesis in Physics at the Laboratory of Physical and Analytical Chemistry (LEPA)
Ecole Polytechnique Fédérale de Lausanne (EPFL) – Switzerland

2004 - 2005 Master of Physics and Technologies (Nanotechnologies specialty) (with honours)
Claude Bernard Lyon 1 University - France

2001 - 2004 Maitrise in fluidic systems and energy management (with honours)
Louis Néel Science Faculty - Belfort - France

Skills

Techniques : AFM, STM, CVD, PE-CVD, SPR, FTIR-ATR, MS, lasers, microfabrication, clean room

Computing : Windows, Mac, Linux, Gnuplot, MS Office, OpenOffice, Inventor, LIMS
C language, Fortran, CUDA, OpenMP, MPI, OpenGL, GTK, HTML, Javascript
Flux-Expert, Comsol

Languages

French	English	Spanish	German
Mother tongue	Fluent	Medium level	Basic

Interests

Mountain bike, table tennis, volleyball, trekking
Photo, plane model

Peer reviewed publications

1. Abonnenc, M., Dayon, L., Perruche, B., Lion, N. & Girault, H. Electrospray micromixer chip for on-line derivatization and kinetic studies. *Analytical Chemistry* **80**, 3372-3378 (2008).
2. Rossier, J. et al. Microfluidic based immunoassay. *Nanobiotechnology* **1**, 311-312 (2005).